ASPECTS OF THE DESIGN AND PERFORMANCE OF BLOWER TUNNEL COMPONENTS

by

RABINDRA DOLATRAY MEHTA

DEPARTMENT OF AERONAUTICS
IMPERIAL COLLEGE
LONDON UNIVERSITY

A thesis submitted for the degree
of Doctor of Philosophy of the
University of London

November, 1978

TO MY PARENTS

SUMMARY

A blower tunnel is an open-circuit tunnel driven by a centrifugal blower at the entry: usually the blower is a standard commercial unit, rather than a special design, with a rotor carrying aerofoil-section blades as distinct from radial vanes. This project was initiated to gain a better understanding of the performance of blower tunnel components and so make their design more scientific, logical and successful. The design and performance of the blower, diffuser and screens are discussed in detail because of the strong influence of these components on tunnel performance. Some of the material has been presented in a review article (Mehta, 1977): this thesis contains extra original work and some of the discussion is superseded by the present one.

Design rules for wide-angle diffusers are presented, based mainly on correlations of data collected from existing designs. For a diffuser using gauze screens for boundary layer control, the important parameters are found to be the diffuser angle, area ratio, number of screens and the overall pressure drop coefficient of the screens.

Screens are by far the most popular means of preventing separation in wide-angle diffusers and so a detailed investigation was carried out on the effects of gauze screens on turbulent flow. An incidental finding is that commercial polyester screens yield more uniform flow, away from the boundary layers, than metal screens, evidently because they are more evenly woven. It is shown that geometric parameters, such as the open-area ratio and co-planarity of the screen, and aerodynamic parameters, such as the magnitude and direction of the incident flow, can affect the pressure drop and, hence,

the uniformity of the emerging flow-field. A more accurate formulation for the deflection coefficient or "refractive index" of a screen is also proposed.

Tests on single-inlet centrifugal blowers revealed vortices in the outlet flows. It is shown how this swirling motion can be used to advantage in preventing separation on the wide-angle diffuser walls.

Contraction and working section designs, which have been studied widely over the years, differ little between open-circuit and closed circuit tunnels, and are thus discussed here in lesser detail.

Details of an experiment on the effects of free-stream turbulence on large scale structure in turbulent mixing layers are also included.

ACKNOWLEDGEMENTS

I am extremely grateful to my supervisor, Professor P. Bradshaw for his guidance and inspiring supervision throughout the duration of this project.

Help from the technical staff, in particular Messrs. J. Coles, L. Eals, A. Gill and J. O'Leary is greatly acknowledged.

I would like to thank all my colleagues for many stimulating discussions and Mr. D. H. Wood and Dr. P. H. Hoffmann also for thoroughly checking the typescript.

Mrs. H. A. Bastin deserves a special mention for her very efficient typing and Mrs. K. S. Mehta for helping with the figure-tracings.

I am deeply indebted to all the members of my family for moral and financial support.

LIST OF CONTENTS

LIST OF FIGURES

Figure		Page

LIST OF SYMBOLS

Notation

A	Area <u>or</u> diffuser area ratio <u>or</u> log.law constant
C	Constant in Collar's equation
c	Contraction ratio
c_f	Skin friction coefficient
C_p	$= \frac{P - P_{at}}{\frac{1}{2}\rho U_{in}^2}$, local total pressure coefficient
d	Screen wire diameter <u>or</u> honeycomb cell diameter
d_w	Hot-wire diameter
E	Young's modulus <u>or</u> hot-wire total voltage output
e	Fluctuating voltage
F	Force coefficient parallel to the gauze
H	Power input <u>or</u> boundary layer shape parameter
H_f	Rate of heat transfer from hot-wire
h	Working section height
K	$= \frac{\Delta p}{q}$, screen pressure drop coefficient <u>or</u> Karman constant
K_{sum}	$= \sum \frac{\Delta p}{q}$, sum of pressure drop coefficients of all the screens in a diffuser
k	Wave number <u>or</u> thermal conductivity
k_f	Thermal conductivity of fluid
L	Diffuser length
ℓ	Screen mesh length <u>or</u> honeycomb cell length <u>or</u> hot-wire length
M	Moment coefficient for screened diffuser
Nu	Nusselt number
n	Number of screens within a diffuser

Notation

O.P.	$= \frac{\Delta p}{\frac{1}{2}\rho U_{ex}^2}$, blower operating point
P	Total pressure
p	Static pressure
Δp	Static pressure drop across screen <u>or</u> fan static-pressure rise
Q	Volume flow rate through blower
q	$= \frac{1}{2}\rho U^2$, dynamic pressure
R	Radius of curvature of surface
r_1	Inner radius of rotor
r_2	Outer radius of rotor
R	Overheat ratio
Re	Reynolds number
R_{uv}	$= \overline{uv}/\sqrt{\overline{u^2}}\sqrt{\overline{v^2}}$; u, v correlation coefficient
T	Mean temperature
T_f	Temperature of fluid
T_w	Temperature of wire
U, V, W	Mean velocity components; U-axial (x), V-normal (y), W-spanwise, (z)
u, v, w	Fluctuating velocity components
U_e	Free stream velocity
U_{ex}	$= \frac{Q}{A_{out}}$, average mean velocity of blower exit flow
u_τ	$= \sqrt{\tau_w/\rho}$, friction velocity
x	Axial distance in streamwise direction

Greek Symbols

α	$= \frac{\phi}{\theta}$, deflection coefficient of screen or temperature coefficient of resistivity
β	$= \left(1 - \frac{d}{\ell}\right)^2$, screen open-area ratio
δ	Boundary layer thickness or cross wire yaw angle
δ^*	Boundary layer displacement thickness
η	$= \dfrac{p_{out} - p_{in}}{\frac{1}{2}\rho(U_{in}^2 - U_{out}^2)}$, diffuser efficiency
θ	Boundary layer momentum thickness or angle between incident flow and local normal to the screen or half the diffuser angle
λ	$= \dfrac{H}{\frac{1}{2}\rho_o U_o^3 A_o}$, tunnel power factor
μ	Viscosity or $= \frac{1}{\alpha}$, screen refractive index
ν	$= \frac{\mu}{\rho}$, kinematic viscosity
ρ	Density
τ	Total shear stress
τ_w	Wall shear stress
ϕ	Angle between emerging flow and local normal to the screen or power spectral density
ψ	Cross-wire effective angle
ω	Fan rotational speed, rad/s or radian frequency

Subscripts

o	Working section (undisturbed)
1	Upstream of screen
2	Downstream of screen
at	Atmosphere

Subscripts

in	Inlet
out	Outlet
θ	Screen inclined to the incident flow

CHAPTER 1

INTRODUCTION

The design of a blower-driven wind tunnel such as that shown in Fig. 1.1 is a combination of art, science and commonsense, the last being the most essential. It is difficult and unwise to predict firm rules for tunnel design. This is mainly due to the wide variety of tunnel designs and the lack of understanding of the flow, in particular, turbulent shear layers in wind tunnel components like the diffuser, screens and the blower itself. Moreover, in blower tunnels, the return circuit flow through the laboratory, which can affect the tunnel flow symmetry significantly, depends on such varied factors as the size of the laboratory and the position of the tunnel and other obstacles. It is more feasible and sensible to predict approximate design boundaries based on data from existing tunnels which are known to perform satisfactorily. In this project, design boundaries or suggestions have been drawn both from data on existing tunnels and from results of some original experiments on the more important tunnel components.

The earliest wind tunnels were open-circuit suction designs with an unobstructed intake and an axial fan at the exit, Fig. 1.2, although the Wright Brothers' tunnel had an axial fan in the intake. The expanding passage or "diffuser" downstream of the working section is intended to decelerate the flow and recover some of its kinetic energy in the form of a static pressure rise, thus reducing power consumption. Some sort of transition section between the working section and the fan is essential unless the working section is circular, and the optimum fan efficiency is obtained if the cross-sectional area at the fan is between 2 and 3 times that of the working section so that some of the static pressure is recovered. It is, therefore, usual to place the fan near (often at) the end of the diffuser.

Since the 1930s, when the strong effect of free-stream turbulence in triggering early transition of the laminar boundary layer became apparent, emphasis has been laid on wind tunnels with low levels of turbulence and unsteadiness. Consequently, most wind tunnels too large for a laboratory, and many laboratory-size tunnels as well, have been designed as closed-circuit types to ensure a smooth return flow. A possible distinction between turbulence and irrotational unsteadiness, and their causes in wind tunnels, is discussed by Bradshaw and Pankhurst (1964). Essentially, working section disturbances with a wavelength greater than the working section length itself should be classified as unsteadiness and measured as such. Genuine turbulence can be regarded as consisting of random vortex lines and is, therefore, three-dimensional, rotational and has no strongly-preferred direction of motion. In high performance tunnels, mean velocity variations across the working section are expected to be less than $\pm$ 0.2% in magnitude and $\pm$ 0.1^{o} in direction about the mean, with a turbulence intensity level (measured with a low frequency cut-off corresponding to a wavelength equal to the length of the working section) less than 0.1%. The high pass filter setting may typically be 5 - 10 Hz, depending on the working section size, and the low pass setting, to discount the high frequency noise generated within the electronic equipment, about 10 KHz: little tunnel turbulence remains at frequencies above this.

It has been found that open-circuit blower tunnels with centrifugal blowers (with backward-facing aerofoil-type blades) at the entry, Fig. 1.1, are much less sensitive to disturbances in the entry flow than suction tunnels. Open-circuit tunnels usually have dust filters attached to their inlets which reduce these disturbances anyway. Also, centrifugal blowers run with reasonable steadiness and efficiency over a much wider range of flow conditions than axial fans do, so that quite large changes in power factor can be accepted. The power factor:-

$$\lambda = \frac{H}{\frac{1}{2}\rho_o U_o^3 A_o}$$

is defined as the ratio of input power to the rate of kinetic energy flux in the working section. Furthermore, disturbances or blockage in the working section can greatly affect the flow into a fan downstream but have virtually no aerodynamic effect on an upstream blower. Some of the first blower tunnels designed include: Clauser's boundary layer tunnel (1954) and the Liverpool University 4' x 2' tunnel (1959); the latter had an axial fan.

The general arrangement of a blower tunnel is similar to that of a suction tunnel. However, a diffuser is generally needed between the blower and the settling chamber, while the diffuser downstream of the working section is no longer necessary for the fan's sake. It may even be omitted if flexibility of working-section arrangements is more important than pressure recovery. Pressure recovery in the diffuser that matches the blower to the settling chamber is usually unimportant for reasons mentioned below, and it is now customary for this diffuser to be a rapid ("wide-angle") one with some means of boundary layer control. For a blower operating at maximum efficiency, the dynamic pressure at exit is much less than the static pressure rise and, therefore, only a few per cent of the working section dynamic pressure. Consequently, a small static pressure recovery or even an overall loss, due to boundary layer control devices, can be accepted in the wide-angle diffuser. Such diffusers have also been used for some time past in closed-circuit tunnels, usually between the fourth corner and the settling chamber: McLellan and Nichols (1942), Squire and Hogg (1944), RAE 4' x 3' (1946), Squire and Winter, (1953) and Cambridge University cascade tunnel (Rhoden, 1951). In both cases, the object is to reduce the overall length of the tunnel. Details of many tunnels, together with advice on low speed wind tunnel design, can be found in Bradshaw and Pankhurst (1964).

The main aim of wind tunnel design is to produce a steady flow with spatial uniformity in the working section, over a range of Reynolds numbers. The Reynolds number (Re), which is proportional to the ratio of a typical inertia force to a typical viscous force and strongly influences the behaviour of boundary layers and wakes, is the most important non-dimensional group as far as low speed wind tunnel design is concerned. It is not essential to reproduce the exact Re in model tests since transition of boundary layers can be artificially stimulated and quantities like the skin friction, whose variation with Re is known, modified accordingly. For a given Re, the required speed of the flow is inversely proportional to the model size. The upper speed limit for blower tunnels is set by the tunnel power and structural limitations. The power consumption of a tunnel increases as $(\text{speed})^3$ and loads on the tunnel structure and model increase as $(\text{speed})^2$. The annoyance value of draughts in the room also increases as $(\text{speed})^2$. Consequently, a working section Re per metre of more than about 3×10^6 (a speed of about 40 ms^{-1}) is rare in blower tunnels of whatever size, and commercial blowers capable of producing such a speed in a working section more than about 1 m^2 in area are also rare.

The configuration of a wind tunnel is often decided by the size of the working section. Most tunnels with a working section diameter greater than about a metre have return circuits with cascades of corner vanes. (The term "diameter" is defined as the diameter of a circle with the same cross-sectional area as the component). One of the main reasons for this is that a large open-circuit tunnel would be of rather inconvenient dimensions, mainly in length; in a return-circuit tunnel, the exit diffuser can accommodate the first corner. However, in order to save laboratory space or due to the lack of it, some blower tunnels nowadays also incorporate a corner in the exit diffuser, thus exhausting vertically upwards (or back towards the inlet with two corners). This problem is further magnified by the requirement that the open-tunnel axis must not be too near the ceiling, floor or side walls, and the inlet must not be closer than 1 - 1½ times its own diameter from the end wall. This is to ensure that the "open return" circuit through the laboratory is not unduly interfered with. It has been known for blowers placed with their inlet too near an obstruction to develop a "bath-tub" vortex at the entry which can result in a fall of the blower RPM and, hence, the efficiency. In some suction tunnel installations, a honeycomb or screen partition has to be fitted across the room to ensure that the return flow arrives at the entry with a relatively small degree of swirl, although in most cases, it is sufficient to install a honeycomb or splitter at the tunnel entry. On the other hand, a room containing an open-circuit tunnel should not be too large since the performance of these tunnels is liable to suffer from draughts which may themselves induce a vortex motion. Consequently, outdoor tunnels almost always have return-circuits.

On average, closed-circuit tunnels have a better flow and lower power factor than the average open-circuit tunnel mainly because most open-circuit tunnels are small and often without exit diffusers. Since the disturbed air from the working section is not directly recirculated in an open-circuit tunnel, and because of the absence of corner vanes in most cases, one would tend to believe the converse, and indeed the Indian Institute of Science at Bangalore has built a 14' x 9' (4.3 m x 2.7 m) open-circuit tunnel with a maximum speed of 350 ft/s (100 m/s) and a power factor of about 0.15. An important point to note is that the working section pressure in a blower tunnel with an exit diffuser is always less than atmospheric and so spurious jets, normal to the mainstream, result from holes left unpatched. Also, an open-circuit tunnel flow suffers less from temperature changes since it is not directly recirculated and so working section conditions are more nearly constant with time than those in an unvented return-circuit working section.

Blower tunnels are often used for cascade tests, boundary layer studies and similar work where the flow leaving the working section is greatly disturbed. The omission of an exit diffuser necessarily makes the power factor, λ greater than unity because the whole of the kinetic energy flux through the working section is lost at exit, but the gain in flexibility of working section arrangement usually outweighs this. Some of the blower tunnel working sections used in the Aeronautics Department at Imperial College are shown in Fig. 1.3. Even with such varied working section arrangements, a high-quality flow can be obtained in a well-designed blower tunnel. This, together with the saving of space and constructional costs, makes the blower tunnel an attractive proposition both for general purpose work and for specialised working section arrangements.

The main components of a blower tunnel, starting from the upstream end, are the centrifugal blower, wide-angle diffuser, settling chamber, contraction, working section and sometimes an exit diffuser, Fig. 1.1.

The air is sucked through the centrifugal blower inlet and a total-pressure rise imposed upon it. It is important to assess the quality of the flow from a centrifugal blower and how it changes with loading, because the performance of components downstream is dependent on it. In the wide-angle diffuser the cross-section is expanded, usually in the least possible axial distance subject to the avoidance of severe flow separation which can lead to unsteadiness in the working section flow. The most popular means of preventing severe separation in the diffuser is to install wire-gauze screens. Screens operate by reducing the total pressure of high-speed regions more than that of low-speed regions (e.g. boundary layers) so that downstream of the region of static pressure perturbations caused by the screens, the velocity is more uniform and the boundary layer further from separation. The screens in the wide-angle diffuser incidentally help to reduce the turbulence of the flow, but further screens and the honeycomb intended primarily to reduce turbulence are installed in the settling chamber, where the cross-sectional area is largest, so as to minimize the losses. The honeycomb reduces irregularities in the flow direction, removing any swirl still present, and reduces the turbulence level, and the screens improve the flow uniformity and steadiness besides further reducing the turbulence intensity. In the contraction, the mean velocity is increased and percentage spatial or temporal variations are further reduced. This flow, with the desired quality, then passes through the working section. The exit diffuser and corner option is settled by considering the tunnel power factor and working section flexibility. The order in which these components are discussed below reflects the relative importance attached to them as far as the tunnel performance is concerned, rather than a recommended sequence of design. Each chapter is nearly self-contained, vital information from other chapters being repeated for convenience.

We start the detailed discussion of blower-tunnel design with an account of the design and performance of wide-angle diffusers (Chapter 2) followed by a critical analysis of the flow through gauze screens (Chapter 3) and of the aerodynamic performance of centrifugal blowers with special reference to the exit flow (Chapter 4). The design of the remaining tunnel components, contraction, settling chamber and working section, is much the same as for return-circuit tunnels and is discussed in Chapter 5. Blower-tunnel design rules and suggestions derived or inferred from the previous chapters are summarized in the form of conclusions in Chapter 6.

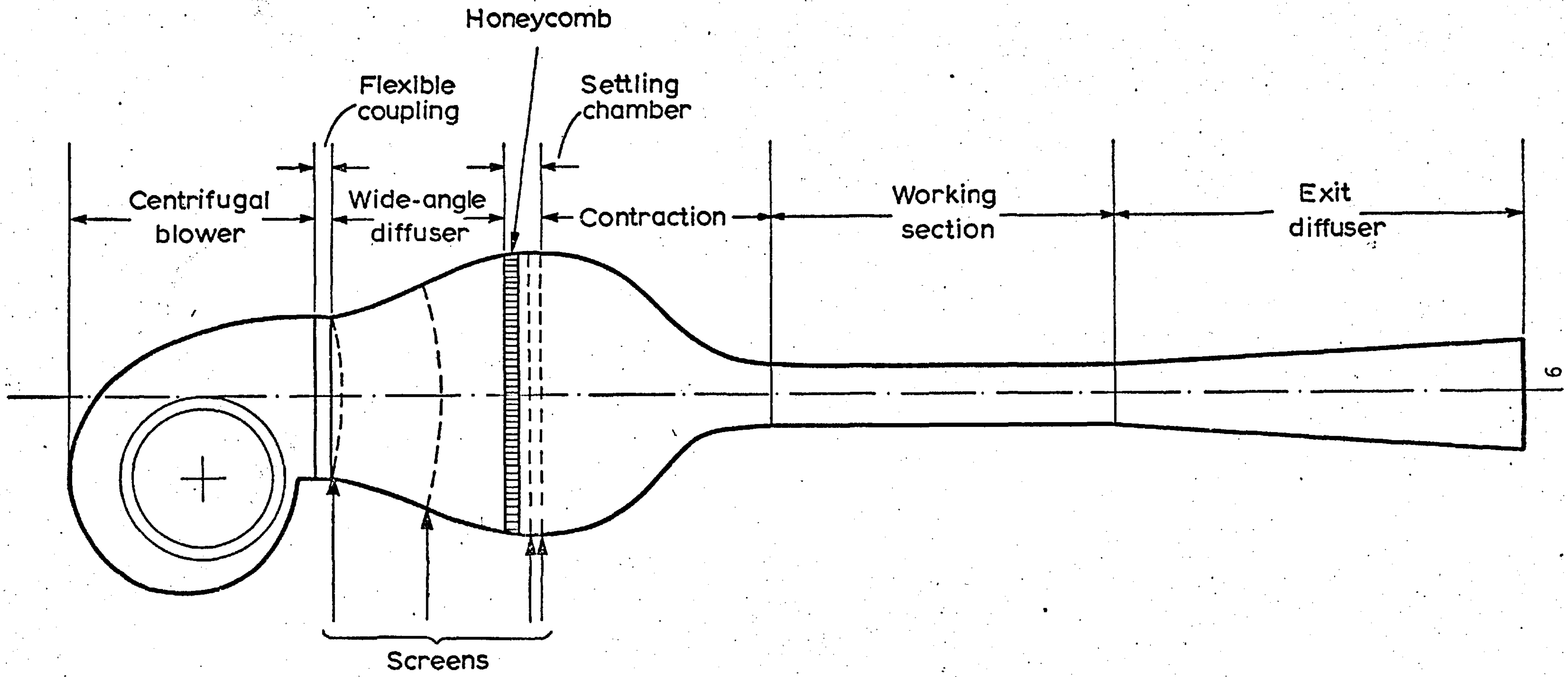

Fig. 1.1 The main components of a typical blower tunnel. (Not to scale)

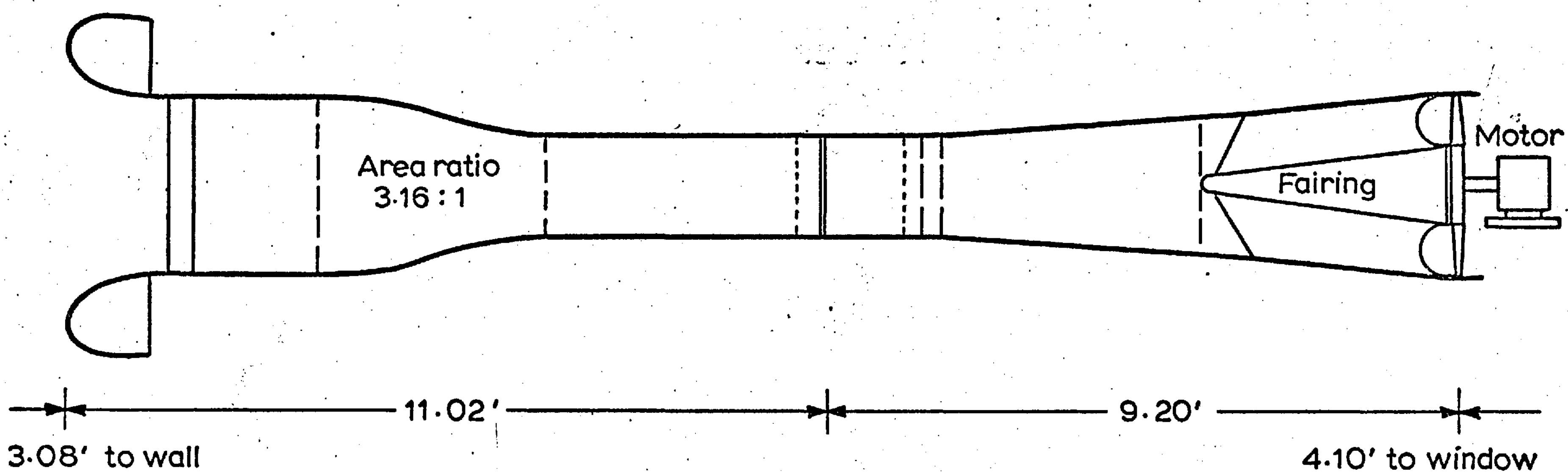

Fig. 1.2 NPL 18 in. suction tunnel (1947). (Bradshaw and Pankhurst, 1964).

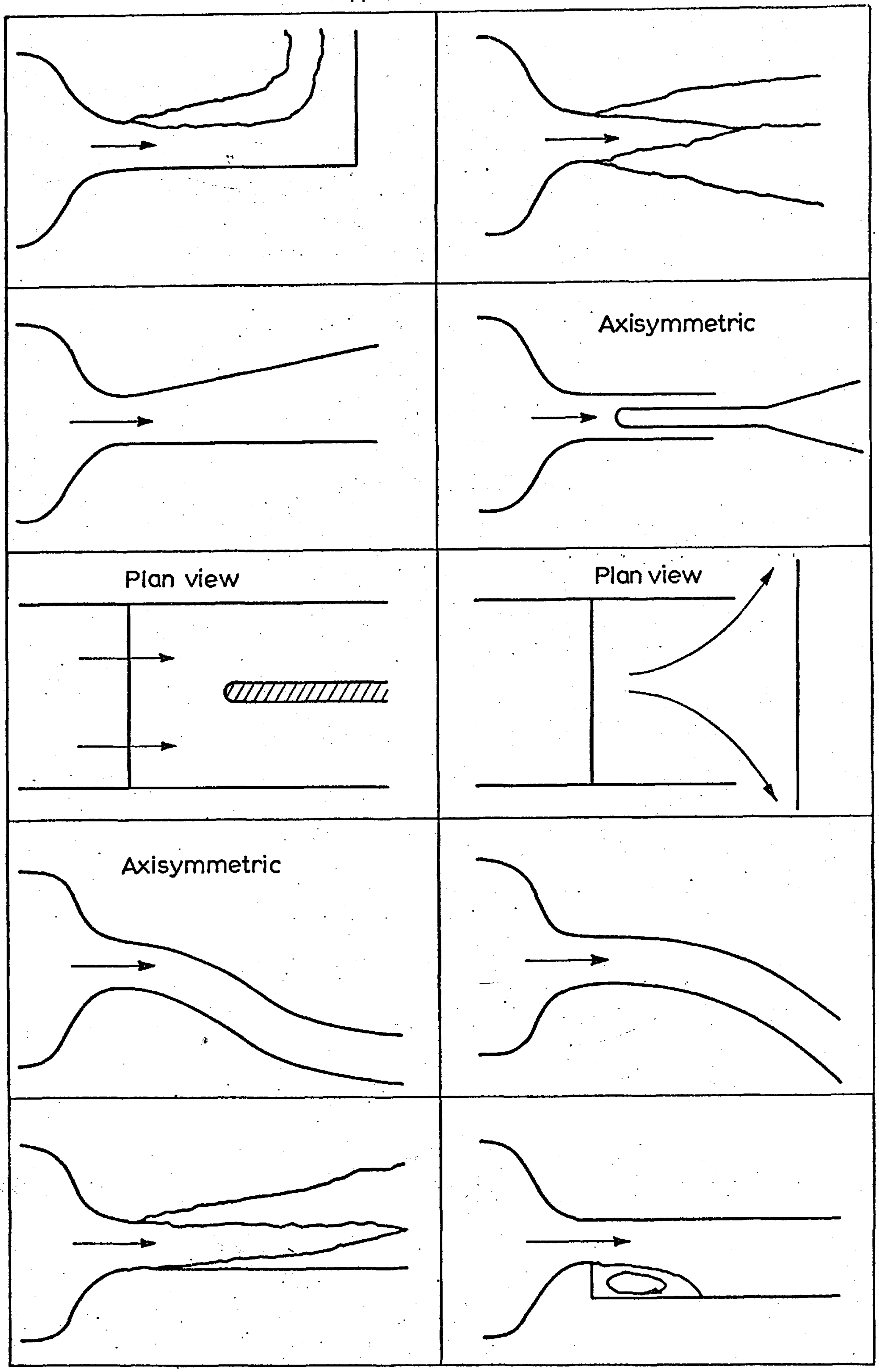

Fig. 1.3 Blower tunnel configurations used at Imperial College.
(Wavy lines are shear-layer edges).

CHAPTER 2

WIDE-ANGLE DIFFUSERS

2.1 General Considerations

Although diffusers are widely used, their flow characteristics are still not fully understood. The flow through a diffuser inevitably depends on its geometry, defined by the area ratio, wall expansion angle, cross-sectional shape and wall contour. Other parameters such as conditions at entry and exit and boundary layer control devices, if any, also affect the diffuser performance. With an arbitrary combination of these parameters, the flow through a diffuser becomes too difficult to predict in detail. The issue is further complicated by the occasional presence of boundary layer separation caused by the adverse pressure gradients necessarily present in a diffuser. It was in fact this separation in a conical diffuser that inspired Prandtl and in 1904, the concept of boundary layers emerged.

These features, coupled with the general problems of predicting the behaviour of turbulent flow, make the diffuser one of the least understood fluid flow devices. Almost all the knowledge acquired about diffusers is empirical.

Diffusers can be classified into two distinct categories:-

(i) Exit diffusers. Exit diffusers, as fitted, for example, after a wind tunnel working section, generally have very gentle expansions with an "equivalent cone angle" of between about 5^{o} (for best flow steadiness) and 10^{o} (for best pressure recovery), and an area ratio (outlet to inlet) not exceeding about 2.5. The equivalent cone angle of a diffuser is defined as the included angle of a circular cone having the same inlet area, outlet area and length as the given diffuser. In the case of a two-dimensional diffuser, the concept of an equivalent wedge is more useful. It is important to have a reasonable degree of flow steadiness in the exit diffuser, since otherwise the pressure recovery tends to fluctuate with time, and, therefore, so does the tunnel speed if the input power is nearly constant. The flow in this class of diffusers is intended to be fully attached and their design is fairly well catered for by existing methods. For a review, see Cockrell and Markland (1974).

(ii) Wide-angle diffusers. The uniformity of flow in a wind tunnel can be greatly improved if a contraction section or nozzle of large area ratio is provided immediately upstream of the working section. If a large diffuser area ratio is required, so as to provide a large contraction ratio, a long conventional diffuser, with an equivalent cone angle of 5°, is undesirable economically. For instance, if a contraction ratio of 12 is required, a 5° diffuser with a length of 20 times the working-section diameter would be needed. A short diffuser, with a large area ratio and, consequently, a large equivalent cone angle, is then installed. This is a "wide-angle" diffuser, defined as a diffuser in which the cross-sectional area increases so rapidly that separation can be avoided only by using boundary layer control. In this survey, all diffusers with an equivalent cone angle of greater than 6° are taken as wide-angle diffusers, although this is by no means a universal definition.

A wide-angle diffuser should be regarded as a means of reducing the length of a diffuser of given area ratio, rather than a device to effect pressure recovery. Uniformity and steadiness of the flow at the diffuser exit are of prime concern since this affects the performance of vital components downstream. In particular, intermittent separation in the wide-angle diffuser would almost certainly result in an unacceptable level of flow unsteadiness in the working section. Effectively, the static pressure rise is sacrificed for compactness and for uniformity and steadiness of the exit flow.

One of the most popular means of preventing separation in wide-angle diffusers is by introducing screens of perforated metal or, more usually, woven wire gauze. For the smaller blower tunnels, the cheaper plastic (nylon or polyester) mesh screens may be strong enough. A screen is usually specified by the "mesh", defined as the number of openings per lineal inch ($1/\ell$), and by the wire diameter (d). Given these two specifications, the screen open-area ratio β, equal to $(1 - d/\ell)^2$ for square meshes, can be determined.

Gauze screens make the velocity profile more uniform and thus reduce the boundary layer thickness. The ability of a boundary layer to withstand a given adverse pressure gradient is increased when the boundary layer thickness is decreased, because pressure-gradient parameters such as $(\delta^*/\tau_w)\,\frac{dp}{dx}$ are smaller for a given $\frac{dp}{dx}$. Therefore, a screen, besides removing the direct effects of boundary layer growth and incipient separations, gives the boundary layer a new lease of life so that a further pressure rise can be negotiated without separation. However, the corner flow in a wide-angle diffuser of rectangular cross-section is still liable to separate because of secondary flow effects, but, providing that the separation region remains confined to the corner region, this just "fills-up" the corners and does not present a major problem, especially since the pressure recovery is not of primary importance. Screens also reduce the turbulence intensity level in the whole flowfield and refract the incident flow, towards the local normal, downstream of the gauze. These last two factors, however, do not necessarily take the boundary layer further away from separation, although further downstream of the screen, the boundary layer growth rate could be reduced due to lower entrainment from the core flow which now has a lower turbulence level, remembering that tunnel boundary layers often have high free-stream turbulence - even when the flow is not a fully developed duct flow which it sometimes is.

The effectiveness of a conventional woven wire screen depends largely on its pressure drop coefficient (K), which is defined as the ratio of the static pressure drop across the screen (Δp) to the dynamic pressure of the uniform parallel flow approaching the screen ($q = \frac{1}{2}\rho U^2$). Thus, $K = \Delta p/q$; K is a function of β, the Re based on the wire diameter, and θ, the inlet flow angle. The refractive index of the screen (μ), defined as in optics, is about $0.9\sqrt{1 + K}$, for small angles of incidence. Allowance for its effect on lateral component velocity (Batchelor, 1970) modifies simple formulae for the attentuation factor for velocity non-uniformity. The simple formulae suggest that a single screen with K = 2 eliminates small non-uniformities.

A detailed analysis of flow through gauze screens is given below in Chapter 3.

In a wide-angle diffuser, it is better to use several screens, each with a relatively low value of K (say between 1 and 2) and preferably placed at the points where the flow would otherwise separate, than to use a single screen with a large K. This is because increasing K at one station in the diffuser has little effect on the skin friction at a station much further downstream. The most efficient diffuser, needing the fewest screens, is in general one with curved walls, which distributes the extent of the adverse pressure gradient. However, straight-wall diffusers, with discontinuities of wall slope at entry and exit, are easier to build and perform satisfactorily if the equivalent cone angle is not too large. In inviscid flow, a stagnation point occurs at a concave corner and an infinite velocity at a convex corner, and it is only the presence of the boundary layer that smooths out the flow. Even so, separation is liable to occur upstream of a concave corner (at least in the absence of boundary layer control) with reattachment further downstream, thus setting up a separation bubble in the corner. In the case of a convex corner, separation is liable to occur at the corner and persist for a long distance downstream. The positioning of screens, as will become apparent later, is also of vital importance, particularly in straight-wall diffusers.

Diffuser behaviour is greatly affected by the flow conditions at entry. A relatively thin boundary layer with steady flow conditions at entry would, no doubt, delay separation and improve pressure recovery considerably. Conversely, non-uniform or inclined entry flow can lead to early separation. Liepe (Kachhara, 1973) investigated the effect of swirling flow, characteristic of single-inlet centrifugal blowers (see Chapter 4), in conical diffusers and found that the distribution of longitudinal velocity component was more important than that of the circumferential one. Liepe concluded that although rotation decreased the diffuser efficiency, it was possible to use it to advantage in preventing separation. In our tests on centrifugal blowers (Section 4.2), it was also found that swirling flow could, if suitably controlled, aid flow attachment in a wide-angle diffuser. The effect of inlet conditions on the outlet velocity profile is less in screened diffusers than in any other type of diffuser because of the strong effect of gauze screens on the whole flowfield.

Diffuser efficiency (η) can be defined as the ratio of the gain in pressure energy to the loss in kinetic energy. For the simplest case where the velocity is uniform over the cross-section:-

$$\eta = \frac{p_{out} - p_{in}}{\frac{1}{2}\rho(U_{in}^2 - U_{out}^2)} \qquad (2.1)$$

This efficiency is generally low when the prevention of separation depends on the action of one or more screens. The principal losses are due to the pressure drop across the screens. Since, as explained in Chapter 1, this is not of primary importance in blower tunnel entry diffusers, little will be said about efficiency in what follows.

Section 2.2 presents an analysis of about a hundred wide-angle diffusers, installed mainly on low-speed wind tunnels. Section 2.3 reviews further wide-angle diffusers using boundary layer control devices other than screens and Section 2.4 is a discussion of design rules based on the analysis of Section 2.2.

2.2 Optimum Design Charts for Wide-Angle Diffusers

The four most important parameters in a wide-angle diffuser are:-

(i) the area ratio, A;

(ii) the diffuser angle, 2θ;

(iii) the number of screens within the diffuser, n;

(iv) the pressure drop coefficient of each screen, K.

The diffuser angle 2θ is defined as the angle between two straight lines joining the inlet to the outlet, as shown in Fig. 2.1. If the diffuser angles are different in plan view and in elevation, the larger is taken to define 2θ. This definition is slightly different from the "equivalent cone angle" defined in Section 2.1 but is probably more relevant for short diffusers.

In analysing published data, the pressure drop coefficient of each screen is estimated in terms of β, from Collar's (1939) equation: $K = C(1 - \beta)/\beta^2$, where the constant C is taken as 1. The validity of this equation for varying speeds and four different screens is discussed in Section 3.3.2. This formula may be consistently overestimating slightly for the screens near the diffuser entry, where the flow speed is relatively high, say greater than 10 m/s, and underestimating slightly for the screens near the exit. However, the overall effect on the present analysis is negligible.

Schubauer and Spangenberg (1948) inferred design rules from their own experimental results. In this investigation, data have been collected from many sources. Results are biased towards the Schubauer and Spangenberg rules because many later designers have relied on them, evidently successfully. The present analysis can be regarded as a reassessment and extension of the 1948 rules. Schubauer and Spangenberg used screens to obtain "fully filled" conditions (negligible regions of separation) in straight-walled diffusers of circular cross-section, aiming for zero pressure recovery. They also designed and tested a natural streamline-shape diffuser, and derived a relationship between A and K for straight-walled diffusers (Fig. 2.4).

The data collected for this analysis were taken not only from the "successful" diffusers, but also from a few in which separation occurred or which otherwise performed unsatisfactorily. A successful configuration is defined herein as one in which the flow is attached almost everywhere and has a fairly uniform velocity profile with an acceptable turbulence intensity level at the outlet. On the whole, diffusers of which their designers have been proud enough to write them up in the literature have been assumed successful. As well as recording parameters (i) to (iv) above, a note was made of some of the other geometrical parameters of the diffuser, like the cross-sectional and wall shapes, the screen shape (i.e. whether plane or curved), and of the type of wind tunnel (return or open-circuit) to which the particular diffuser was fitted. All the collected data are tabulated in chronological order in Table 1, and combinations of parameters are plotted in Figs. 2.2, 2.3 and 2.4.

It must be noted that most of the diffuser geometry measurements were taken from small published drawings and are thus susceptible to small errors. It is thought, however, that this will not affect the overall conclusions in any critical way.

In Fig. 2.2, the area ratio is plotted against the diffuser angle. The number of screens for each configuration is specified, and smooth curves have been drawn to enclose the successful configuration points for combination of 0, 1, 2 and 3 screens. The diffuser cross-section and wall shape for each configuration are also shown in this figure. The line AB differentiates between diffusers with straight walls and curved walls and curve CD is the zero-screen, unseparated-flow limit suggested by Kline <u>et al</u> (1957).

Fig. 2.3 is based on the same axes as Fig. 2.2, but to a different scale, and shows diffusers using various other methods for boundary layer control.

Fig. 2.4 is a plot of the sum of pressure drop coefficients of all the screens, K_{sum} $(\Sigma \frac{\Delta p}{q})$, vs area ratio. A straight line (EF) is drawn so as to include the maximum number of successful configurations, and passing through the point $K_{sum} = 0$, $A = 1$, which represents the limiting case of no diffuser at all. In this figure, diffusers containing curved screens are distinguished from those containing plane ones. A configuration is defined as containing curved screens if half or more of the total number of installed screens are curved. The dotted and chain-dotted lines in this figure show the formulae of Schubauer and Spangenberg (1948) and of Squire and Hogg (1944), respectively.

The implication of these results for wide-angle diffuser design are discussed in Section 2.4.

2.3 A Review of the Other Types of Boundary Layer Control Devices

2.3.1 Splitter System

The main effect of a splitter system is to increase the total displacement thickness of the boundary layers so that the effective diffusion angle becomes smaller. In potential flow, a symmetrically placed splitter would have no effect.

Splitters in wide-angle diffusers were extensively tested by Raju and Rao (1964). The system consisted of a conical diffuser, split into eight, roughly triangular, expanding passages. Assuming uniform or axisymmetric flow at the inlet, each passage captures an equal proportion of the diffuser mass flow. Due to boundary layer growth in the smaller included angle of the inner corners of the passages, a larger reduction of mass flow per unit area occurs along these corners. This, together with the high adverse pressure gradient, causes the flow to separate in the corner, and immediately a long bubble is formed near the diffuser axis, the rear portion containing a well-defined, intense vortex. The bubble deflects the incoming flow outwards and after passing through the narrow "throat", the flow is entrained by the vortex. A small separation trip placed on the cluster apex is sufficient to maintain the vortex-type flow pattern. The entrance loss can be reduced by sharpening the vane leading edges. Flow uniformity depends on the vortex position, which can be suitably varied. For this splitter, satisfactory uniform flow was obtained at the exit, with about 55% efficiency, at an area ratio of 15 (configuration 23).

Welsh (1976) reviews some passive flow control devices including one with radial spikes - "star" - which is a variation of the Raju and Rao idea, although this device has finite thickness and does not span the whole length of the diffuser. He found that a star with eight arms proved most satisfactory; the same number as Raju and Rao, although this system produced a double-peaked profile. The geometry and location of the star were found to be strongly dependent on the inlet flow condition. Welsh successfully used a star flow control device in a wide-angle diffuser of area ratio 4 and $2\theta = 22^o$ (configuration 57).

2.3.2 Suction Slots

The idea of using suction slots to control boundary layer separation is originally due to Griffith (Griffith and Meredith, 1936). The wall is shaped so that the diffuser has constant high velocity upstream of the slot and constant low velocity downstream. Thus, all the flow retardation takes place over the slot. Let us consider a streamline in the boundary layer, immediately upstream of the slot, above which the fluid possesses sufficient kinetic energy to overcome the pressure increase occurring across the slot. The streamline considered must then be made to stagnate on the downstream slot lip. Thus, by removing through the slot those fluid particles having insufficient kinetic energy to overcome the adverse pressure gradient, separation is prevented. This category of diffusers, like for example the Griffith diffuser, is found to have a performance far superior to that of comparable straight-walled diffusers. Yang et al (1973) also used slots satisfactorily on Griffith diffusers of both circular and annular cross-section (configuration 47). However, suction slots may not be very successful in diffusers with rectangular cross-sections.

A review of boundary layer suction experiments and methods of calculating laminar boundary layers with suction is given in Lachmann (1961).

2.3.3 Trapped Vortex

The original idea of separation control by a trapped vortex is due to Ringleb (1961). On the basis of potential flow theory, and using a few results from viscous flow theory, he derived the condition for a flow in a 2-D duct containing two standing vortices. The vortex energizes the boundary layer through forced mixing with the outer stream. Difficulty has been experienced in retaining a stable vortex system since energy is lost within the cusp due to skin friction.

There are two common methods of energizing the vortex. Haight and O'Donnell (1974) used a jet from a slot which reinserted into the flow the energy lost (configuration 48). Adkins (1975) used what is probably a simpler scheme, a "bleed-off" from the vortex, which is replaced by air of a higher energy level from the mainstream (configuration 52). By locating a fence just downstream of the vortex, the amount of bleed required for a given area ratio can be controlled. This diffuser exhibited low total pressure loss and high static pressure recovery, and so a high efficiency.

2.3.4 Vanes

Small inlet guide vanes placed near or at the diffuser inlet can improve performance appreciably (Moore and Kline, 1958). If the flow is at an incidence to the vanes in "side-view", they act as simple aerofoils, reducing the pressure gradient on the main wall, and this is believed to be their function and mechanism for separation delay. Moore and Kline used multiple, short, straight vanes placed just downstream of the throat and eliminated all separation up to diffuser angles of 45^{o} (configuration 13). For a wide-angle diffuser with $2\theta = 45^{o}$ and length-to-entrance-width ratio 8, five vanes (length to entrance width ratio $\approx$ 2) were successfully used.

A variation of this idea was used by Lawson (1971) for his "egg-box" diffuser. He expanded 3.46 : 1 from the swirl-free exit annulus of contra-rotating fans to a rectangular duct (height = tip diameter). Three uniformly spaced horizontal plates divided the diffuser into 4 equal area layers. Curved vertical vanes divided each layer into 8 equal-area ducts. The appreciable design and manufacturing effort produced a good outlet distribution with an efficiency of about 0.75.

Another variation of this is to use vortex generators, which shed longitudinal vortices, increasing mixing in the boundary layer. Mabey and Sawyer (1974) prevented separation in their wide-angle diffuser (configuration 50) by mounting two contra-rotating vortex generators of "gothic" planform at 15^o incidence. Taylor (1950) gives some useful design criteria for typical diffuser application.

2.3.5 Miscellaneous Methods

The Pope and Goin (1965) perforated cone is used in several blow-down supersonic wind tunnels. Their cone faces upstream from the settling chamber, into the diffuser, and straightens the flow through the numerous perforations. This type of cone, with an included angle of 90^o, was used by Azzouz and Pratt (1968) in their inlet diffuser ($A = 5.5$, $2\theta = 60^o$). Gibbings (1973) used a variation of this method and employed an upstream-pointing pyramid gauze in a wide-angle diffuser of area ratio 16.7 and $2\theta = 54^o$, a very severe geometry. These upstream-facing cones are used as flow straighteners rather than flow spreaders for which purpose a downstream-facing cone, fitted at the diffuser entry, would be more successful. The upstream-facing cone obviously has a smaller pressure drop and perhaps also acts like a splitter, reducing the overall diffuser angle.

Migay (Kachhara, 1973) used transverse ribs, with vortices set up in between, to prevent separation in a wide-angle diffuser. He found that the maximum advantage due to these was realised at $2\theta = 40 - 45^o$, when the energy spent in the vortices per unit of energy saved due to suppression of separation was a minimum.

Tennant (1973) used a form of moving wall for boundary layer control in a wide-angle diffuser. He had two cylinders, one on each side of the diffuser entrance, rotating in the flow direction. The slow-moving fluid in the boundary layer initially formed in the diffuser inlet is accelerated by the moving walls.

2.3.6 Summary of Boundary Layer Control Methods

Diffusers with very severe geometries (large A and 2θ) require a large number of screens for satisfactory performance. Access for cleaning becomes difficult and if the entry speed is high, the loading of the first few screens may be severe. All these factors suggest that other methods of boundary layer control may be preferable to screens for diffusers of extreme geometry.

All these boundary layer control methods increase mixing in the boundary layer above its natural level and so promote transport of momentum towards the wall, thus delaying separation. The effectiveness of these methods, therefore, falls with increase in entry boundary-layer thickness. These methods do have certain advantages over screens in that they can cope with solid particles or vapour that might be present in the stream and also do not support any large aerodynamic loads. Furthermore, vanes and splitter clusters can remove any swirl in the flow and can act as sound absorbers or heat exchangers.

However, for common diffuser geometries, screens should be used, since they serve two purposes by not only preventing or delaying separation, but also lowering the turbulence intensity level and generally steadying the flow. Most of the other devices, such as splitters and vanes, actually increase the turbulence level by shedding turbulent wakes. Moreover, screens are easier to install than most of the other boundary layer control devices discussed. The results of this survey (Figs. 2.2 and 2.3) seem to justify these suggestions.

2.4 Discussion

2.4.1 Design Rules

In Fig. 2.2, the curves enclose diffusers which are claimed or implied by their originators to be virtually free of separation, with fairly uniform velocity profiles and acceptable turbulence levels at exit. A few configurations that did not perform satisfactorily are also shown on the figure and most of them lie outside their respective curves. All the curves have an approximately hyperbolic shape. As the value of n increases, the hyperbola vertex moves to a higher value of 2θ and, to a lesser extent, also to a higher value of area ratio, thus implying a greater dependence of n on 2θ.

The asymptotic behaviour of the upper parts of the curves implies that one can have infinitely long diffusers, free of separation. According to Townsend (1976) the maximum diffuser angle for a 2-D channel, for which unidirectional, self-preserving, fully-developed flow is possible without any form of boundary layer control is 4.3^o. Thus, if we assume that roughly the same result applies to diffusers of near-square cross-section, all the curves should eventually asymptote towards a line $2\theta = 4.3^o$, since we are only considering a finite number of screens in the infinitely long diffusers. As far as the lower regions of the curves are concerned, there must exist an accepted separation limit line beyond which, with short and very wide-angled diffusers, we have, in effect, flow over a backward facing step. This maximum diffuser angle probably depends on the pressure-drop coefficient of the corner screen, but a safe limit suggested by the collected data in Fig. 2.2 is $2\theta = 55^o$.

The hypothesized limit line (EF) in Fig. 2.4, which is represented by the equation: $A = 1.14\ K_{sum} + 1$, includes not only most of the successful combinations, but also a few unsuccessful ones. These unsuccessful configurations satisfying the limiting line in this figure do not, as it turns out, satisfy their respective curves in Fig. 2.2.

These particular diffusers have about the right K_{sum} for the given area ratio, but too large a diffuser angle, and include configurations 3c and d, and 5f and i. On the other hand, the unsuccessful configuration 14d satisfies its curve in Fig. 2.2, but not the one in Fig. 2.4, implying that the number of screens installed is enough but not the overall K-value. There are no unsuccessful configurations satisfying both the hypothesized curves except 44 and 50, which will be discussed later.

Thus, an overall design hypothesis is put forward that if a diffuser configuration, with a sensibly-chosen wall shape and sensibly-located screens, satisfies its respective curves in both the Figs. 2.2 and 2.4, then it should perform successfully. Wall shape and screen location are discussed in more detail in Section 2.4.2.

A few of the apparently successful configurations do not satisfy both the hypothesized conditions. Although, as mentioned before, the curves are not inflexible, we now take a closer look at these so-called "abnormal" cases (5s, r; 12 and 23d, e). (Configurations 43 and 56 are used as test-cases and are discussed below in Section 2.4.3).

Diffuser 12 was used as a jet muffler and thus primary attention was given to reducing the noise level of the jet. The walls were made of perforated metal sheet with a 2 in thick outer covering of fibreglass. This arrangement could, in effect, provide suction at the walls, thus preventing possible separation. In any case, the flow did, apparently, separate at the sharp inlet corner. The other point to note is that this diffuser had a free outlet and thus the adverse static-pressure gradient is not increased just upstream of the outlet, as is the case with diffusers whose wall angle changes abruptly at the start of a parallel duct.

Raju and Rao (1964) tried various screen arrangements for their wide-angle diffuser ($A = 15$, $2\theta = 38^o$). About nine screen arrangements were found to give relatively steady flow, but only two (23d and e), gave a good degree of filled condition in the diffuser. The exit velocity profiles for these two arrangements were, however, found to be very similar to that of a fully developed turbulent pipe flow, implying a high turbulence intensity level, which may not be acceptable.

In the case of Schubauer and Spangenberg's (1948) diffuser A (5j, k, l), attached flow was achieved in all three cases, but 5j with the six 22-mesh screens gave an overall efficiency nearer to zero, the others giving negative efficiencies. With diffuser B, the suggested optimum combination (5r) of two 54-mesh and one 30-mesh screen gave a slight separation in the diffuser. The five 30-mesh screens (5p), although claimed to be "too many" seem to give a "fully filled" condition and this is the combination suggested for diffuser B by Figs. 2.2 and 2.4. The velocity profile for diffuser C (5s) showed that the boundary layer was quite thick and some asymmetry in the flow near the exit was also noted. This reinforces the suggestion of Fig. 2.4 that a higher K may be needed in this case.

2.4.2 Analysis of the Design Rules

The rules embodied in Figs. 2.2 and 2.4 seem to suggest a satisfactory procedure for wide-angle diffuser design, provided that certain other design factors are kept in mind.

In analysing these factors, it became apparent that diffuser designs fall into two major categories. In the first category are diffusers which are designed simply to fulfil the requirements - perhaps not very accurately specified in the first place - with the finer design points ignored. In the other category fall diffusers designed with a more cautious attitude, where all the optimum design points have been considered. The latter category includes the larger return-circuit wind tunnels because of the greater financial risks involved.

(i) Inlet conditions. The first important factor involves the flow conditions at entry to the diffuser, which, as discussed above, affect the diffuser performance markedly. In the case of diffuser 50a, it seems surprising that the flow should separate, considering its location in Fig. 2.2. The reason for malfunction could well be the rather thick boundary layers at the diffuser entry, and a high adverse pressure gradient in the diffuser, due to the high flow Mach number in the working section. On the other hand, Squire (1953) obtained attached flow in an unscreened diffuser of area ratio 16 and diffuser angle 10^{o}, presumably thanks to the thin inlet boundary layer. As will be seen in Section 4.2.2, the flow out of a centrifugal blower is far from uniform, but emerges in a swirling motion which is found to aid wall flow attachment and static pressure recovery (Neve and Wiransinghe, 1978).

(ii) Screen positioning. Wall shapes and screen location can be critical. Straight-walled diffusers really need screens at, or just inside, the inlet and outlet to suppress separation altogether, but even this is not essential for acceptable performance, as can be seen from the number of successful straight-walled, one-screen diffusers (Fig. 2.2). The basic rule, though, is to place a screen where the diffuser wall angle changes suddenly, since these are the points where the flow is most likely to separate. The screen positioning (and in fact also the screen shape) is, therefore, closely related to the wall shape.

A classic example of adverse screen positioning is provided by diffuser 44. This diffuser diverges in two sections, in one plane at a time. The two screens were not installed at the points where the wall angle changed, but halfway along each section. Moreover, a honeycomb was installed immediately upstream of the diffuser entry, thus straightening the flow which has then to be persuaded to expand through the diffuser - not a recommended design procedure. Thus this diffuser, although it satisfies both the suggested design criteria, failed to perform satisfactorily because some even more basic design factors had not been considered.

Often, in a diffuser without any abrupt changes in wall angle, a screen of relatively high resistance is placed near the entry, followed by one or two, depending on the geometry, of relatively lower resistance near the exit. Schubauer and Spangenberg (1948) showed that with one screen, the extent of separation was reduced by placing it nearer the diffuser entrance. A more precise guide to screen positioning is now proposed.

In diffusers where no obvious screen location is indicated, the following "moment-type" analysis may be applied. We start by defining three non-dimensional parameters:-

$$M_o = \sum_1^n K_r \equiv K_{sum} \tag{2.2}$$

$$M_1 = \frac{1}{M_o} \sum_{r=1}^{n} \frac{x_r}{L} K_r \tag{2.3}$$

$$M_2 = \frac{1}{M_0} \sum_{r=1}^{n} \left(\frac{x_r}{L} - \frac{1}{2}\right)^2 K_r \tag{2.4}$$

x_r denotes the location, measured from the inlet, of a screen with pressure drop coefficient K_r, and L is the overall diffuser length.

M_0 or K_{sum} defines the sum of the pressure drop coefficients of all the screens in the diffuser, and for a given area ratio, the minimum acceptable value of M_0 is given by Fig. 2.4. The number of screens required in the diffuser (n) can be determined from Fig. 2.2. For a given diffuser, having determined M_0 and n, the values of M_1 and M_2 have to be optimized by inserting suitable values of x_r/L in eqs. 2.3 and 2.4, respectively.

M_1 tends to zero if the screen positioning is biased towards the inlet and tends to unity if the screens are located nearer the outlet. The optimum value of M_1, for uniform screen distribution, is, therefore, about 0.5. The optimum value of M_2, which is related to the spacing between the screens, depends on the diffuser wall angle at inlet and outlet. Sharp inlet and outlet corners require screens if separation is to be avoided there. In this case, the optimum value of M_2 is about 0.17. On the other hand, if the diffuser has curved fairings at the corners (and the use of these is strongly recommended), then the optimum value of M_2 is about 0.04 (lower for a single screen). These values quoted for M_2 are essentially for $n \leq 4$.

Although these M-values should not be taken as infallible, they should be of use as a more concrete guide on screen positioning. If the diffuser entry conditions can be predicted accurately (which is rare in practice), then it is possible to calculate the flow in detail and thus predict the presence and location of boundary layer separation (e.g. Senoo and Nishi, 1977) and the screens can then be installed appropriately.

(iii) Wall shape (side-view). Straight-walled diffusers are easier and cheaper to construct, but curved-walled diffusers can be used to advantage. Often when large area ratios are involved, straight walled diffusers expanding in two sections, in one plane at a time, are employed. With these, it is advisable to expand in the horizontal plane first because of the undesirable effects of the blower tongue on the flow in the vertical plane.

The number of screens required in a diffuser employing curved walls could well be reduced, and the efficiency increased at the same time. It is evident from Fig. 2.2 that almost all the curved-wall diffusers lie to the right of line AB, given by the equation: $A = 0.1\ (2\theta) + 1$, thus implying that curved walls have been used on diffusers with the larger diffuser angles.

Gibson (1910) and Ackeret (Patterson, 1938) found that the diffuser efficiency was improved when the walls were bell-shaped, although large losses were experienced in the exit sections due to the higher adverse pressure gradients imposed there. Küchemann and Weber (1953) describe a trumpet-shaped diffuser with a resistance at the outlet. This type of diffuser was found to operate without separation and at the same time, pressure was also recovered.

Earlier, McLellan and Nichols (1942) conducted experiments on this type of trumpet diffuser and obtained satisfactory performance for $2\theta < 30^0$ and $A < 3$.

For this type of arrangement, the relation $A = \sqrt{1 + K}$ seems to hold well (private correspondence, D. M. Rao).

Squire and Hogg (1944) analysed the flow of a jet through a screen and this led to what is known as a streamline diffuser, with an inflected wall shape. The desirable condition of constant-pressure diffuser walls would be realised if these were shaped to coincide with the free streamlines of the jet. Pressure recovery would obviously not be possible, but flow separation could be prevented, and, according to Gibson (1959), the performance of such a diffuser might be superior to that of a diffuser with multiple screens, possibly involving an overall pressure loss. The same idea of shaping the walls was also used by Yang et al (1973), where instead of a screen, suction slots were used at a similar streamwise position. Schubauer and Spangenberg (1948) used this idea to design a successful one-screened diffuser (5s).

Potential flow methods are sometimes used to determine diffuser wall shapes. The common method is to represent the potential flow through the duct on a complex plane and specify the required boundary velocity on a hodograph plane. This is then related to the physical plane by conformal transformation. Kachhara (1973) used this method to design some axisymmetric screened-diffusers and found that, in general, the theoretical and experimental results differed, mainly due to the rapid boundary layer growth. He concluded that potential theory is justified in designing wall shapes for diffusers in which boundary layers do not separate, but remain thin along the entire length. These necessary conditions reflect the inadequacy of potential flow methods in simulating real flow situations. However, it is perhaps fair to say that potential flow methods are good enough in most cases, although it may be just as easy to design wall shapes by eye and then subject them to a trial and error treatment.

Very often, though, straight-walled diffusers are employed, with curved screens installed at the points of discontinuity in wall angle. Sharp inlet corners must, however, be avoided since they undoubtedly promote separation. The need for a radiused inlet was re-emphasized by the present author's measurements (Section 2.4.3). In the simplest case, the fairing need merely be a bent piece of plywood, tacked over the sharp corner.

(iv) <u>Screen shape</u>. It is an advantage for the screens to intersect the diverging walls and streamlines at right angles, so that the refraction of the flow by the screens does not itself tend to produce separation (see Section 3.1). So curved screens, usually spherical caps or circular arcs, are installed in the diffuser, usually where the wall angle changes, at right angles to the downstream wall so as to refract the flow in a desirable direction. Curved screens can be held in metal frames (e.g. channel sections) pressed into circular arcs and lined with wooden strips so that the gauze may be firmly embedded between two frames. In 2-D diffusers, the screens may be clamped on two sides only, with plenty of slack. It has been found (Bradshaw, 1972) that at practical tunnel speeds, the screens fill out into a nominal catenary shape with no apparent tendency to unsteadiness, although this would depend to some extent on the material of the screen. Small gaps on the unsupported sides do not seem to matter: in fact, they probably help in evening out the boundary layers on the four walls. On inspecting the collected data, it was found that in most cases curved screens had been used when the walls were curved as well.

Another alternative is to use a plane, "variable-K" screen. This normally comprises one screen, concentrically superimposed on another (with the same K-value). This combination then has a higher resistance in the centre and it thus imposes a higher pressure drop on the relatively higher speed regions near the diffuser axis. Kachhara (1973) found that for equivalent values of K, outlet profiles were more uniform with a plane "variable-K" gauze than with a plane "constant-K" gauze. He gives an optimum value, for uniform outlet profile, for the ratio of the screen diameters as 0.84. Of course, the losses through a "variable-K" gauze are greater due to the relatively higher K in the middle. A plane, "constant-K" screen will, in general, exhibit this "variable-K" effect in a wide-angle diffuser anyway since the pressure drop is reduced by streamline inclination (see Section 3.4.3) which is necessarily higher near the diffuser walls.

(v) Cross-sectional shape. Most of the diffusers plotted in Fig. 2.2, and especially those with an area ratio of over 3, are seen to have square or rectangular cross-sections. The main, obvious reason for this is that rectangular diffusers are much easier and cheaper to build than circular ones. It is advisable to fillet the corners between adjacent walls, especially in small tunnels, whose designs are likely to be more adventurous. Gibson (1910) considered the effects of three sectional shapes, circular, rectangular and square, on diffuser efficiency. He concluded that for a given rate of expansion, the circular duct was the most efficient, followed by the square one. As mentioned before, for wide-angle diffusers used as entry diffusers, as most of the ones plotted are, pressure recovery is not of major importance, and this probably explains the preference for square cross-sections in practice. Also this is a more convenient cross-sectional shape since most working sections and blower outlets are rectangular. So, unless pressure recovery is important, a rectangular or square diffuser cross-section (with corners filleted) is adequate.

(vi) Tunnel circuit. In Table 1, a note is made of the type of tunnel circuit from which the particular diffuser configuration is taken, and most are found to originate from open-circuit tunnels. This is because most return-circuit wind tunnels employ long, gradually expanding diffusers with 2θ of about 5^{0}, so that at most, only a moderate expansion through a wide-angle diffuser is needed. Most wide-angle diffusers, especially those of high area ratio, were designed for small blower tunnels and it is, therefore, not surprising to see (Table 1) that all the diffusers with $A > 4$ originate from open-circuit tunnels.

2.4.3 Comparison and Verification of Design Rules

The curve (CD) in Fig. 2.2 is the limiting curve for no appreciable separation, in a 2-D duct with no screens, as suggested by Kline et al (1957). Noting that it is for a 2-D duct, it still seems to suggest configurations of a very conservative nature. The general shape tends towards that of the newly hypothesized zero-screen limit.

In Fig. 2.4, the second postulated curve for successful operation is compared with two existing theories. For a diffuser with n screens, Schubauer and Spangenberg (1948) derived a formula for a straight-walled diffuser of circular cross-section, which gives the area ratio in terms of K for each screen as:-

$$\frac{A_n}{A_{in}} = (K_1 + 1)^{\frac{1}{2}}\ (K_2 + 1)^{\frac{1}{2}}\ \ldots\ (K_n + 1)^{\frac{1}{2}} \qquad (2.5)$$

Since a diffuser with two screens of equal K is quite a common configuration, this optimum combination line is plotted (dotted in Fig. 2.4) using this formula, which reduces to: $A = K + 1$. This

TABLE 1

Details of Wide-Angle Diffusers Used for Data Correlation

Wide-Angle Diffuser Origin	Diffuser Angle 2θ	Area Ratio A	Wind Tunnel Circuit	Diffuser Wall Shape	Diffuser Cross-Section	Number of Screens or B-L Control Device	Sum of Pressure drop Coefficients K_{sum}
1. Patterson (1938)							
(a) Peters	8°	2.34	-	Straight	Circular	-	-
(b) Gibson	10°	2.25	Open	"	"	-	-
(c) Gibson	10°	9	"	"	"	-	-
(d) Gibson	10°	9	"	"	Rectangular	-	-
2. McLellan, Nichols (1942)	30°	3	"	Curved	Circular	1	4.3
3. Squire, Hogg (1944)							
(a)	40.1°	2	"	Curved	"	3	6
(b)	34.7°	3.5	"	Straight	"	5	5
(c)	64.1°	4	"	Curved	"	3	6 *
(d)	560	4	"	Straight	"	3	6 *
4. Squire, Hughes (1944)							
(a)	17.1°	1.5	"	Curved	"	1 (Curved)	0.8
(b)	31.7°	2.0	"	Curved	"	1 (Curved)	1.33
5. Schubauer, Spangenberg (1948)							
(a) Diffuser A	28°	4	"	Straight	"	1	0.72 *
(b) A	28°	4	"	"	"	1	1.20 *
(c) A	28°	4	"	"	"	1	1.40 *
(d) A	28°	4	"	"	"	1	1.25 *
(e) A	28°	4	"	"	"	1	1.48 *
(f) A	28°	4	"	"	"	1	2.95 *
(g) A	28°	4	"	"	"	1	1.55 *
(h) A	28°	4	"	"	"	1	1.90 *

* Unsuccessful Configuration

(i) Diffuser A	28°	4	Open	Straight	Circular	1	3.04 *
(j) A	28°	4	"	"	"	6	3.38 **
(k) A	28°	4	"	"	"	5	3.89
(l) A	28°	4	"	"	"	3	3.81
(m) Diffuser B	90°	4	"	"	"	1	0.51 *
(n) B	90°	4	"	"	"	1	1.16 *
(o) B	90°	4	"	"	"	1	1.22 *
(p) B	90°	4	"	"	"	5	3.89
(q) B	90°	4	"	"	"	3	3.81
(r) B	90°	4	"	"	"	3	4.48 **
(s) Diffuser C	7.5°	4	"	Curved	"	1	1.26
6. Squire (1953)							
(a)	6°	4	"	Straight	"	-	-
(b)	8°	4	"	"	"	-	-
(c)	10°	4	"	"	"	-	-
(d)	10°	16	"	"	"	-	-
7. Dryden, Abbott (1949)	7.2°	2.42	Return	"	"	-	-
8. Rhoden (1951)	30°	3.6	Open	"	Rectangular	1 Curved honeycomb.	-
9. Reid (1953)							
(a)	17.4°	2.63	"	"	Rectangular	1 Curved	5.69
(b)	18.9°	3.5	"	"	"	1 (Curved)	5.69
(c)	15.9°	4	"	"	"	1 (Curved)	5.69
(d)	15.2°	5	"	"	"	1 (Curved)	5.69
(e)	10.7°	5	"	"	"	1 (Curved)	5.69
10. Squire, Winter (1953)	46.5	3.66	Return	"	Octagonal	3	5.64

* Unsuccessful Configuration   ** Optimum Configuration

Table 1 (contd)

11.Green,Lilley(1955)	58.5°	17.5	Open	Curved	Circular	3 and Suction	
12.Campbell (1957)	45°	8	"	Straight	"	2 (Curved)	6.3
13.Moore,Kline (1958)							
(a)	7°	2.0	"	"	Rectangular	Vanes	-
(b)	45°	7.7	"	"	"	"	-
14.Gibson (1959)							
(a)	19.8°	2.55	"	Curved	Circ+Octag.	1 (Curved)	2.05
(b)	19.8°	2.55	"	"	"	"	1.36
(c)	19.8°	2.55	"	"	"	"	1.40
(d)	19.8°	2.55	"	"	"	"	0.83 *
15 Robertson, Fraser (1960)	12°	2	"	Straight	Circular	-	-
16 Savage (1960)							
(a)	38.4°	2.95	"	Curved	"	Slots	-
(b)	20°	2.95	"	Straight	"	"	-
(c)	24°	5.65	"	"	Rectangular	"	-
17. Migay(1962- Kachara,1973)	31°	4.35			Circular	Transverse Ribs	-
18. Bradshaw,Hellens (1964)	35°	1.81	Return	"	Rectangular	2 (Curved)	3.3
19.Bradshaw, Pankhurst (1964)							
(a) NPL 36"x27"	56.6°	1.54	Return	"	"	2	3.2
(b) NPL Duplex	22.4°	3.2	Open	"	Circular	-	- *
(c) McKinnon Woods 13' x 9	30.6°	1.93	Return	"	Octagonal	3	

* Unsuccessful Configuration

TABLE 1 (contd)

(d) Manchester Univ. Low Turb.	32.2°	1.74	Return	Straight	Rectangular	4	4.0
20.Domholdt, Moszynski(1964)							
(a)	30°	2.75	"	"	"	3	3.72
(b)	8.2°	2.9	"	"	Circular	-	-
21. Feil (1964							
(a)	60°	3.05	Open	"	Circular	Vanes	-
(b)	80°	3.05	"	"	"	"	-
22.NPL 9'x7' W/T (1964)	37.7°	2.0	Return	Curved	Rectangular	3 (2 curved)	5.64
23.Raju, Rao (1964)							
(a)	38°	15	Open	Straight	Circular	4	5.0 *
(b)	38	15	"	"	"	3	4.2 *
(c)	38	15	"	"	"	3	4.0 *
(d)	38	15	"	"	"	3	6.4
(e)	38	15	"	"	"	2	5.4
24. CSIRO, Australia (1965)							
(a)	47.3°	1.92	Return	"	Rectangular	3	2.63
(b)	24.3	1.92	Open	Curved	"	1 (Curved)	1.23
(c)	26.2°	1.71	"	"	"	1 (Curved)	0.99
(d)	24°	3.14	"	"	"	2 (Curved) And Honeycomb	2.87
25. Bradshaw (1967)	38.6°	2.27	"	"	Rect.→Circ	2 (Curved)	3.76

TABLE 1 (contd)

26. Carlson et al (1967)							
(a)	10.5°	2.1	Open	Curved	Rectangular	-	-
(b)	19°	3	"	"	"	-	-
27. Rao (1967)	38°	15	"	Straight	Circular	8 Vane Splitter	-
28. Ali (1968)							
(a)	28°	2.25	Return	Curved	Octag→Rect	1	4.0 **
(b)	28°	2.25	"	"	"	1	1.06
(c)	28°	2.25	"	"	"	1	3.02
29. Azzouz, Pratt (1968)							
(a)	14.3°	4.8	Open	Straight	Rectangular	-	-
(b)	60°	5.44	"	"	Circular	Perforated Cone	-
30. Bachmeier (1968)	28°	3.15	"	"	"	Trapped Vortex	-
31. Bradshaw (1968)							
(a) NPL 15"x10"	41.7°	2.26	"	Curved	Rectangular	2 (Curved)	3.76
(b) NPL 36"x36"	43.7°	2.25	Return	Straight	"	"	3.76
(c) NPL 18" Octagonal	7.7°	3.24	Open	"	Circular	-	-
32. Vogel (1968)	33.7°	2.6	"	Curved	Rectangular	1 (Curved)	4.77
33. Imperial College 24"x2" (1969)	31.2°	2.65	"	"	"	4 (2 Curved)	6.4
34. Johnston, Powars (1969)							
(a)	10.5°	2.1	"	Straight	"	-	-
(b)	19°	3	"	"	"	-	- *

TABLE 1 (contd)

35. NAE 30'x30' V/STOL W/T (1969) (a) (b) (c)	 50° 12° 6°	 2.05 4.0 2.25	 Return " "	 Straight " "	 Circular " "	 1 - -	 1 - -
36.Imperial College 6" (1970)	43.7°	3.49	Open	"	Rectangular	2 (Curved)	3.2
37.Lawson (1971)	46.7°	3.46	"	Curved	Circular	Vane Cluster	-
38. Pirrello et al (1971) (a) Grumman 26" (b) Boeing 9' x 9'	 7° 8.4°	 2.69 2.56	 " "	 Straight "	 Octag.→Circ. Circular	 - -	 - -
39. Bradshaw(1972)	18.2°	2.19	"	"	Rectangular	2 (Curved)	3.19
40.Fielder,Gessner (1972) (a) (b) (c)	 14° 20° 30°	 1.98 2.40 3.14	 " " "	 " " "	 " " "	 Tangential Fluid Injection " "	 - - -
41.Boldman, Neumann (1973)	13°	6.55	"	"	Circular	-	- *
42 Gibbings (1973)	54°	16.7	"	"	Circ→Rect	Pyramid Gauze	1
43. Kachara (1973 (a) Diffuser A (b) Diffuser A1 (c) Diffuser B (d) Diffuser C (e) Diffuser D	 20.2° 29.3° 33.6° 34.8° 29.5°	 3.99 3.86 3.99 3.78 4.0	 " " " " "	 Curved " " " "	 Circular " " " "	 1 1 1 1 (Variable-K) 1 (Curved)	 2.37 2.37 2.37 2.69 2.64

TABLE 1 (contd)

44. Manchester Univ. Blower Tunnel (1973)	46.3°	2.98	Open	Straight	Rectangular	2 (Curved)	3.73 *
45. Runstadler, Dolan (1973)							
(a)	16°	4.09	"	"	"	-	-
(b)	14°	4.68	"	"	"	-	-
(c)	12°	4.57	"	"	"	-	-
(d)	10.5°	3.94	"	"	"	-	-
(e)	13°	3.96	"	"	"	-	-
(f)	9°	3.36	"	"	"	-	-
(g)	7°	2.85	"	"	"	-	-
(h)	16°	5.21	"	"	"	Suction Slots	-
(i)	12°	4.15	"	"	"	"	-
46.Tennant (1973)							
(a)	8.5°	1.75	"	Curved	"	Rotating Cylinders	-
(b)	11.3°	2.0	"	"	"	"	-
47. Yang et al(1973)	25.7°	3.0	"	"	Circular	Slots	-
48. Haight,O'Donell (1974)	19.0°	1.73	"	"	Rectangular	Trapped Vortex	-
49 Juhasz (1974)	86.4°	2.5	"	"	Circular	Wall Suction	-
50. Mabey,Sawyer(1974)							
(a)	13.2°	3.74	Return	Straight	"	-	- *
(b)	13.2°	3.74	"	"	"	Vortex Gens	-

TABLE 1 (contd)

51.Watts et al.(1974)	45°	4.77	Open	Straight	Rectangular	4	5.05
52.Adkins (1975)	30°	3.2	"	"	Circular	Trapped Vortex	-
53.G.A.Slow Speed W/T Salisbury,Australia (1975)	16.5	1.27	"	Curved	Rectangular	2 (curved)	2.46
54.Juhasz (1975)	86.4°	4.0	"	"	Circular	Wall Suction	-
55.Smith (1975)	20°	4.0	"	Straight	"	Trapped Vortex	-
56.Imperial College Test Diffusers (1976)							
(a) I	20°	4	"	"	Rectangular	2	4.8
(b) II	33°	4	"	"	"	2	4.5
(c) III	46°	4	"	"	"	3	4.2
(d) IV	46°	2	"	"	"	2 (1 Curved)	2.5
57. Welsh (1976)	22°	4	"	"	Circular	Star Splitter	-

curve is seen to lie just within the postulated curve ($A = 1.4\ K_{sum} + 1$), thus enclosing most of the successful combinations. On recalculating several of the configurations, using this formula, it was found that they not only lay within the line EF, but very close to the actual values used. This suggests that many designers have relied on the rules put forward by Schubauer and Spangenberg (1948).

Squire and Hogg (1944) made a simplified analysis of screen combinations in relation to wind tunnel design, which yielded some interesting results. They considered an example of a jet in an infinite, ideal fluid impinging normally onto a screen, and using the Bernoulli and continuity equations, they derived:-

$$A = (4 + K)/(4 - K) \qquad (2.6)$$

This formula holds accurately only for small values of K since it assumes that the velocity is uniform over the cross-section of the jet at the screen position. The theory becomes less and less exact as K increases. In Fig. 2.4, it is seen that this formula (chain-dotted) agrees well with the hypothesized curve up to $K_{sum} \approx 2.4$. Beyond this, the curve diverges rapidly towards the asymptote, $K_{sum} = 4$. These theories, with the different circumstances in mind, seem to agree well with the hypothesized curves.

In order to supplement the postulated design rules, some flow visualization tests, using wool-tufts, were conducted on diffusers cut from polystyrene blocks. The details of the diffusers tested, and results obtained, are given in Table 2. Four different geometries, chosen so that each satisfied a different limit in Fig. 2.2, were constructed. Each diffuser was built in 2 - 3 sections so that screens could be sandwiched between sections and the whole arrangement then housed in a wooden box attached to a blower tunnel (Fig. 3.4). The entry to the box was 108 x 108 mm (4.25 x 4.25 in). All the diffusers had straight walls, with sharp corners between adjacent walls and also at entry and exit. Diffusers I, II and III were found to suffer from severe secondary flow effects in the corners between adjacent walls and were, consequently, fitted with triangular polystyrene fillets, which reduced this problem. These three diffusers diverged equally in both planes, but diffuser IV was two-dimensional and was specially constructed to determine the effectiveness of a curved screen. Diffusers II, III and IV had short parallel ducts attached to their exits and thus the adverse pressure gradient was probably increased just upstream of the diffuser outlet, due to the abrupt change in wall-angle. Although the raw surface finish on the diffuser walls was satisfactory, especially on those cut from fine-grained polystyrene, they were all plastered with Polyfilla, followed by a coat of emulsion paint, giving a smooth, impervious surface.

The first column in Table 2 gives the diffuser geometry and the "theoretical" minimum number of screens and K_{sum} required, as given by Figs. 2.2 and 2.4, respectively. The tests were performed at a Re per metre of about 10^6 with two extreme entry flow conditions: an almost fully developed flow from a long (3m) channel and the flow from a contraction with relatively thin boundary layers ($\delta \simeq 5$ mm). The boundary layer was tripped at the contraction exit as shown in Fig. 3.4. The results presented in Table 2 are, however, generalized for all entry flow conditions, in accordance with the design rules. The pressure drop coefficients of the screens were determined using Collar's (1939) equation (with C = 1.0) and the M-values using eqs. 2.2, 2.3 and

TABLE 2

Wide-Angle Diffuser Test Results (Configuration 56 in Figs. 2.2 and 2.4)

Diffuser Details	n	M_o (K_{sum})	M_1	M_2	OBSERVED FLOW CONDITION.
I A=4	1	3	0	0.25	Flow near entry attached - tends to separate towards exit.
$2\theta=20^\circ$ $n \not> 1$	1	3	0.33	0.028	Flow downstream of screen attached but separated on two walls upstream.
$K_{sum} \not> 2.5$	2	4.5	0.11	0.18	Flow tended to separate near exit.
	2	4.8	0.12	0.17	Steady and attached but separation on one wall near exit.
II A=4	1	3	0	0.25	Separation on all walls.
$2\theta= 33^\circ$ $n \not> 2$	2	4.5	0.12	0.18	Wall flow attached but separation on fillets towards exit.
$K_{sum} \not> 2.5$	2	4.7	0.25	0.17	Flow unsteady and separated between screens, but attached and steady downstream of second screen.
	2	4.5	0.5	0.03	Flow downstream of both screens attached and steady-not observable near entry.
III A=4 $2\theta= 46^\circ$	2	4.5	0.17	0.17	Separated on two walls downstream of second screen.
$n \not> 3$	2	4.7	0.18	0.17	Flow condition near exit improved-less separation
$K_{sum} \not> 2.5$	3	6.2	0.38	0.18	Flow downstream of second and third screens attached and steady.
	3	4.2	0.4	0.16	Wall flow attached throughout-slight separation on fillets upstream of first two screens.
IV A=2	1	1.5	0	0.25	Separation immediately downsteam of screen.
$2\theta= 46^\circ$ $n \not> 1$	1 (Curved)	1.5	0	0.25	Flow attached immediately downstream of screen-separated near exit.
$K_{sum} \not> 1$	2	2.5	0.4	0.25	Flow slightly unsteady and tended to separate, near exit.
	2 (1 Curved)	2.5	0.4	0.25	Steady and attached flow throughout.

2.4.

The combination listed last for each diffuser was found to be the optimum and is the one plotted in Figs. 2.2 and 2.4. For diffuser I, it seems evident that a higher M_1 (screens nearer the exit) is required, but the sharp inlet, by inducing separation, makes this optimization difficult. One screen seems quite inadequate for diffuser II and this agrees with Fig. 2.2. With two screens, the wall flow improves with increasing M_1. Diffuser III, which lies quite near the two-screen limit in Fig. 2.2 (configuration 56c) seems to operate fairly satisfactorily with two screens. The corner and exit flow condition was, however, improved considerably by installing three screens. The results from diffuser IV exemplify the usefulness of a curved screen in maintaining attached flow.

Kachhara (1973) gives a detailed account of the construction and testing of five axisymmetric, wide-angle diffusers. This report was encountered after the present design rules had been derived and is used here as a test case. The geometrical details of these diffusers are given in Table 1 (configuration 43) and their performance details are given in Table 3, which is based on the same format as Table 2.

All the diffusers were found to operate unsatisfactorily (i.e. with flow separation) without any screens: in agreement with Fig. 2.2. However, they all performed satisfactorily with one screen, when suitably positioned, and this is not in complete agreement with Fig. 2.2. All but one configuration (43a) are seen to lie beyond the one screen limit line in Fig. 2.2, although two of them (43b and e) are not very far beyond. In Fig. 2.4, diffusers 43d and e are within the successful operation line, EF, whereas diffusers, 43a, b and c, although not quite within, lie very close to the boundary. The values

TABLE 3

Analysis of Kachhara's (1973) Wide-Angle Diffuser Test Results.
(Configuration 43, in Figs. 22 and 24).

Diffuser Details	n	M_o (K_{sum})	M_1	M_2	OBSERVED FLOW CONDITION
A	1	2.37	0.303	0.039	Transitory separation downstream of screen.
A=3.99	1	3.61	0.376	0.015	Separation upstream of screen.
$2\theta=20.2^o$	1	2.37	0.317	0.033	Steady attached flow.
$n \approx 1$	1	2.41	0.324	0.031	Steady attached flow.
$K_{sum} \approx 2.62$	1	2.37	0.345	0.024	Steady attached flow.
A1	1	2.37	0.475	0.0005	Separation downstream of screen.
A=3.86	1	3.61	0.565	0.004	Separation upstream of screen.
$2\theta= 29.3^o$	1	2.37	0.519	0.0004	Steady attached flow.
$n \approx 2$					
$K_{sum} \approx 2.5$					
B	1	3.03	0.468	0.001	Separation downstream of screen.
A=3.99	1	3.61	0.534	0.0012	Separation upstream of screen.
$2\theta= 33.6^o$	1 (Curved)	2.41	0.494	0.00003	Steady attached flow.
$n \approx 2$					
$K_{sum} \approx 2.62$	1	2.37	0.494	0.00003	Steady attached flow.
C	1	2.37	0.366	0.018	Separation downstream of screen.
A=3.78	1	2.37	0.384	0.014	Separation downstream of screen.
$2\theta= 34.8^o$	1	3.03	0.421	0.006	Separation upstream of screen.
$n \approx 2$	1	3.03	0.384	0.014	Steady attached flow.
$K_{sum} \approx 2.44$	1 (Variable -K)	2.69	0.369	0.017	Steady attached flow-uniform outlet profile
D	1	2.12	0.389	0.0122	Separation downstream of screen.
A=4	1	2.37	0.389	0.0122	Separation downstream of screen.
$2\theta= 29.5^o$	1 (Curved)	2.64	0.389	0.0122	Steady attached flow.
$n \approx 2$					
$K_{sum} \approx 2.63$					

of M_1 and M_2 for the optimum combinations in Table 3 are, in general, slightly less than the optimum values quoted in Section 2.4.2. It must be noted that Kachhara's (1973) diffuser tests were performed with favourable inlet flow conditions - a uniform velocity profile with thin boundary layers.

Kachhara's results seem to lend support to the design rules, but our test results seem to imply that small separations or unsteadiness may be acceptable in a wind tunnel diffuser. Also, it is clear that these rules must not be taken as infallible or inflexible, but it is hoped that they will be of use as a confirmation and extension of Schubauer and Spangenberg's (1948) work.

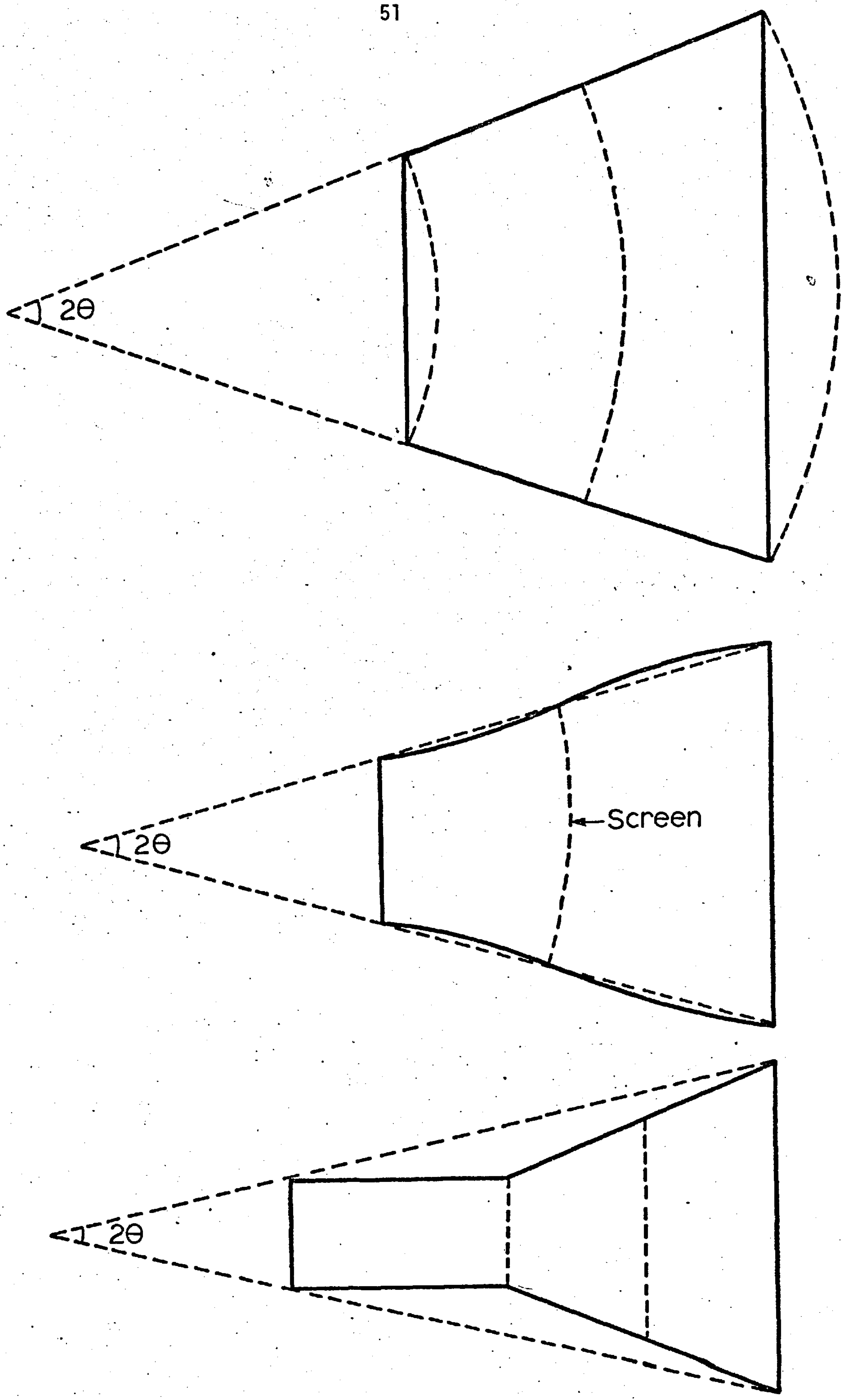

Fig. 2.1 Typical wide-angle diffusers showing definition of diffuser angle 2θ

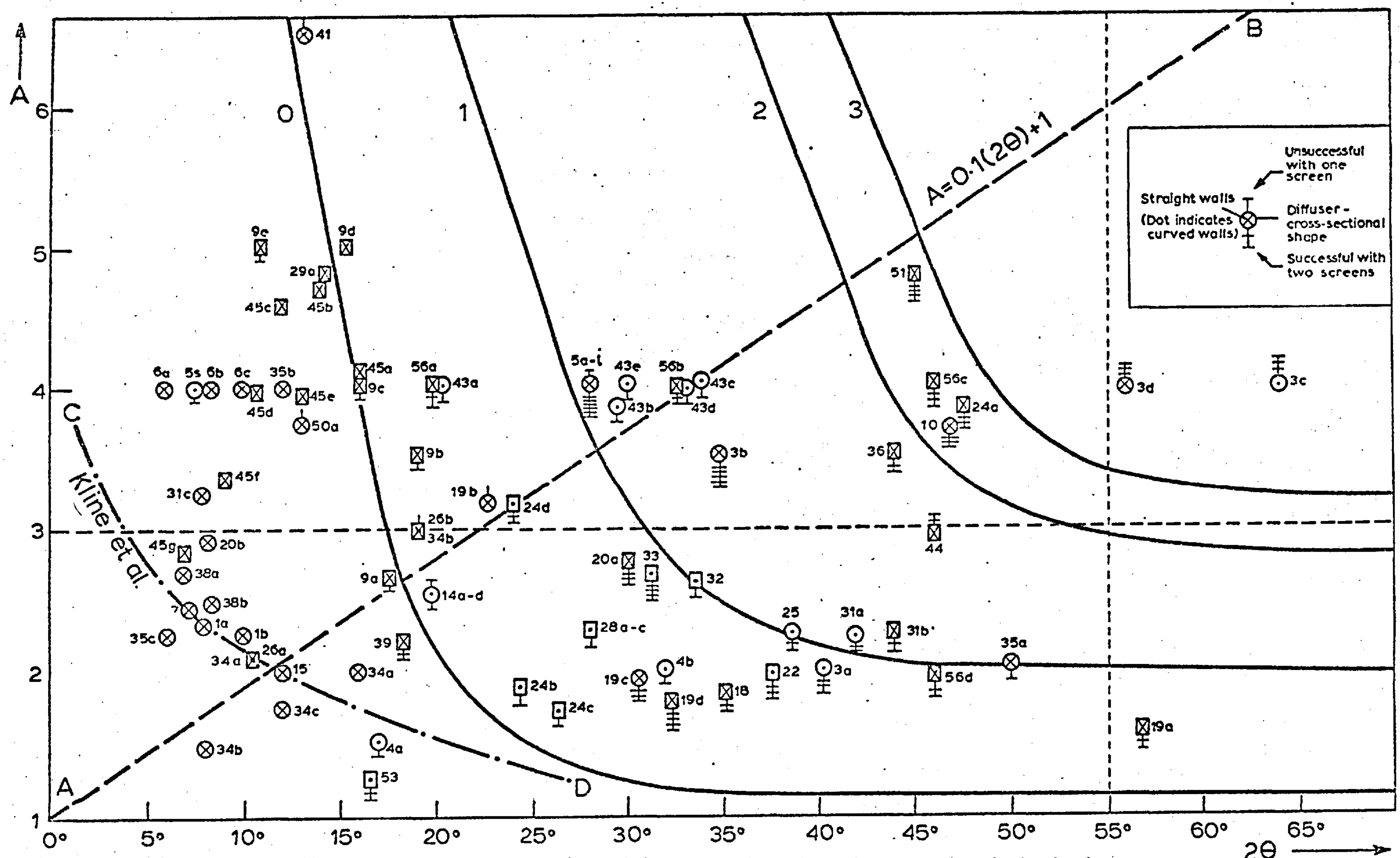

Fig. 2.2 A vs 2θ for diffusers with screens (or without any boundary layer control device). (Numbers refer to Table 1).

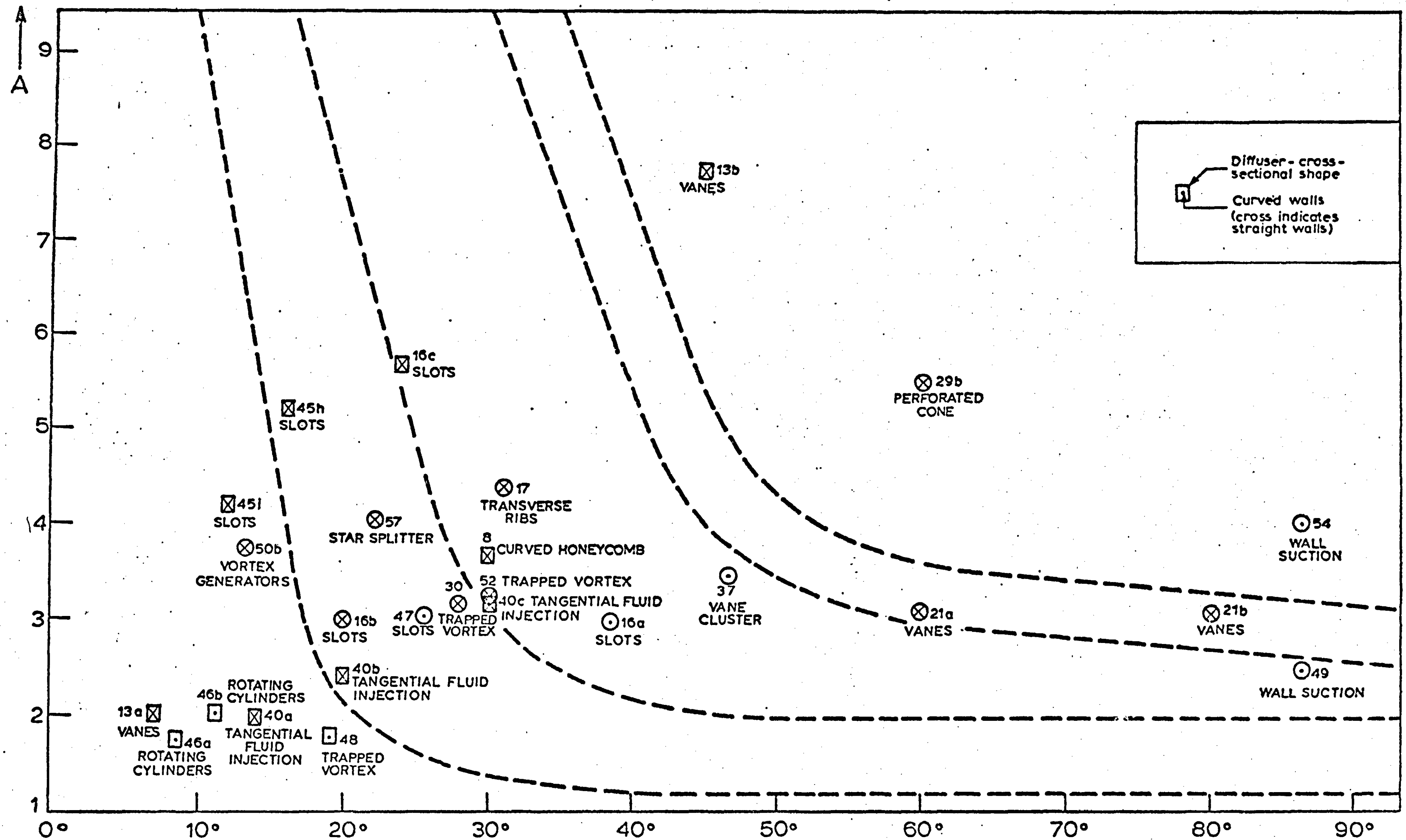

Fig. 2.3 A vs 2θ for diffusers employing devices other than screens. (Dotted lines are boundaries from Fig. 2.2).

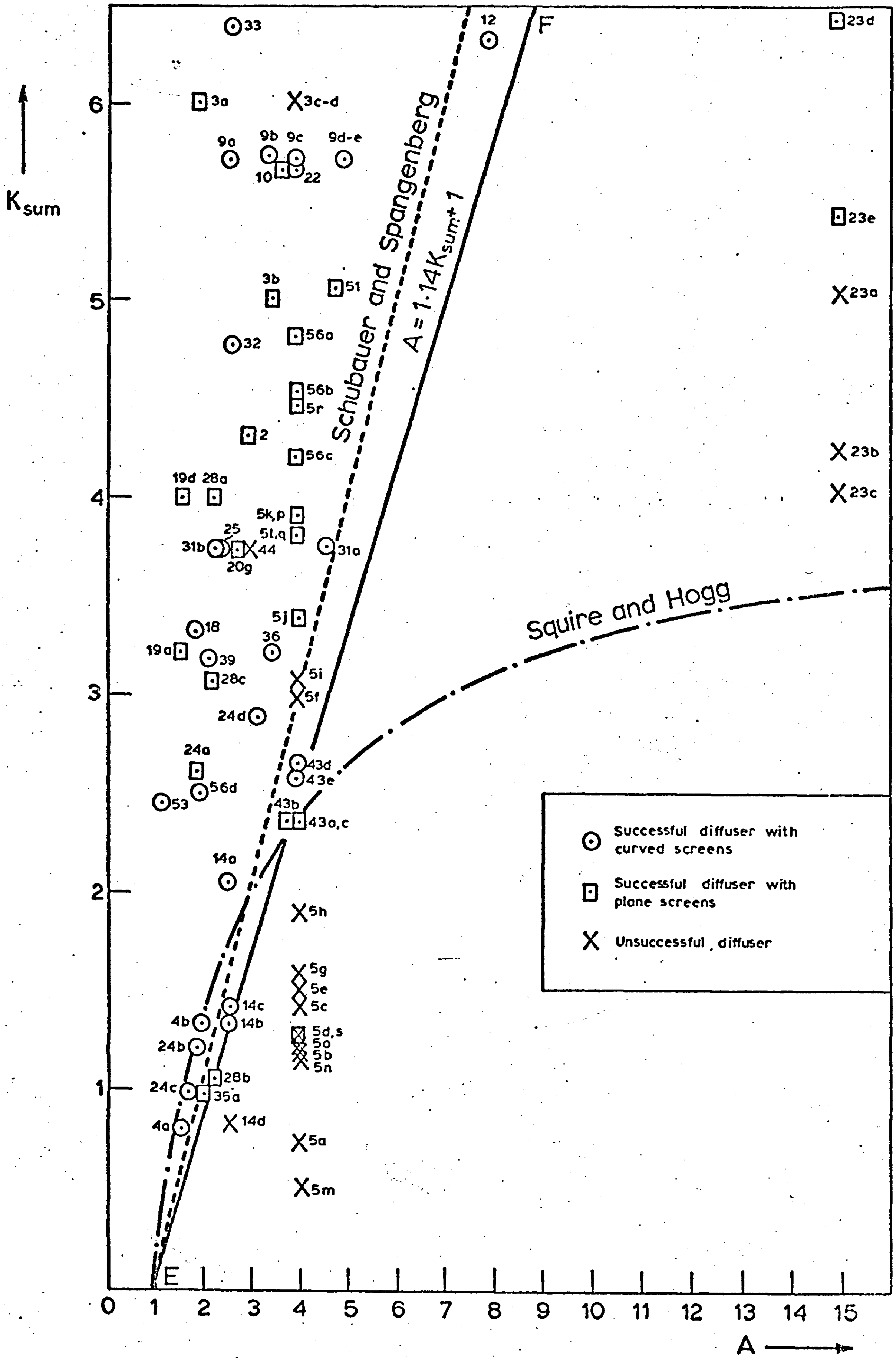

Fig. 2.4 K_{sum} vs A for diffusers with screens

CHAPTER 3

SCREENS

3.1 Introduction

3.1.1 Basic Principles

In engineering fluid mechanics, screens are used for seemingly contradictory purposes:-

(a) The production of a uniform time-mean velocity profile from arbitrary non-uniform conditions upstream, or the production of a specified shear velocity profile, normally from uniform conditions.

(b) The suppression of turbulence existing upstream of the screen, or the controlled generation of grid turbulence.

For wide-angle diffuser and settling chamber applications, only the first purposes in each category are relevant, and hence are the only ones discussed here. These screens are normally made of metal wires (e.g. brass, phosphor bronze and stainless steel) interwoven to form square or rectangular meshes with typically 20 - 40 meshes per lineal inch. Screens woven from nylon or polyester threads are also now being used when the wind loads are not expected to be very high. It is revealed below how the aerodynamic properties of the two types of screens differ significantly, presumably because of detailed differences in the weave.

Screens are installed in the settling chamber to improve flow uniformity throughout the cross-section. Screens in a wide-angle diffuser can, if carefully installed, also perform this function, as well as their specific task of suppressing separation, so that in principle the number of screens in the settling chamber can be reduced. An additional effect of gauze screens is to refract the incident (inclined) flow towards the local normal to the screen. This is why screens installed in wide-angle diffusers are often curved. Screens with the open-area ratios normally required (of the order of 0.6) are available commercially and although there is a restriction on the maximum width available in a single piece (about 1.5 m), this does not present a problem for screen sizes normally required for blower tunnels.

The action of the gauze is described in terms of two parameters:-

(i) K ($= \Delta p/q$), the screen pressure drop coefficient;

(ii) α ($= \phi/\theta$), the deflection coefficient, defined as the ratio of the flow emergence angle (ϕ) to the incidence angle (θ). θ and ϕ are measured from the normal to the screen (Fig. 3.1).

Note that the refractive index of a screen (μ) defined as in optics is equal to $1/\alpha$ for small θ. We expect the functional relationships for K and α to be:-

$$K = f_1\ (\beta, Re, \theta)$$
$$\alpha = f_2\ (\beta, K, \theta)$$

For a plane screen placed normal to the axis of the flow, and for $K > 0.7$, a generally accepted semi-empirical relation due to Schubauer et al (1950) is:-

$$\alpha = \frac{1.1}{(1 + K)^{\frac{1}{2}}} \tag{3.1}$$

3.1.2 Review of Previous Work

(a) General

Screens have been used to improve flow quality in wind tunnels since the 1930s. Prandtl (1933) noted that when screens were installed the velocity distribution improved, and he gave a simple theory for this effect. The effect of screens in reducing the turbulence intensity levels became apparent later. Dryden and Schubauer (1947) gave a physical explanation for this effect: turbulent eddies of larger scale than the screen mesh size are decreased, and although at the same time smaller scale eddies may be introduced, they decay much more rapidly than the original large scale motions would do in the absence of the screen. The overall effect is that at some distance downstream, both the turbulence intensity and scale have been reduced.

Taylor and Batchelor (1949) produced a detailed analysis of the effect of gauze screens on small disturbances. This theory is linearized on the assumption that there is negligible natural decay of turbulence while the field is translated through the "region of influence" (length comparable to the size of the energy containing eddies). For the case in which the turbulence far upstream is isotropic, the equations for the factors of reduction of turbulence intensity become relatively easy to compute (Batchelor, 1970). The numerical reduction factors given by these equations and Townsend's (1951) measurements (Table 4) are for initially-isotropic turbulence. Dryden and Schubauer (1947) derived a simple theory for the reduction of turbulence intensity based on the assumption that the effect of a screen is partly to absorb the kinetic energy of the turbulence. Both

TABLE 4

Factors of Reduction of Mean Velocity Variation and Turbulence Intensity by Gauze Screens.

(i) U - component mean velocity

K	1	2	3	4
$\frac{1+\alpha-\alpha K}{1+\alpha+K}$ (Taylor-Batchelor)	0.36	0.1	-0.022	-0.086

with $\alpha = 1.1/\sqrt{1+K}$

(ii) V - component mean velocity

K	1	2	3	4
α	0.78	0.64	0.55	0.49

(iii) u - component r.m.s. intensity

K	1	2	3	4
Theoretical (Taylor-Batchelor)	0.44	0.21	0.14	0.13
Experimental (Townsend)	0.45	0.36	0.31	0.28
$1/\sqrt{(1+K)}$ (Dryden-Schubauer)	0.71	0.58	0.50	0.45

(iv) v - w component r.m.s. intensity

K	1	2	3	3
Theoretical (Taylor-Batchelor)	0.74	0.59	0.50	0.45
Experimental (Townsend)	0.66	0.54	0.45	0.40
$1/\sqrt{(1+K)}$ (Dryden-Schubauer)	0.71	0.58	0.50	0.45

these theories ignore the turbulence set up by the screen itself.

The expression for the factor of reduction of U-component mean velocity given by Taylor and Batchelor (1949), $(1 + \alpha - \alpha K)/(1 + \alpha + K)$, implies the interesting possibility that the longitudinal component is completely suppressed by a gauze with $K = 1 + \frac{1}{\alpha}$, which corresponds to $K \simeq 2.8$ if α and K are related as in eq. 3.1. Also, this expression reduces to the one derived by Prandtl (1933), namely: $1/(1 + K)$, when $\alpha = 0$ and to the one due to Collar (1939), namely: $(2 - K)/(2 + K)$, when $\alpha = 1$. Taylor and Batchelor show how the analyses leading to these simpler expressions include unrealistic assumptions, in effect, for α.

According to the Taylor-Batchelor theory, the lateral-component r.m.s. intensity decreases monotonically with increasing K while of the longitudinal component has a flat minimum at $K \simeq 4$. Since, for a given value of K, the reduction of the longitudinal component is greater than that of the lateral component, a reduction of the latter to an acceptable level ensures an acceptable longitudinal intensity. Dryden and Schubauer (1947) give the reduction factor for the turbulence intensity by n identical screens in series as: $1/(1 + K)^{n/2}$. It is thus apparent that, for a given pressure loss, a greater reduction in turbulence intensity is obtained by using multiple screens, each with a comparatively low K. Low K is also desirable for other reasons.

For screens with $\beta < 0.5$, Baines and Peterson (1951) found instabilities in the downstream profiles. Morgan (1960) found that in certain cases, the flow behind a uniform screen was unstable with both spatial and temporal variation. Bradshaw (1965) concluded that this effect was mainly confined to screens with open-area ratios of less than about 0.57, which corresponds to K's of more than about 1.6 (at $Re \simeq 100$). This instability was explained as that caused by the jets emerging from the screen pores, coalescing in random patterns. Because the contraction that follows the screens reduces mean-velocity variations but necessarily leaves the circulation around a fluid element virtually unaltered, this sort of spatial instability leads to weak longitudinal vortices in the working section, which are very effective at producing spanwise variation of boundary layer thickness and surface shear stress in a nominally two-dimensional boundary layer. These variations can be of the order of ± 10% of the mean values but may be unimportant except in boundary layer studies.

(b) Determination of K

Over the years, several expressions have been derived giving the pressure drop coefficient of a screen (K) in terms of its open-area ratio (β).

For square-mesh screens, $\beta = \left(1 - \frac{d}{\ell}\right)^2$. Pinker and Herbert (1967) suggest that this underestimates the effective open-area and propose a "sinusoidal" porosity. This assumes that the flow remains perpendicular to the screen plane as it passes through it. All in all, the above expression giving a projected open-area ratio is adequate.

One of the first deductions for K, which is still used, is due to Collar (1939). He was the first to suggest that the pressure drop coefficient would also vary with Re until a limiting value. Assuming the resistance of a gauze is proportional to the area of the material and to the square of the speed through the holes, he deduced:-

$$K = \frac{C(1 - \beta)}{\beta^2} \tag{3.2}$$

where some dependence of the constant C on Re is to be expected. Collar found that when C was given the value 0.9, the formula fitted the experimental points (for $U \simeq 9$ m/s) very well. Simmons and Cowdrey (1949) found that for a screen placed normal to the flow, and for velocities greater than about 10 m/s, C = 1.0 gave a satisfactory agreement.

Annand (1953) produced a similar semi-empirical fit, based on Simmons and Cowdrey's data:-

$$K = C' \frac{(1 - \beta^2)}{\beta^2} \tag{3.3}$$

Pinker and Herbert (1967) found the general form of Annand's equation agreed best with their extensive measurements and suggested a value of 0.52 for the constant, C' in the high Re limit $\left(\frac{Ud}{\nu} > 600\right)$ for β in the range 0.3 - 0.6.

The drag coefficient of an isolated circular cylinder also decreases with Re until about Re = 10^5 when it flattens out before increasing slightly. Annand also suggested that the pressure-drop coefficient of a screen should increase with a further increase in Re but there is no real evidence for this. Despite some similarities, on the whole it is not plausible to think of a gauze screen as consisting of rows of isolated cylinders since there is strong interaction between wakes of the individual wires.

Wieghardt (1953) plotted K against $Ud/\beta\nu$ (a modified Re based on wire diameter), and found a "best fit" to the experimental data, which included that of Collar (1939) and Simmons and Cowdrey (1949). For $60 > \frac{Ud}{\beta\nu} > 600$, which for typical values of d (0.4 mm) and β (0.6) corresponds to $1.5 < U < 15$ m/s, Wieghardt gives:-

$$K = 6.5 \left[\frac{1 - \beta}{\beta^2}\right] \left[\frac{Ud}{\beta\nu}\right]^{-1/3} \tag{3.4}$$

The effect of the Re factor in eq. (3.4) diminishes as U increases, and the correlated data suggest that K is independent of Re for $\frac{Ud}{\beta\nu} > 600$.

The pressure drop coefficient of a screen, based on the magnitude of the flow velocity, is found to decrease with increasing flow inclination - this can be crudely explained by considering the drag on the wires. Although theoretical and semi-empirical relations have been proposed, no universality has been noted.

For $0 \leq \theta \leq 45^0$, (see Fig. 3.1 for notation), Schubauer et al (1950) found an empirical relation:-

$$\frac{K_\theta}{\cos^2 \theta} = f\ (Re \cos \theta)$$

suggesting that the pressure drop is proportional to the square of the velocity component normal to the screen. Gibbings (1973) derived the same expression by considering the drag force on each wire.

Carrothers and Baines (1965) showed that this relation did not hold for $\theta > 45^0$ and suggested that flow conditions for these higher angles of inclination may be "different" from those at smaller angles ($\theta < 45^0$).

Reynolds (1969) also considered the drag force on the wires and assumed that the actual flow deflection angle at the screen was $(\theta - \phi)/2$ (for $\beta > 0.5$). He obtained:-

$$K_\theta = K \cos^2 \theta \left[\frac{1 + \sec \frac{\theta - \phi}{2}}{2}\right]$$

Simmons and Cowdrey (1945) measured K_θ for $0 < \theta < 60^o$. Their K_θ decreases as approximately Cos θ for all the screens although this relation was not noted by them.

(c) Determination of α

Several workers have developed expressions for the deflection coefficient, but, as for K_θ, no satisfactory agreement has evolved. This is partly due to the difficulties in measuring the flow angles accurately and consistently.

Experimental evidence suggests that ϕ/θ tends to a finite limit, α, as $\theta \rightarrow 0$ (Taylor and Batchelor, 1949) and for $K > 0.7$, Schubauer et al (1950) gave the generally accepted semi-empirical relation defined in eq. (3.1):-

$$\alpha = \frac{1.1}{(1 + K)^{\frac{1}{2}}}$$

This relation was obtained by considering the force coefficient parallel to the plane of the gauze, F_θ. This coefficient can be expressed as a function of θ and ϕ by considering the change in momentum across the screen, giving:-

$$F_\theta = 2 \text{ Cos } \theta \text{ Sec } \phi \text{ Sin } (\theta - \phi) \qquad (3.5)$$

Schubauer et al also obtained an empirical relation, based almost entirely on their own results:-

$$\frac{F_\theta}{\theta} = 2 - \frac{2.2}{(1 + K_\theta)^{\frac{1}{2}}} \qquad (3.6)$$

From eqs. (3.5) and (3.6) an expression for α_θ can be obtained:-

$$\alpha_\theta = \frac{1}{\theta} \text{Tan}^{-1} \{\text{Tan}\,\theta - \theta \,\text{Sec}^2\,\theta \left[1 - 1.1\,(1 + K_\theta)^{-\frac{1}{2}}\right]\}$$

For small ϕ and θ, eq. (3.5) reduces to $\frac{F_\theta}{\theta} = 2\,(1 - \alpha)$ and combining this with eq. (3.6) gives eq. (3.1):-

$$\alpha = \frac{1.1}{(1 + K)^{\frac{1}{2}}}$$

Schubauer <u>et al</u> only considered this limiting case of small θ.

Reynolds (1969) took Schubauer <u>et al's</u> data and produced semi-empirical fits for F_θ on a slightly modified basis. He suggests:-

$$\frac{F_\theta}{2\,\text{Sin}\,\theta} = \frac{2.2\,K_\theta}{8 + K_\theta} \qquad \text{for } \beta > 0.5$$

and:-

$$\frac{F_\theta}{2\,\text{Sin}\,\theta} = \frac{0.9\,K_\theta}{4 + K_\theta} \qquad \text{for } \beta < 0.5$$

He also correlates $F_\theta/\text{Sin}\,2\theta$ with K_θ for $0 < \theta < 45^\circ$ in terms of θ and ϕ and finds satisfactory agreement with Schubauer <u>et al's</u> data.

More recently, Gibbings (1973) also produced an analytic solution for the deflection coefficient, for "small values of K":-

$$\frac{\text{Tan }\phi}{\text{Tan }\theta} = \left[\left(\frac{K}{4}\right)^2 + 1\right]^{\frac{1}{2}} - \frac{K}{4}$$

He then correlates this with Dryden and Schubauer's (1949) results over large ranges of K and θ ($0 < K < 6$ and $0 < \theta < 45^o$) and finds satisfactory agreement.

Simmons and Cowdrey (1949) also measured flow angles through screens but their measurement technique raises doubts about the credibility of their results. For a given θ, they determined ϕ by setting the exit duct at an angle which gave the most uniform velocity profile. But the duct setting was not changed with flow speed since the possibility of variation of ϕ with flow speed was not appreciated.

A more general and recent review on flow through screens is given by Laws and Livesey (1978).

3.1.3 Present Work

It is evident from the above review that although considerable attention has been paid to flow through screens over the years, there is a definite lack of reliable data. Also, no emphasis has been laid on the boundary layer flow which is, of course, very important, in diffuser applications at least. In wind tunnel applications, it is important to assess not only how the flow is perturbed by the screen but also how quickly the flow recovers from the perturbation.

The object of this work was to study the flow, in particular turbulent boundary layers, through gauze screens of different materials and open-area ratios, with emphasis on both the mean and turbulent quantities.

3.2 Experimental Arrangements and Associated Techniques

3.2.1 Wind Tunnels

Almost the whole of the experimental programme on screens was conducted in the Department's 450 x 450 mm (18" x 18") blower-tunnel. This tunnel is driven by a centrifugal blower with an aerofoil-type impeller: it incorporates a wide-angle diffuser and a filleted contraction with an area ratio of 7 : 1 (Fig. 3.2). The tunnel has a maximum speed of about 25 m/s with a turbulence intensity level of about 0.28% at 18 m/s.

The main working section was mounted on castors for mobility. This made it easier to change the screen sample under investigation which was "sandwiched" between two sections of the working section, as shown in Fig. 3.2. Measurements were made through port-holes in the working section floor and through slots in the roof. The boundary layer was tripped at the contraction exit (Fig. 3.2) by an 18 SWG wire, taped along the whole span of the floor and ceiling only.

The inclined screen rig was attached to the downstream end of the working section (Fig. 3.3). The arrangement consisted of a hinged wooden frame of fixed height to which the screen was tacked. The frame could be set at different angles of incidence and wedges made from ½ in thick plywood were inserted in the sides between the frame and the end of the working section. A flexible false roof and fairing with an overall length of about 1 m was inserted in the working section so as to enable the exit height to vary with the angle of inclination of the frame. Displacement thickness effects due to the false roof were found to be negligible, i.e. the tunnel flow symmetry was not significantly affected by the presence or change in position of the false roof.

Some preliminary experiments were also conducted in a 108 x 108 mm (4¼" x 4¼") blower tunnel, (Fig. 3.4). This tunnel has the same general layout as the 450 mm tunnel but with a 3 m long square duct. Screen samples were tested in two positions, as shown in Fig. 3.4.

3.2.2 Screen Samples

The measured geometric details of all the screens used in this investigation are given in Table 5. The measured wire diameters were rounded-off to the nearest standard wire gauge (SWG). They were all formed of interwoven round threads forming square or rectangular meshes. The four screens listed first were the ones most extensively investigated. All the screens, except the brass screen, were of nominally uniform weave and free of wrinkles. The brass screen had a noticeably non-uniform weave and slight wrinkles and was deliberately chosen to try and assess the effects of these imperfections. The screens were cleaned regularly so that the open-area ratio and refractive properties would not change during the investigation (see Section 3.4.4).

3.2.3 Traverse Gears

The standard traverse gear available in the Department was used for most of the measurements. This is a "slide rule" type of traverse with a 6 in stroke driven by a small electric motor. It is also fitted with a linear potentiometer, the output voltage from which is proportional to the traverse displacement and can be monitored on a digital voltmeter. The actual probe position, measured with a height

TABLE 5

DETAILS OF SCREEN SAMPLES

Screen	d (wire diameter) (ins)	ℓ (mesh length) (ins)	β (open-area ratio)
Steel	0.0164	$\frac{1}{15}$, $\frac{1}{16}$	0.556
Brass	0.0108	$\frac{1}{20}$	0.614
Plastic Coarse	0.0114	$\frac{1}{21}$	0.578
Plastic Fine	0.0060	$\frac{1}{40}$	0.578
Steel (1)	0.0148	$\frac{1}{15}$, $\frac{1}{16}$	0.594
Black Steel	0.0148	$\frac{1}{18}$	0.538
Coarse Copper	0.0108	$\frac{1}{24}$	0.549
Plastic	0.0116	$\frac{1}{21}$, $\frac{1}{19}$	0.589
Fine Copper	0.0092	$\frac{1}{20}$, $\frac{1}{19}$	0.674
Fine Steel	0.0076	$\frac{1}{30}$, $\frac{1}{31}$	0.590

gauge, was regularly calibrated against the output voltage. A resistance circuit was used to determine the datum zero position, when the probe just left the surface. The whole traverse gear is mounted on a $3\frac{1}{2}$ in brass disc which fits into brass rings installed at selected positions on the working section centre-line. The disc used here also had two static pressure holes used when measuring velocity profiles. This type of traverse gear can be fitted with various pressure and hot-wire probes.

A "two-dimensional" traverse consisting of two of these traverses was used for some of the spanwise skin friction measurements.

For measurements very close to the screen, a manual traverse gear (0.001 in accuracy) was used, mounted through slots in the working section roof.

3.2.4 Pressure Measurement Instrumentation

(a) Pitot Tubes

All the velocity profiles and most total pressure measurements were made with plane-ended circular Pitot tubes of 1 mm outside diameter. 1 and 2 mm diameter Pitot tubes were also used as Preston tubes for measuring the surface shear stress. For total pressure measurements just upstream of the screen, a cylindrical Pitot tube was used. As far as practically possible, this tube was designed according to the suggestions of Livesey (1956). The correction factors used when analysing the data were also those suggested by Livesey. A 0.38 mm hole was drilled in the side of a 1 mm tube at a distance of 2 mm from the rounded end. The response of this tube compared very favourably with a conventional Pitot tube.

All the tubes were made of hypodermic tubing which stepped down from a 4 mm stem.

(b) Disc-Static Probe

Static pressure profiles were measured with a disc-static pressure probe. The probe had a 0.9 mm thick brass disc of 6.4 mm diameter with a 0.38 mm bore hole through it. This type of probe is insensitive to pitch and is believed to be nearly insensitive to yaw to within ± 3^{o} (Bryer and Pankhurst, 1971). The probe was calibrated against a static pressure tapping, at various speeds, to determine the constant γ in the expression:-

$$\gamma = \frac{p - p_D}{\frac{1}{2}\rho U^2}$$

where p is the true static pressure (from tapping), p_D is the disc static pressure and $\frac{1}{2}\rho U^2$ is the dynamic head at the calibration point. The effects of free-stream turbulence on the response of this probe were found to be negligible.

(c) Yawmeter Probe

A yawmeter probe was used to measure the inclination and total pressure of the flow emerging from an inclined screen. The probe comprised three 1 mm hypodermic tubes soldered together in one plane. The middle tube was plane-ended and the tube on each side bevelled at approximately 45^{o}. The probe was held in a rigid mounting which could be systematically rotated - the angle of rotation was read from an attached protractor to an accuracy of better than a quarter of a degree. This probe was not calibrated for yaw since the flow angles were measured by the "null-reading" method as recommended by Bryer and Pankhurst (1971).

(d) Manometers

Tunnel reference pressures were normally monitored on Betz manometers.

For all other pressure measurements, Furness Controls Type MDC multi-range capacitor micromanometers were used. The voltage output from this type of manometer was monitored on a Solartron LM 1420.2 DVM. These manometers were calibrated regularly against the Betz and the calibrations were found to be linear and constant to a very good degree of accuracy. In order to minimize errors due to eye-averaging of the DVM reading, passive low-pass RC filters with a time constant of about 5 seconds were connected to the manometer outputs.

3.2.5 Data Logging System

The set-up is shown in Fig. 3.5 and was used to measure all the velocity profiles. It consisted of a Solartron Data Transfer Unit (DTU), a Teletype ASR 33 Teleprinter and Solartron LM 1420.2 DVMs, to monitor the inputs. The DTU can receive and scan up to five steady signals simultaneously. Only four channels were used here with inputs from the traverse gear, the pressure probe, the tunnel reference pressure and a "coder box". The coder box is a potentiometer which provides ten discrete voltages used for data reduction purposes. The teletype prints out the data and also punches it on paper tape which can then be read onto a computer disc using a photosensitive reader.

All the logged data were analysed using a modified version of the computer program, VELPROF (de Brederode, 1973). A brief description of the program and details of the modifications are given in Appendix B.

3.2.6 Hot-Wire Anemometry

"Home-made" DISA probes were used for all the hot-wire measurements. 5 μm Wollaston wires were soft-soldered onto the probe prongs and etched under nitric acid leaving a platinum core, typically 1 mm long. (ℓ/d of about 200). For the longitudinal turbulence intensities and mean velocity measurements, taken mainly for cross-check purposes, a DISA U-probe type 55P01 was used. All the other turbulence measurements were taken with a DISA miniature cross-wire probe type 55P51. The wires were cleaned regularly by immersing the probe in an ultrasonic bath.

DISA 55D01 constant temperature anemometers were used to operate the hot-wires. Linearisers were not used since the turbulence intensities were not very high and since triple and higher order turbulent products were not required.

The hot-wires were calibrated regularly - at least before and after each run. The procedures for the static velocity calibrations and determination of the effective wire angles of a X-wire, together with details of the corrections applied, are described in Appendix C. Dynamic calibrations were not made since Chandrsuda's (1976) comparisons showed negligible differences over the speed range of the present experiments.

3.2.7 Analogue Instrumentation

All the turbulence measurements were made analogue-wise in real time. Digital techniques were not used since higher order turbulent products were not required. The experimental set-up is shown in Fig. 3.6.

For the $\overline{u^2}$, $\overline{v^2}$ and $\overline{uv}$ measurements, the cross-wire signals from the anemometers were fed to a differential amplifier through an AC coupled HP/LP filtering system consisting of a passive filter network box and two DISA 55D25 auxiliary units. The low pass filter setting was 10 KHz to remove electronic noise from the equipment and the high pass setting was 5 Hz to remove working section unsteadiness. The mean square of the fluctuating voltage was measured using a DISA 55D35 RMS meter on a Solartron DVM. Details of the processing of this data are given in Appendix D.

For the spectrum measurements, X-wire signals from selected profile points were recorded on an AMPEX FR 1300 Analogue Tape Recorder and analysed later. A Sum and Difference Unit was used to produce signals proportional to u and v. These signals were fed into a Brüel and Kjaer spectrometer (Type 2112) set on one-third octave filters and the output from these integrated over a time constant of 15 seconds set on an externally connected "Watesta" timer. Operational amplifiers, multipliers, integrators and the Sum and Difference Unit form part of the Department's PHI module system and plug into a PHI console with a common ± 15 V power supply.

3.3 Results and Preliminary Discussion

3.3.1 Mean Velocities and Bulk Flow Parameters

Most of the work was done in the 450 x 450 mm tunnel at an undisturbed free-stream velocity of about 18 m/s giving an Re_θ of 1690 at the first measuring station, situated at a distance of 140 mm from the screen position. Measurements at this station (without screen) have been taken as the undisturbed "upstream of screen" values throughout the present analysis.

Fig. 3.7 shows the velocity and semi-logarithmic profiles for the undisturbed turbulent boundary layer at x = 140 mm. The boundary layer has a monotonic increasing velocity profile with a δ_{995} of 14 mm and a well-defined log. region between $y^+ \left(= \frac{yu_\tau}{\nu}\right) = 50$ and $0.2\ \delta_{995}$. The log. law with Coles' constants, K = 0.41, C = 5.0 giving:-

$$\frac{U}{u_\tau} = 5.62 \log y^+ + 5.0$$

is also plotted on this and subsequent semi-log. plots. The wake component ($\Delta U/u_\tau$) value of 1.7 compares well with Coles' (1962) equilibrium value of 1.8 at this Re_θ. The profiles at x = 597 mm (the last measuring station) are shown in Fig. 3.8. A small increase in boundary layer thickness, and consequently in free-stream velocity, is apparent. All the velocity profiles are normalized by U_{ref} - the free-stream velocity at x = 140 mm (without screen).

(a) <u>The Steel Screen</u>

The profiles measured at four stations downstream of the steel screen are presented in Fig. 3.9. A reduction in the boundary layer thickness is apparent although the edge of the boundary layer is not clearly defined. Non-uniformities in the free stream include screen-produced longitudinal vortices but these have almost disappeared by the last station. These longitudinal vortices are presumably formed by the random coalescing of jets emerging from the screen pores and according to Bradshaw (1965) are more prominent for screens with $\beta < 0.57$. This screen has a β of 0.56. There are also signs of an overshoot in the velocity profile near the boundary layer outer edge.

Note that the profile at x = 414 mm was measured on the working section ceiling. This was to make sure that the effects noticed on the floor were not due to any extraneous effects and except for the slight phase shift in the "rippling", this profile seems to represent the recovery process well. The semi-log. profile at x = 140 mm exhibits a log. region but with different constants to Coles' and with no significant wake component. Again recovery is almost complete by x = 597 mm.

(b) The Brass Screen

The trends for the brass screen (Fig. 3.10) are very similar, especially the semi-log. profiles. The velocity profiles, however, exhibit more non-uniformity in the potential core and this is still evident at the last station. Although β for this screen is higher (0.63), the non-uniformity is not too surprising since this screen had non-uniform weave and slight wrinkles which would enhance the coalition process of the emerging jets by affecting directional changes. However, there are no significant signs of any overshoot.

(c) The Plastic Coarse Screen

The velocity profiles for the plastic coarse screen (Fig. 3.11a) show significant changes although the semi-log. profiles (Fig. 3.11c) show trends similar to those for the two metal screens. There is a distinct overshoot in the velocity profile which persists until x = 597 mm. Although the definition of a boundary layer thickness now becomes very subjective, the boundary layer behind this screen is considerably thinner than those behind the metal screens and explains the larger reduction in free-stream velocity. Another new feature is the absence of any large-scale, systematic rippling in the potential flow. The few signs there are at x = 140 mm, disappear very quickly and the profile at x = 597 mm, in this region, is extremely uniform. This feature is demonstrated better in Fig. 3.11b which extends up to a larger y-distance.

(d) The Plastic Fine Screen

The plastic fine screen velocity profiles (Fig. 3.12a) are very similar to those for the plastic coarse screen except the overshoot is larger and more distinct. The semi-log. profile at x = 140 mm (Fig. 3.12b) shows a very small log. region and no wake component at all, but again, recovery from the perturbation is quite rapid. Fig. 3.12c shows the profiles at x = 140 mm with the screen rotated through 90^{o} about its own axis. Similarity of the results proves that the effects noted above are not unique to a certain portion of the screen.

The main differences in the mean flow between the plastic and metal screens are with regard to the overshoot, which is discussed more fully in Section 3.4.1, and the rippling in the core flow. Since the open-area ratios of the plastic screens (0.57) provided no clue, an investigation of the weaving properties was launched. This revealed that the plastic strands were necked at the nodal points so that they were embedded within each other (Fig. 3.13). This implied that the fibres could not slide over each other, thus maintaining the original uniform weave, whereas the metal screens are likely to suffer from this kind of deformation. Also, this means that the overall thickness of the plastic screens is less than 2d, where d is the strand diameter, thus making the screen more nearly co-planar. It seems feasible that the chances of the flow remaining straight and parallel as it goes through the pores would be better if the screen was more nearly co-planar. The measured thickness values are given below in Table 6.

TABLE 6

SCREEN	OVERALL THICKNESS
Steel	2.2 d
Brass	2.0 d
Plastic Coarse	1.8 d
Plastic Fine	1.9 d

The plastic coarse screen, which has the smallest overall thickness, also seems to produce the most uniform core flow.

The supposed presence of strong longitudinal vortices is also probably responsible for variations in the skin friction coefficient, c_f $(= \tau_w/\frac{1}{2}\rho U_e^2)$. In order to investigate this aspect, the spanwise c_f distribution was measured downstream of the screens at three stations with a Preston tube (Figs. 3.14 - 3.18). The c_f values were evaluated using Patel's (1965) calibration. Note the small shift in x-wise position. The undisturbed distributions show a characteristic peaky shape with a peak-to-peak variation of at least 20% about the mean. This strongly suggests the presence of some sort of secondary flows. The distributions downstream of the screens show the expected increase in c_f followed by a gradual recovery, but all except that for the steel screen still have roughly the same peaky shape. The steel screen distribution at x = 105 mm may be indicating the presence of longitudinal vortices - this screen does have the lowest β.

The c_f (z) distribution was then measured at the end of the working section (x = 2.4 m) across the whole tunnel span. As shown in Fig. 3.19, the flow is dominated by strong secondary flows and none of the screens have affected it significantly. The source and nature of this secondary flow is discussed in more detail later in Section 5.1.3. These results, therefore, suggest that the longitudinal vortices shed by the screen will not persist in a boundary layer already dominated by strong secondary flows.

In order to assess Re effects, the mean velocity profiles at the first station were also measured at a reduced free-stream velocity of about 10 m/s (Figs. 3.20 - 3.21). The most noticeable feature is the absence or reduction of the overshoot, and the semi-log. profiles are correspondingly affected. As far as the rippling is concerned, there seems to be no Re dependence except for the plastic fine screen where the non-uniformities seem to have increased slightly.

The distributions of the boundary layer thicknesses, skin friction coefficient and shape parameter are plotted in Figs. 3.22 - 3.26. The boundary layer thickness, δ for these was defined as the point where the velocity reached 0.9 times the undisturbed free-stream value (i.e. U/U_{ref} = 0.9) and the integral parameters were calculated upto this point. This was to avoid the effects of local non-uniformities near the boundary layer edge. The integral parameters were calculated using Simpson's Rule for unequal steps and the c_f values obtained from the VELPROF fitting routine described in Appendix C.

The effects on these parameters of the metal screens are of the same order of magnitude and smaller than for the plastic screens. The plastic fine screen produces the maximum perturbation on all the parameters. This is surprising because it does not seem to correlate with β which is smallest for the steel screen (0.56) and largest for the brass screen (0.61). The rate of recovery $\left(\text{i.e. } \frac{d\delta}{dx} \text{ etc.}\right)$ of each parameter is similar for all the screens. Fig. 3.22 shows that the boundary layer growth rate is much less than the typical value for a "constant-property boundary layer in a mild pressure gradient", about $\frac{d\delta}{dx} = 0.015$ (Cebeci and Bradshaw, 1977).

The c_f distribution shows the expected increase downstream of the screens and then a monotonic decreasing recovery, at different rates for different screens. Surprisingly, the shape factor (H) distribution shows the same trend as c_f. The increase in c_f is plausible since the thinner boundary layer now has a large contribution from the viscous stress $\left(\mu \frac{\partial U}{\partial y}\right)$. Large values of H (2.3 $\sim$ 3.5) indicate a laminar boundary layer. There are indications that the plastic fine screen, at least, may be re-laminarising the boundary layer (H = 3.6 at x = 140 mm). In fact, the semi-log. profile at x = 140 mm (Fig. 3.15a) for this screen is also analogous to that of a re-laminarised boundary layer. Re-laminarisation normally takes place when boundary layers are accelerated, like for example through a contraction. In this particular case, since the screen thins the boundary layer, the streamlines in the boundary layer must be expected to converge towards the wall and so to maintain a constant mass flow $(\int U dy = \psi)$, a slight acceleration is experienced but this on its own could probably not cause the observed effects. The change in H between x = 140 mm and x = 597 mm is comparable to that observed in the transition region of a flat plate boundary layer (see Fig. 16.5, Schlichting, 1968).

3.3.2 Pressure Drop Coefficients

The pressure drop coefficient of a screen, K is defined as the ratio of the static pressure drop across it (Δp) to the dynamic head of the approaching flow ($\frac{1}{2}\rho U^2$). Hence:-

$$K = \frac{\Delta p}{\frac{1}{2}\rho U^2}$$

However, in finite ducts, measuring Δp as a difference in static pressures across the screen leads to errors and this is what most of the workers have been doing.

Applying Bernoulli's equation to the flow along a streamline and denoting the upstream of screen values by subscript 1 and the downstream ones by 2:-

$$P_1 = P_2 + \Delta P$$

where ΔP is the total pressure drop across the screen. Then:-

$$p_1 + \frac{1}{2}\rho U_1^2 = p_2 + \frac{1}{2}\rho U_2^2 + \Delta P$$

Therefore:-

$$\Delta P = p_1 - p_2 + \frac{1}{2}\rho(U_1^2 - U_2^2)$$

So by measuring $p_1 - p_2$, one measures the actual pressure drop across the screen <u>minus</u> the drop in dynamic pressure across the screen due to boundary layer effects in a finite tunnel. So for all measurements in finite ducts, the pressure drop <u>must</u> be measured as a difference in total pressures.

In this investigation, the downstream total pressure was measured by a Pitot tube at $x = 597$ mm, where the screen-produced non-uniformities were small. Even then the final pressure reading was averaged over a y-wise distance of about 50 mm in the potential core.

K is plotted against a modified Re ($Ud/\beta\nu$) for the four screens in Figs. 3.27 - 3.30. The theoretical formulae of Wieghardt (1953), Collar (1939) and Annand (1953) are also plotted for comparison. For the brass screen, Wieghardt's formula overestimates K by as much as 20% at the lower speeds ($U < 15$ m/s). The agreement for the steel screen is better ($\sim$ 10%). The accuracy of K-prediction by this formula may well be expected to suffer with increasing β. Collar's equation, even with $C = 0.9$, and Annand's formula both overestimate K in the high Re limit. Since Wieghardt's empirical fit was based on data suffering from errors of the type discussed above, one would expect this formula to underestimate K, especially at the lower speeds where displacement effects are larger. From the formulae available, the one due to Wieghardt is still the most accurate, in predicting the right trend, over the whole velocity range considered here ($0 < U < 20$ m/s). However, a need to re-formulate this equation with more reliable data is evident.

Surprisingly, all the formulae seem to predict the plastic screen K-values much more accurately. This is mainly because these plastic screens are exhibiting high-K properties for their open-area ratio (0.57) compared to the metal screens. At a given flow speed, the plastic fine screen produces the highest pressure drop. This explains a lot of the results in Section 3.3.1. This high-K property must be at least partly attributable to the co-planarity of these screens and formulae such as Wieghardt's (dependent only on β and Re) and based only on metal-screen data should be applied with caution.

3.3.3 Turbulent Quantities

Extensive measurements of the Reynolds stress components ($\overline{u^2}$, $\overline{v^2}$ and $\overline{uv}$) were made downstream of the four screens at three stations, x = 105, 257 and 562 mm. Note that these measuring stations are not quite the same as those for the velocity profiles because of the difference in probe lengths. They are, however, the same as those for the spanwise c_f measurements. All the Reynolds stress components presented here are normalised by a local U_e^2 for each station - the velocity at y = 50 mm.

Figs. 3.31 - 3.35 show the longitudinal mean square intensity ($\overline{u^2}/U_e^2$) profiles. The undisturbed profile indicates a root-mean square intensity level in the potential core of about 0.28%. The $\overline{u^2}$ in the boundary layer is reduced drastically by all the screens, especially the plastic screens. The plastic fine screen has reduced $\overline{u^2}/U_e^2$ by about 93% at y = 3 mm. Recovery is almost complete by the last station (x = 562 mm) especially with the metal screens. The rise in the free-stream intensity level is almost entirely due to the screen produced turbulence. This is seen to dissipate with increasing x. There are also signs of slight rippling in this region at x = 105 mm.

Figs. 3.36 - 3.40 show the lateral mean square intensity ($\overline{v^2}/U_e^2$) profiles. The undisturbed free-stream root-mean square intensity level is about 0.4% - about 1.5 times the $\overline{u^2}$ level. This just confirms the effect of the contraction which is to reduce $\overline{u^2}/U_e^2$ more than $\overline{v^2}/U_e^2$ (see Section 5.1.1). The effects of the screens on $\overline{v^2}$ are very similar to those on $\overline{u^2}$, but the percentage reduction in the boundary layer is less - 89% for the plastic fine screen at y = 3 mm. This just confirms that screens affect the longitudinal turbulence component more than the lateral one. Again, the increase in the free-stream level is evident. There are very little signs of systematic rippling except perhaps for the plastic fine screen at x = 105 mm. On the whole, the $\overline{v^2}$ recovery is noticeably faster than $\overline{u^2}$ and this indicates a tendency to isotropy.

The shear stress profiles ($\overline{uv}/U_e^2$) are presented in Figs. 3.41 - 3.45. The $c_f/2$ values tabulated on the figures are those measured by a Preston tube and the shear stress profiles are expected eventually to asymptote towards this wall shear stress value. The points near the surface, y ≃ 3 mm are obviously affected a little by wall interference effects. The effects of the screens on $\overline{uv}$ are again similar to those on $\overline{u^2}$ and $\overline{v^2}$, only the reduction is greater.

Most of the total shear stress in the small region near the wall is probably viscous shear stress; the total shear stress, τ is defined as:-

$$\tau = \mu \frac{\partial U}{\partial y} - \rho \, \overline{uv}$$

The rippling in the potential core is more evident in these profiles for all the screens, with the shear stress often changing sign.

It is evident from all these Reynolds stress profiles that the effect of the screen is almost to obliterate the turbulence in the outer layer of the boundary layer and also to generate some turbulence of its own even in the free stream. The action of the screen is to reduce the scale of the oncoming turbulence to a size which is correlated with the screen mesh size which then dissipates more quickly. In a boundary layer the large eddies, which extend over most of the width of the outer layer and which are responsible for producing most of the shear stress, are affected by a screen in this way and this explains the greater effect of a screen on $\overline{uv}$. The results presented above confirm this in principle since the greatest reduction of the turbulent quantities (especially $\overline{uv}$) is by the plastic fine screen (ℓ = 1/40 in). The drastic reduction of the Reynolds stresses, in particular that of $\overline{uv}$ in the outer layer, implies that the velocity profile in this region is almost "frozen" with very little turbulent production $\left(- \overline{u_i u_j} \frac{\partial U_i}{\partial x_j}\right)$ - the full transport equations and the interpretations of the terms are given in Appendix E.

If the local Re ($Ud/\beta\nu$) of the screen wires is greater than about 80 (true for most practical applications), the wire wakes will be turbulent and the screen will contribute turbulence to the flow. This implies that the amount of turbulence contributed should be correlated with the wire diameter and indeed in the above results, the steel screen (d = 0.0164 in) contributed the most while the plastic fine screen (d = 0.0060 in) contributed the least. The reason why the turbulence in the boundary layer, which is correlated with the screen mesh size, has dissipated relatively fast compared to the screen produced turbulence in the core flow, which is correlated with the wire diameter, is that the dissipation term $\left[\nu \overline{u_i \; (\partial^2 u_i/\partial x_j^2)}\right]$ is much greater in the boundary layer.

Another source of turbulence contribution is the non-uniformities produced by the screen in the mean flow. The rippling observed in the mean velocity profiles in the core flow implies a shear ($\partial U/\partial y$) with changing sign which means there is positive and negative turbulent production. Negative production is by no means unique to this flow and implies a transfer of energy from the turbulence to the mean flow - a compression of the vortex lines rather than stretching. This explains the rippling in the turbulent quantity profiles. The $\overline{uv}$ profiles change sign and ripple more since the dominant production term in the turbulent energy equation for this case is $- \overline{uv} \frac{\partial U}{\partial y}$.

In order to assess the efficiency of the turbulence as a supporter of shear stress, the correlation coefficient, R_{uv} ($= \overline{uv}/\sqrt{\overline{u^2}} \sqrt{\overline{v^2}}$) profiles are plotted in Figs. 3.46 - 3.50. The profiles only extend up to the nominal boundary layer edge. The results show that in the region of recovery from the effects of the perturbation the efficiency of maintenance of shear stress is reduced, more so for the plastic screens than the metal ones. The reduction is not as marked as the shear stress itself because the intensities are also reduced, but the structural changes involved are obviously large. Again R_{uv} has recovered to the undisturbed value by x = 562 mm for all the screens. Recovery is much quicker in the regions nearer the wall (but still in the outer layer) as indicated by the profile at x = 257 mm and indeed there is even an overshoot indicated for the steel and plastic fine screens. This suggests an increased activity in this region and indicates the re-organisation of the large (shear-stress-producing) eddies in the "new" turbulence. Although the actual values of R_{uv} in the region beyond the boundary layer are ratios of small measured quantities, and hence not so accurate in detail, the trends shown up are consistent and interesting. Fig. 3.51 shows this extended profile for the steel screen and the approximately sinusoidal variation with changing sign is consistent with the positive and negative production in this region.

In order to determine the effects of a screen on the structure of the turbulence in wave number space, a spectral analysis was carried out on one screen (plastic coarse screen). Measurements were made at three y-positions (0.25, 0.50 and 0.75 δ_0; δ_0 ($\equiv \delta_{995}$) is the undisturbed boundary layer thickness) and at two stations (x = 105 and 257 mm) on nominally the same streamlines in y. All the spectral densities have been normalised by U^2_{ref} so that direct comparison is more justifiable. The area under the curve is thus equal to the intensity and not 1.0. So:-

$$\int \frac{\phi_{11}}{U^2_{ref}} (k_1)\, dk_1 = \frac{\overline{u^2}}{U^2_{ref}} \qquad \text{and} \qquad \int \frac{\phi_{22}}{U^2_{ref}} (k_1)\, dk_1 = \frac{\overline{v^2}}{U^2_{ref}}$$

The ϕ_{11} results are presented in Figs. 3.52 - 3.54 plotted on logarithmic ($\log_{10}$) scales. The - 5/3 law which comes from Kolmogorov's universal equilibrium assumptions is also plotted in these figures (with an arbitrary intercept) for the undisturbed case, to verify the normality of the measured spectra. The - 5/3 law is valid in the viscosity - independent inertial subrange which links up the low-wave number, energy-containing range to the very high-wave number viscous dissipation range. The spectral density in the energy-containing range is reduced by the screen in all three cases at x = 105 mm - this indicates the reduction of $\overline{u^2}$ by reducing the scale of the oncoming turbulence. At higher wave numbers the ϕ_{11} spectra now falls-off more slowly, indicating a contribution which would be the screen produced turbulence. The "recovery" at x = 257 mm is only indicated at y = 0.25 δ_0. In the other two cases no significant change has occurred. This is because the y = 0.5 δ_0 streamline is now near the boundary layer edge and the outermost one is well beyond the boundary layer; most of the immediate re-organisation takes place well within the boundary layer, as indicated by the R_{uv} profiles.

The ϕ_{22} results presented in Figs. 3.55 - 3.57 show very similar trends to ϕ_{11} but to a lesser extent; screens affect the longitudinal turbulence component more than the lateral one. There is a curious dip in all the spectra at log. $k_1 \simeq 1.8$ which seems inexplicable.

3.4 Further Discussion and Results

3.4.1 Overshoot in Mean Velocity Profiles

In the results presented above, the most interesting single phenomenon observed has been the overshoot in the velocity profile near the boundary layer edge. In effect, we get a velocity or total pressure excess where there was a defect, i.e. in the boundary layer.

Other workers have also noticed this effect, mainly for screens with K > 1. Owen and Zienkiewicz (1957) obtained a "bulge" in the velocity profile generated from a row of cylindrical rods. Corner (1971) obtained a distinct overshoot downstream of a metal screen with K = 2.55. Lau and Baines (1968) did some experiments on flow through screens and showed that the overshoot increased with increasing K for K > 1. They gave an explanation for this effect by considering the energy balance with some rather ill-founded assumptions. Their main assumption was that the streamlines are not subjected to large deflections and so there is no change in velocity on a streamline before the screen. Clearly, this assumption is not justifiable since, depending on the K-value of the screen, the boundary layer is thinned-down and the streamlines must, therefore, converge towards the wall and experience an acceleration (to maintain a constant mass flow).

It is in fact this very effect that suggests an explanation for the whole phenomenon. In a finite tunnel, the streamlines passing through the screen right against the wall and on the tunnel centre-line must be expected to be straight and parallel. So there is a region, most probably near the boundary layer edge, where the streamline inclination has a maximum. Fig. 3.58 shows a very simplified version of this effect in a diffuser. As mentioned in Section 3.1.2, K is found to decrease with increasing flow inclination. This means that the streamlines near the boundary layer edge suffer an even smaller pressure drop which could result in the overshoot.

In order to verify that the point of minimum pressure drop is at a finite distance from the wall, the pressure drop along individual streamlines was calculated from the velocity profiles (Appendix F). Fig. 3.59 shows the plot of the "pressure-loss deficit":-

$$\left(= \frac{(p_1 - p_2) - \Delta P}{\frac{1}{2}\rho U_e^2} \right)$$

along a streamline against the streamfunction, ψ. The curves for all the screens have a well-defined point of minimum pressure drop at a finite distance from the wall. For a given screen, this point does not in general match with the position of the overshoot. Now remembering that:-

$$\Delta P = K \times \frac{1}{2}\rho U^2 \times \mathrm{Cos}^m\,\theta$$

where m is an empirical factor, ΔP will be a minimum where $U^2\ \mathrm{Cos}^m\theta$

is a minimum and this is not necessarily the point where the overshoot appears. Note that the curves asymptote to:-

$$K - \frac{p_1 - p_2}{\frac{1}{2}\rho U_e^2};$$

they would asymptote to zero only in an infinite tunnel. Fig. 3.59 also indicates that the plastic screens produce a bigger deficit in pressure loss than the metal screens and the plastic fine screen even more so. This is in general agreement with the extent of the overshoot in the velocity profiles. This distinction between the plastic and metal screens suggests once again that the properties of the screens themselves may be responsible for these effects.

On measuring the x-wise deflection of the screens on the tunnel centre-line, due to wind loading, at various speeds (Fig. 3.60) it was found that the plastic screens deflected more, i.e. stretched more than the metal ones. Even in the high-speed limit the plastic screens are continuing to stretch, i.e. it is genuine elasticity, not just sag being taken up. This may be because the local stress and strain are much higher at the points where the necked plastic fibres meet. Large screen deflections imply large screen inclination angles near the wall, and this must be expected to affect the pressure drop as well.

This was verified by measuring the total-pressure profiles downstream of the steel screen at x = 50 mm for two different situations:-

(i) With the screen straight (in side-view);

(ii) With the screen deliberately curved into a semicircular shape, as shown in Fig. 3.61.

The inclined part of the screen (about 50^{o} to the floor) has produced a distinct overshoot (about 20%) near the wall. The profiles collapse well for the region of zero inclination.

Now since the deflection, and hence the screen inclination, is speed-dependent, (Fig. 3.62 shows the measured plastic fine screen shape at two different velocities), the extent of the overshoot must also be speed-dependent and indeed a comparison of Figs. 3.12 and 3.21 has already shown that the overshoot at $U_e = 10$ m/s is considerably less than at higher speeds.

Now this implies that the overshoot for this screen was more a result of screen inclination than streamline inclination since we would expect the streamline inclination to increase with decreasing flow speed. Screen deflection alone cannot be responsible for the overshoot since Owen and Zienkiewicz (1957) had a grid consisting of a row of rods, which is not expected to deflect, and they still observed an overshoot in velocity profile. The reason why this effect is observed mainly for screens with $K > 1$ is that as K gets larger, the boundary layer is thinned down more and so the streamline inclination is increased. So as regards the overshoot, the important parameters are the pressure drop coefficient of the screen (which determines the streamline inclination) and the flexibility of the screen (which determines the screen inclination). Screen deflection (ΔL, say) must be expected to be dependent on the wire elasticity, wind loading (which is correlated with β) and also the ratio of screen mesh length to tunnel height (which determines the number of affected, high-stress and strain, nodal points along a fibre). Hence:-

$$\frac{\Delta L}{h} = f\left(\frac{E}{K\rho U^2}, \beta, \frac{\ell}{h}\right)$$

Now the screen inclination has a maximum near the wall, if the final screen shape under load is assumed to be a spherical cap, and so for the combined effect of streamline and screen inclination to have a maximum effect, another relevant parameter must be δ_0/h, where δ_0 is the undisturbed boundary layer thickness and h is the working section height. In the above tests this ratio had a value of about 0.03. It was a pure coincidence that the high streamline inclination occurred at a y-position where the screen inclination was also very high, but the coincidence may be repeated in real small blower tunnels.

Some preliminary investigations had been conducted in a 108 x 108 mm duct where $\delta_0/h \simeq 0.3$. Figs. 3.63 - 3.65 show the velocity and semi-log. profiles measured at four stations, upstream and downstream of three different screens. The details of the measuring positions are shown in Fig. 3.4 and details of the screens tested in Table 5. The tests were performed at an undisturbed free-stream velocity, U_{ref} of about 20 m/s compared to 18 m/s in the 450 mm tunnel and this was reduced by about 10% through the screen due to displacement thickness effects. All the velocity profiles are normalised by U_{ref}. The velocity profiles at x = 64 mm do not show any distinct overshoot, even for the plastic screen. In fact, at about y = 10 mm there is a distinct defect although the profile is still increasing monotonically. This defect is less apparent with the coarse copper screen which has the lowest β (0.549). Some local wiggles are apparent near the boundary layer edge but the recovery for all the screens is almost complete by x = 521 mm. The semi-log. profiles, even at this smaller x-distance, are also not as badly deformed as in the previous results from the 450 x 450 mm tunnel. A distinct log. region with Coles' constants is apparent at x = 64 mm but still no wake component. Again recovery is almost complete by x = 521 mm. This effect of δ_0/h is shown up even better in Figs. 3.66 - 3.68 where the profiles measured at the same stations as the ones above are compared with one measured far upstream (x_1 = 292 mm) where δ_0/h = 0.05. Slight overshoots are indicated at x_1 = 292 mm for the black steel and steel screens but not at x = 64 mm. The semi-log. profiles indicate that the recovery at x_1 = 292 mm is almost complete but that at x = 216 mm (a smaller x-wise distance) is also very near completion, especially that for the black steel screen. The reason for these differences between screens is that the open-area ratio, β, of the black steel screen is much lower (0.538) than that of the fine copper screen (0.674) with that of the steel screen being 0.556, implying that the streamline inclination for the black steel screen is the highest. A direct comparison with the 450 x 450 mm results is also possible since the same steel screen was tested in both the rigs. The profile at x_1 = 292 mm (Fig. 3.66a) is very similar, qualitatively to that at x = 292 mm in the 450 mm tunnel (Fig. 3.9a); the δ_0/h ratios are of the same order, 0.05 and 0.03, respectively. On the other hand, a comparison of the profile at x = 521 mm (Fig. 3.66a) with that at x = 597 mm (Fig. 3.9a) shows the apparent difference in terms of the overshoot.

So these results confirm that streamline inclination is basically responsible for the overshoot in mean velocity profiles and with flexible screens (e.g. plastic) this effect is accentuated by the screen inclination, at least for some values of δ_0/h.

3.4.2 Measurements Very Close to the Screen

So far we have concentrated on the recovery process of the flow from the perturbation produced by the screen. In order to assess the exact nature of the perturbation, we need measurements close to the screen, upstream and downstream. Velocity profiles were measured, in the 450 mm tunnel, close to the steel and plastic fine screens and detailed pressure measurements were made close to the plastic fine screen (within x = ± 50 - 60 mm). All the measurements near the steel screen were made at a free-stream velocity of about 18 m/s while all the plastic fine screen measurements (except where otherwise stated) were made at a reduced velocity of about 13 m/s, mainly to reduce the screen deflection and thus overshoot.

Figs. 3.69 and 3.70 show the velocity profiles measured upstream of the steel and plastic fine screens, respectively with a single hot-wire. These profiles just indicate a reduction in the boundary layer thickness as the flow approaches the screen implying a convergence of the streamlines towards the wall. The downstream profiles for the steel screen (Fig. 3.71) clearly show the wavy non-uniformity produced by the screen throughout the flowfield. The peak-to-peak variation about the mean at x = 12 mm is about 7%. These ripples tend to disappear more quickly within the boundary layer because of the higher turbulent mixing. By x = 41 mm the boundary layer has emerged and signs of the overshoot have appeared at about $y \simeq 11$ mm. However, the profiles downstream of the plastic fine screen (Fig. 3.72) at $U_e \simeq 18$ m/s show no such non-uniformities in the core flow although the overshoot is very evident. This confirms the conclusions reached above about the plastic screens yielding more uniform flow in the potential core. However, the profiles at $U_e \simeq 13$ m/s

(Fig. 3.73) do show some non-uniformities, about 2.5% peak-to-peak variation about the mean. This indicates again what the Pitot results suggested, that for this screen, the non-uniformities may be speed-dependent.

All the pressure profiles presented below were measured with respect to a reference static pressure in the working section and normalised by the tunnel reference pressure. The total pressure profiles measured upstream of the plastic fine screen with a cylindrical Pitot tube are presented in Fig. 3.74. Again this just indicates the expected increase in total pressure at a given y; $V < 0$ as the flow approaches the screen. The static pressures were measured with the disc-static tube described in Section 3.2.4. The static-pressure profiles (Fig. 3.75) indicate almost zero transverse pressure gradient in the boundary layer at x = - 43.0 mm. The static pressure drop in the boundary layer then decreases towards the screen as the streamlines converge and the velocity along them increases. The static pressure in the free stream increases gradually, indicating a slight drop in velocity due to displacement thickness effects. The velocity profiles calculated from these measurements are plotted in Fig. 3.76. They just show the expected trend of the boundary layer thickness decreasing. However, at x = - 3.0 mm there is a small overshoot at about y ≃ 10 mm. This implies that there is an appreciable streamline inclination near the boundary layer edge but the increase in the pressure drop due to this increase in velocity is obviously outweighed by the effects of streamline and screen inclination.

The total pressure profiles downstream of this screen, measured with a conventional Pitot tube, are presented on a highly expanded scale in Fig. 3.77. The overshoot seems to emerge very near the wall, and the non-uniformity in the core flow is well-defined and persistent. The static pressure profiles (Fig. 3.78) confirm the basic principles of a screen: it affects a higher pressure drop in the higher velocity regions. Unfortunately, the overshoot occurs too near the wall for the effects to be apparent in these results. The effects of the screen on static pressure are best described in Fig. 3.79 where the distribution is plotted for three y-positions. The evaluated velocity profiles downstream of the screen are presented in Fig. 3.80. The non-uniformity of about 2% at x = 16.5 mm is consistent with the 3% non-uniformity noted in the hot-wire profile at x = 14 mm (Fig. 3.73).

From the evaluated velocity profiles the streamline shapes were calculated numerically. The streamlines are plotted in Fig. 3.81 and show an increasing inclination as the streamfunction, ψ increases, with a maximum well beyond the boundary layer. Since the overshoot for the plastic fine screen emerges very near the wall, it is probably more attributable to screen deflection than streamline inclination. This agrees with the earlier observations that the overshoot decreases with decreasing flow speed leading to a smaller screen deflection.

3.4.3 Inclined Screen Results

It is evident from the results discussed above that streamline and screen inclination play an important role in determining the form of the emerging flowfield, It has long been known that the pressure drop through a screen, and even the deflection coefficient, are significantly affected by screen inclination but, as shown in Section 3.1.2, the exact forms of the correlations have not been satisfactorily established. In the present investigation, the variation with inclination of the pressure drop and deflection coefficient of four screens was investigated in the 450 mm tunnel. The experimental rig and measuring techniques are described in Section 3.2.

The yawmeter probe was positioned sufficiently far downstream of the screen at about 500 mm from the surface (still within the potential core) to minimize the effects of the screen produced non-uniformities. However, since all the measurements were consistently taken on the centre-line of the emerging flowfield, the effects of this on the variation of the parameters with θ would be negligible anyway. Three of the screens used here are the same samples that were used in the main analysis above. The steel screen had to be replaced by a steel (1) screen with a higher β of 0.594.

(a) Pressure Drop Coefficient

The results for the variation of the pressure drop coefficient, K_θ, with screen inclination, θ, are presented in Figs. 3.82 - 3.85. The values of K_θ at $\theta = 0$ agree to within 5% with the previously measured values (Section 3.3.2) which were averaged over a part of the screen. The dashed curves in these figures show a Cos θ relation forced to fit K ($\theta = 0$) at the two speed limits. On the whole, the Cos θ agreement over the speed and β ranges investigated for both types of screens is good to within about 7%. So these results imply a relation:-

$$K_\theta = K \cos^m \theta \quad , \quad \text{with } m = 1.0 \tag{3.7}$$

However, at low speeds, a distinct overshoot is indicated at about $\theta = 10^o$, especially for the plastic screens.

For comparison some results of Simmons and Cowdrey (1945) and Dryden and Schubauer (1949) are plotted in Figs. 3.86 - 3.99. Two points emerge from these results. Firstly, the overshoot at low speeds is present in all the measurements at about $\theta = 10^{o} - 15^{o}$. There seems to be no obvious explanation for this effect. Secondly, in the high Re limit, the Cos θ relation seems to work better for the higher β screens. For the screens with low β (~ 0.3) a higher value of m (about 1.4) gives a better fit. The implications of this seem feasible since one would expect a screen with low β (wires closer together) to be affected more by inclination than one with a higher β (wires further apart).

Purely intuitive "normal component of velocity" arguments, of course, suggest a $\text{Cos}^2\,\theta$ relation which Schubauer et al (1950) apparently found. However, a close look at their plotted results (the data was not tabulated) does indicate a shift in trend as β increases from 0.21 to 0.67. Also the rather large scaling on the $K_\theta/\text{Cos}\,\theta$ axis, to accommodate all their data, makes it difficult to see individual detail and assess how well the data really collapsed.

For screens normally used in wind tunnels, β is of the order of 0.6 and so a Cos θ relation is applicable.

(b) Deflection Coefficient

The deflection coefficient, α_θ, defined herein consistently as ϕ/θ, is plotted for the four screens in Figs. 3.90 - 3.93. As expected, for a given θ, α_θ asymptotes to a finite value in the high Re limit. However, there is also a strong dependence of α_θ on θ, with the deflection coefficient decreasing with increasing θ. This dependence is again more distinct for the plastic screens.

Fig. 3.94 shows a comparison of the present trends with those of Dryden and Schubauer (1949) and Simmons and Cowdrey (1945) in the limit of high Re. As mentioned before (Section 3.1.2), Simmons and Cowdrey's results may contain errors. It is, however, reasonable to assume that the errors are consistent and of about the same order for all the screens and, therefore, should not affect the qualitative trends significantly. All the results due to Dryden and Schubauer show a general trend that is opposite to the present one - α_θ increases with θ, although the variations are not monotonic. However, Simmons and Cowdrey's results indicate a definite change in trend as β increases and for the $\beta = 0.49$ screen, $d\alpha_\theta/d\theta$ has just gone negative. A closer look at Dryden and Schubauer's data indicated that at lower speeds ($U \sim 5$ m/s), their trend also changed between $\beta = 0.34$ and 0.69, as shown in Fig. 3.94. Also, from the present results, for the metal screens at least, $\frac{d\alpha_\theta}{d\theta}$ is very much less negative for the steel (1) screen ($\beta \sim 0.59$) than for the brass screen ($\beta \sim 0.61$). So once again, it is apparent that screens with low β (less than 0.5, say, can behave very differently from those with $\beta > 0.5$. Reynolds (1969) also makes this distinction with his formulations. His mathematical models generally agree with Schubauer <u>et al's</u> (1950) data but were obtained by simply considering the drag on the screen fibres.

In trying to correlate the experimental F_θ/θ with K_θ for the present results, it was realised that there was a strong dependence of this function on θ. F_θ is the force coefficient parallel to the plane of the gauze and is defined in eq. (3.5). F_θ was evaluated using eq. (3.5). In fact, Reynolds (1969) had also hinted this. A simple correlation of the type given by Dryden and Schubauer (1949):-

$$\frac{F_\theta}{\theta} = 2 - \frac{2.2}{(1 + K_\theta)^{\frac{1}{2}}}$$

for all θ seems rather optimistic. In order to try and determine the functional relationship between α_θ, θ and K_θ, a more realistic procedure was followed here.

For each screen, F_θ/θ was plotted against θ for three values of K_θ (0.5, 1.0 and 1.5). The finite values of F_θ/θ as $\theta \rightarrow 0$ were extrapolated graphically and these then plotted against K_θ. This gives the limiting case of small θ. A best fit to the data gave:-

$$\frac{F_\theta}{\theta} = 0.68 - \frac{0.62}{(1 + K_\theta)^{\frac{1}{2}}} \tag{3.8}$$

which has the same form as Dryden and Schubauer's formula.

Combining eqs. (3.5) with (3.8), for small θ, we obtain:-

$$\alpha = 0.66 + \frac{0.31}{(1 + K)^{\frac{1}{2}}} \tag{3.9}$$

instead of the generally accepted form given in eq. (3.1):-

$$\alpha = \frac{1.1}{(1 + K)^{\frac{1}{2}}}$$

For a screen with K = 1, eq. (3.9) gives α = 0.88 whereas eq. (3.1) gives α = 0.77, a difference of about 10%. This implies that the generally accepted form for α (eq. 3.1) may be consistently underestimating slightly for the screens normally used in wind tunnels

($\beta \geq 0.57$).

To determine the dependence on θ, the quantity:-

$$\frac{F_\theta}{\theta} \Bigg/ \left[0.68 - \frac{0.62}{(1 + K_\theta)^{\frac{1}{2}}}\right] \equiv F, \text{ say}$$

was then plotted against θ. The plot indicated a linear variation giving:-

$$F = 1.0 + 1.5\,\theta$$

So for large θ:-

$$\frac{F_\theta}{\theta} = \left[0.68 - \frac{0.62}{(1 + K_\theta)^{\frac{1}{2}}}\right] (1.0 + 1.5\,\theta) \tag{3.10}$$

and combining this with eq. (3.5) gives for α_θ:-

$$\alpha_\theta = \frac{1}{\theta} \,\mathrm{Tan}^{-1} \left[\mathrm{Tan}\,\theta - \frac{\theta}{2} \,\mathrm{Sec}^2\,\theta \left(0.68 - \frac{0.62}{(1 + K_\theta)^{\frac{1}{2}}}\right) (1.5\,\theta + 1.0)\right] \tag{3.11}$$

This semi-empirical prediction formula is compared with the measured values of α_θ in Figs. 3.90 - 3.93 for $\theta = 10^\circ, 40^\circ$ - the measured values of K_θ were used. Considering the graphical techniques used, the accuracy of the agreement (well within 10%) is very encouraging and probably acceptable for most purposes. Obviously more reliable data is needed for screens with $\beta > 0.5$ before the values of the empirical constants can be finalised.

3.4.4 Effects of Dirt Accumulation on Screen Performance

Since flow over isolated cylinders has been studied and well understood over the years, screens are often regarded for analysis purposes, as consisting of rows of cylindrical rods and cylinder theories are then applied to the flow through screens. Although this is never a good approximation because of the strong interaction of flow over individual wires, a purely geometrical effect that is always ignored is the actual deformation of the cylindrical shape itself.

No tunnel is absolutely free of dirt and this tends to accumulate on the screen wires, thus creating an arbitrary cross-sectional shape. Fig. (3.95) shows a screen sample before and after a 4000 Km (125 hrs. at 9 m/s) run. This sample was attached to a blower tunnel exit and so the amount of dirt accumulated is underestimated compared to that say, on the first screen in the settling chamber. Quite clearly these dirt particles must affect not only the pressure drop but also the refractive properties of the screen. The first effect is often noticeable in practice when the maximum speed of a tunnel is found to decrease due to increased loads. The second effect was conclusively demonstrated by measuring the spanwise c_f distribution in a tunnel working section before and after cleaning the last screen in the settling chamber (Fig. 3.96). The peak-to-peak variation about the mean was reduced from about 16% to 6%. The variation is caused by the presence of longitudinal vortices formed by coalescing jets from the screen pores.

3.5 Concluding Remarks

Basic differences have been shown to exist between the effects of plastic and metal screens. This is mainly due to the different weaving properties and elastic moduli of the fibres.

Overshoot in mean velocity is attributed to the effects of streamline and screen inclination and is greater for plastic screens due to the latter effect. An important parameter in determining the extent of the combined effect is the ratio of boundary layer thickness to tunnel height. Beyond the boundary layer, metal screens produced more non-uniformities than the plastic ones and this is correlated with the uniformity of weave. Recovery of the mean flow is complete by about x = 600 mm, although the overshoot with plastic screens is persistent. This does not create a problem for settling chamber applications in boundary layer tunnels since the contraction tends to reduce non-uniformities and also very often re-laminarizes the boundary layer which must then be systematically tripped.

The effect of all the screens on the turbulence structure is similar :the existing turbulence is almost completely obliterated and a "new" boundary layer is formed, with increased activity in the inner part of the outer layer. A distinction is drawn between the turbulence shed from the screen due to the reduction in scale of the pre-existing turbulence (correlated with the mesh size) and that due to the turbulent wire wakes (correlated with the wire diameter). The recovery of the turbulence structure is also complete by about x = 560 mm.

The correlation of β with K is different for plastic and metal screens. Although Wieghardt's formula tends to overestimate for the metal screens, and more so as β increases, it still gives a better estimate of K than the other available formulae over the velocity range investigated here ($0 < U < 20$ m/s). Ironically, these formulae which are mainly based on data from metal screens, seem to work better for plastic screens, but note that for plastic screens, K is not <u>only</u> a function of β and Re. A need for more data and better formulations is evident.

The overall distance, upstream and downstream of the plastic fine screen within which the static pressure is affected is of the order of 60 mm (about 4 δ_0). This "region of influence" must provide the lower limit on the spacing of multiple screens if flow distortion is to be avoided.

The most important results to emerge from this investigation were those for K_θ and α_θ. There has been too much reliance on one or two sets of data whose accuracy is questionable. Analytic solutions which use simplified arguments for what is a rather complex flowfield do not help in bridging the gap. The results presented here clearly show that an important parameter in determining the trends is the screen open-area ratio. For screens normally used in wind tunnels, $\beta \sim 0.6$, and so the relations derived here are more applicable. More reliable data is essential because of the important implications of the new formulation for the limiting value of α.

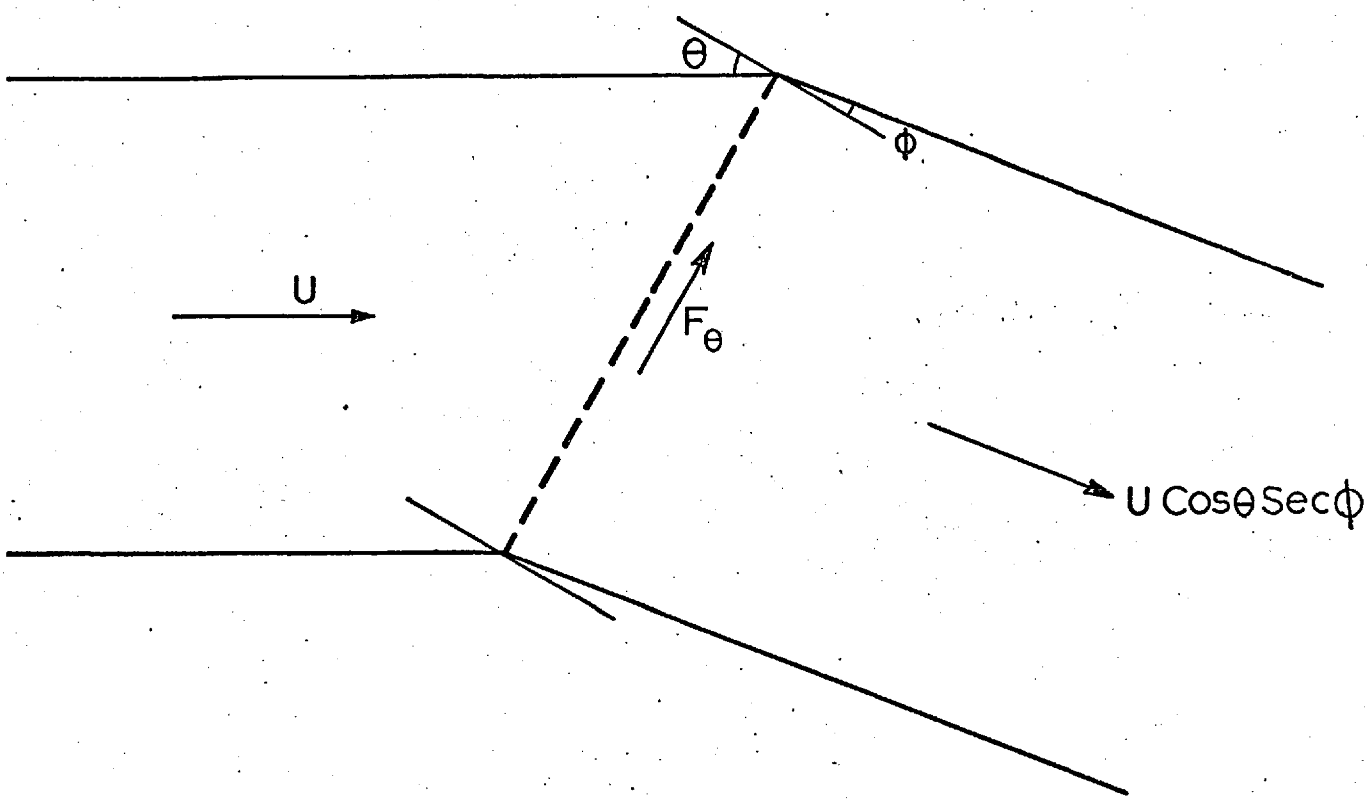

Fig. 3.1 Flow through an inclined plane screen.

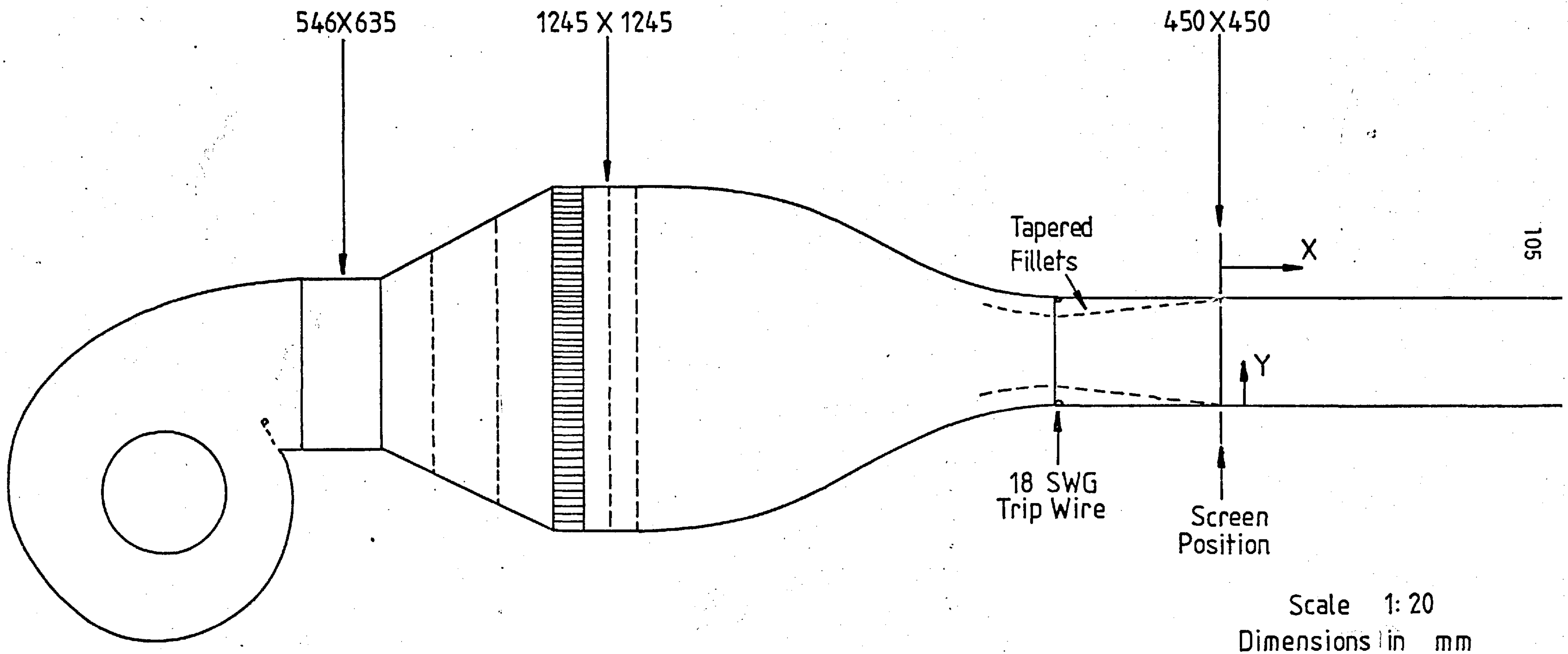

Fig. 3.2 450 x 450 mm test rig.

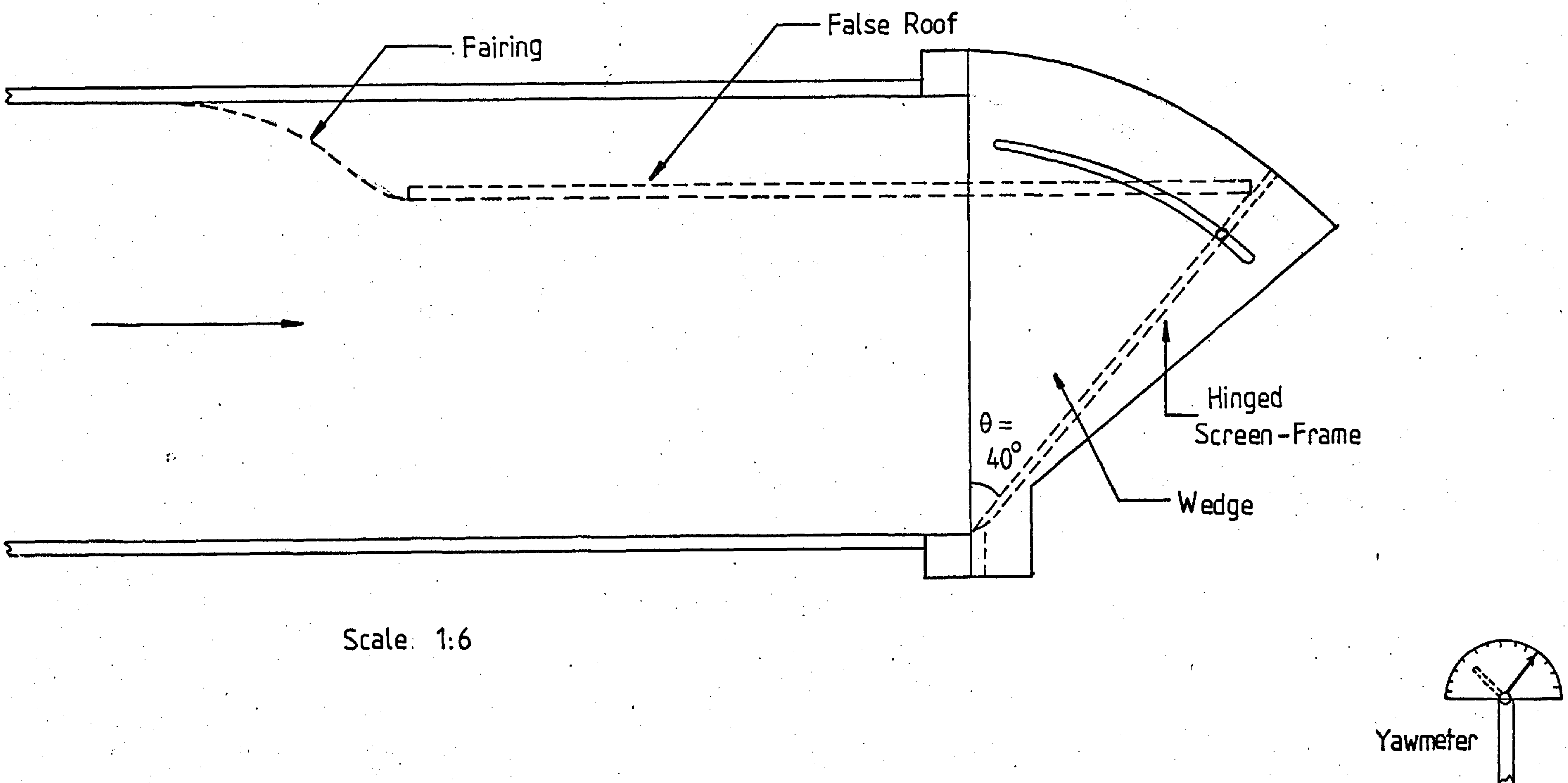

Scale 1:6

Fig. 3.3 Inclined screen rig.

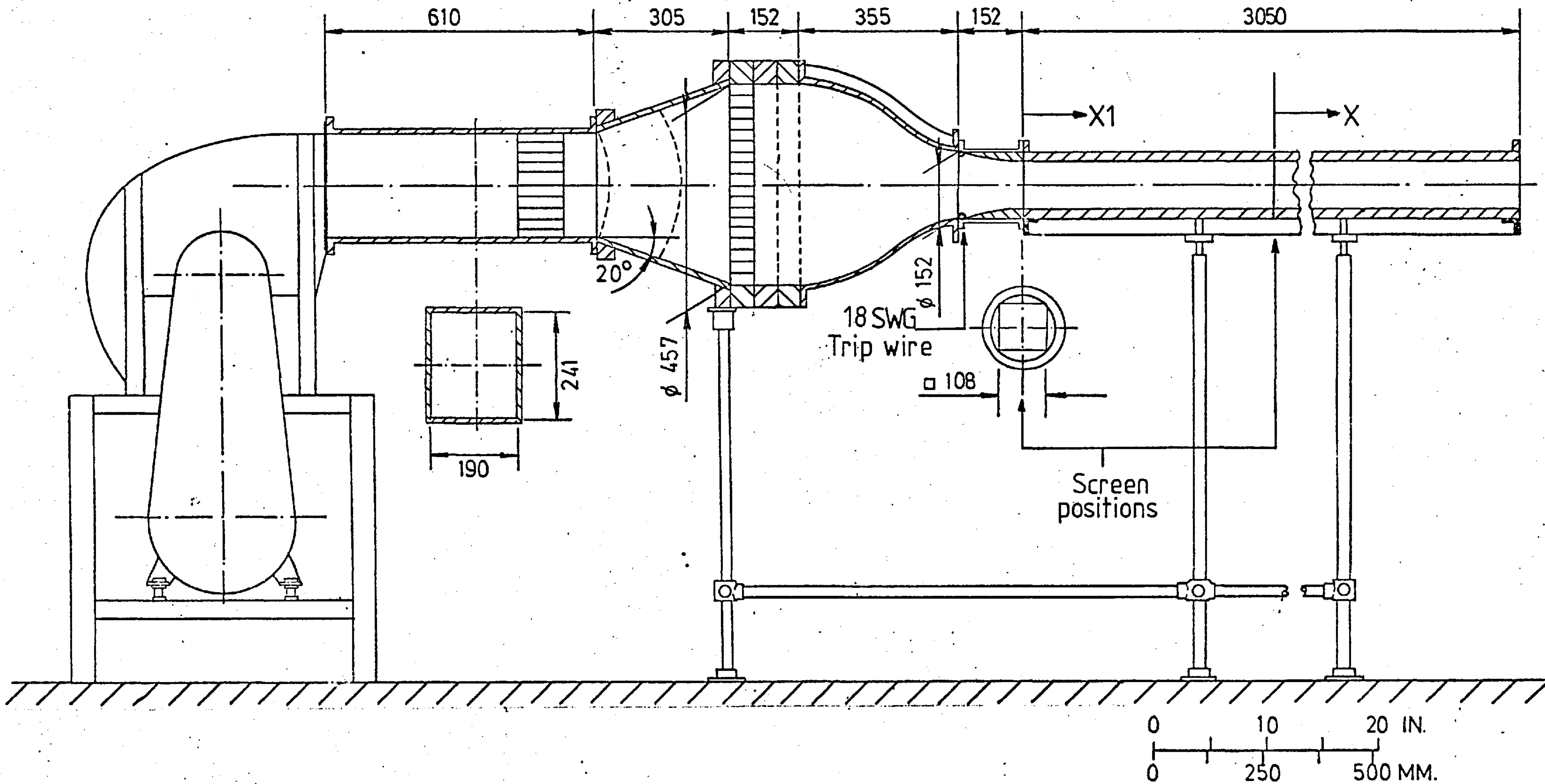

Fig. 3.4 108 x 108 test rig.

Scale 25·4 mm. :2 mm.

Dimensions in mm

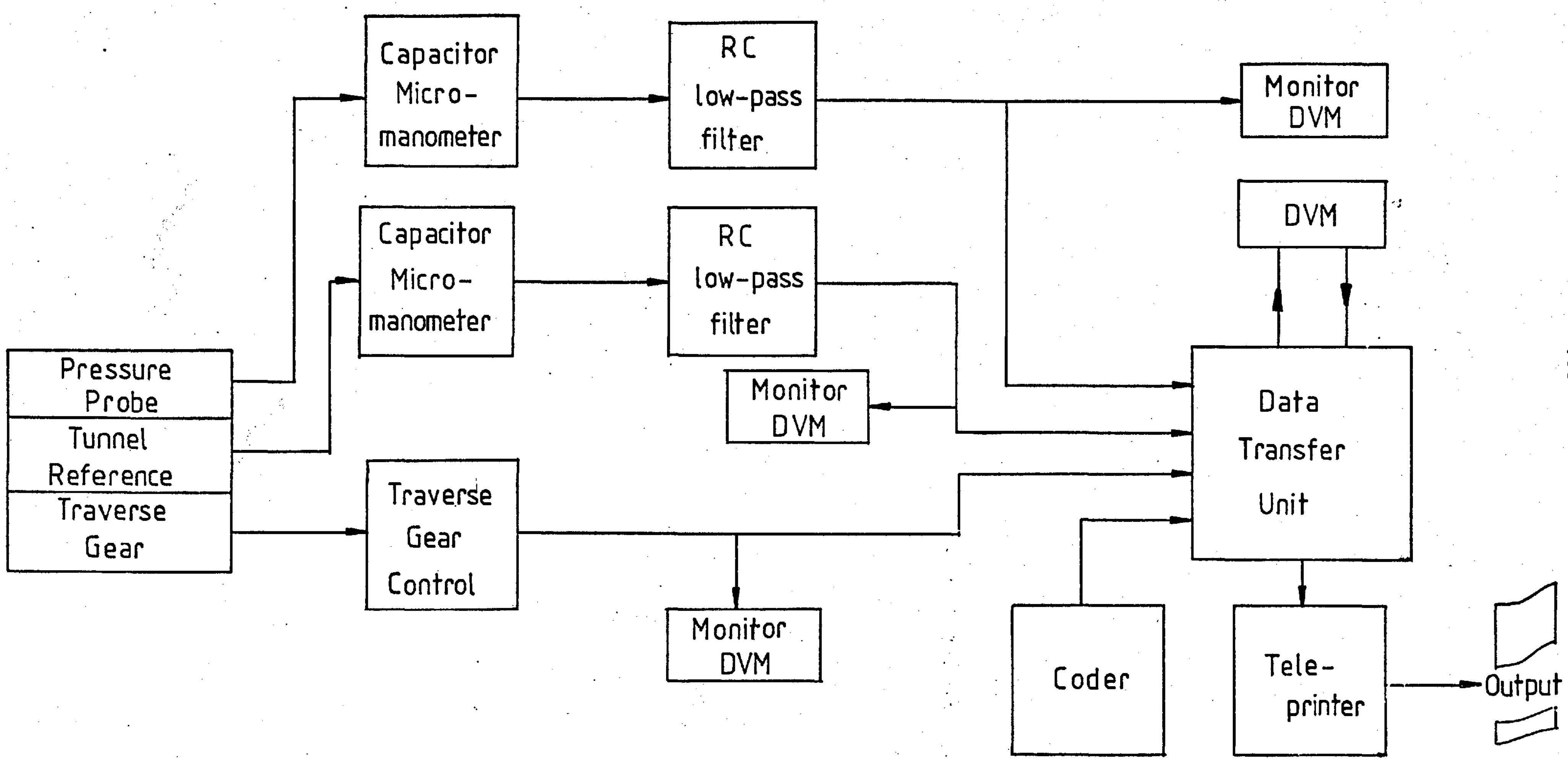

Fig. 3.5 Data logging system for mean velocity profile measurements.

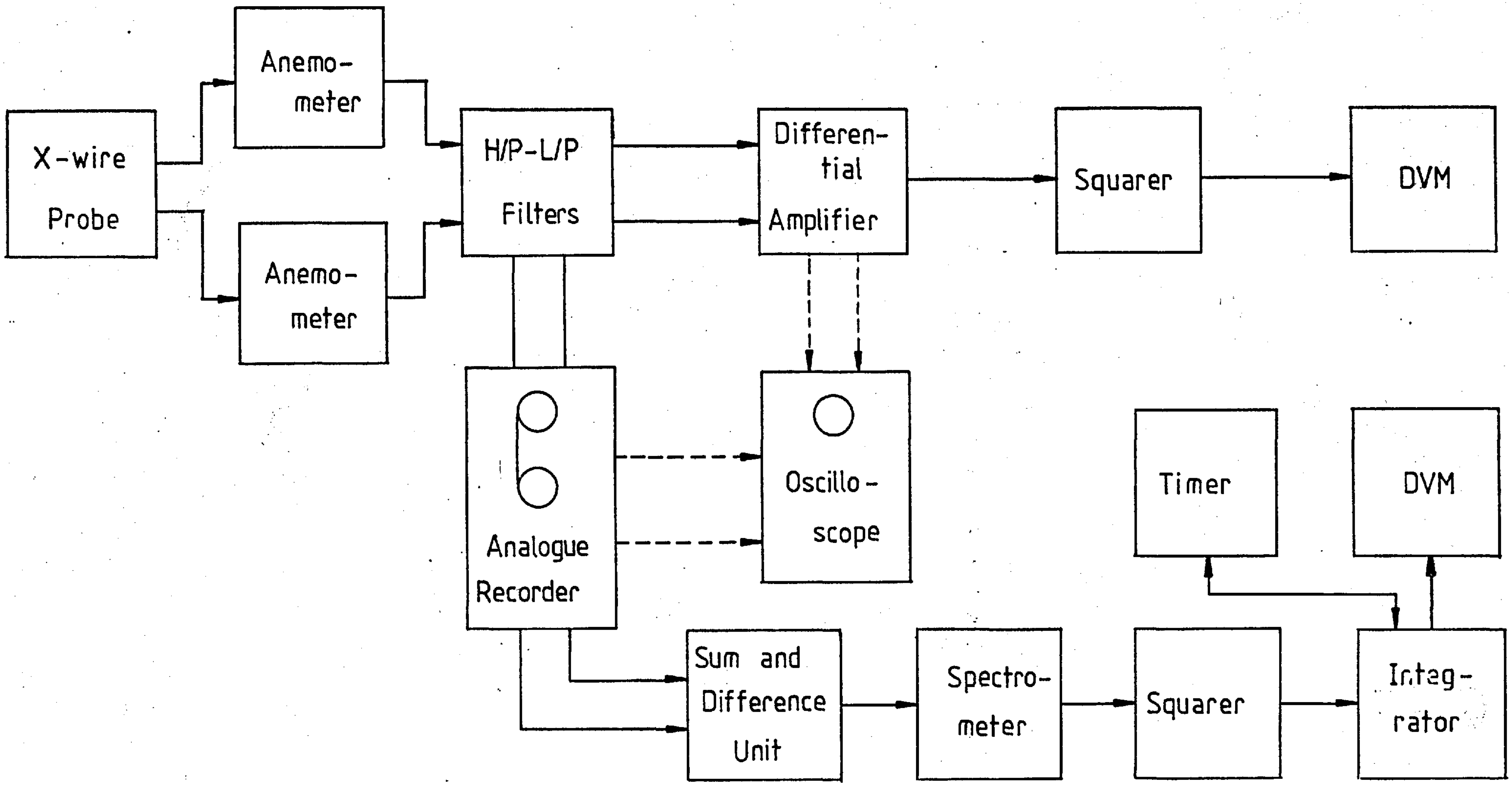

Fig. 3.6 Apparatus for turbulence measurements.

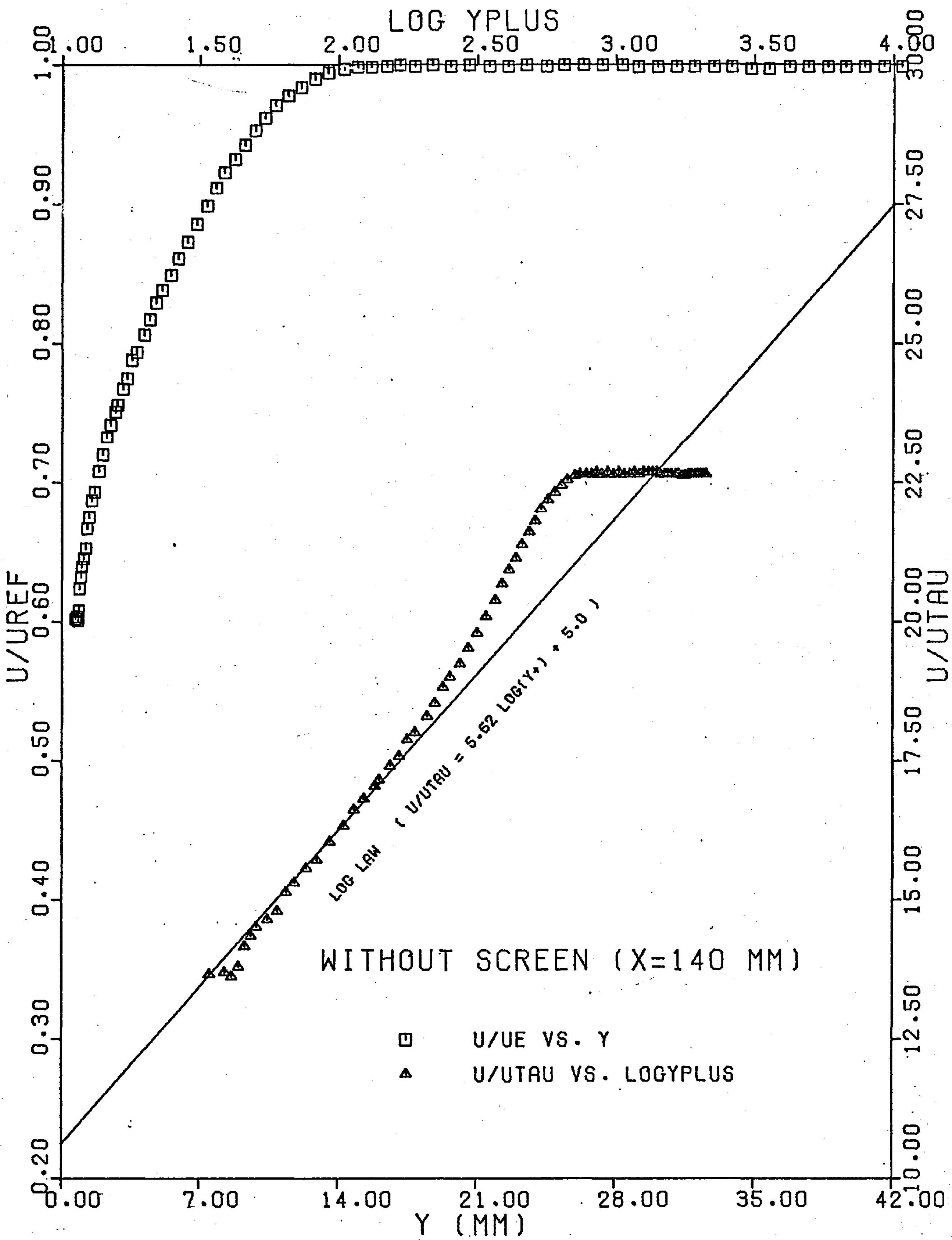

Fig. 3.7 Mean velocity and semi-log. profiles for the undisturbed boundary layer at x = 140 mm.

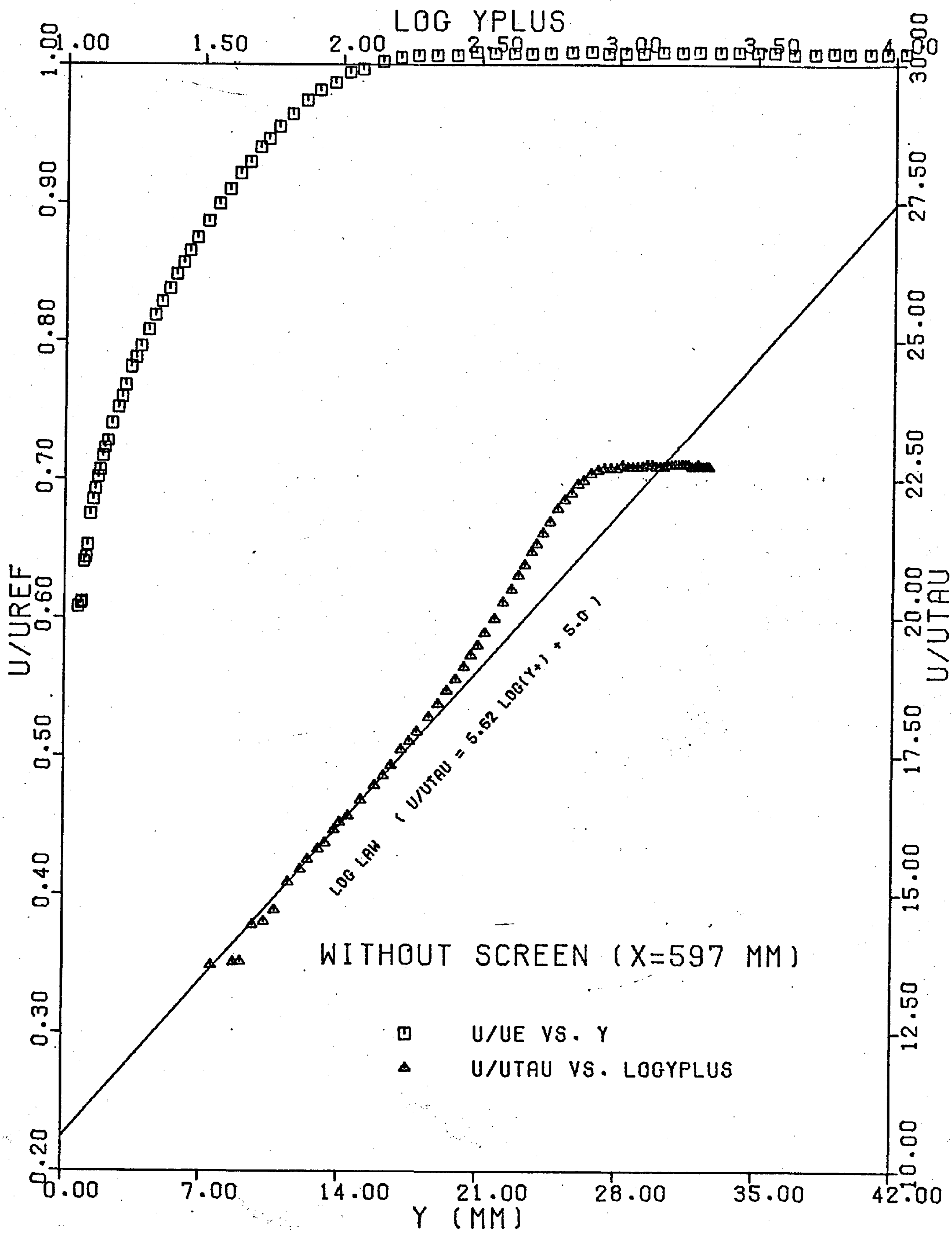

Fig. 3.8 Mean velocity and semi-log. profiles for the undisturbed boundary layer at x = 597 mm.

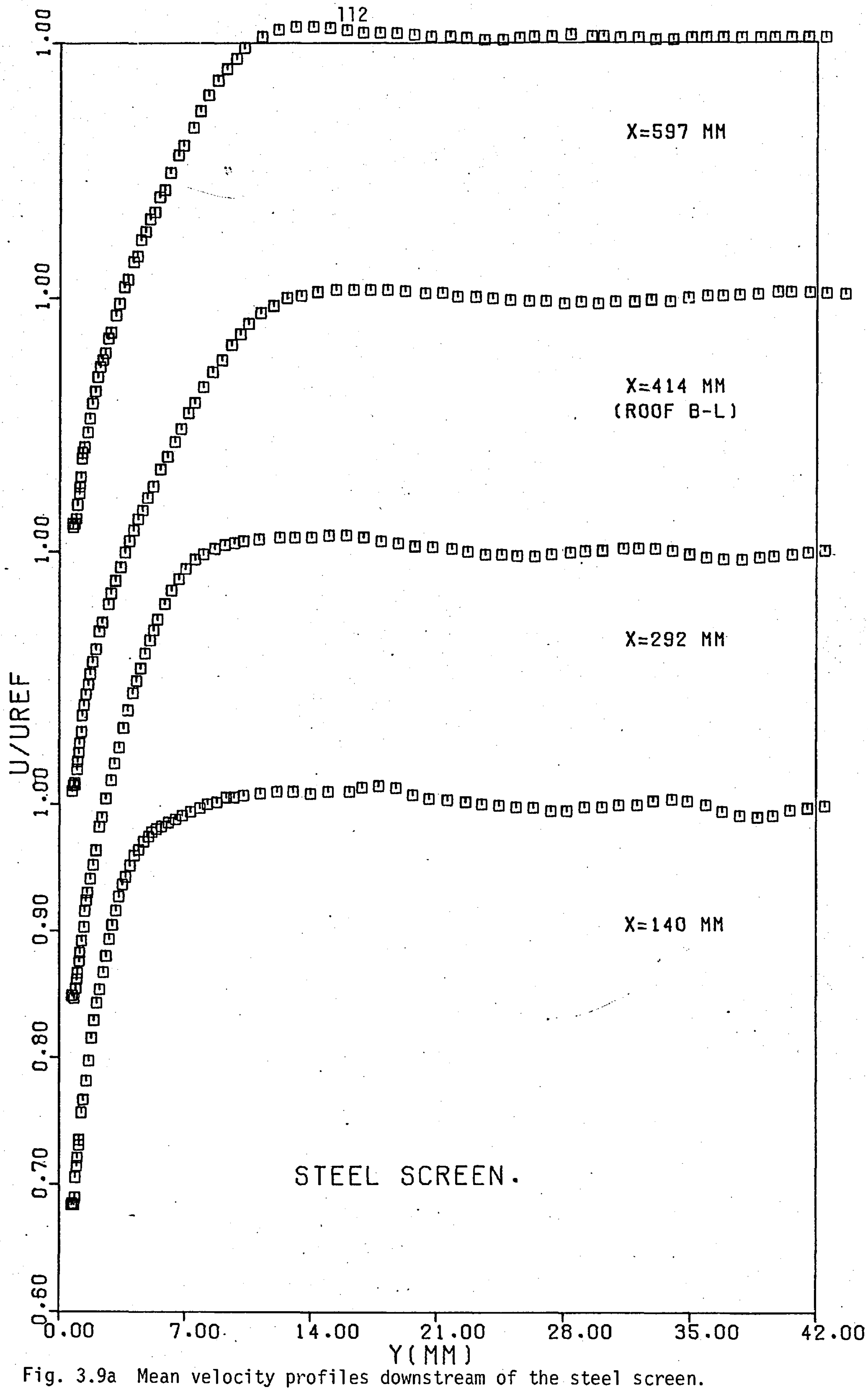

Fig. 3.9a Mean velocity profiles downstream of the steel screen.

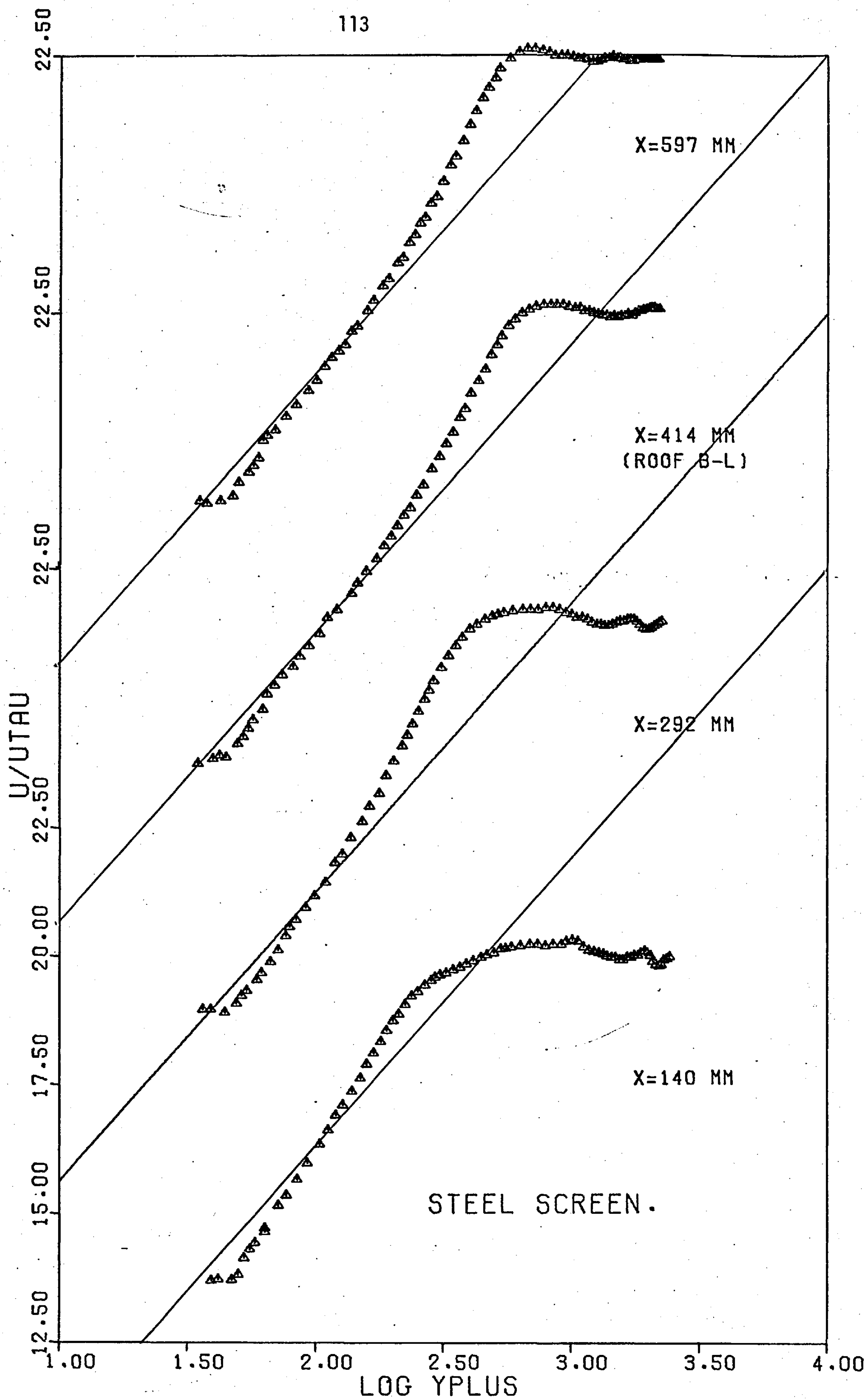

Fig. 3.9b Semi-log. profiles downstream of the steel screen.

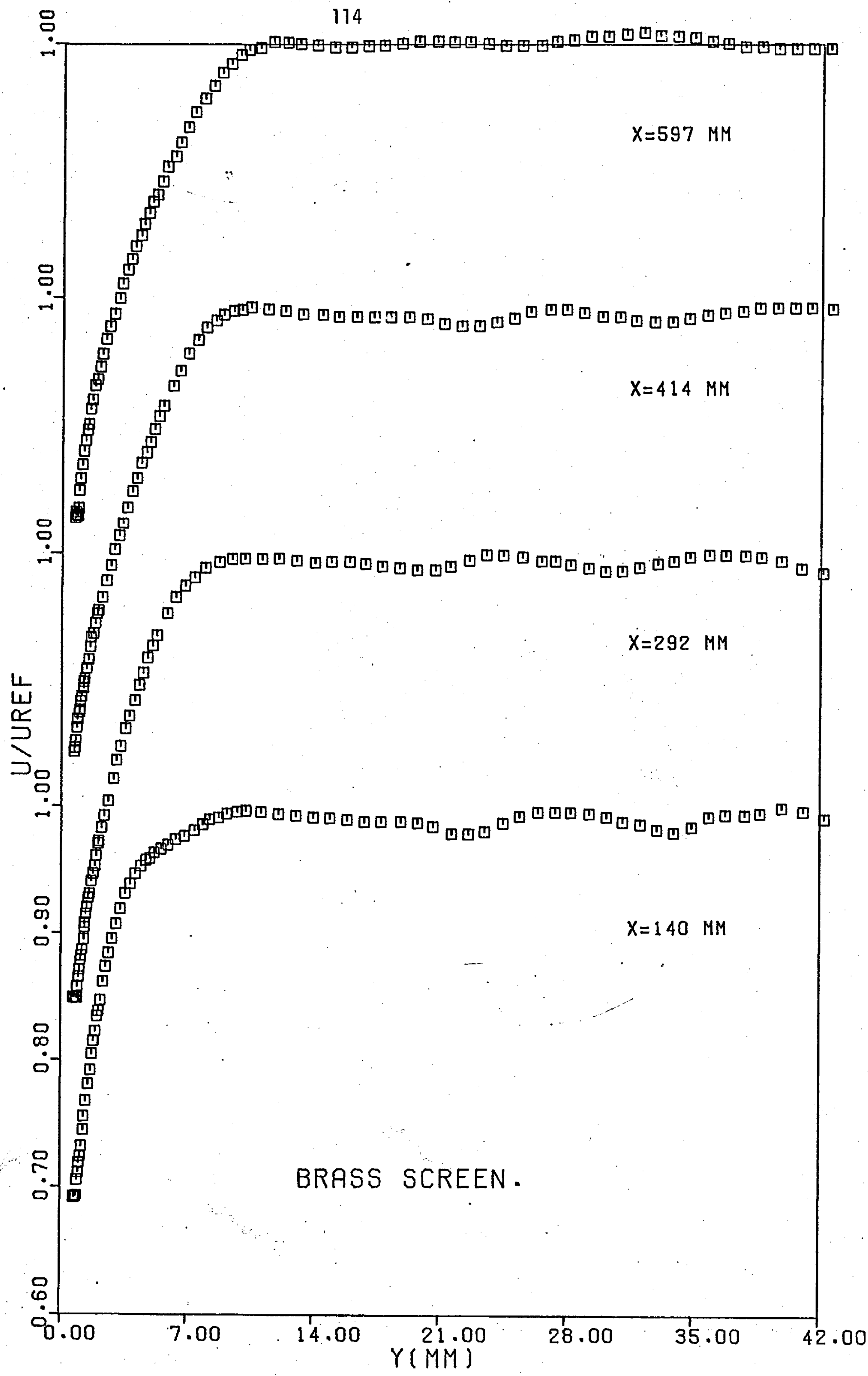

Fig. 3.10a Mean velocity profiles downstream of the brass screen.

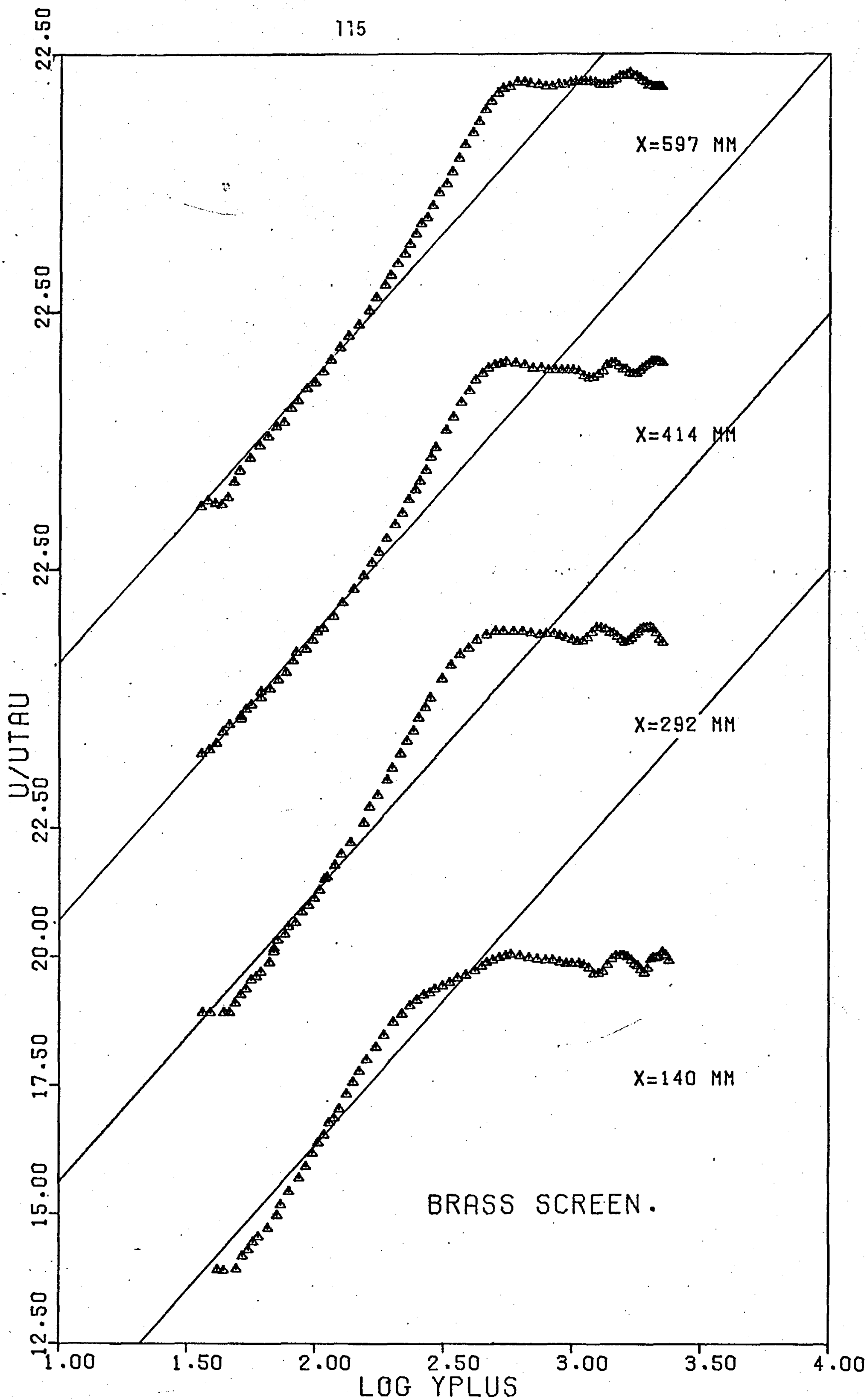

Fig. 3.10b Semi-log. profiles downstream of the brass screen

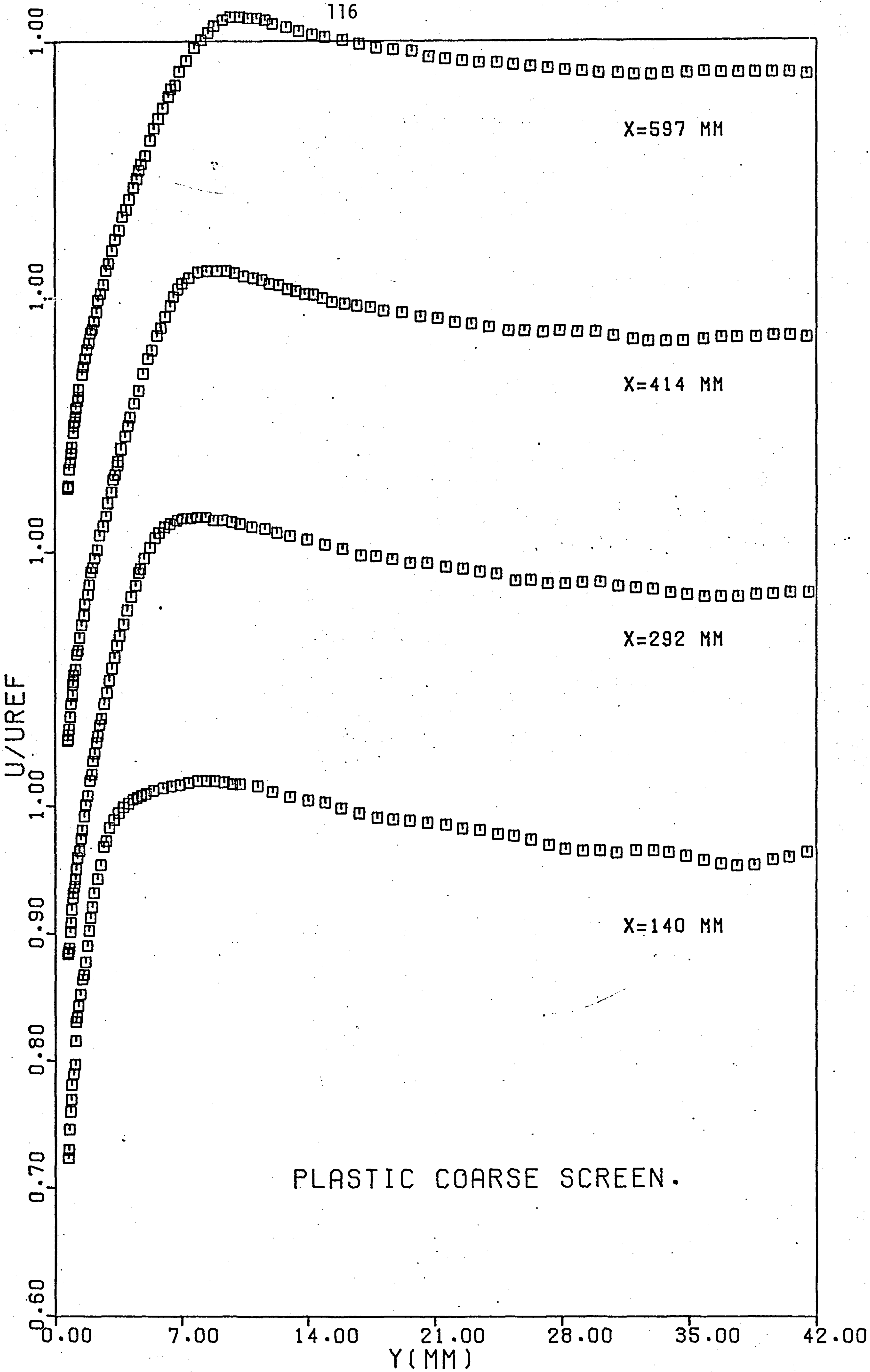

Fig. 3.11a Mean velocity profiles downstream of the plastic coarse screen.

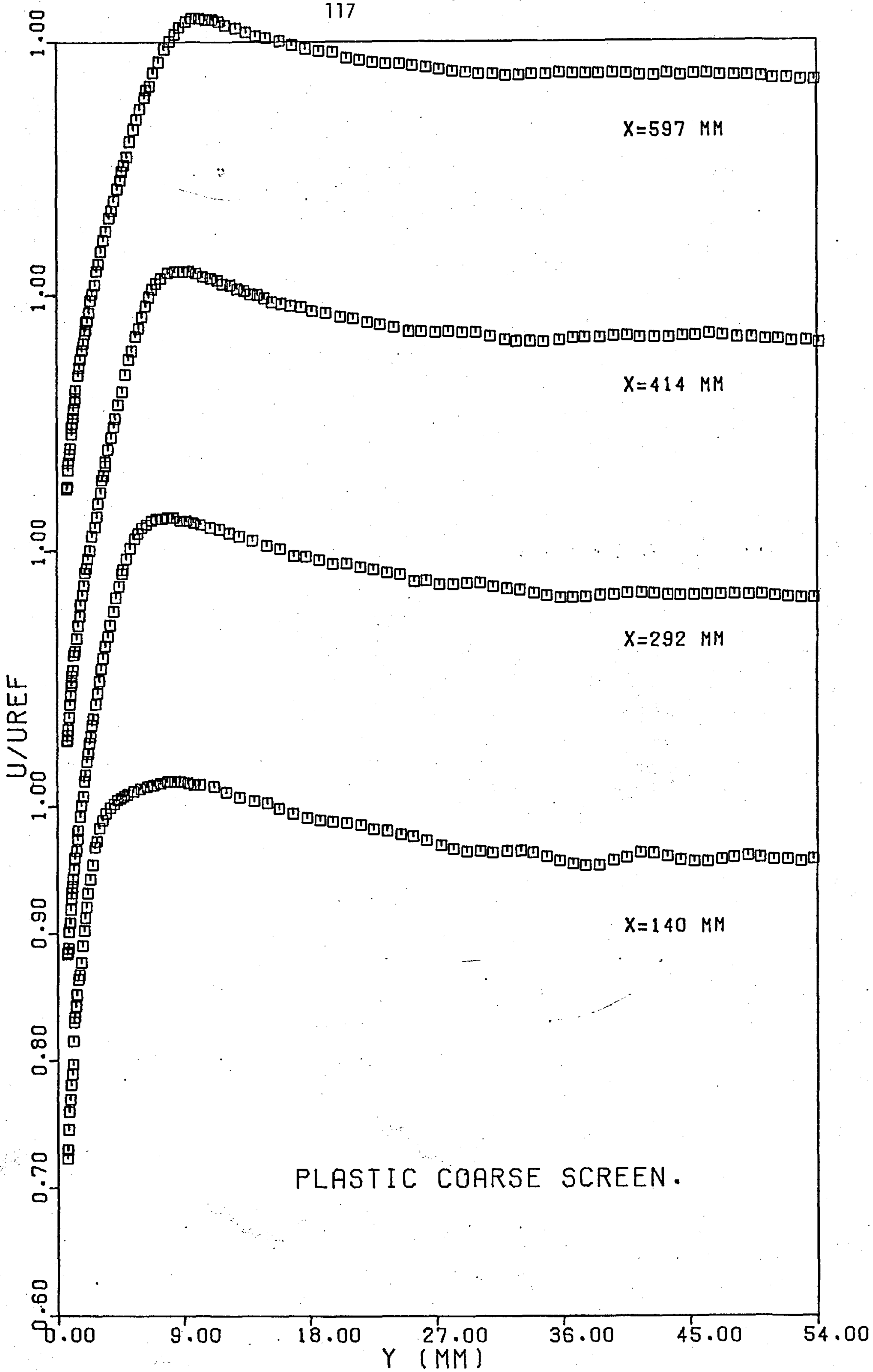

Fig. 3.11b Mean velocity profiles extending upto y = 54 mm behind plastic coarse screen.

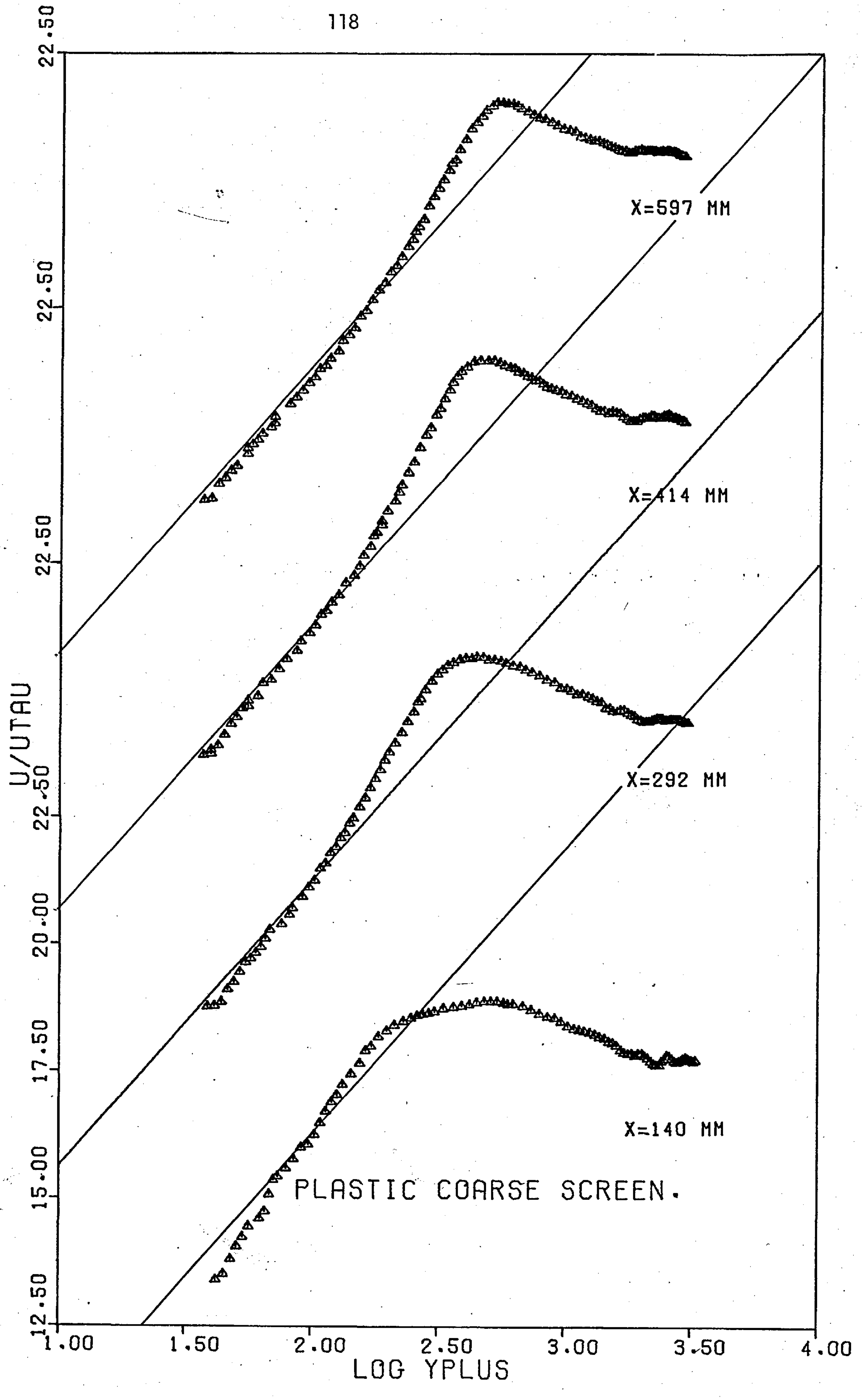

Fig. 3.11c Semi-log. profiles downstream of the plastic coarse screen.

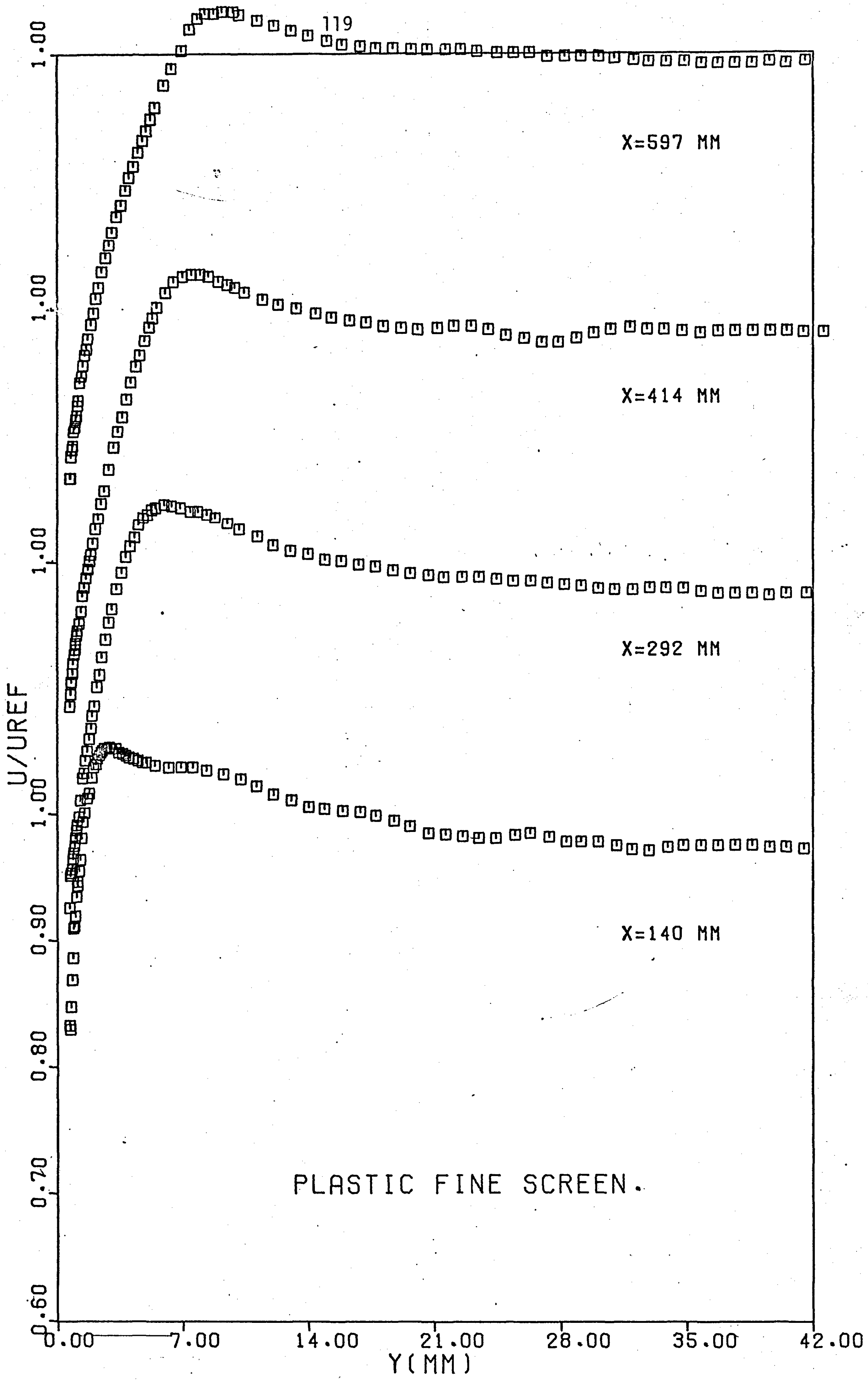

Fig. 3.12a Mean velocity profiles downstream of the plastic fine screen.

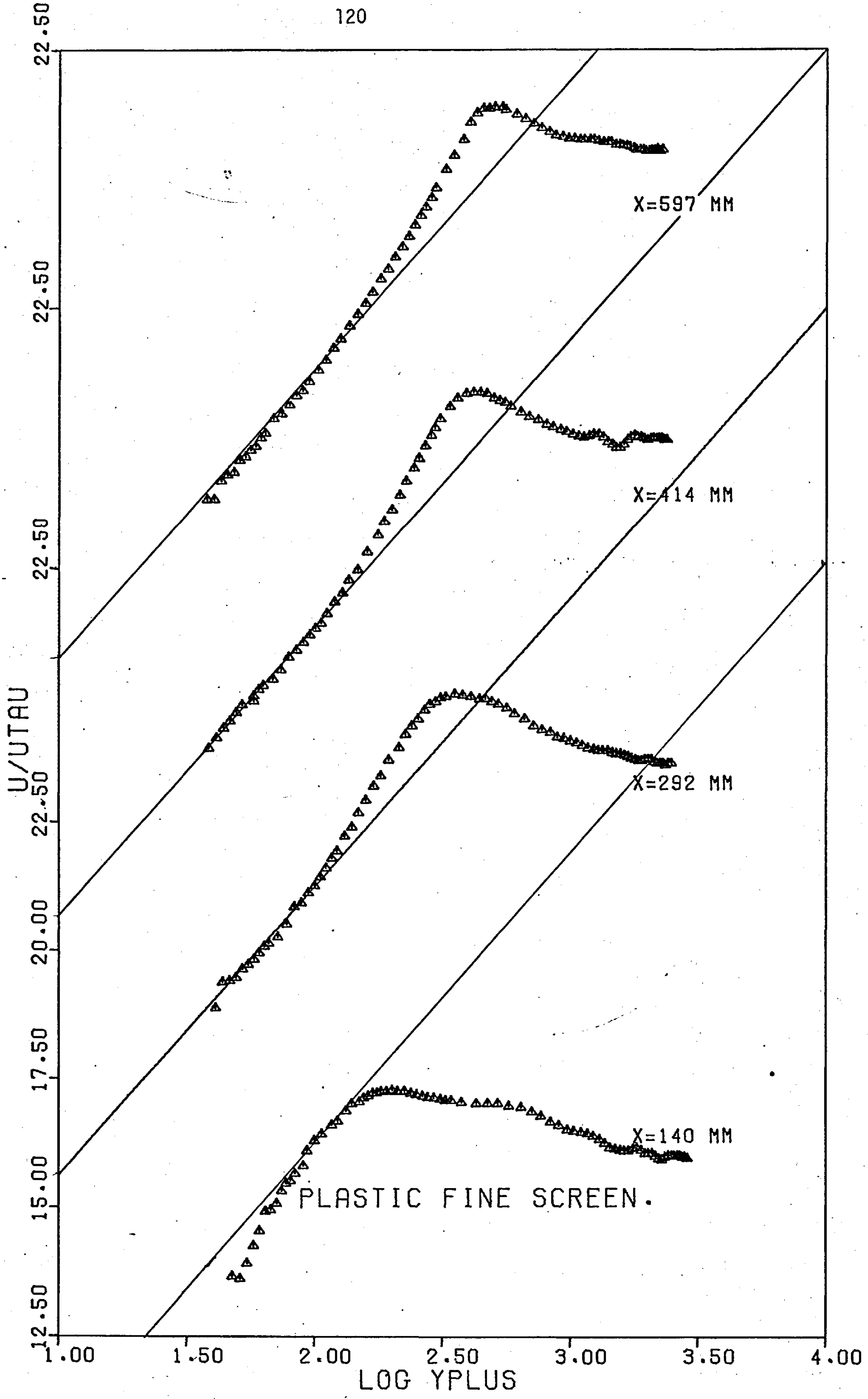

Fig. 3.12b Semi-log. profiles downstream of the plastic fine screen.

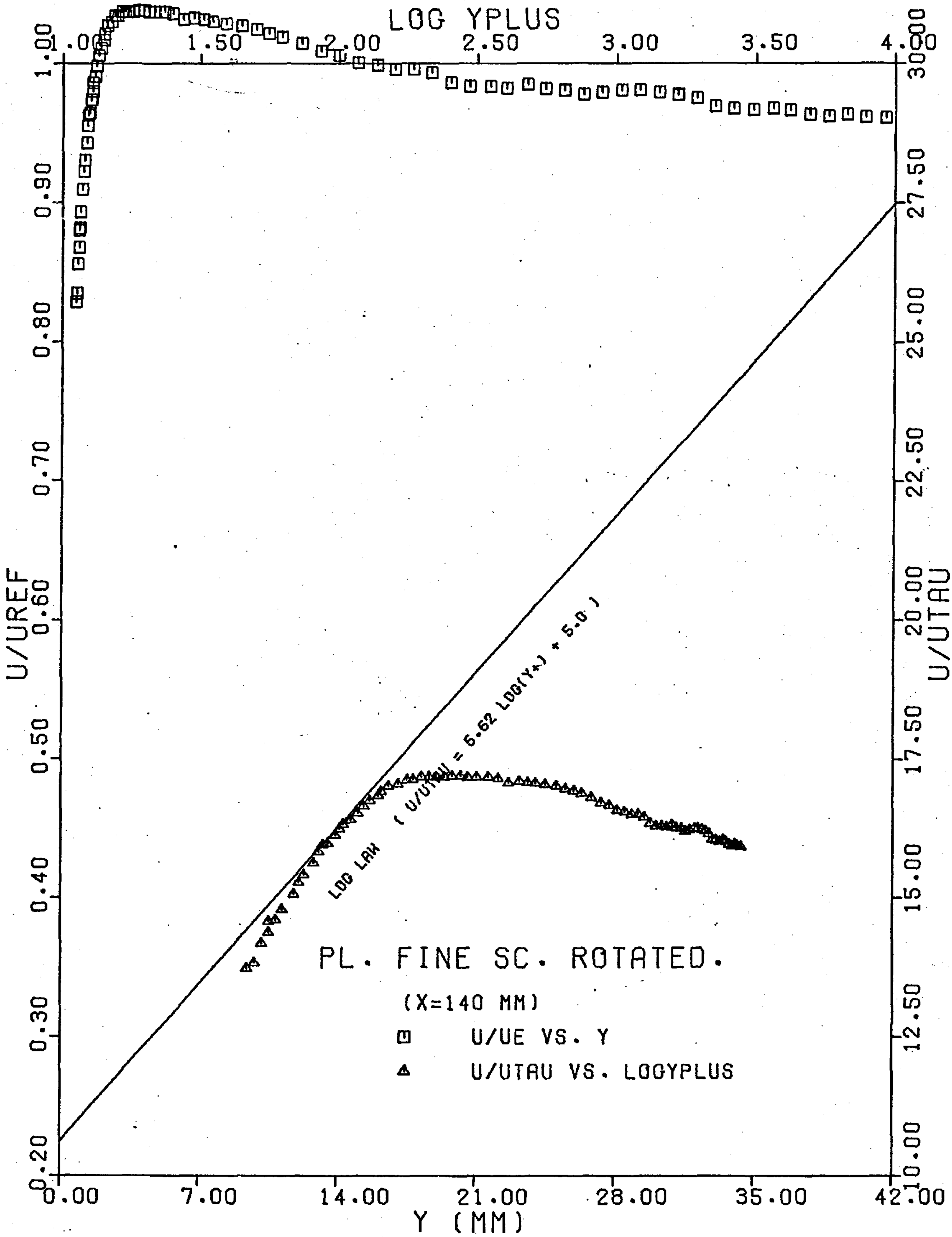

Fig. 3.12c Mean velocity and semi-log. profiles with the plastic fine screen rotated through 90^0.

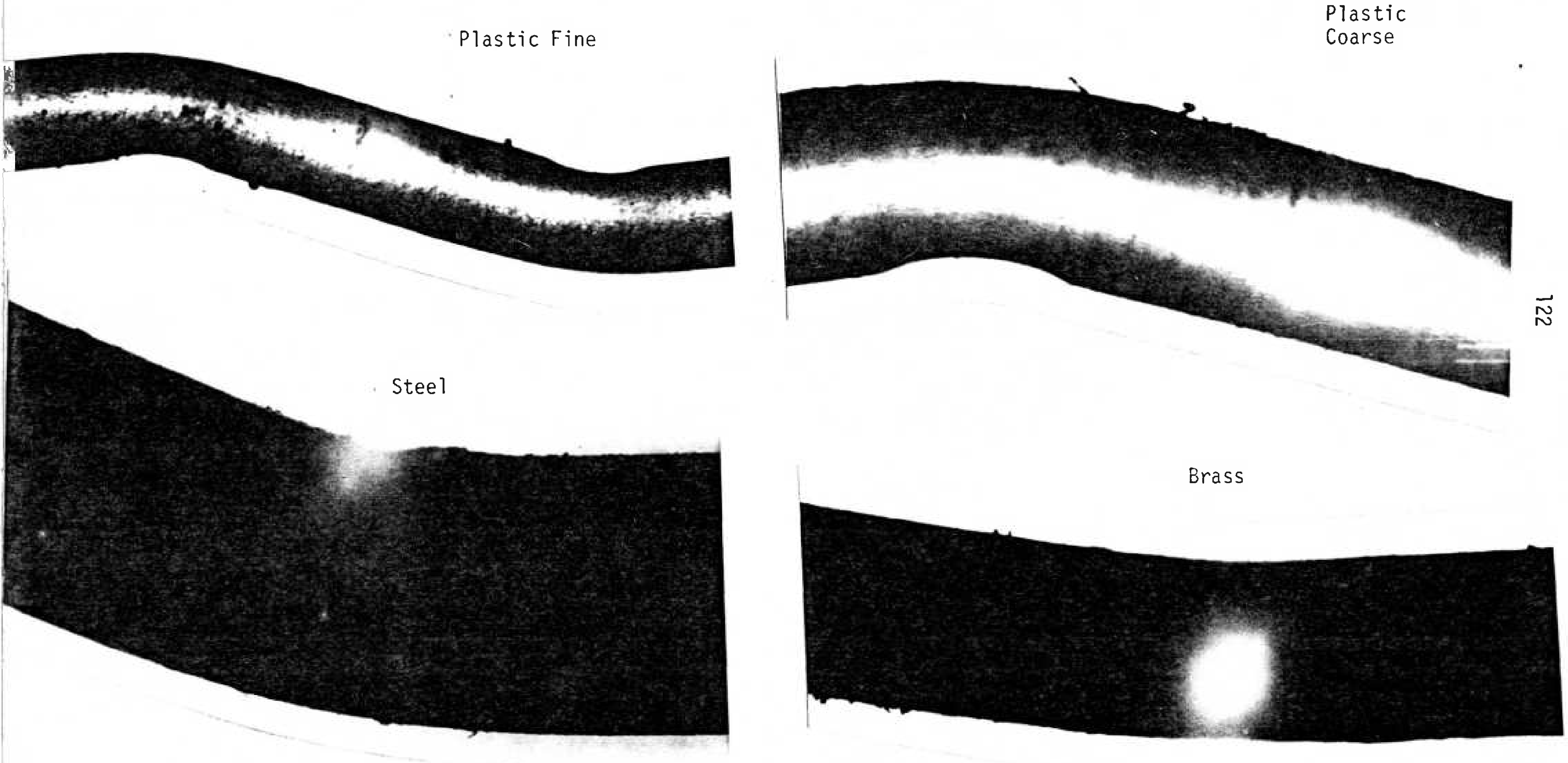

Fig. 3.13 Photograph of the screen wires showing the necked plastic strands.

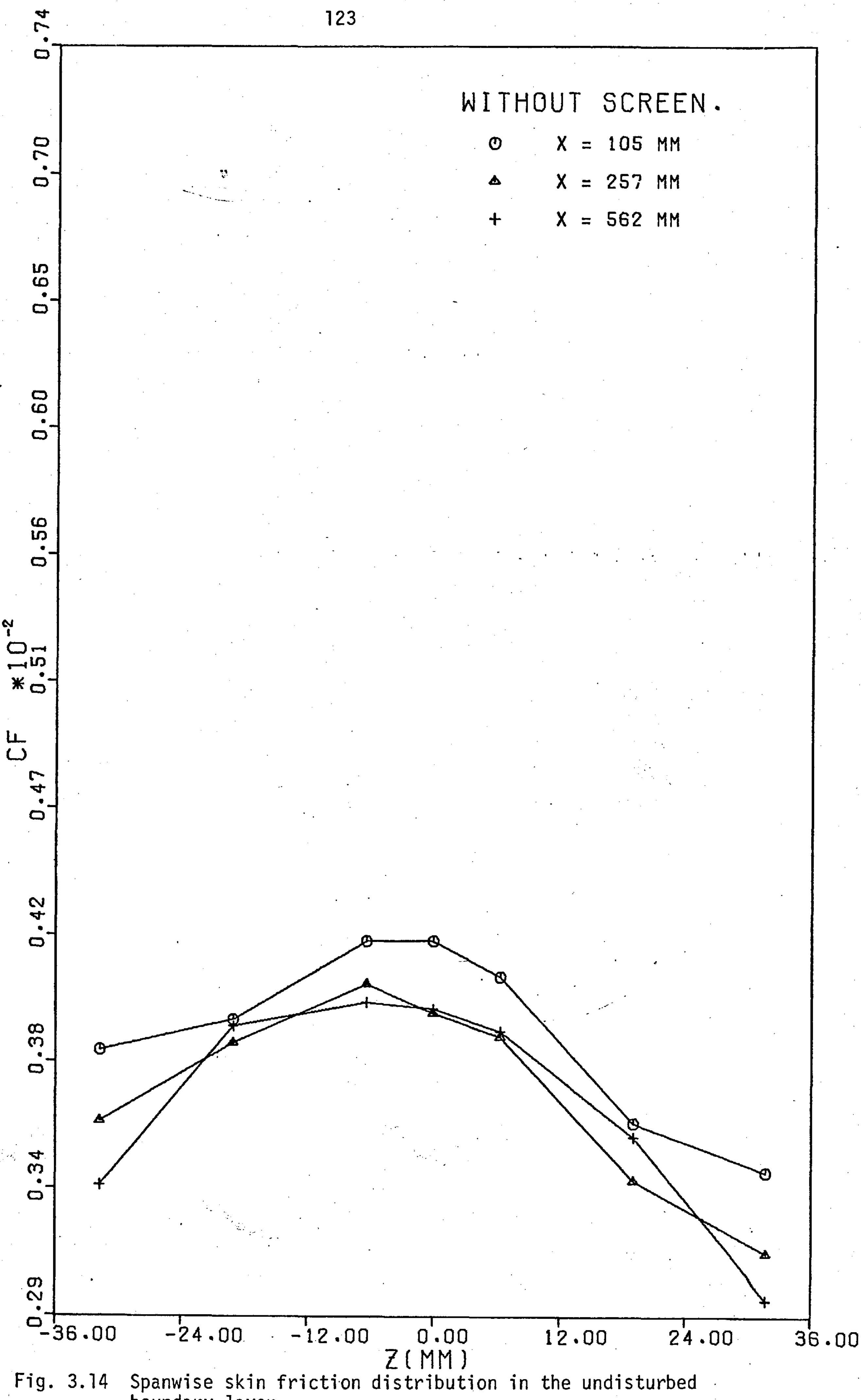

Fig. 3.14 Spanwise skin friction distribution in the undisturbed boundary layer.

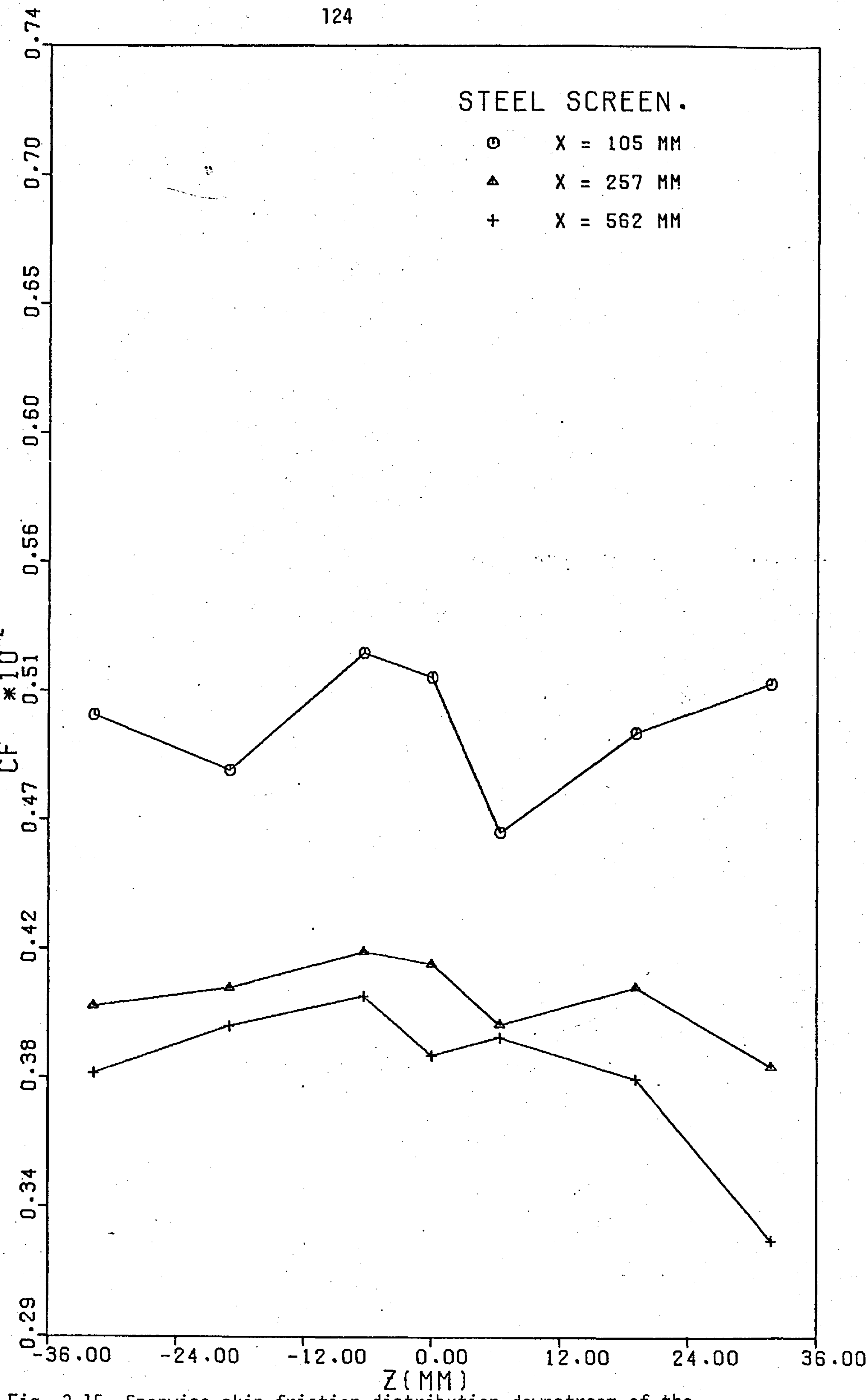

Fig. 3.15 Spanwise skin friction distribution downstream of the steel screen.

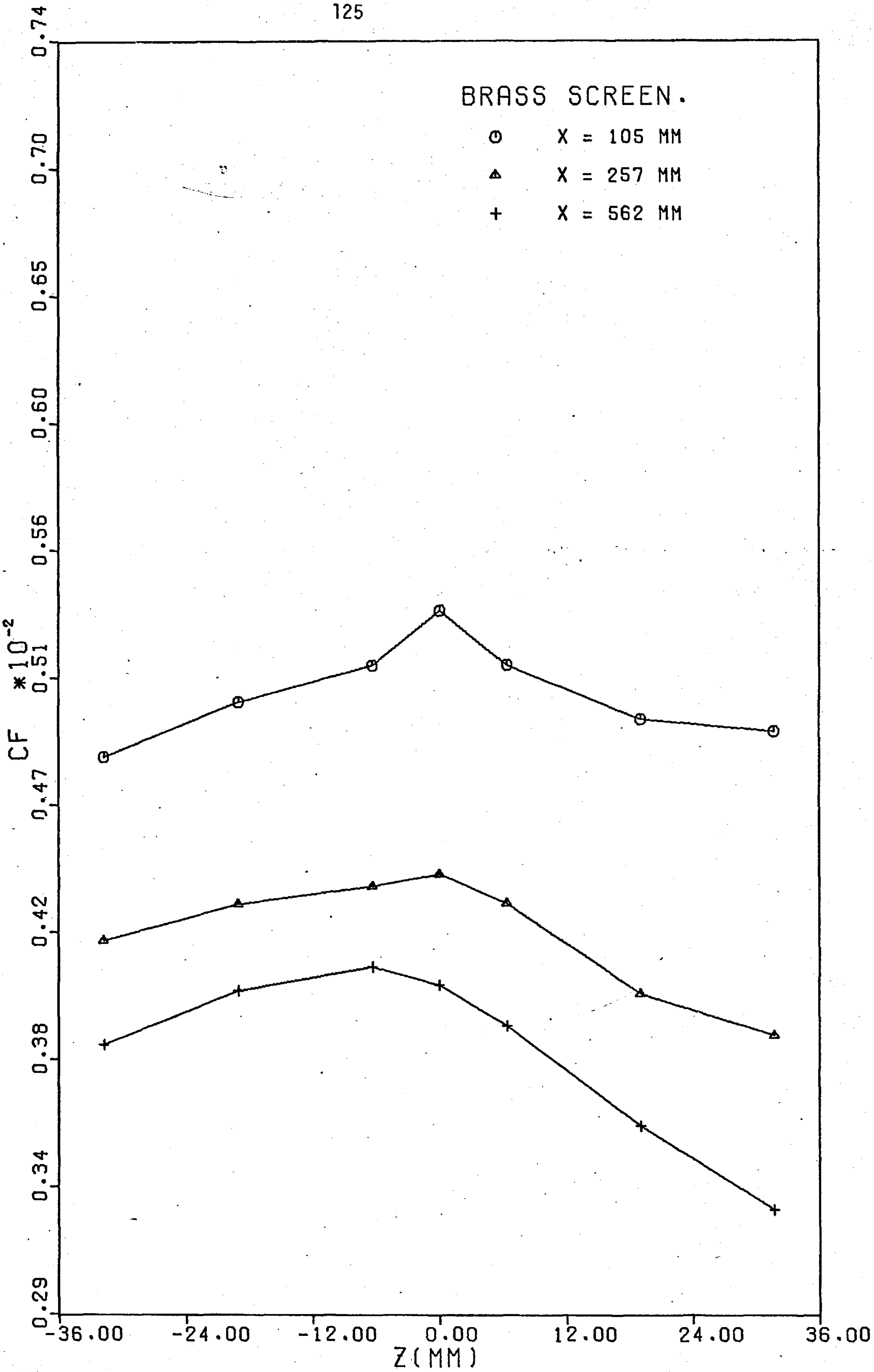

Fig. 3.16 Spanwise skin friction distribution downstream of the brass screen.

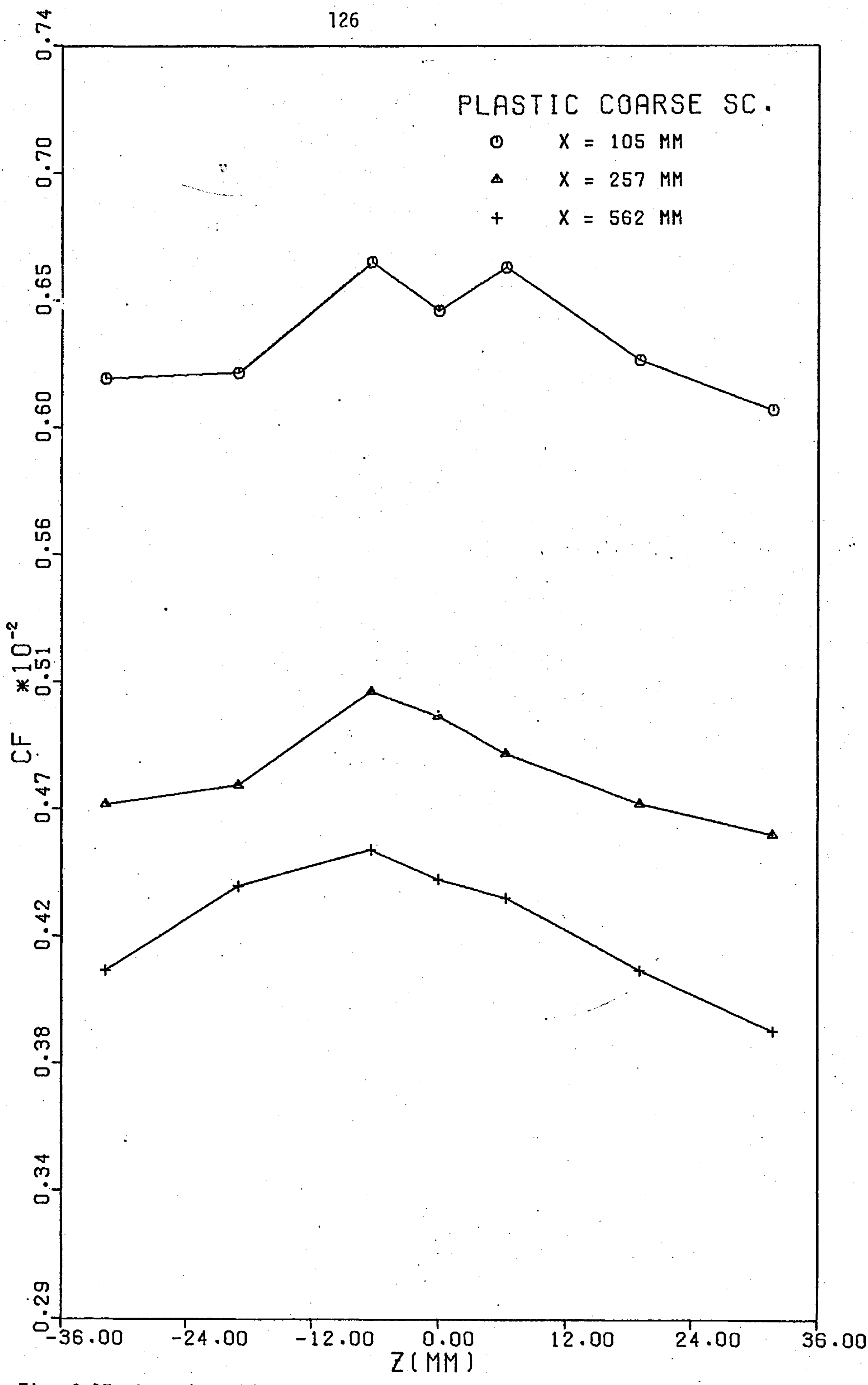

Fig. 3.17 Spanwise skin friction distribution downstream of the plastic coarse screen.

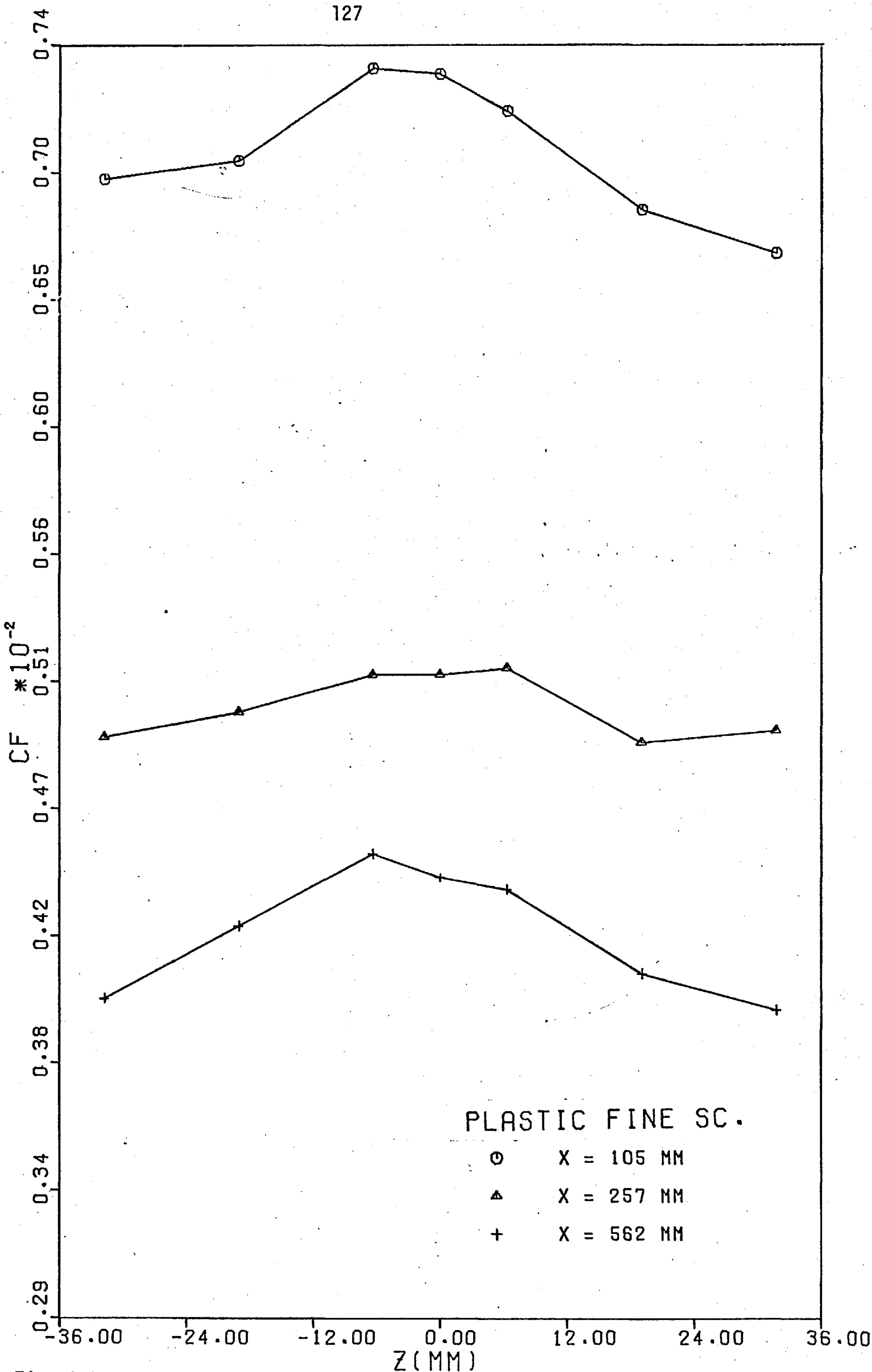

Fig. 3.18 Spanwise skin friction distribution downstream of the plastic fine screen.

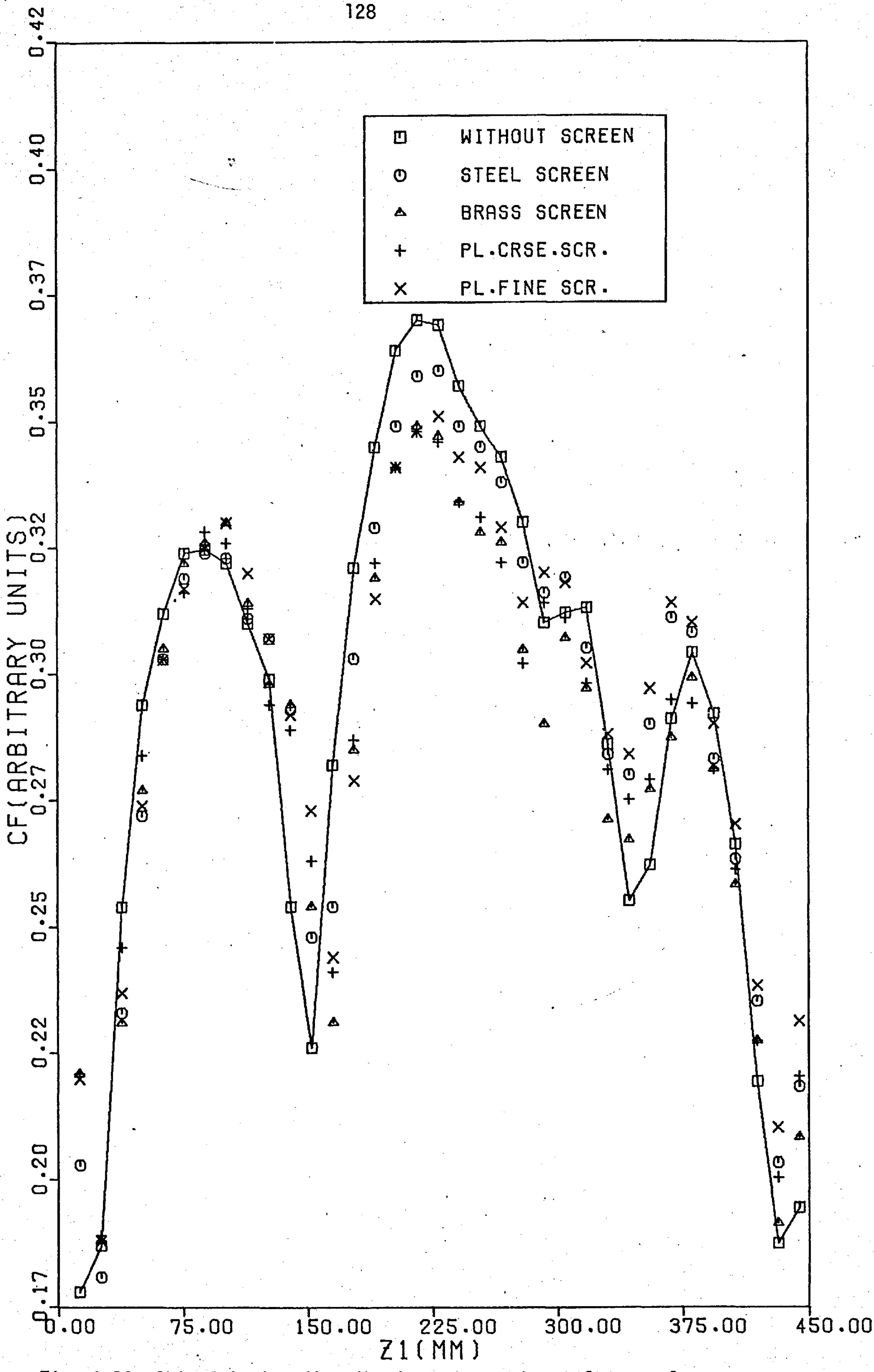

Fig. 3.19 Skin friction distribution across the whole tunnel span at x = 2.4 m.

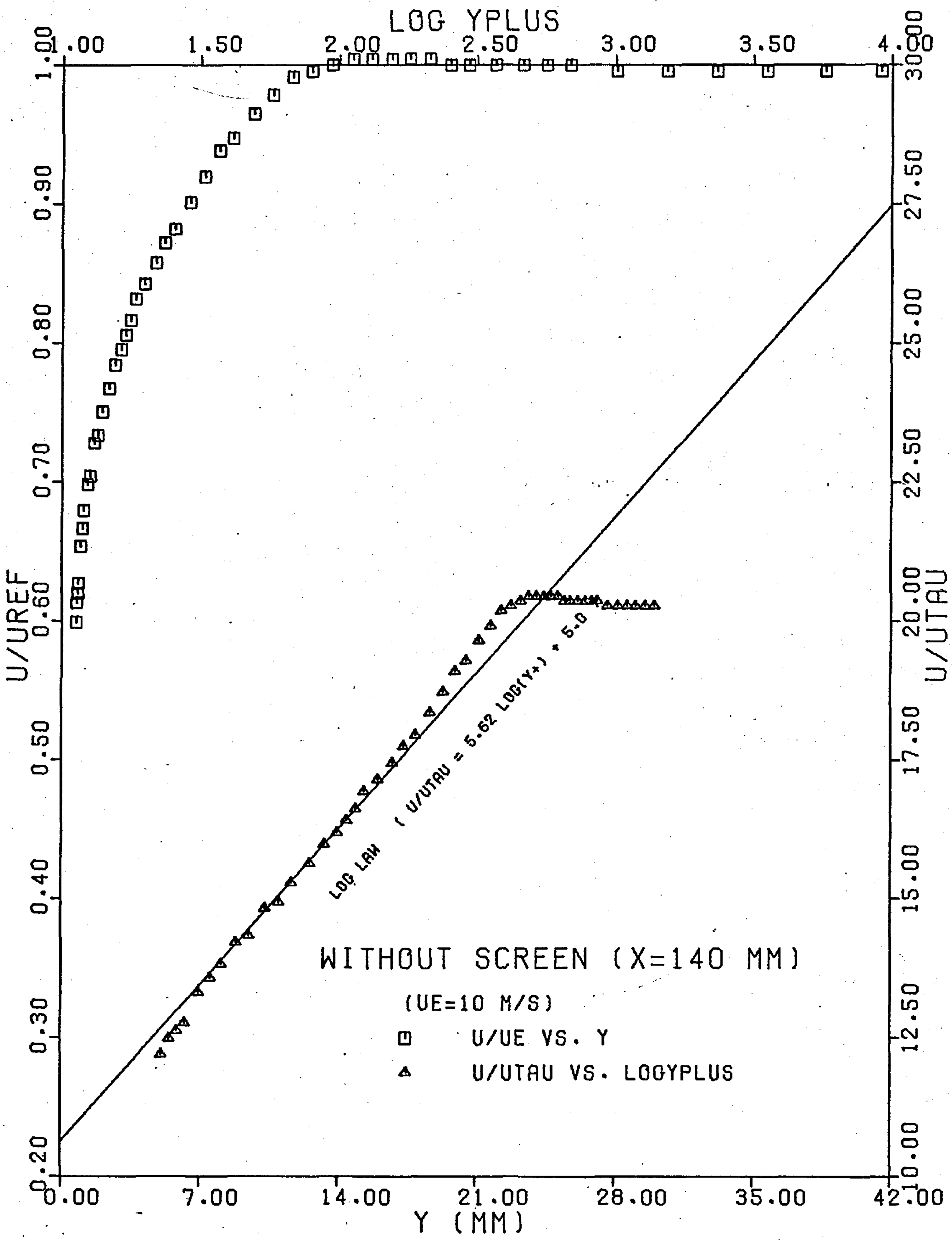

Fig. 3.20 Mean velocity and semi-log. profiles for the undisturbed boundary at x = 140 mm (U_e = 10 m/s).

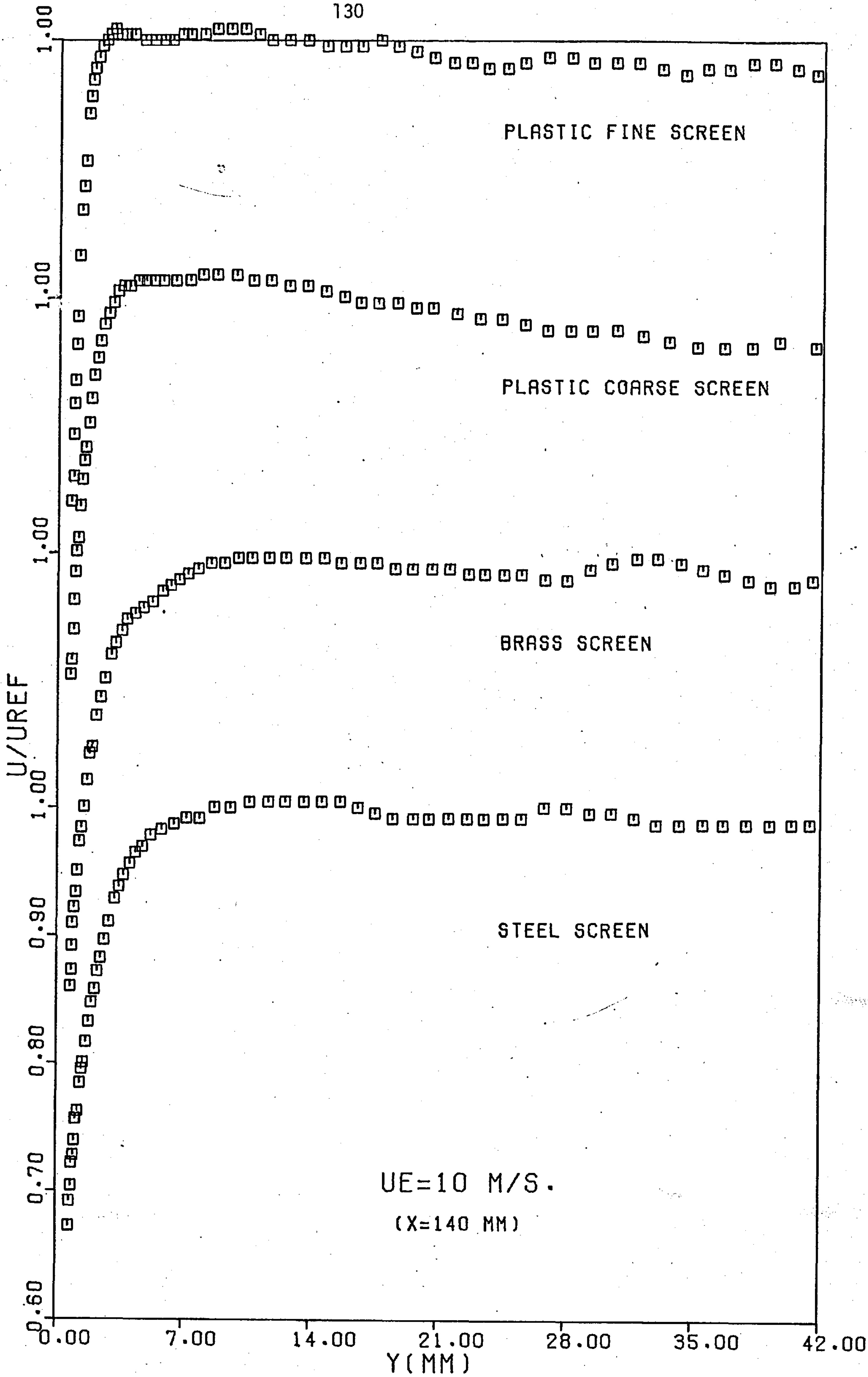

Fig. 3.21a Mean velocity profiles at a reduced free stream velocity.

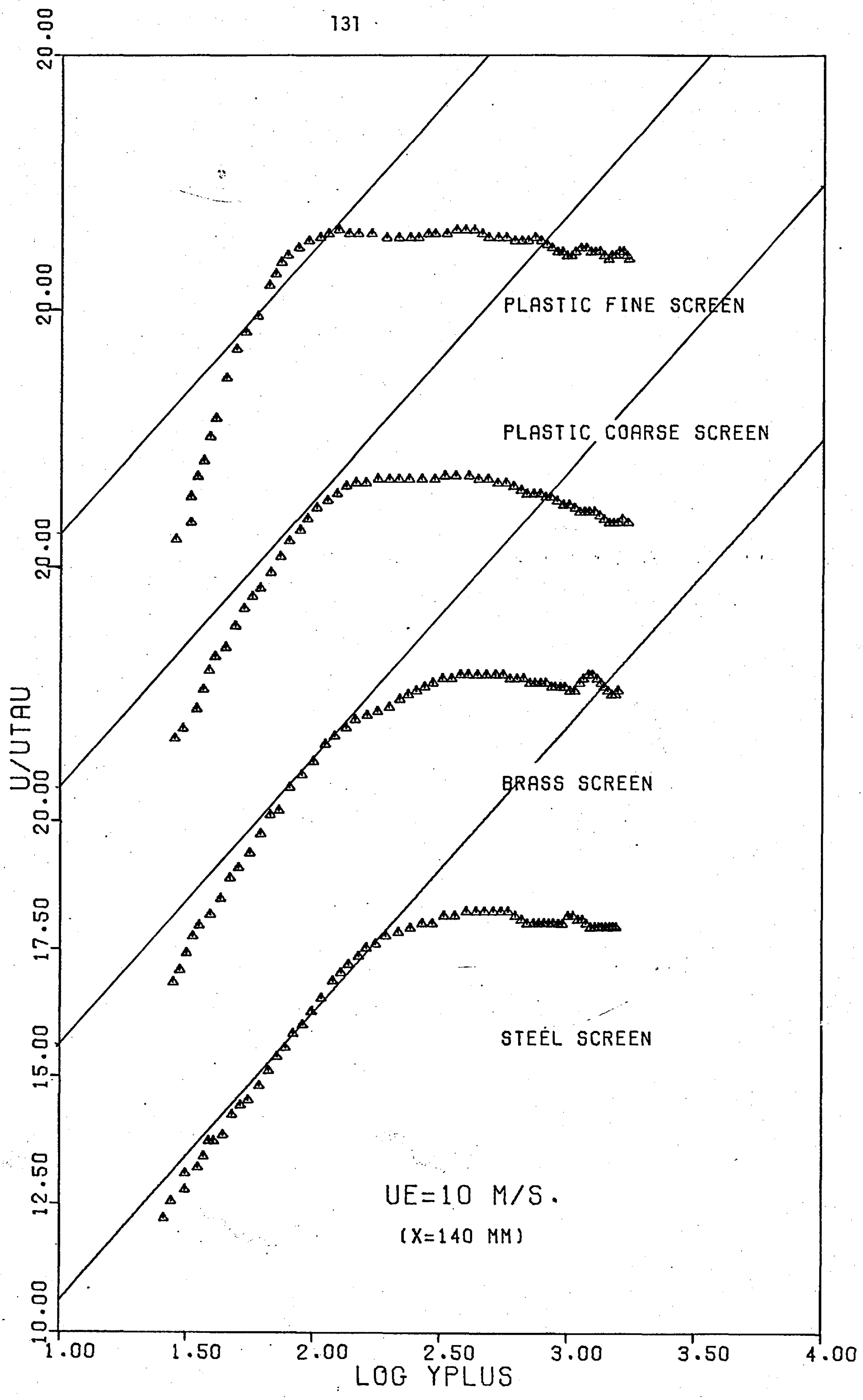

Fig. 3.21b Semi-log. profiles at a reduced free stream velocity.

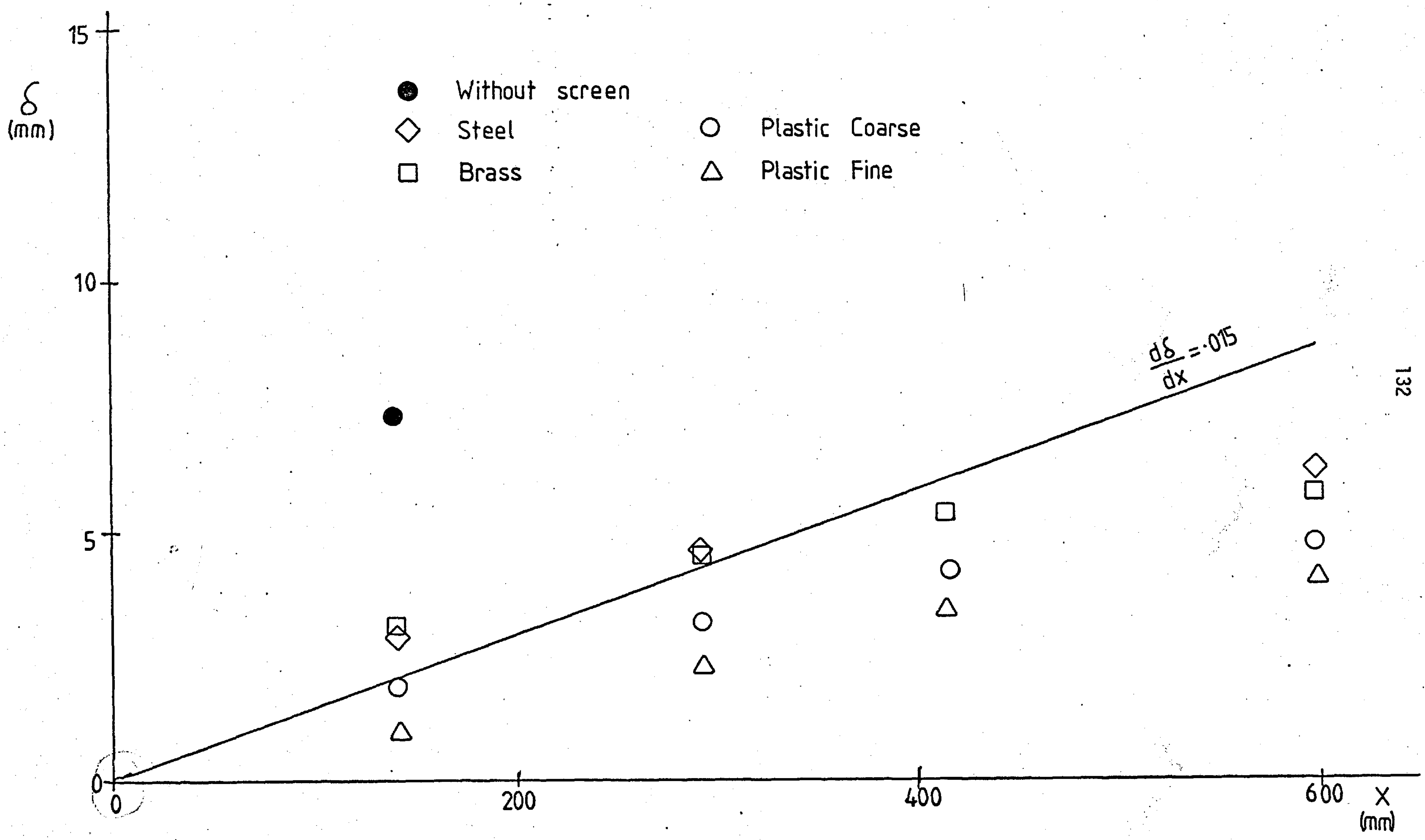

Fig. 3.22 Boundary layer thickness distributions.

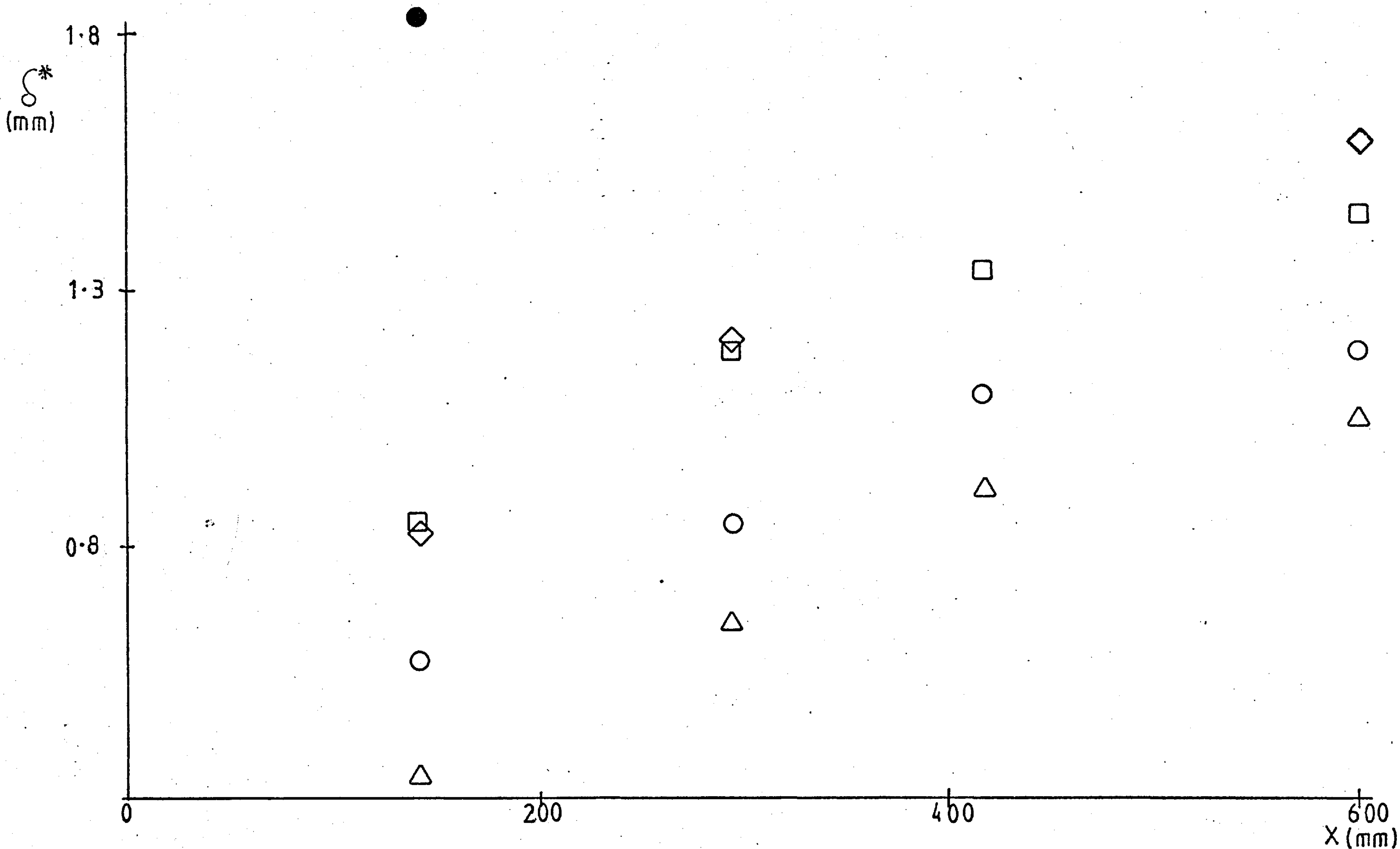

Fig. 3.23 Displacement thickness distributions. (For legend, see Fig. 3.22).

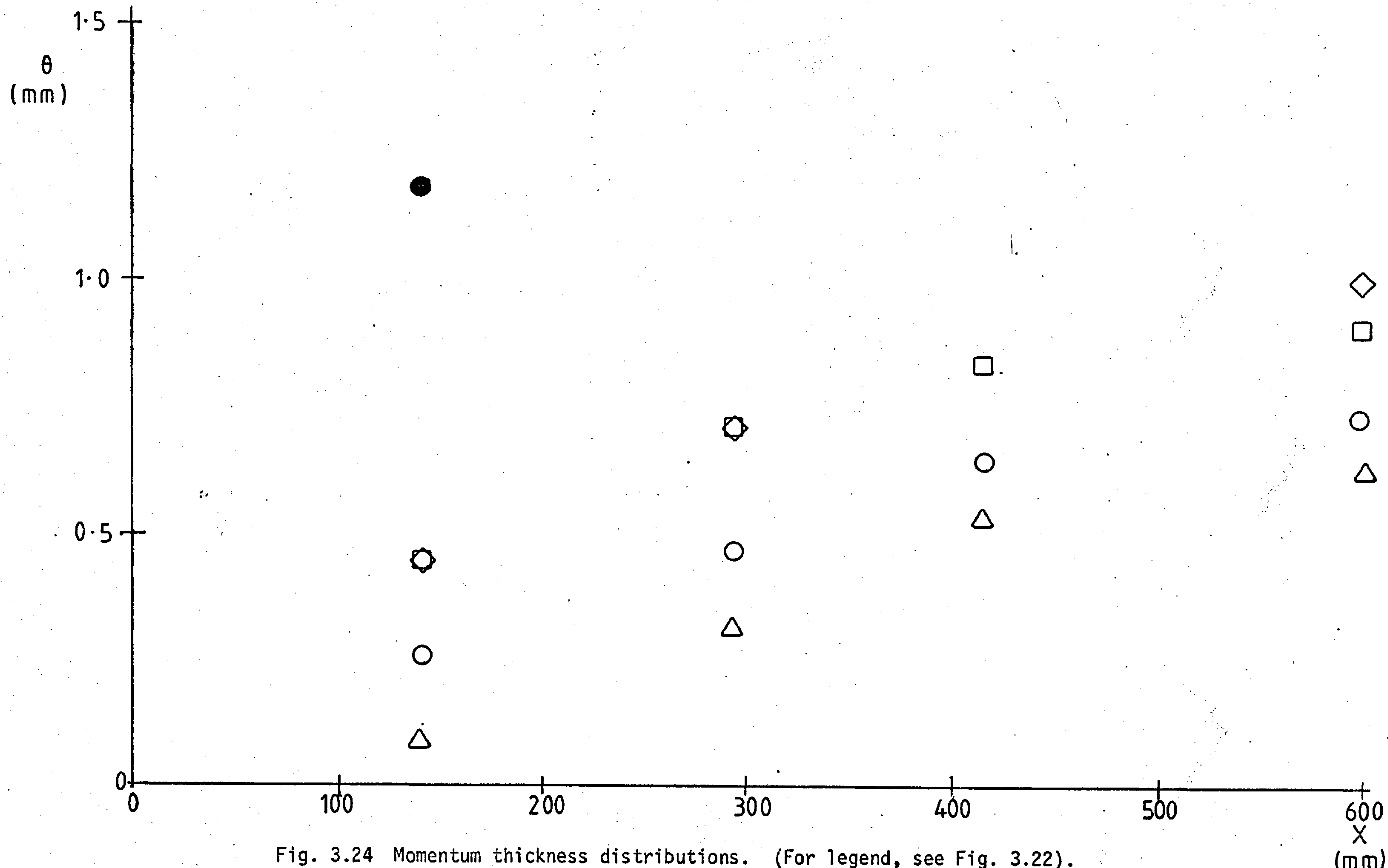

Fig. 3.24 Momentum thickness distributions. (For legend, see Fig. 3.22).

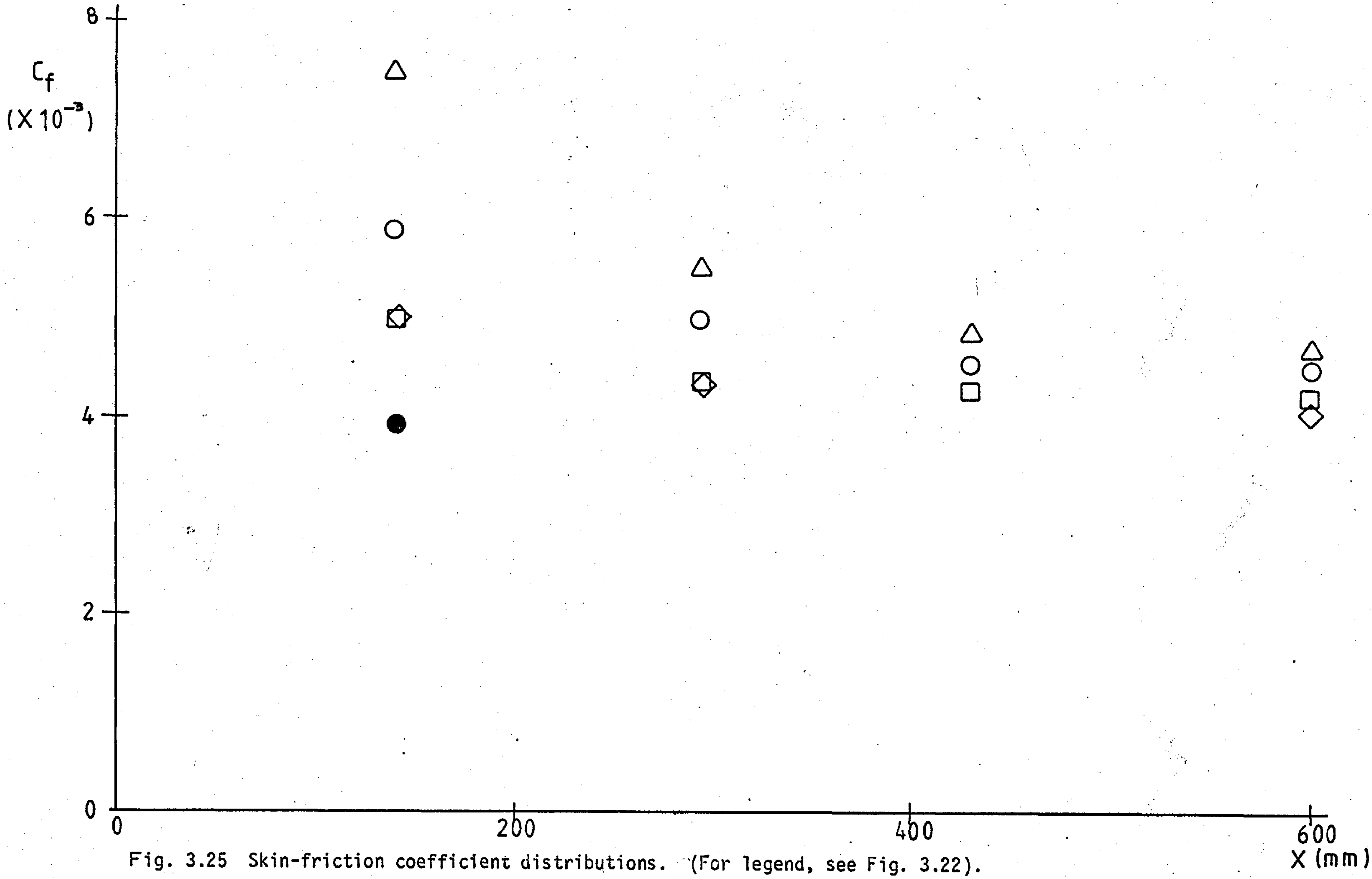

Fig. 3.25 Skin-friction coefficient distributions. (For legend, see Fig. 3.22).

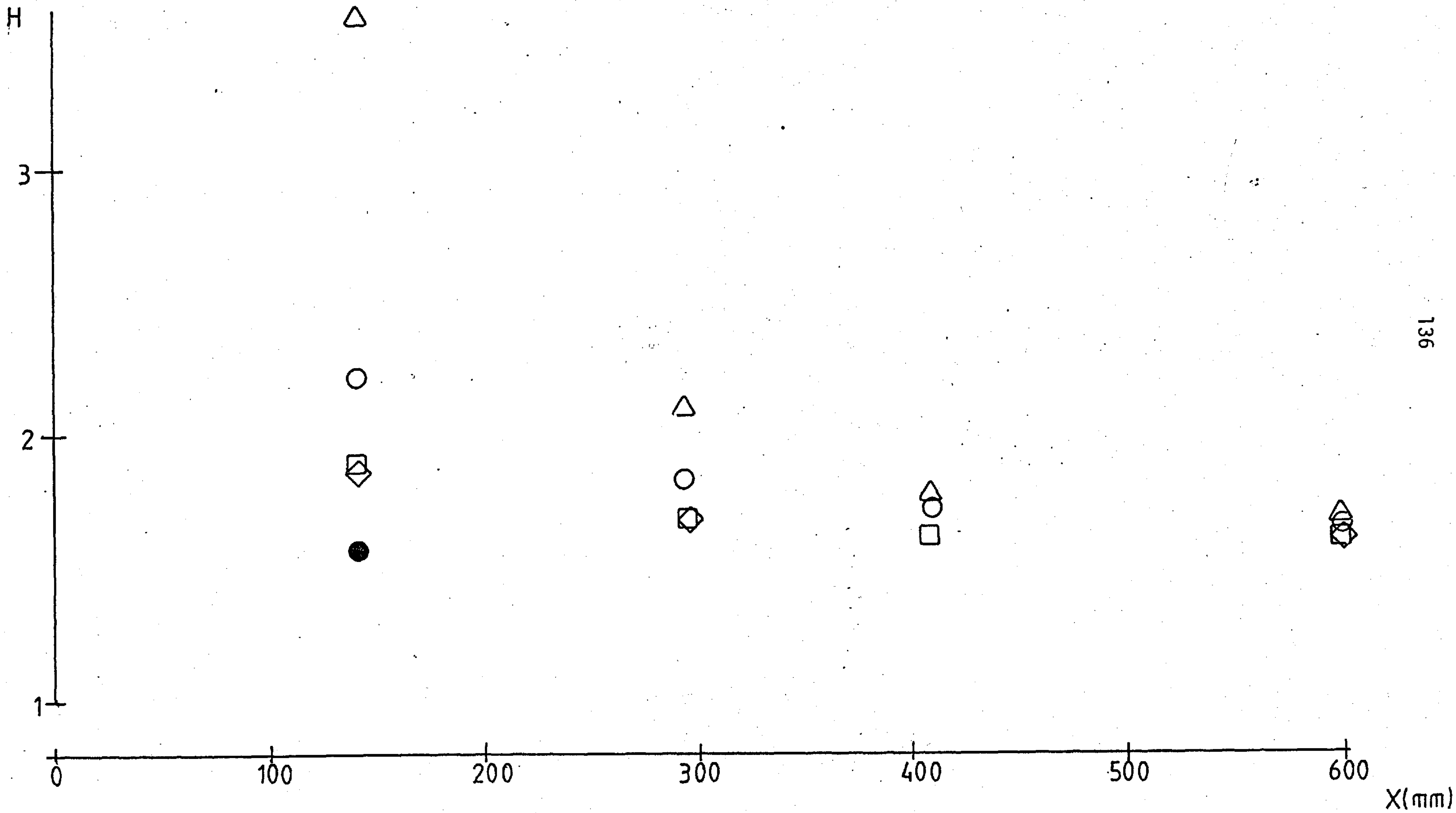

Fig. 3.26 Boundary layer shape factor distributions. (For legend, see Fig. 3.22).

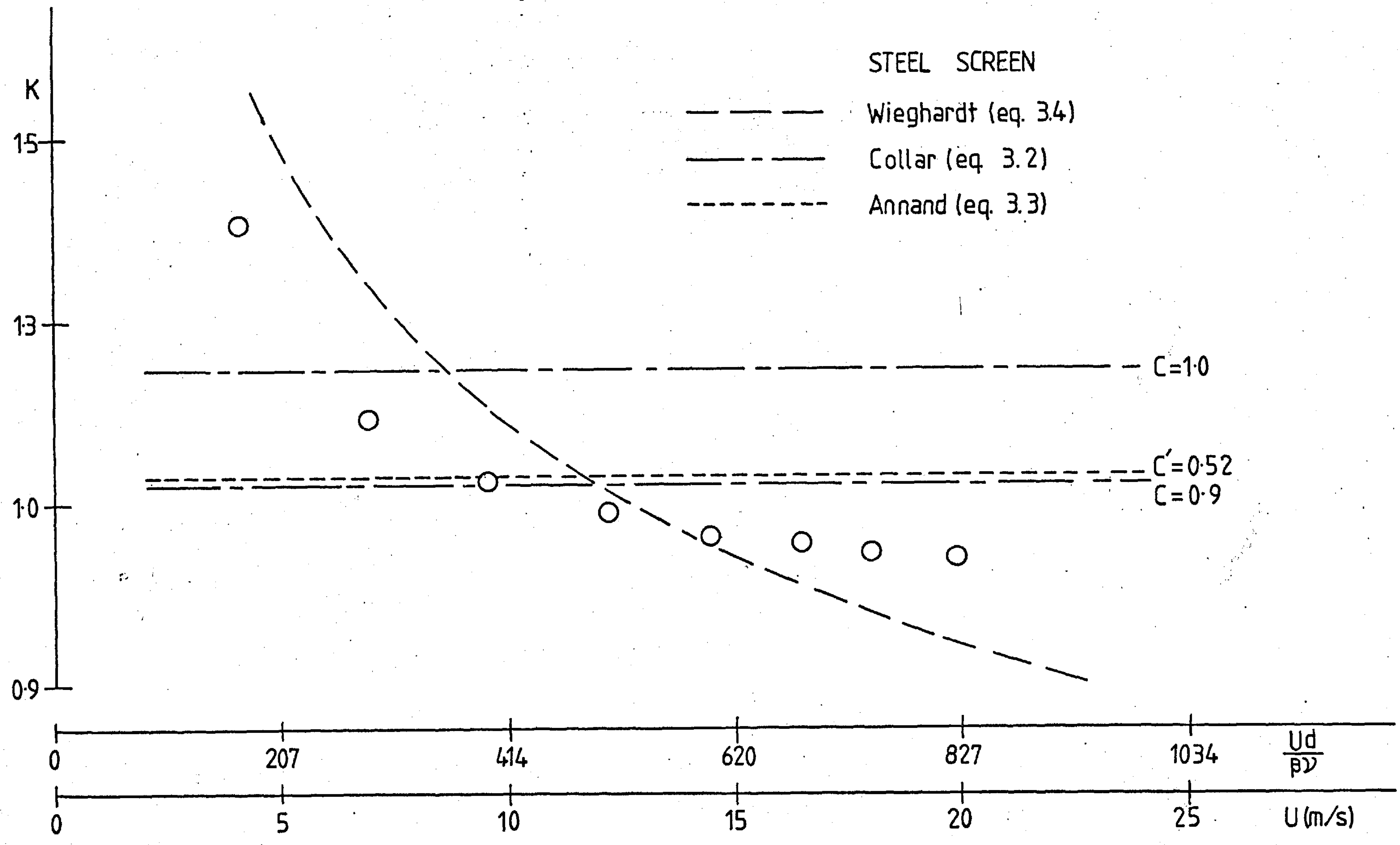

Fig. 3.27 Variation of pressure drop coefficient of the steel screen with flow speed.

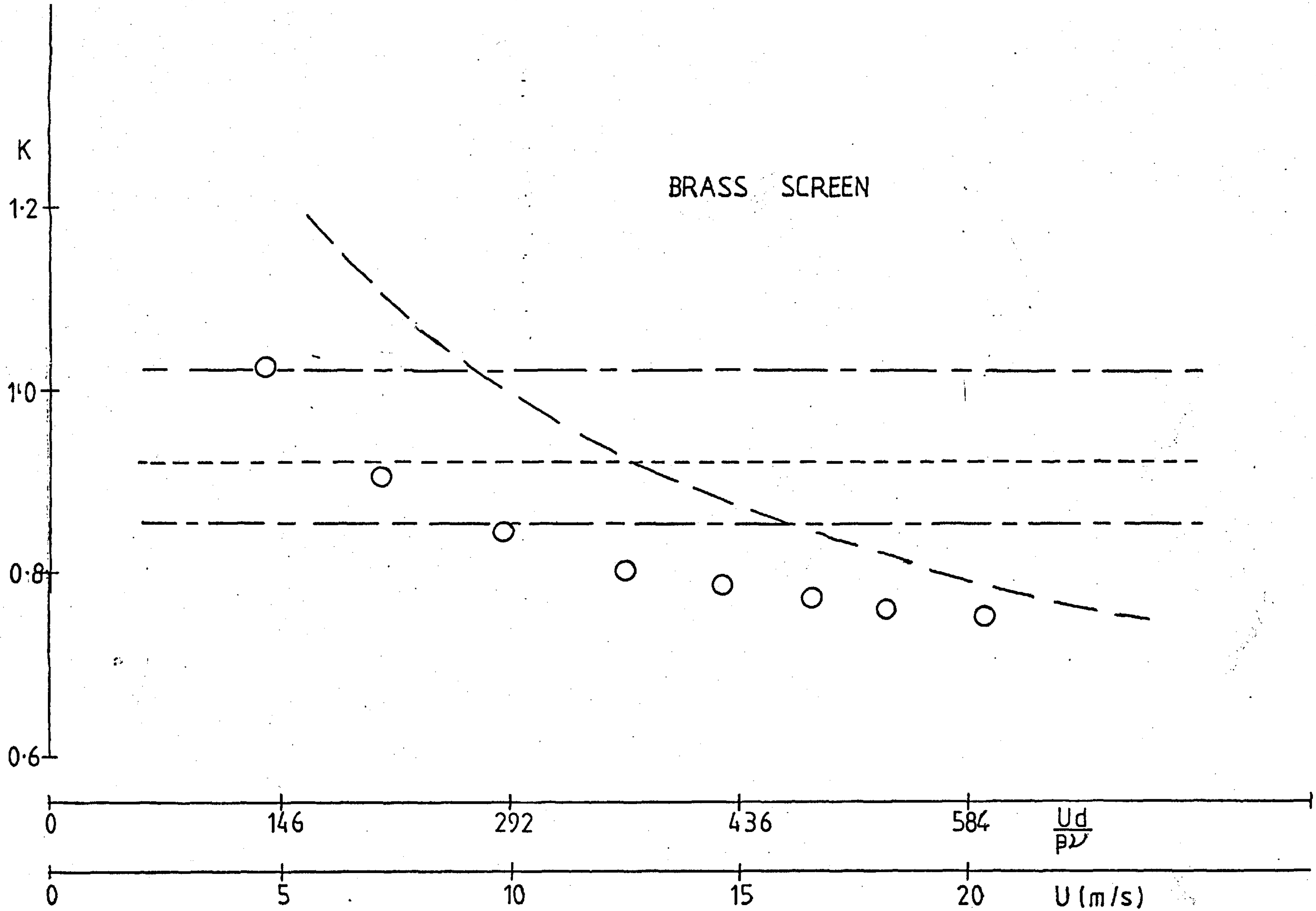

Fig. 3.28 Variation of pressure drop coefficient of the brass screen with flow speed. (For legend, see Fig. 3.27).

PLASTIC COARSE SCREEN

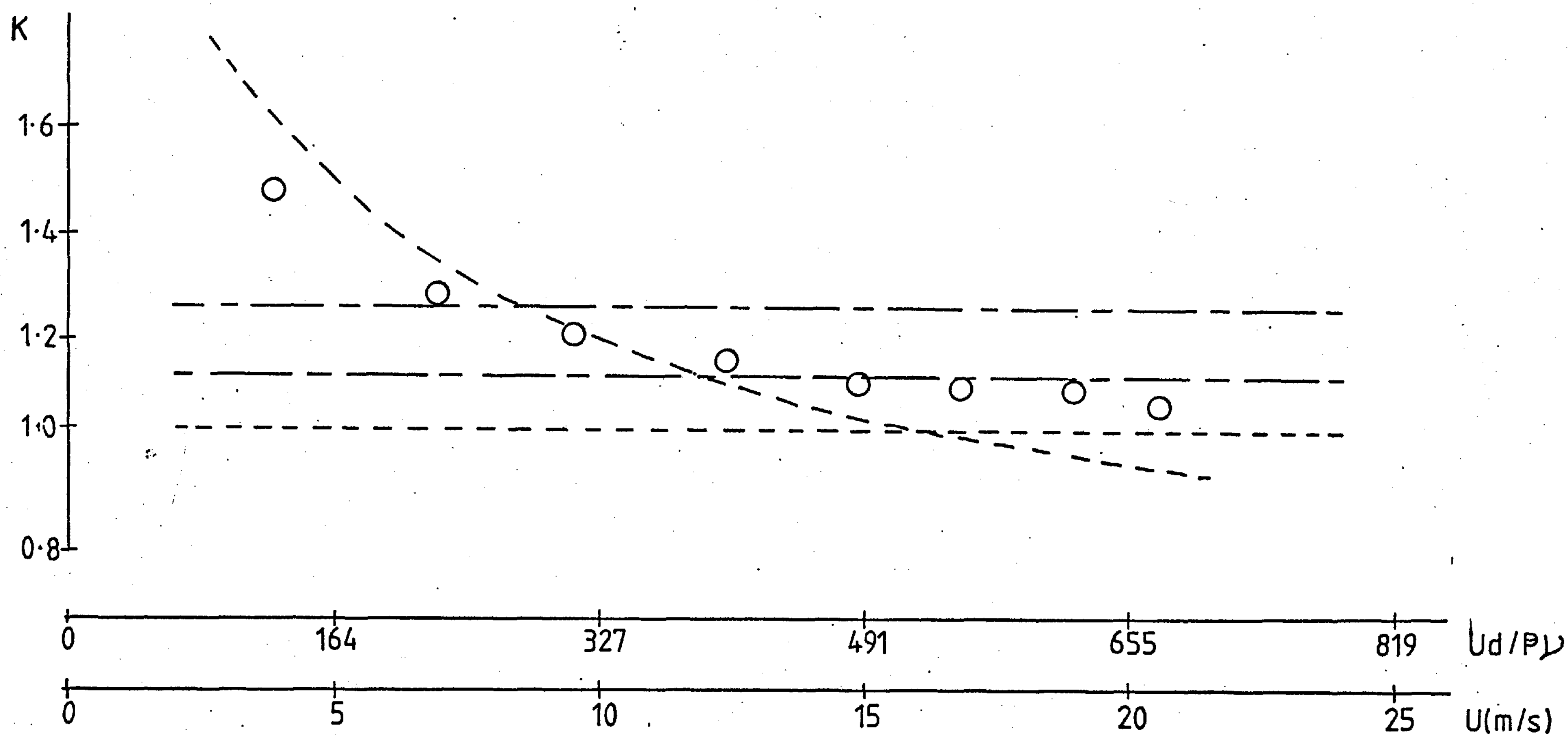

Fig. 3.29 Variation of pressure drop coefficient of the plastic coarse screen with flow speed. (For legend, see Fig. 3.27).

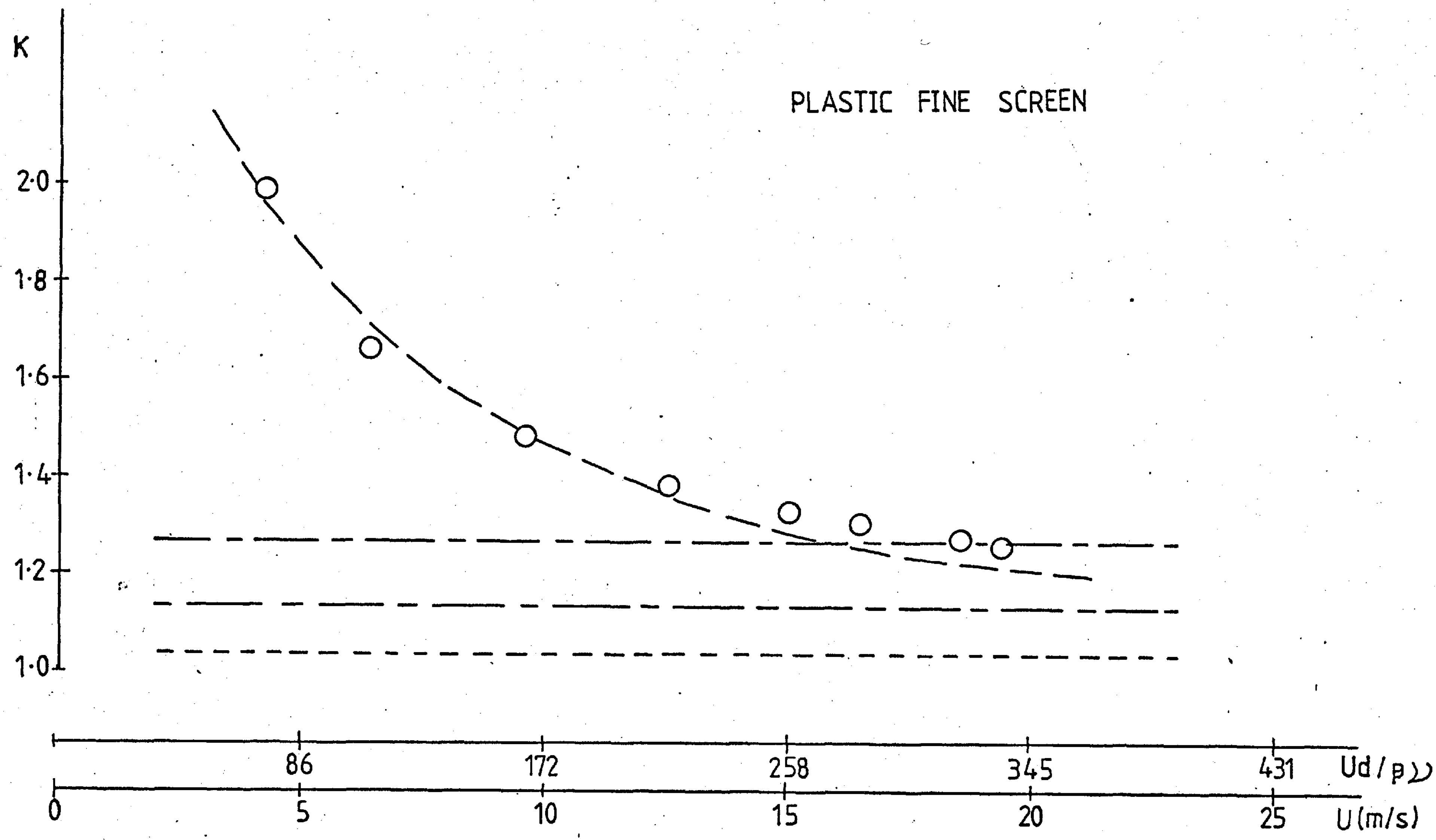

Fig. 3.30 Variation of pressure drop coefficient of the plastic fine screen with flow speed. (For legend, see Fig. 3.27).

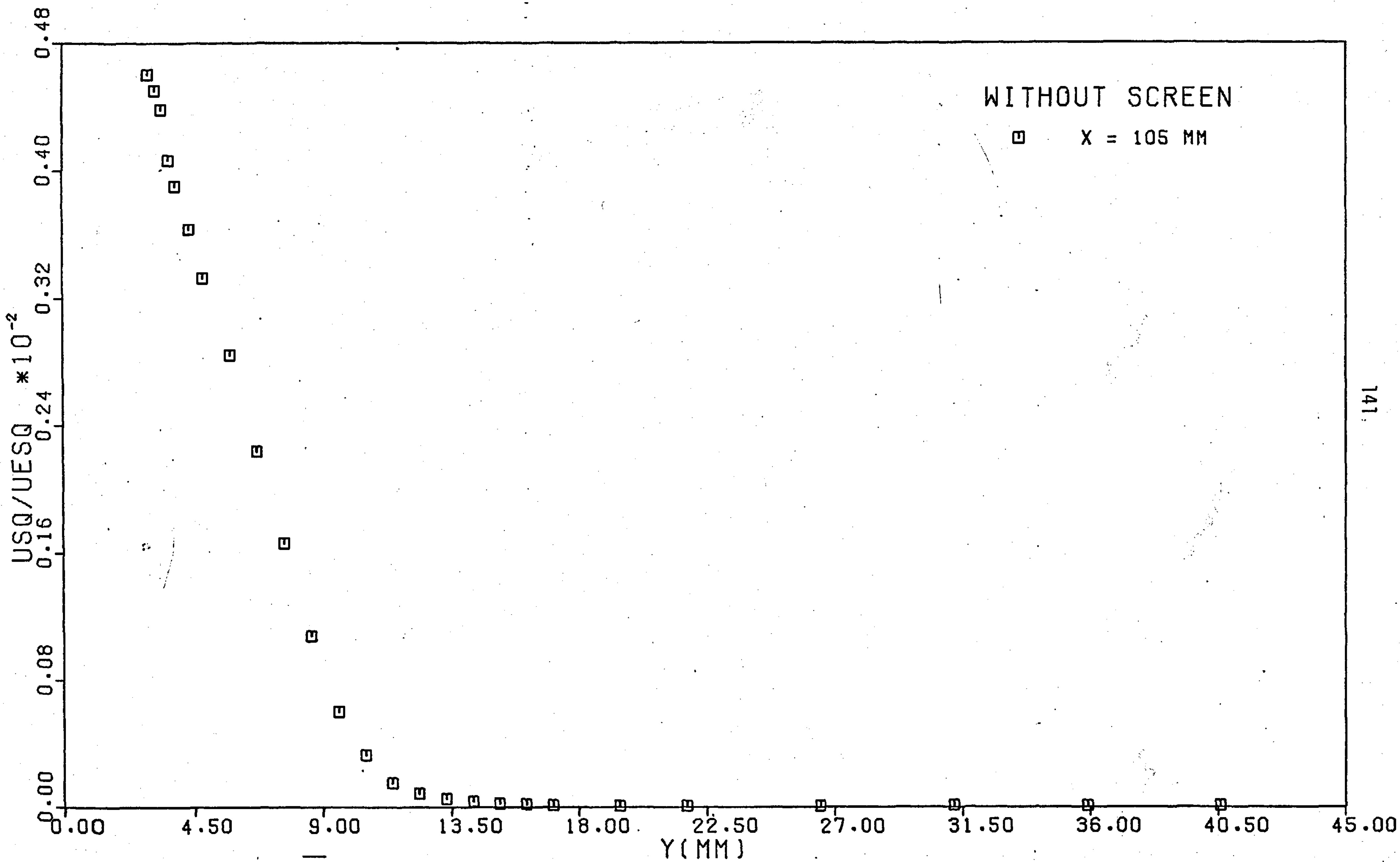

Fig. 3.31 $\overline{u^2}$ profile in the undisturbed boundary layer at x = 105 mm.

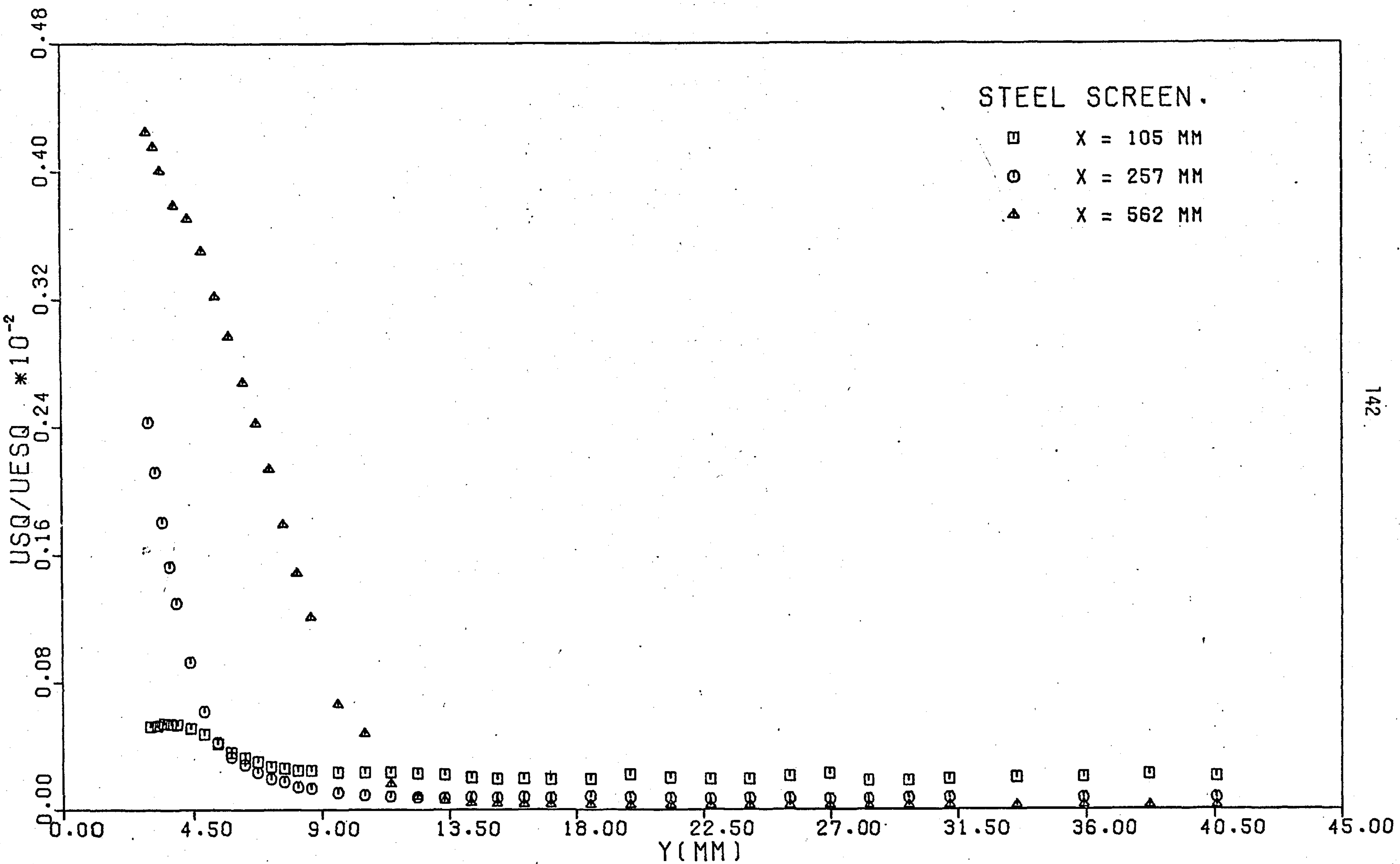

Fig. 3.32 $\overline{u^2}$ profiles downstream of the steel screen.

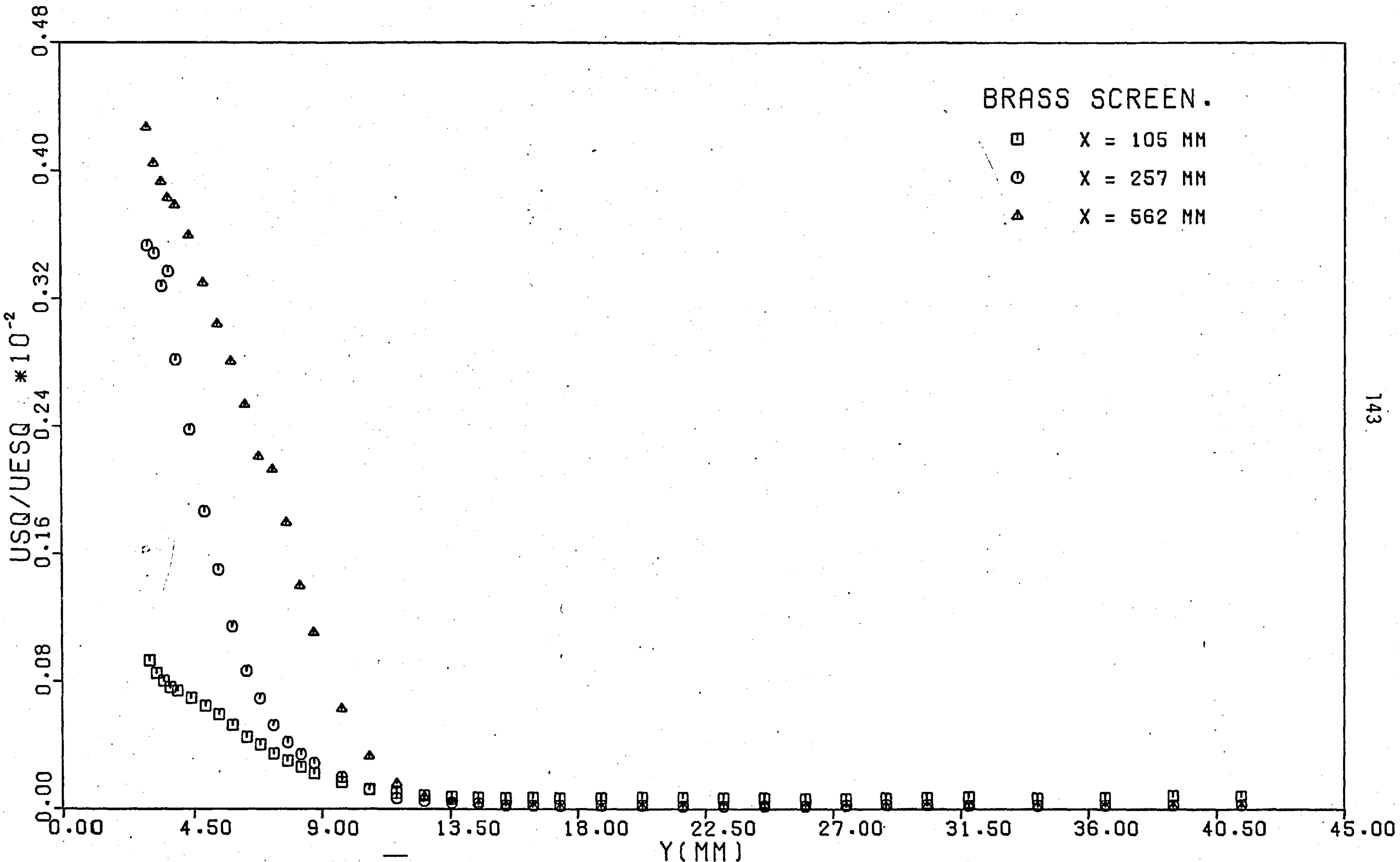

Fig. 3.33 $\overline{u^2}$ profiles downstream of the brass screen.

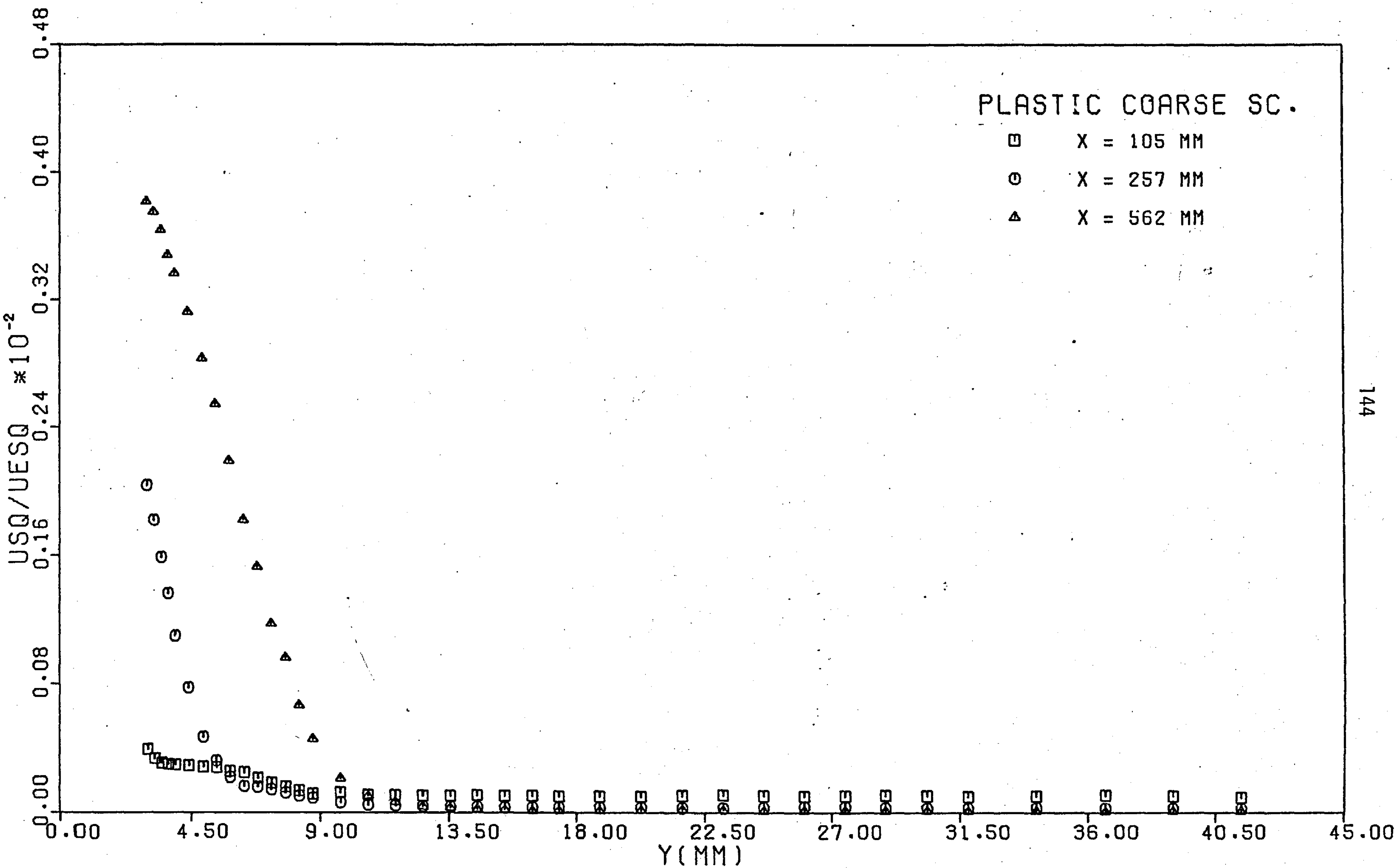

Fig. 3.34 $\overline{u^2}$ profiles downstream of the plastic coarse screen.

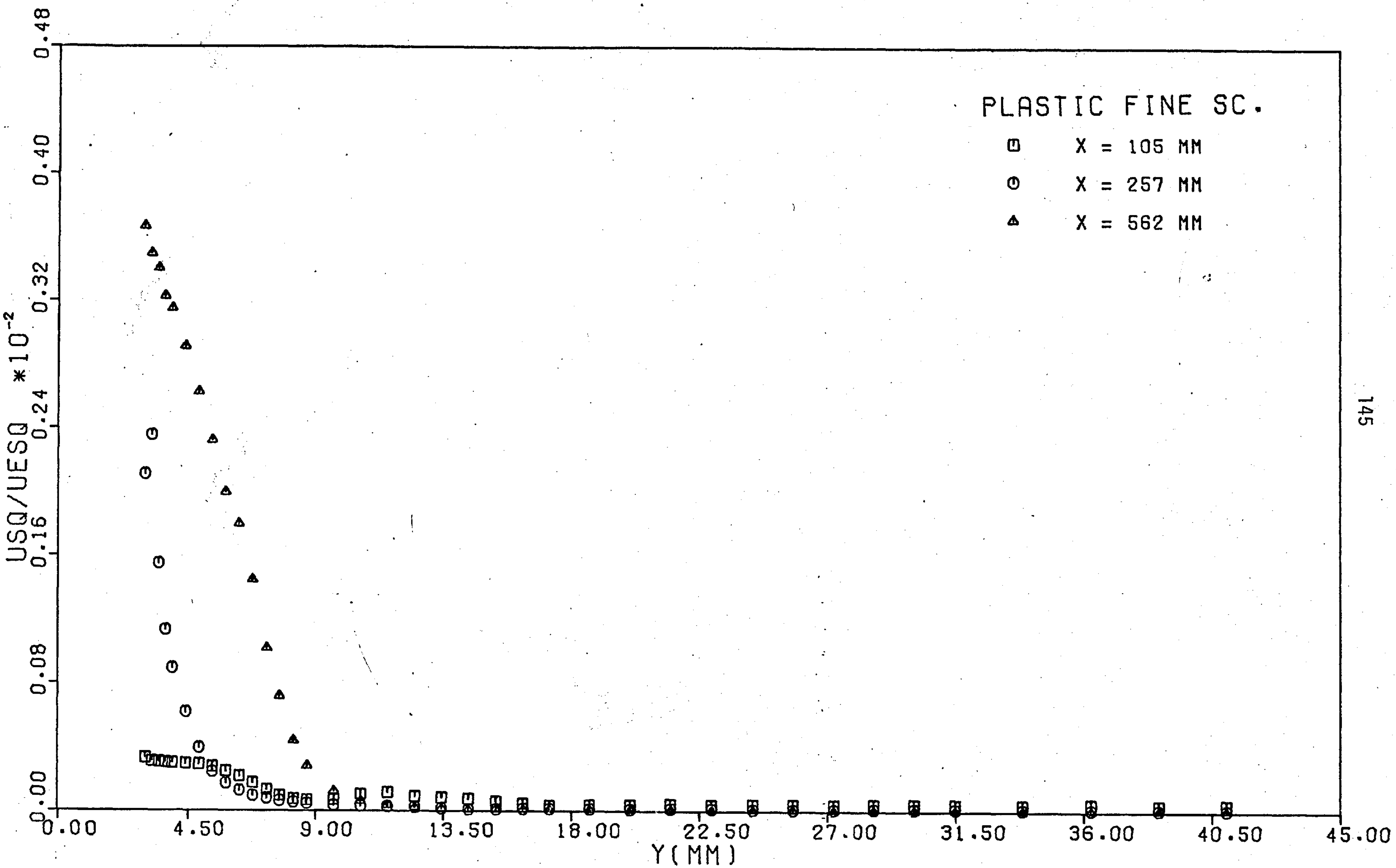

Fig. 3.35 $\overline{u^2}$ profiles downstream of the plastic fine screen.

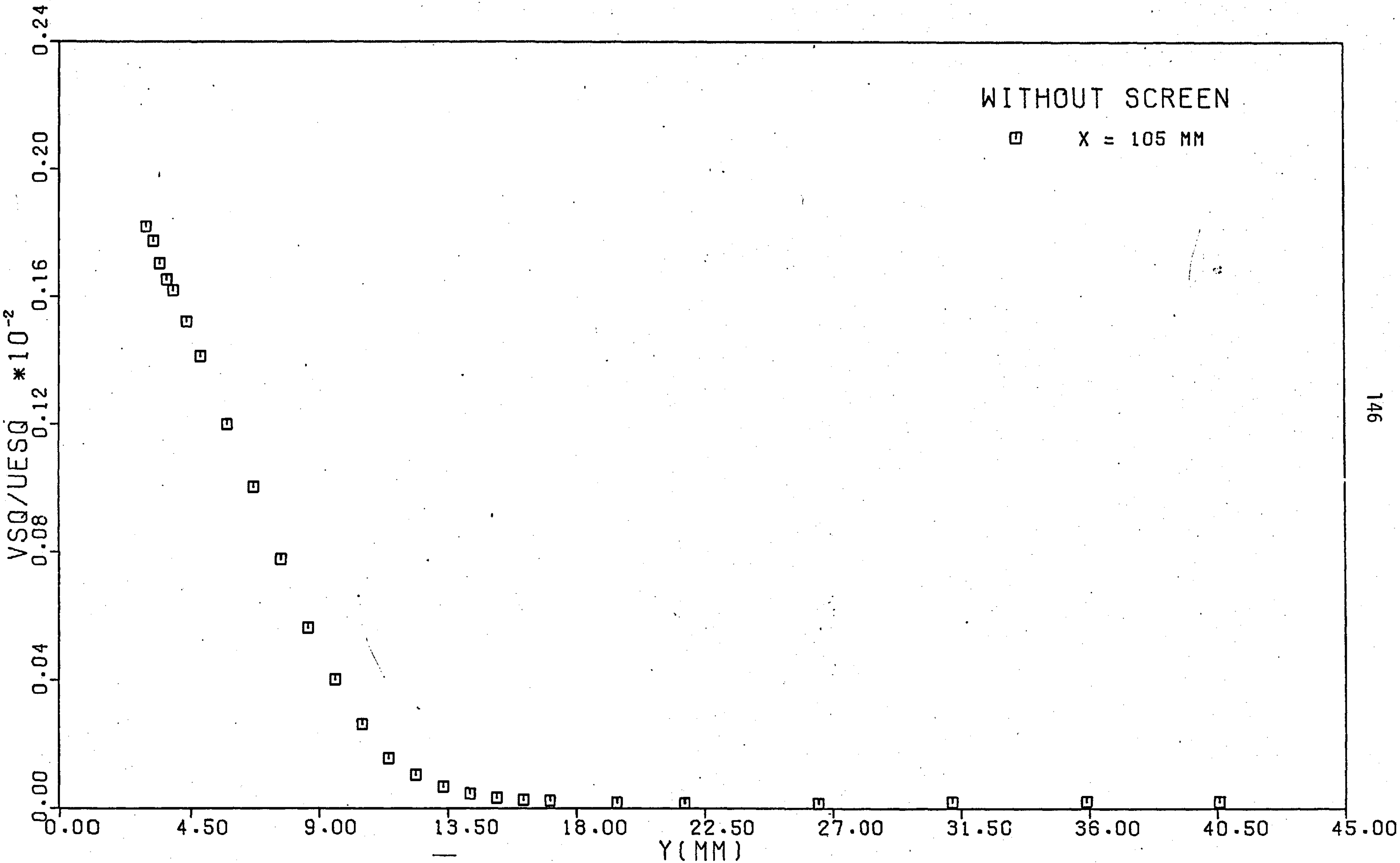

Fig. 3.36 $\overline{v^2}$ profile in the undisturbed boundary layer at x = 105 mm.

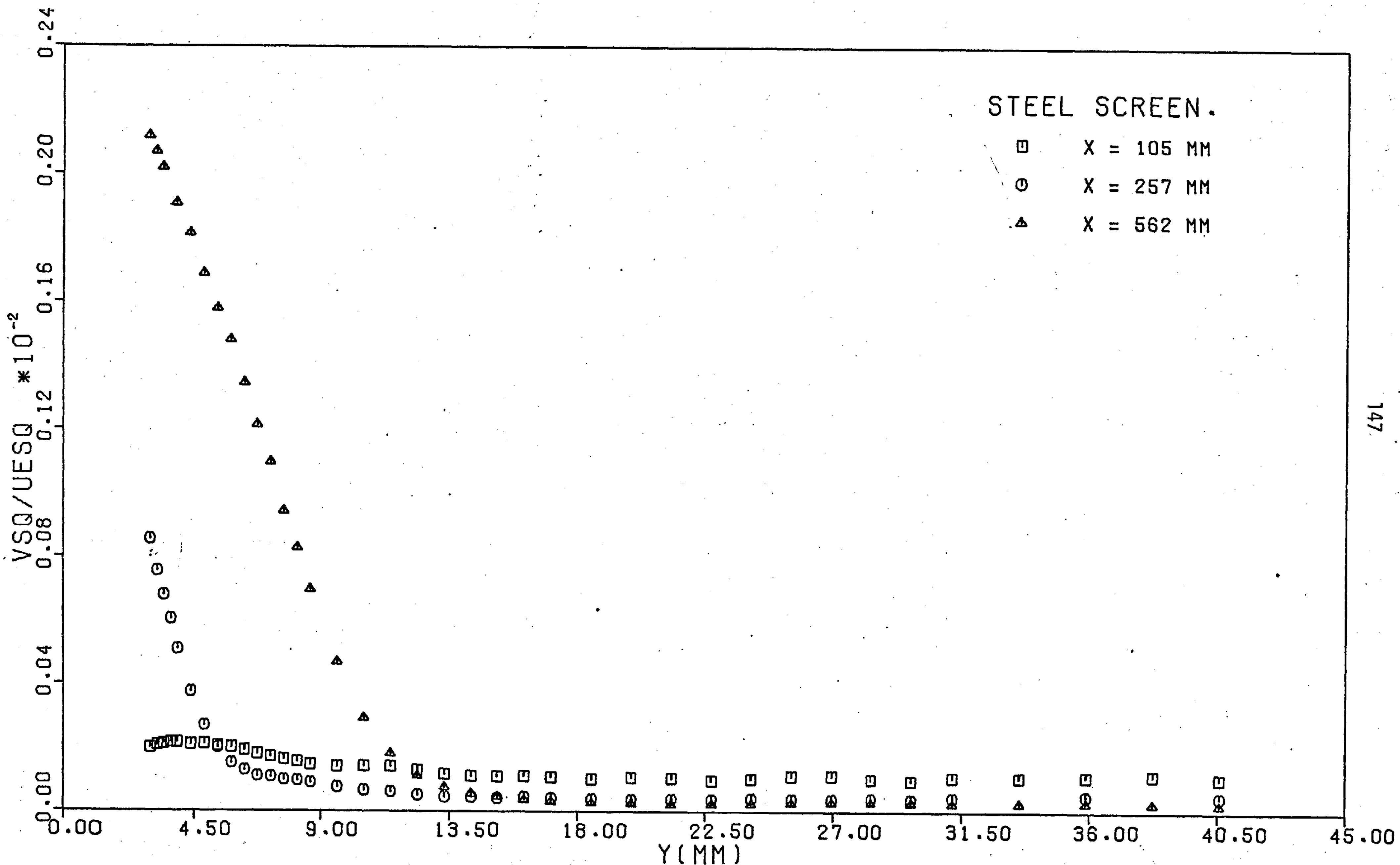

Fig. 3.37 $\overline{v^2}$ profiles downstream of the steel screen.

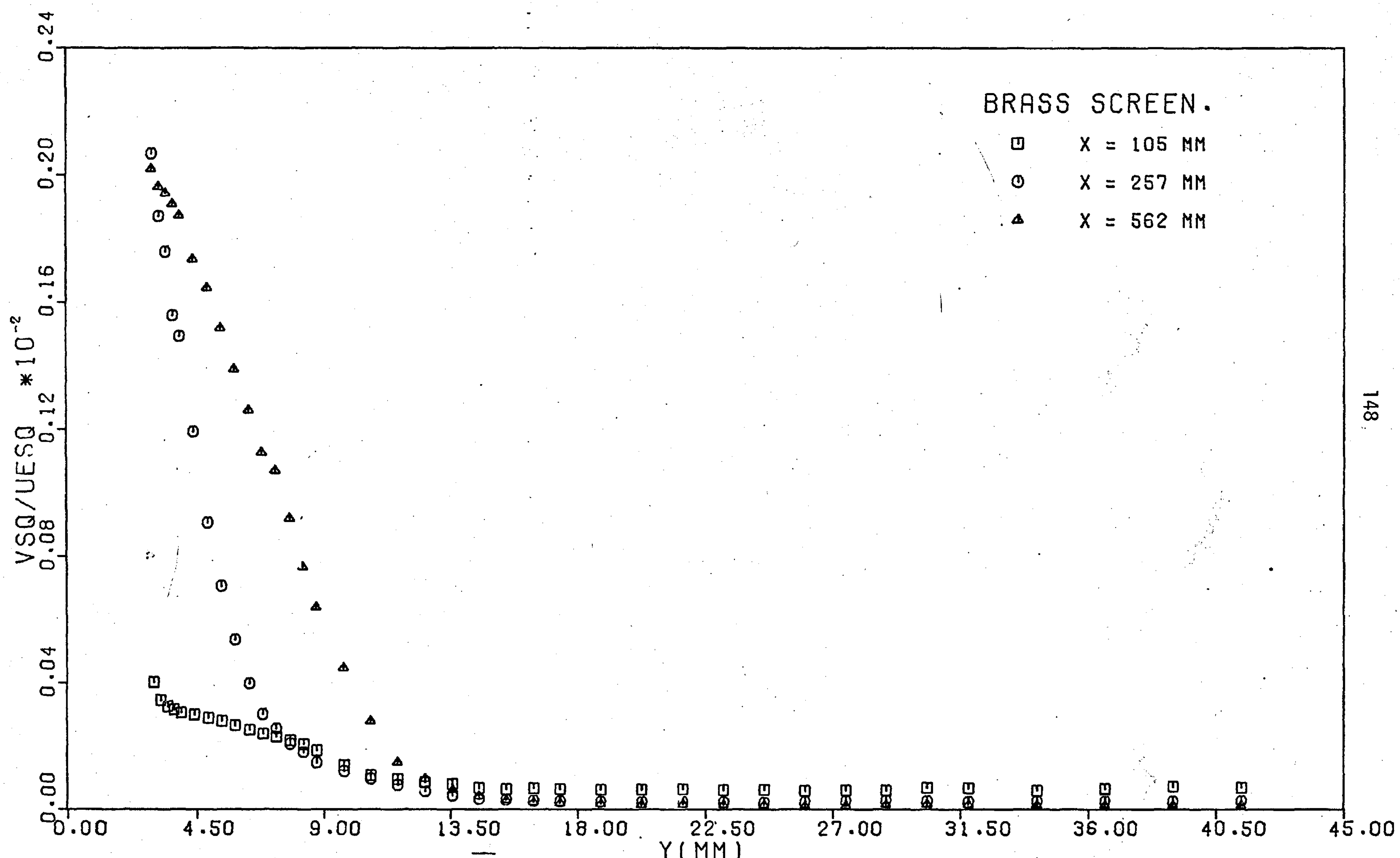

Fig. 3.38 $\overline{v^2}$ profiles downstream of the brass screen.

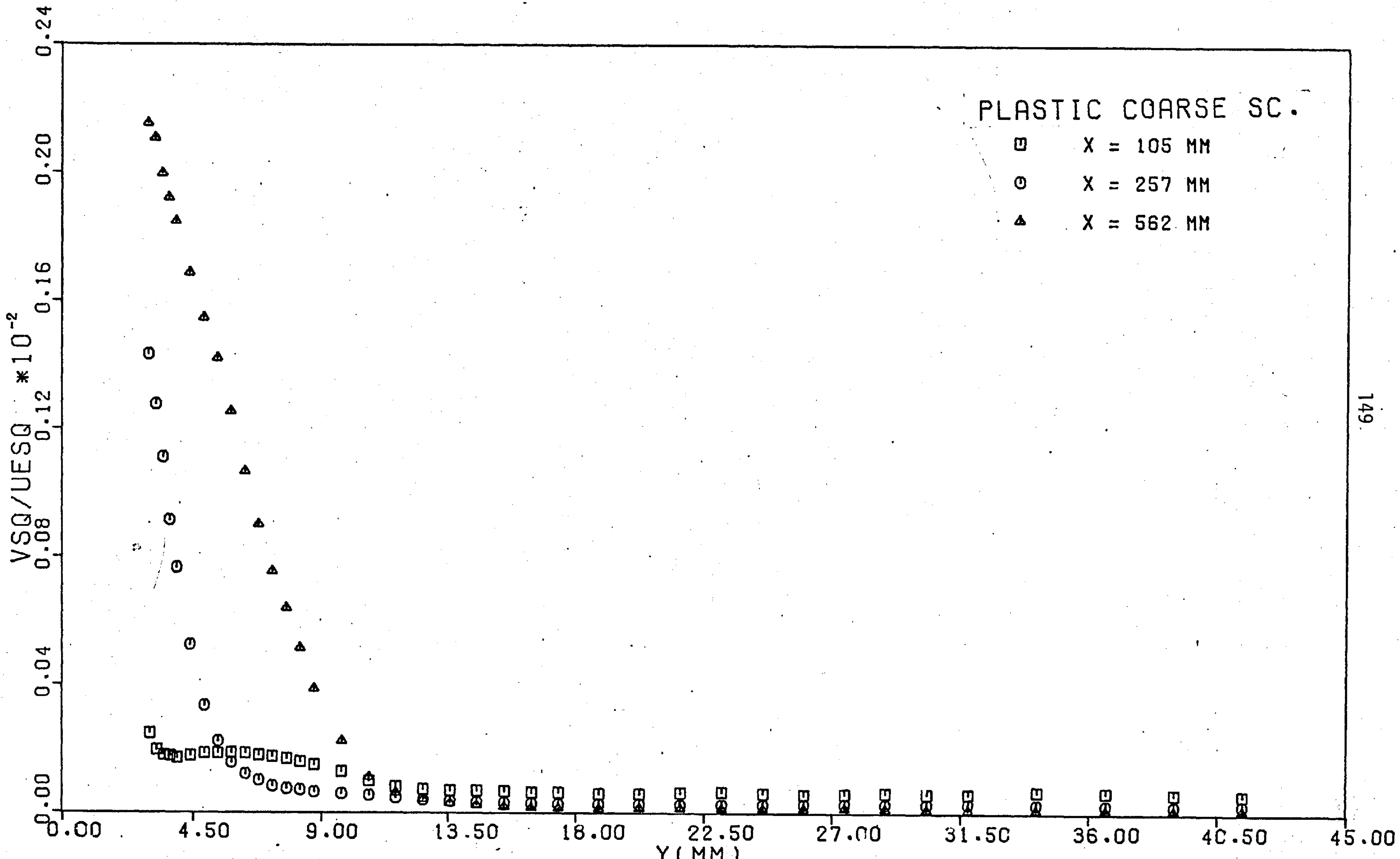

Fig. 3.39 $\overline{v^2}$ profiles downstream of the plastic coarse screen.

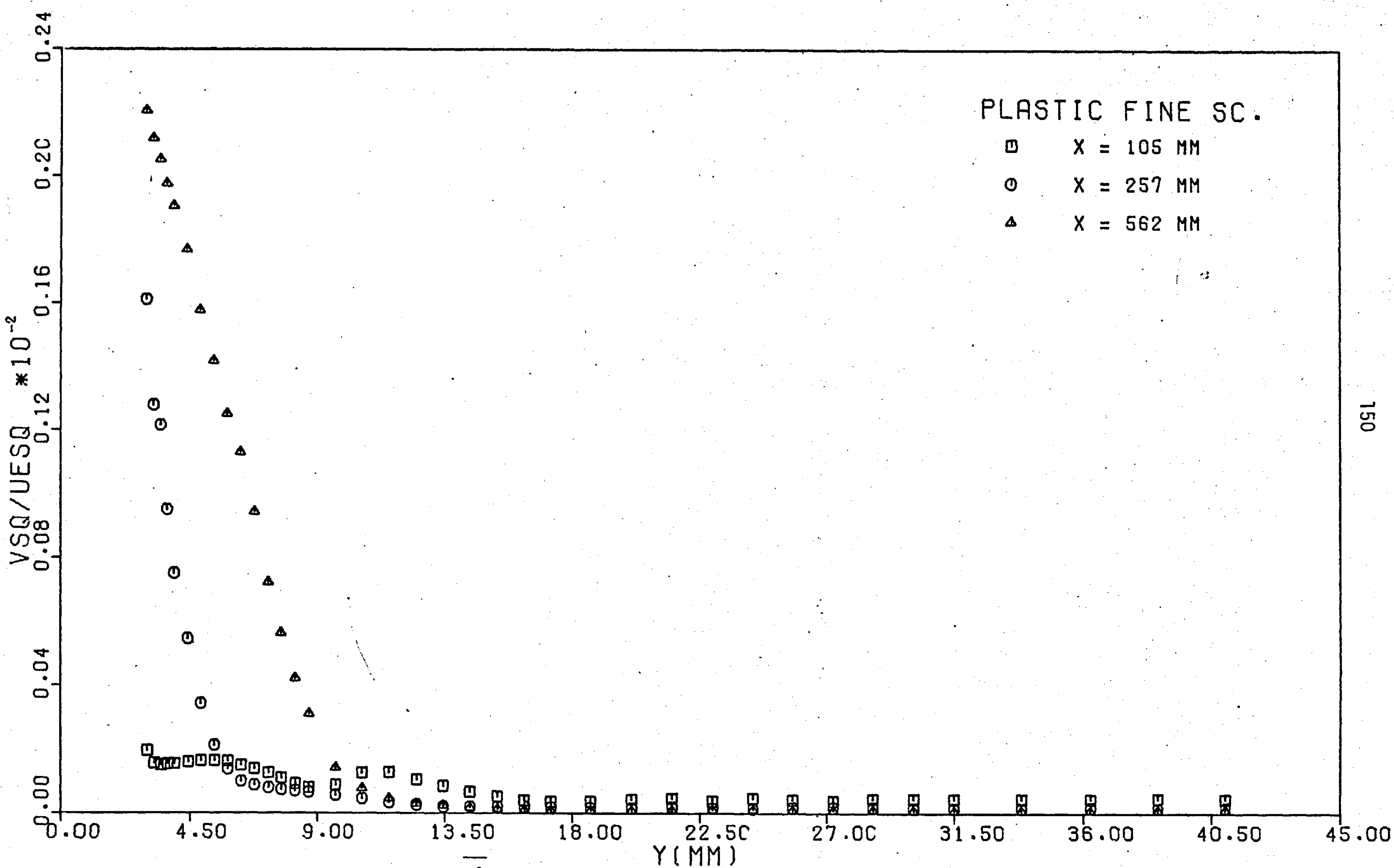

Fig. 3.40 $\overline{v^2}$ profiles downstream of the plastic fine screen.

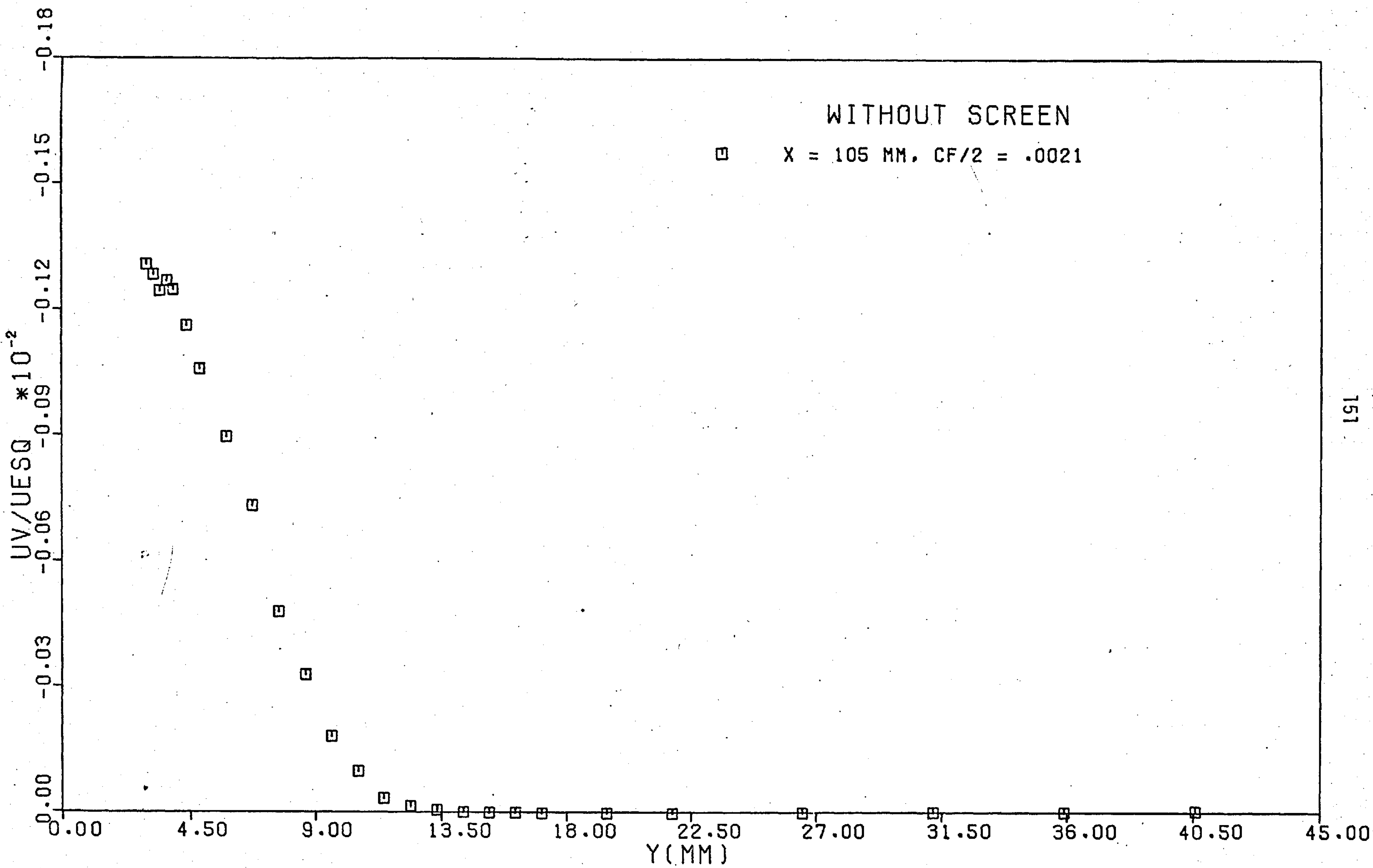

Fig. 3.41 $\overline{uv}$ profile in the undisturbed boundary layer at x = 105 mm

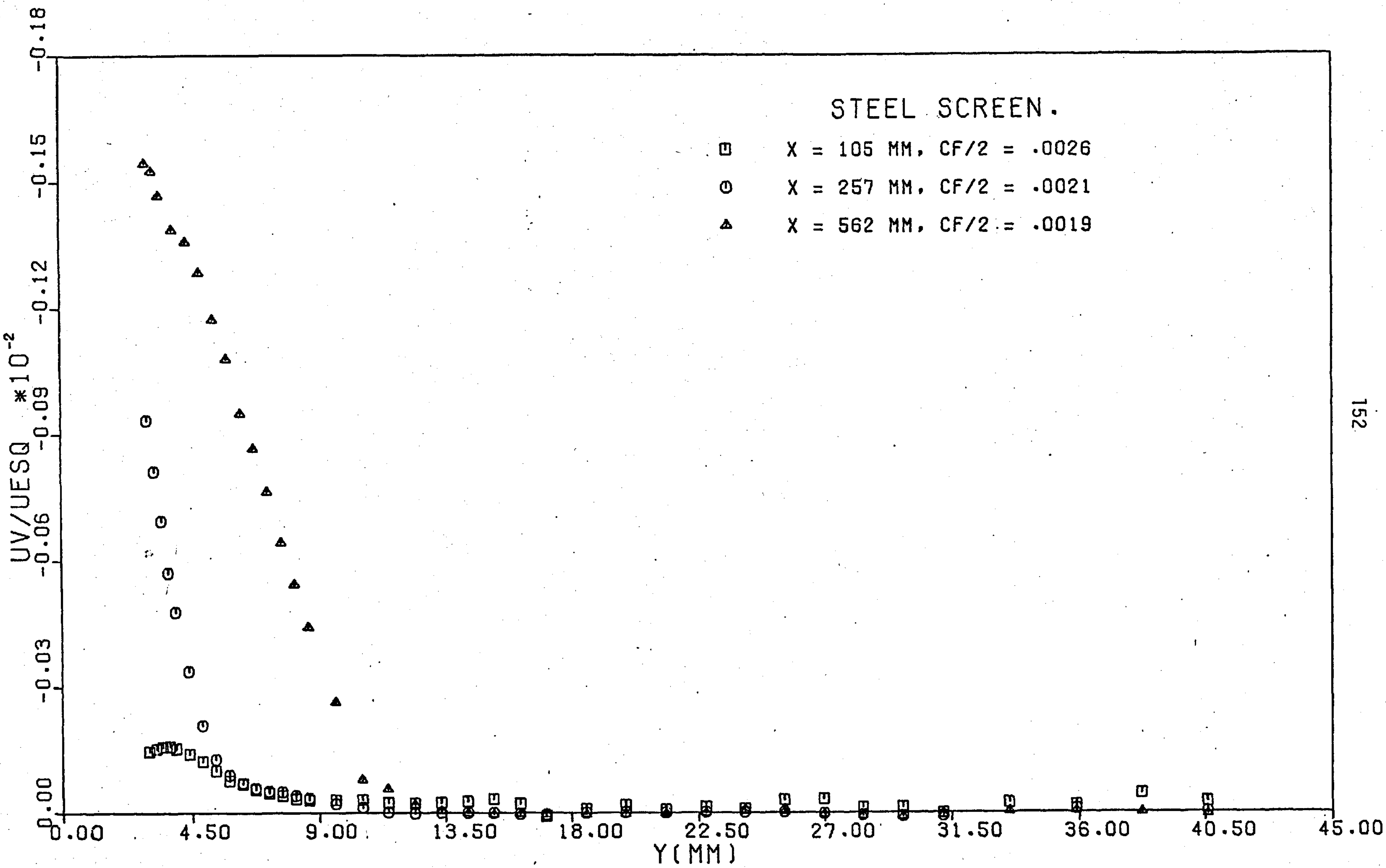

Fig. 3.42 $\overline{uv}$ profiles downstream of the steel screen.

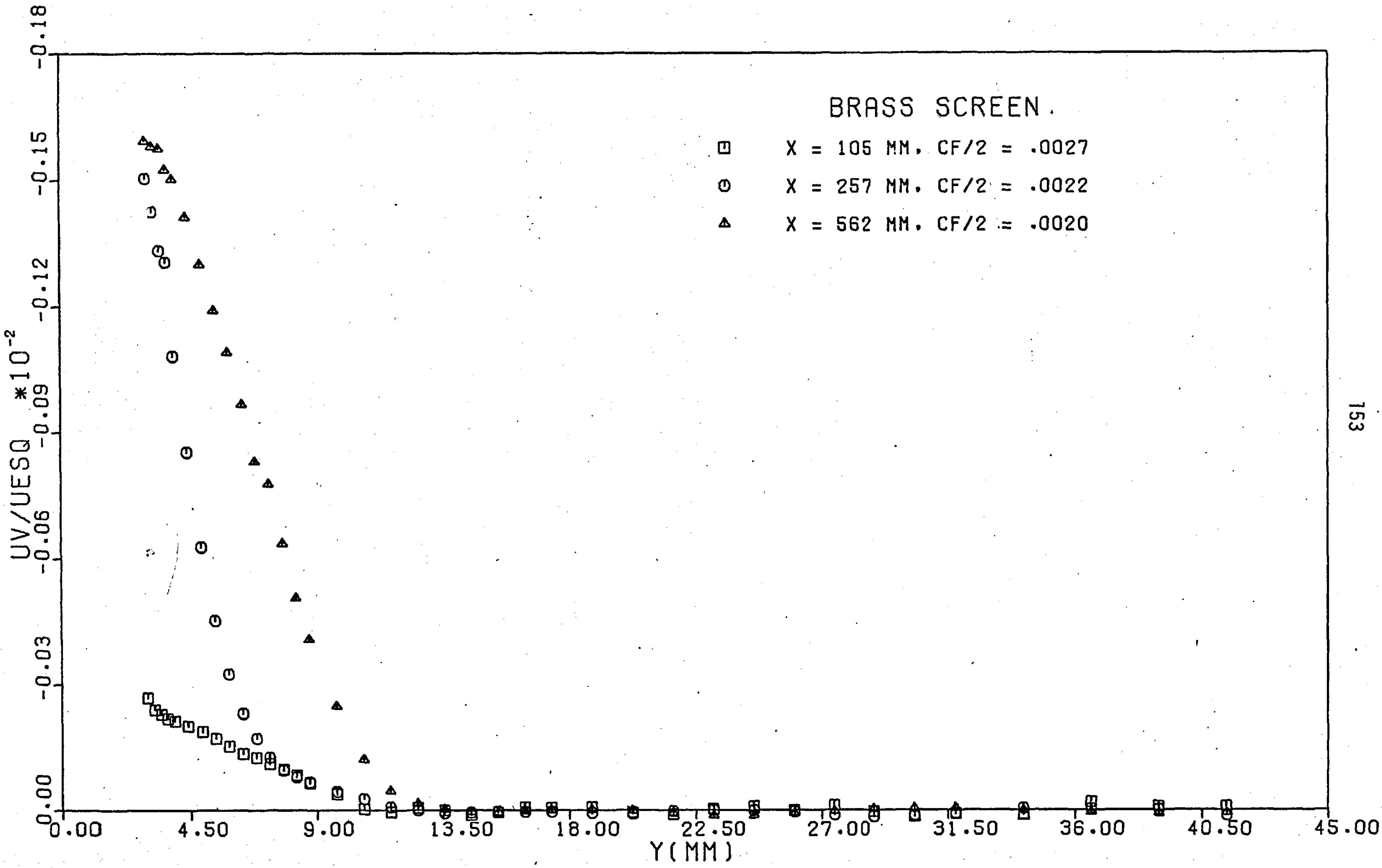

Fig. 3.43 $\overline{uv}$ profiles downstream of the brass screen.

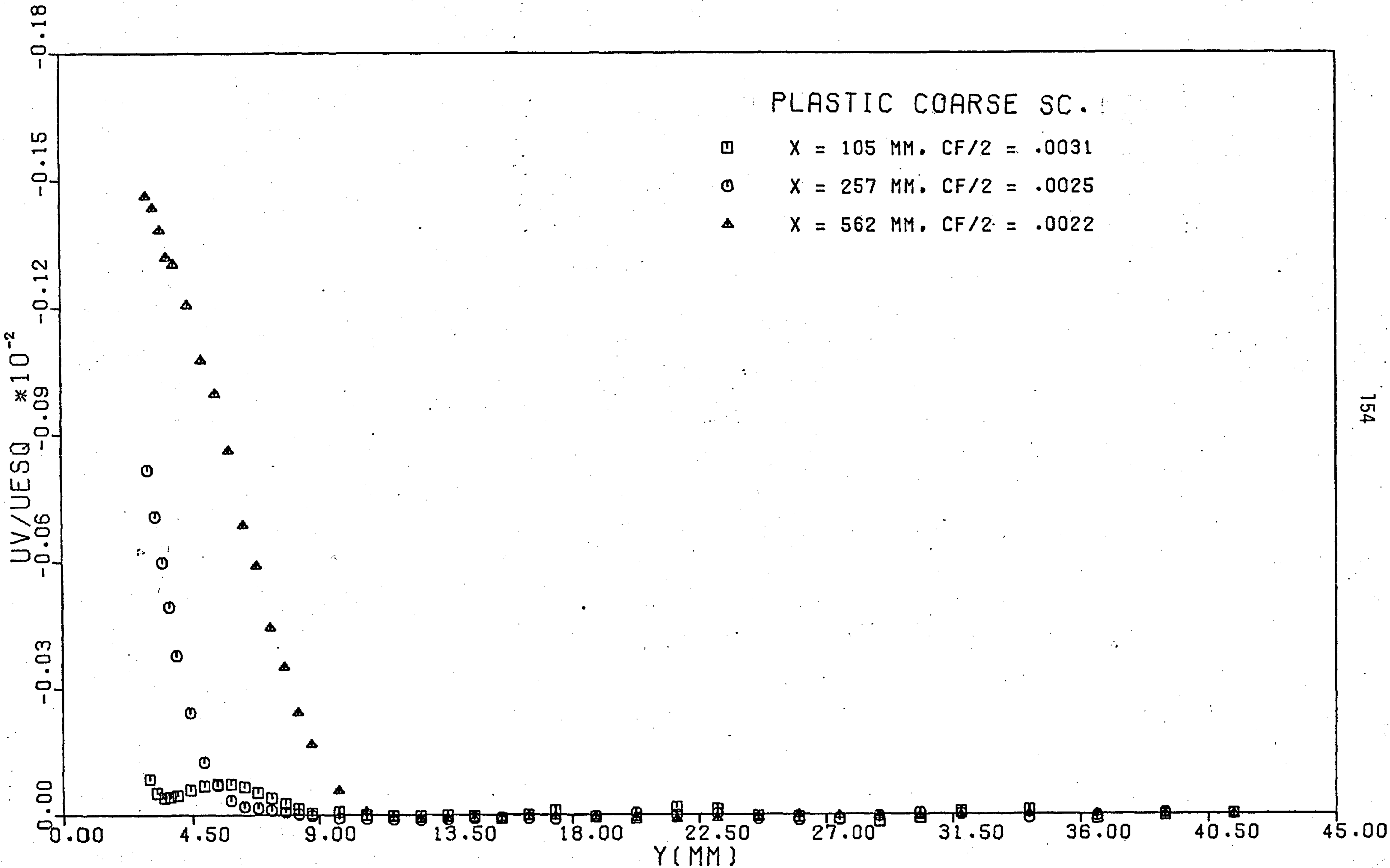

Fig. 3.44 $\overline{uv}$ profiles downstream of the plastic coarse screen.

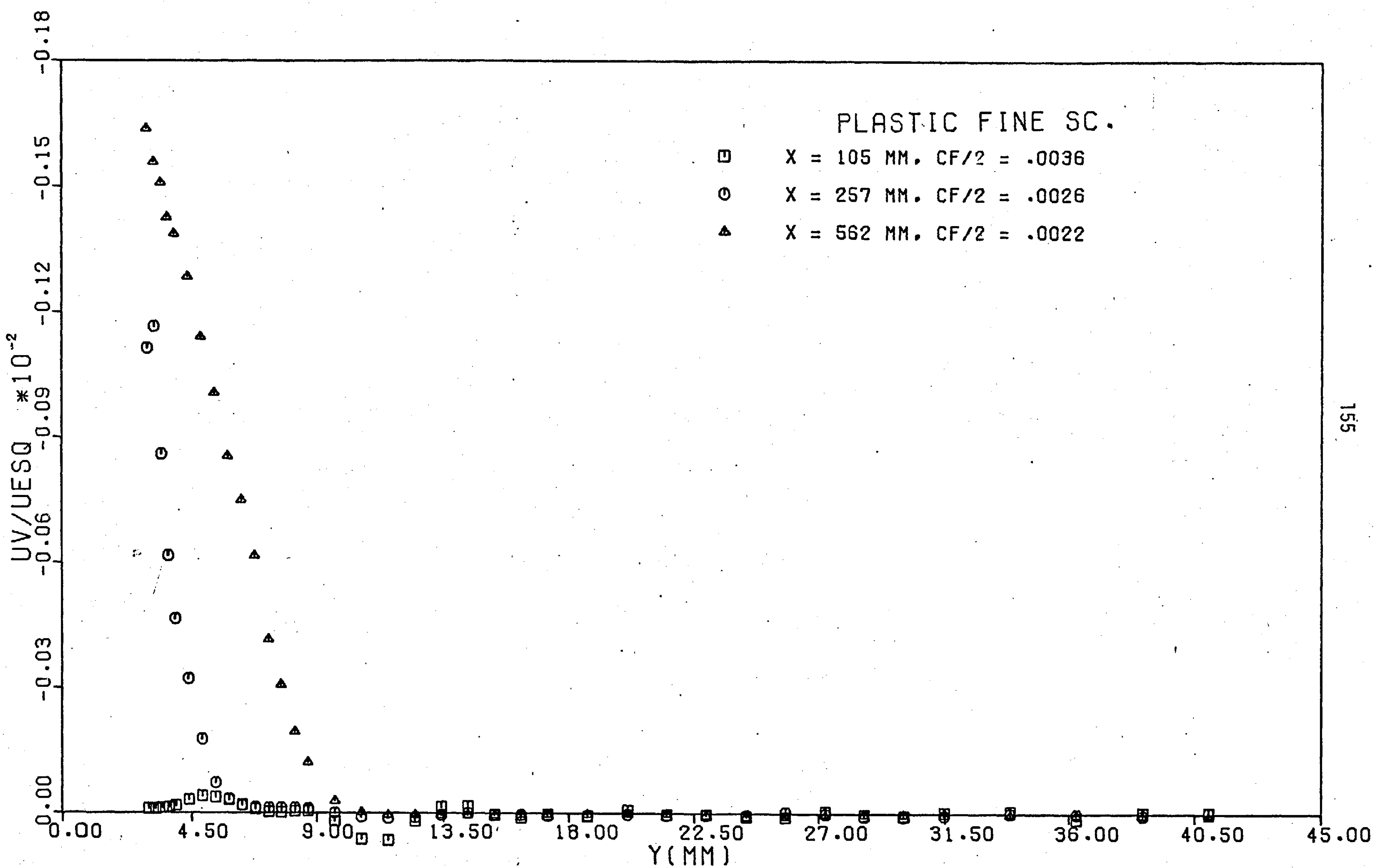

Fig. 3.45 $\overline{uv}$ profiles downstream of the plastic fine screen.

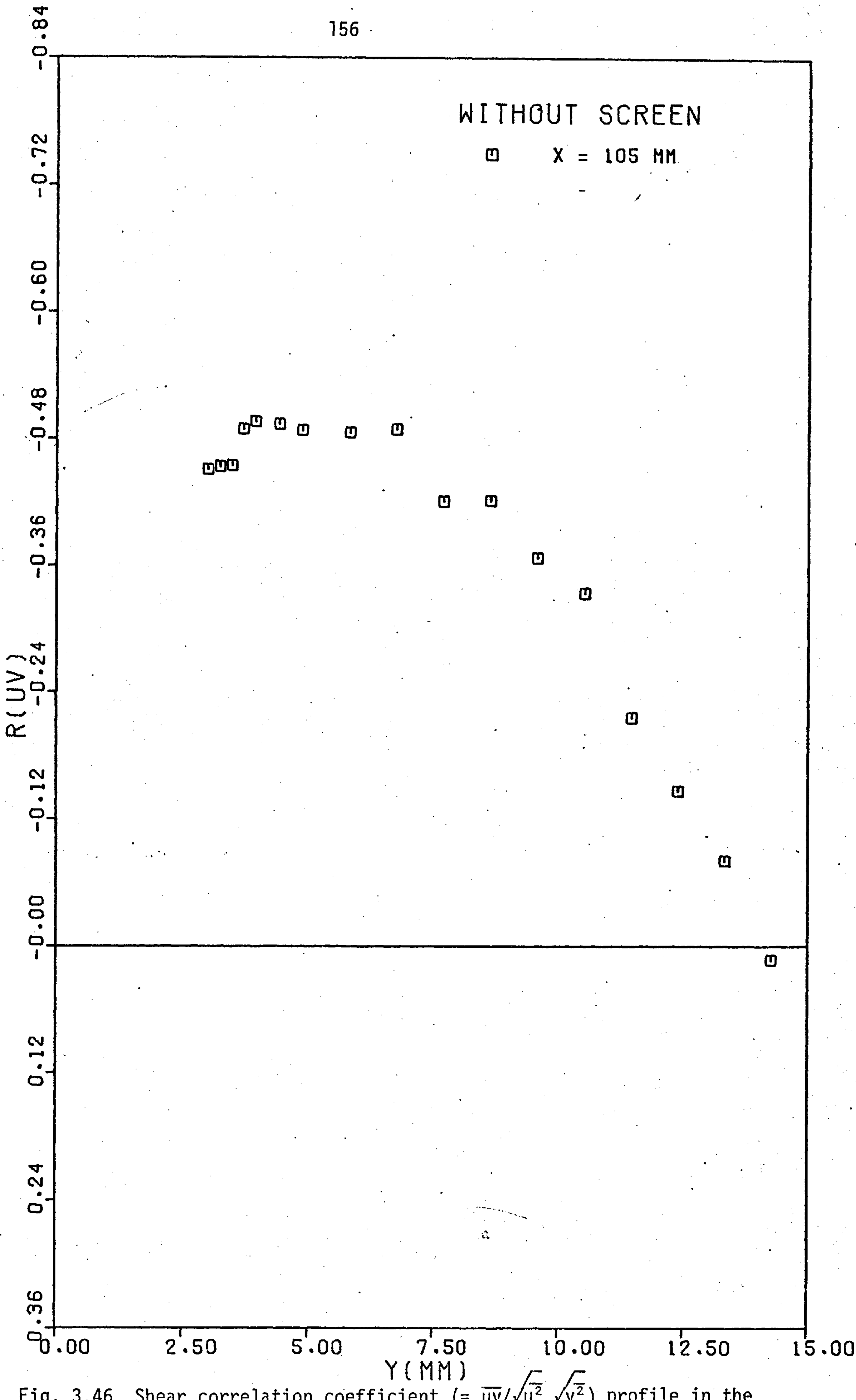

Fig. 3.46 Shear correlation coefficient (= $\overline{uv}/\sqrt{\overline{u^2}}\ \sqrt{\overline{v^2}}$) profile in the undisturbed boundary layer.

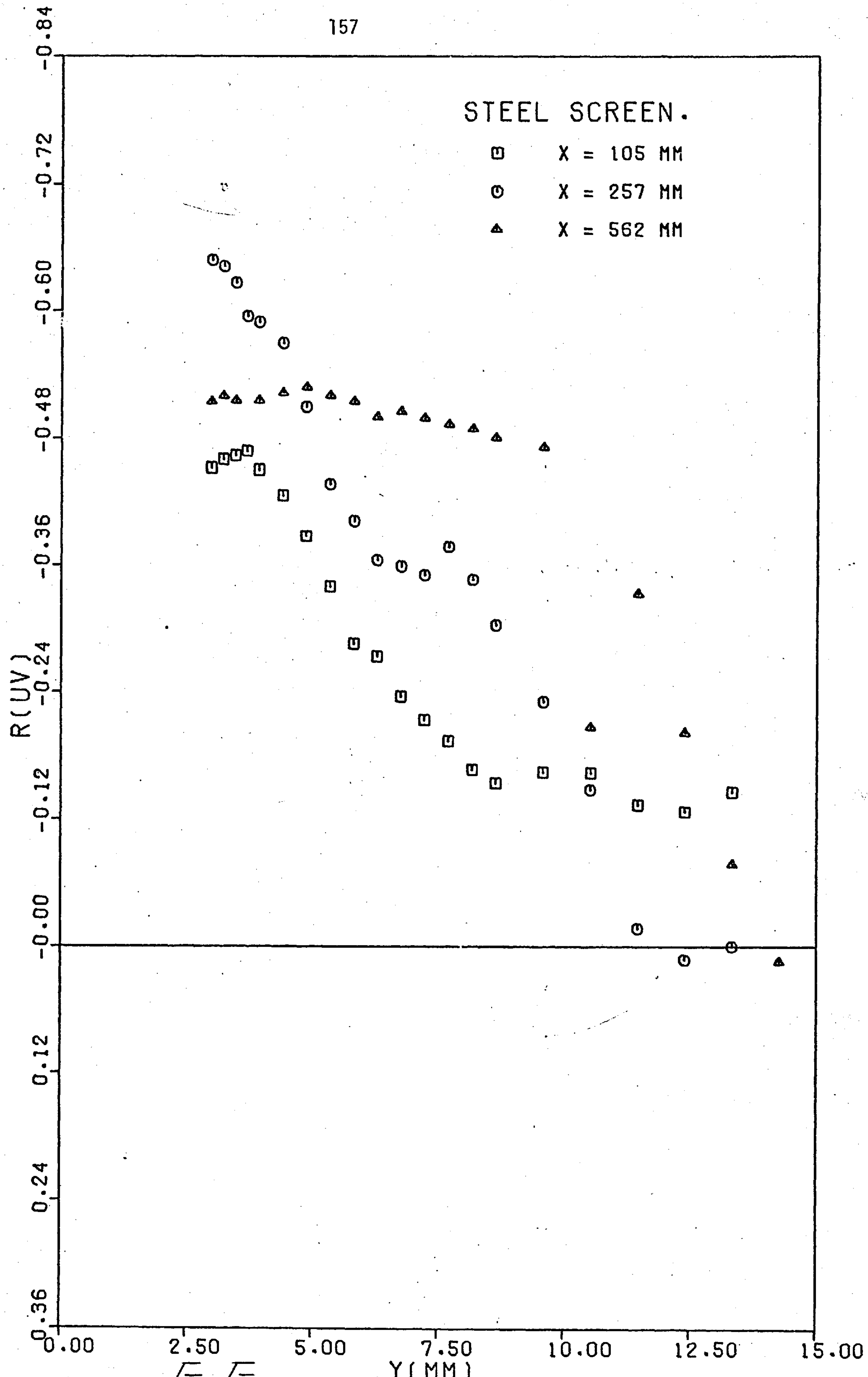

Fig. 3.47 $\overline{uv}/\sqrt{\overline{u^2}}\sqrt{\overline{v^2}}$ profiles downstream of the steel screen.

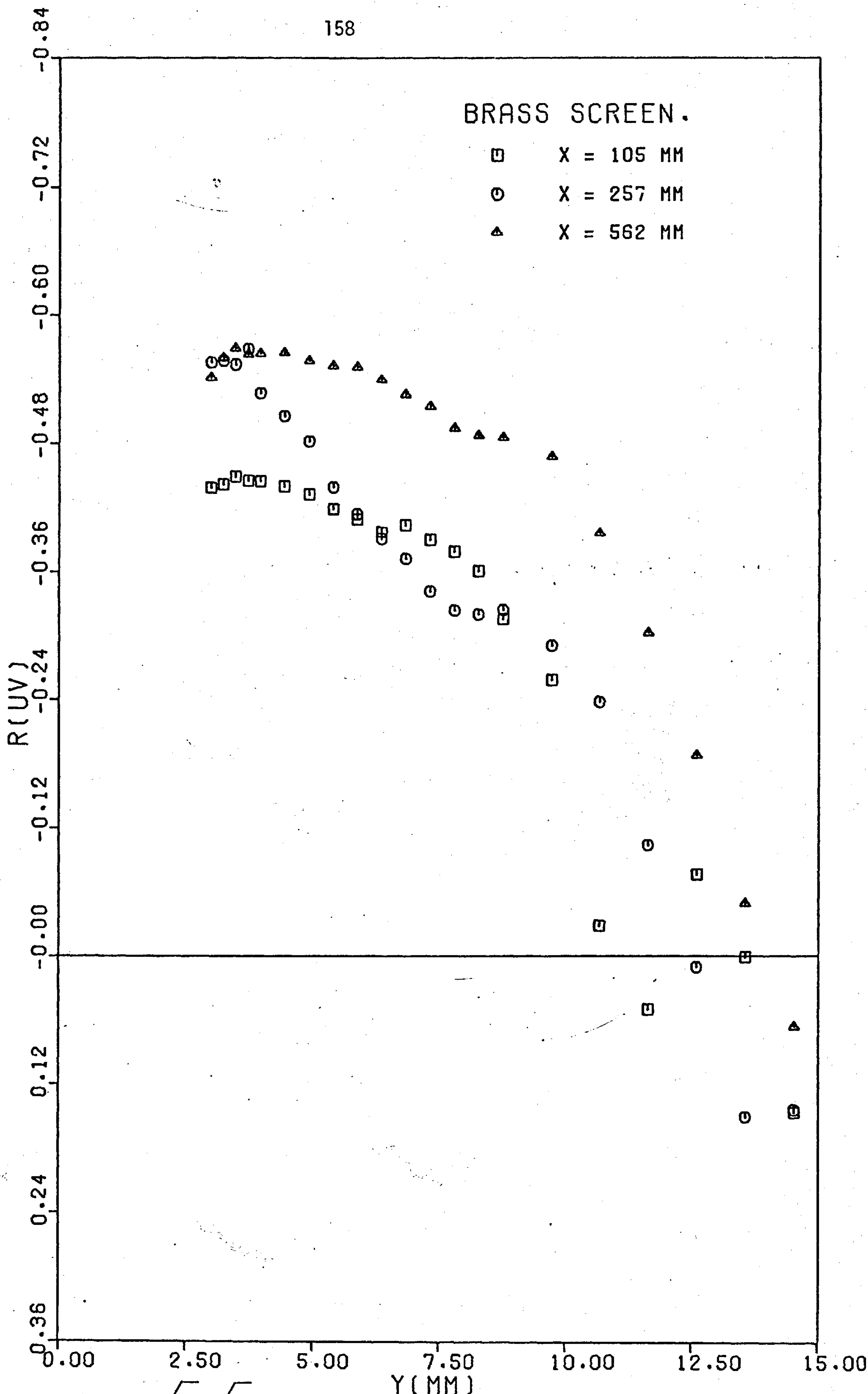

Fig. 3.48 $\overline{uv}/\sqrt{\overline{u^2}}\sqrt{\overline{v^2}}$ profiles downstream of the brass screen.

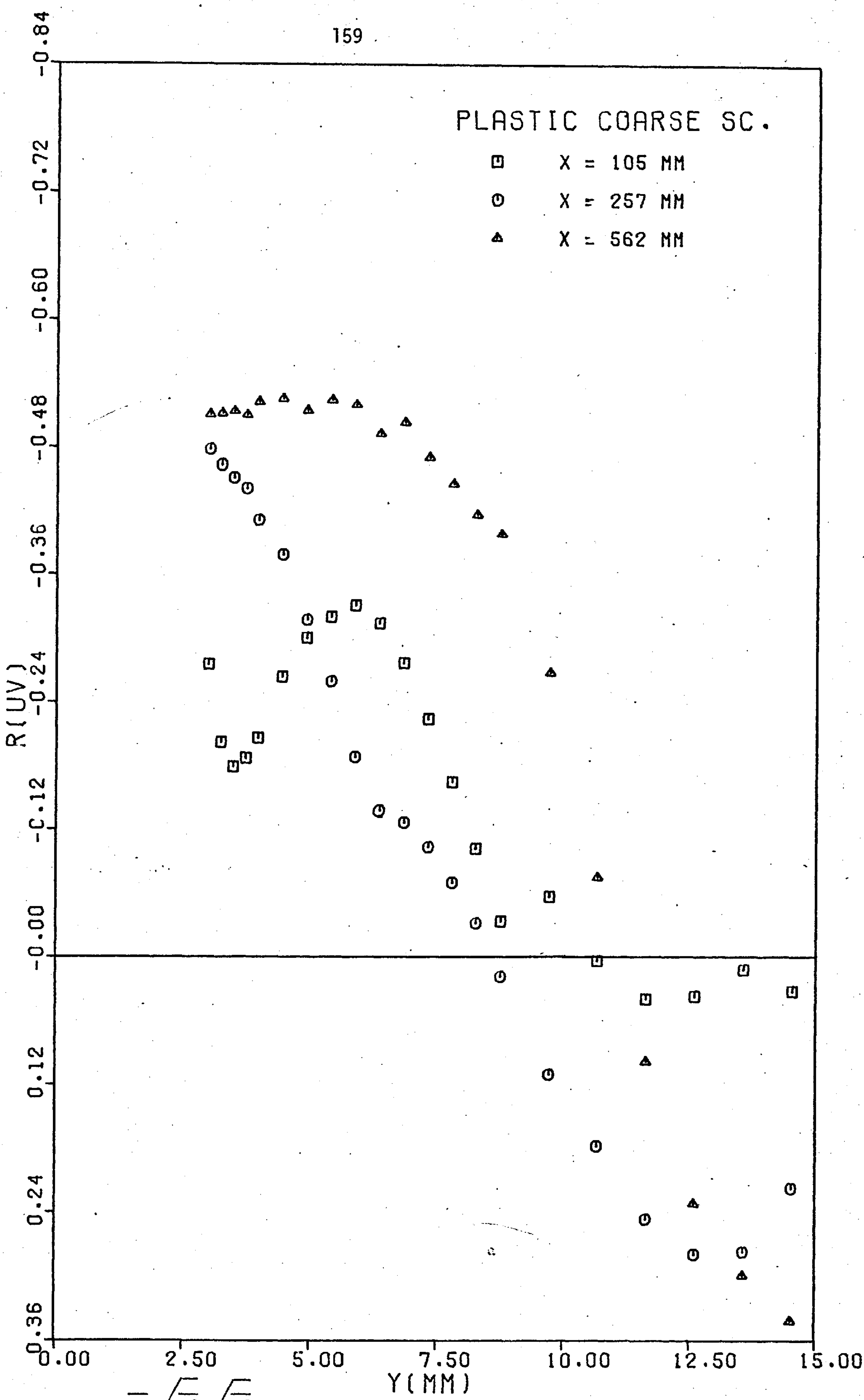

Fig. 3.49 $\overline{uv}/\sqrt{\overline{u^2}}\,\sqrt{\overline{v^2}}$ profiles downstream of the plastic coarse screen.

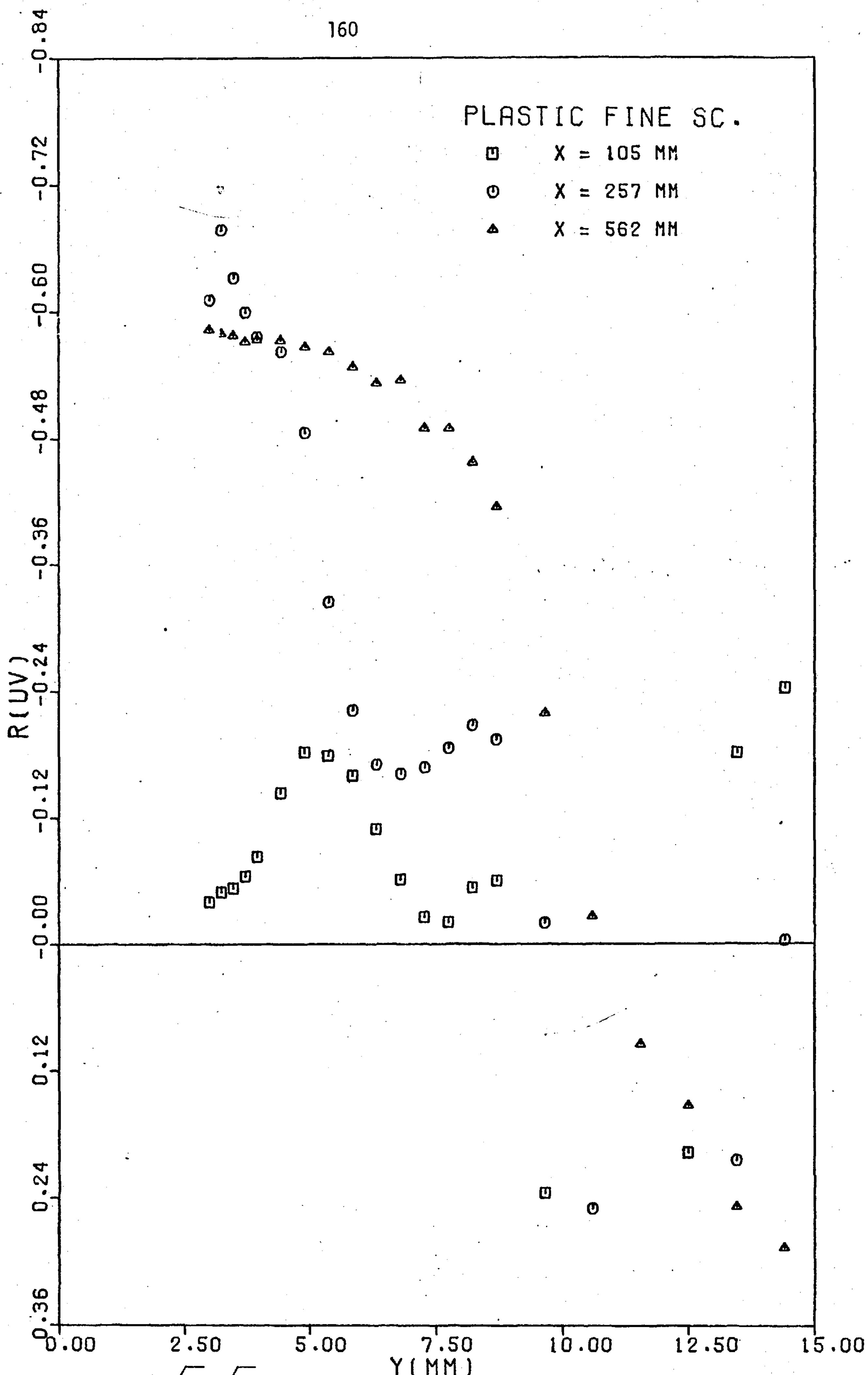

Fig. 3.50 $\overline{uv}/\sqrt{\overline{u^2}}\sqrt{\overline{v^2}}$ profiles downstream of the plastic fine screen.

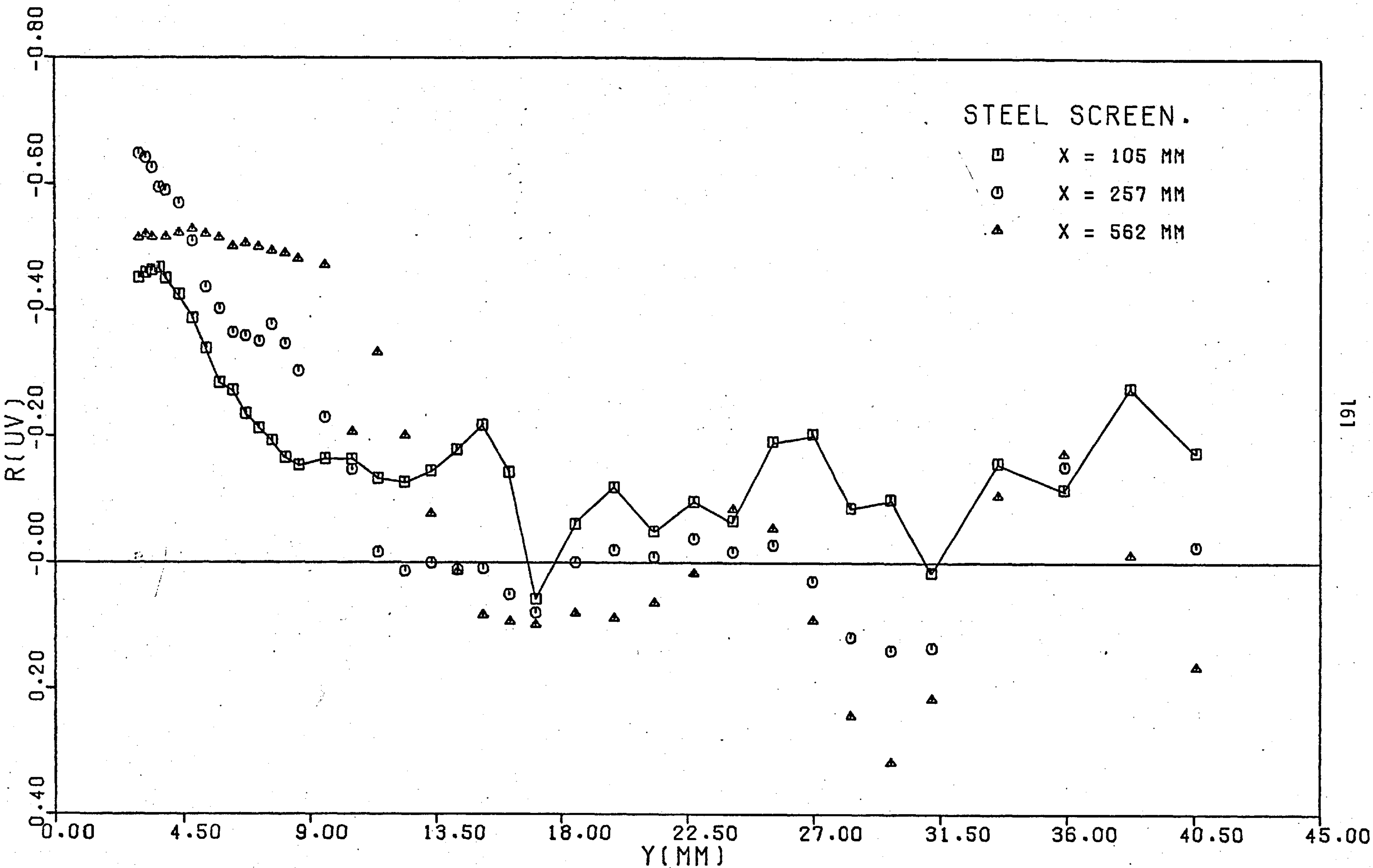

Fig. 3.51 Extended R_{uv} profile downstream of the steel screen.

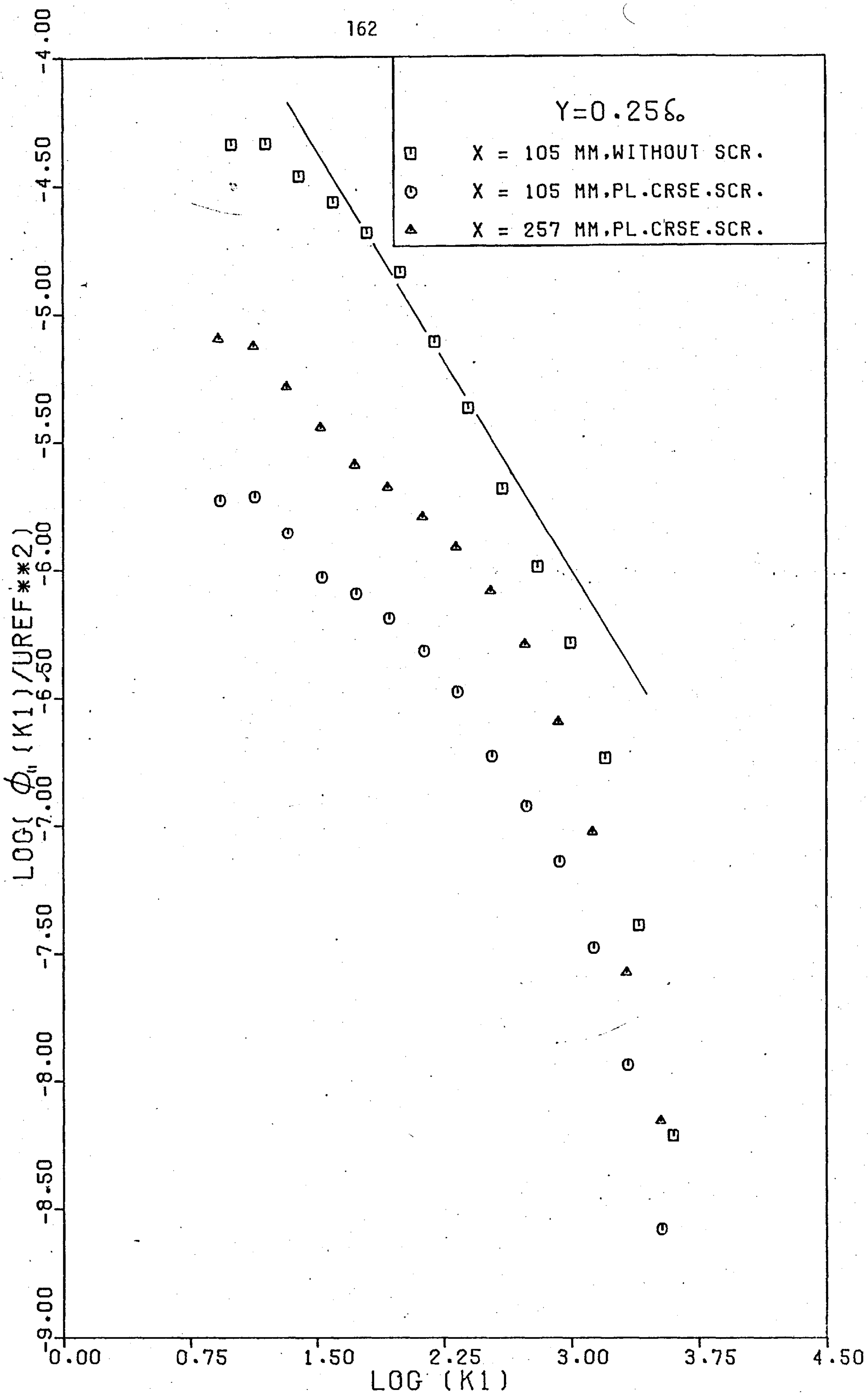

Fig. 3.52 ϕ_{11} spectra at y = 0.25 δ . (δ_0 is the undisturbed boundary layer thickness at x = 105 mm).

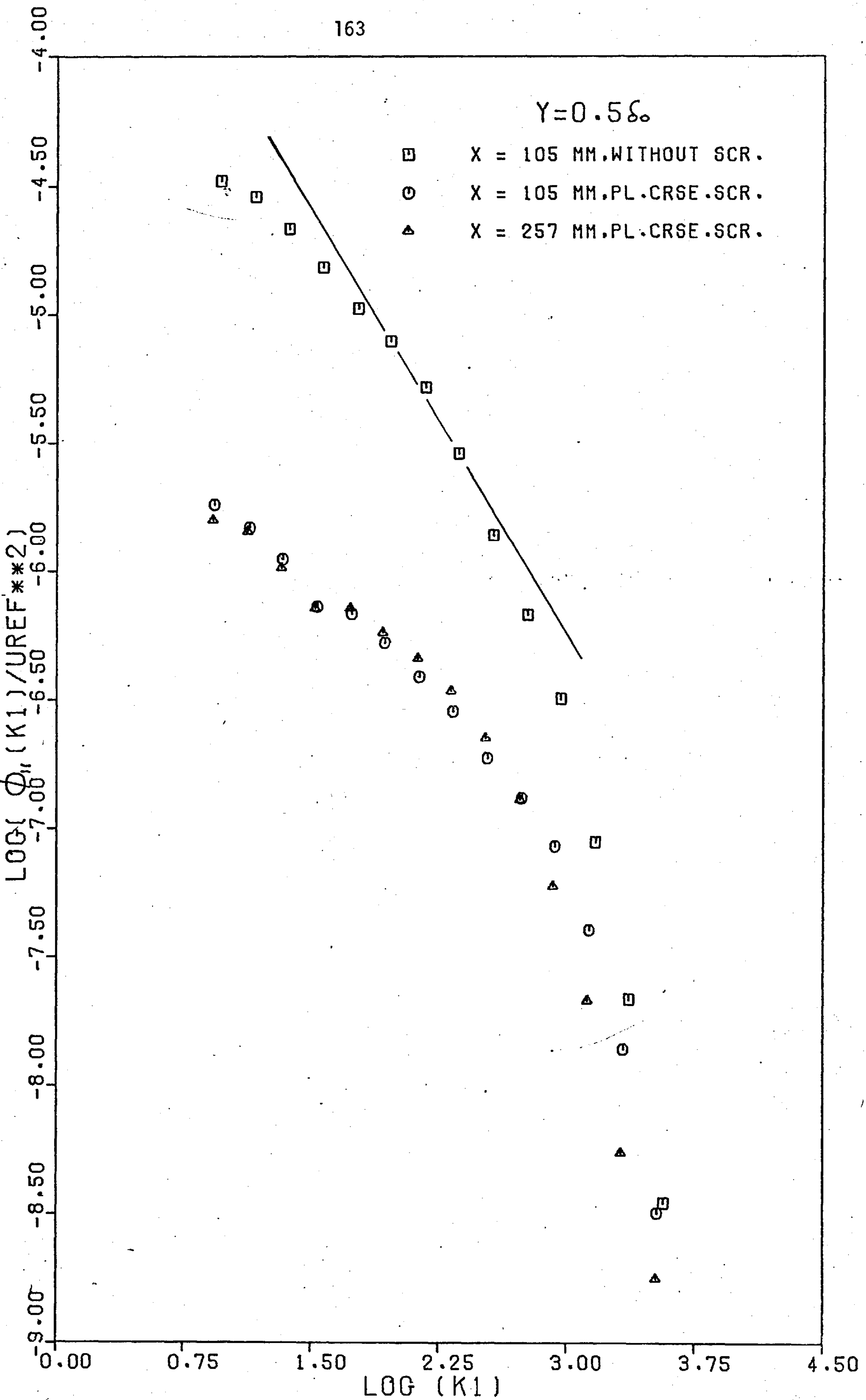

Fig. 3.53 ϕ_{11} spectra at $y = 0.50\ \delta_0$

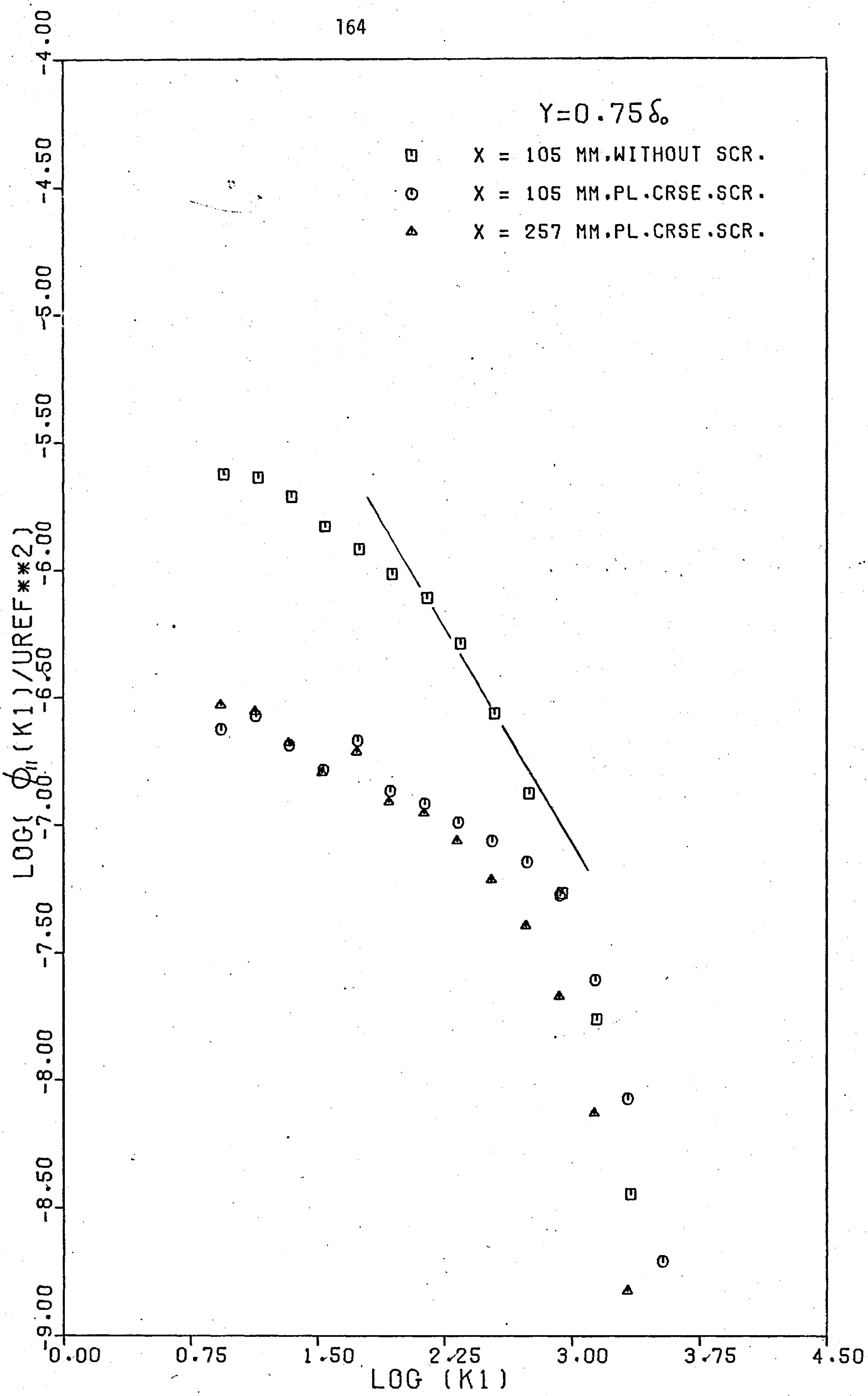

Fig. 3.54 ϕ_{11} spectra at $y = 0.75\ \delta_0$

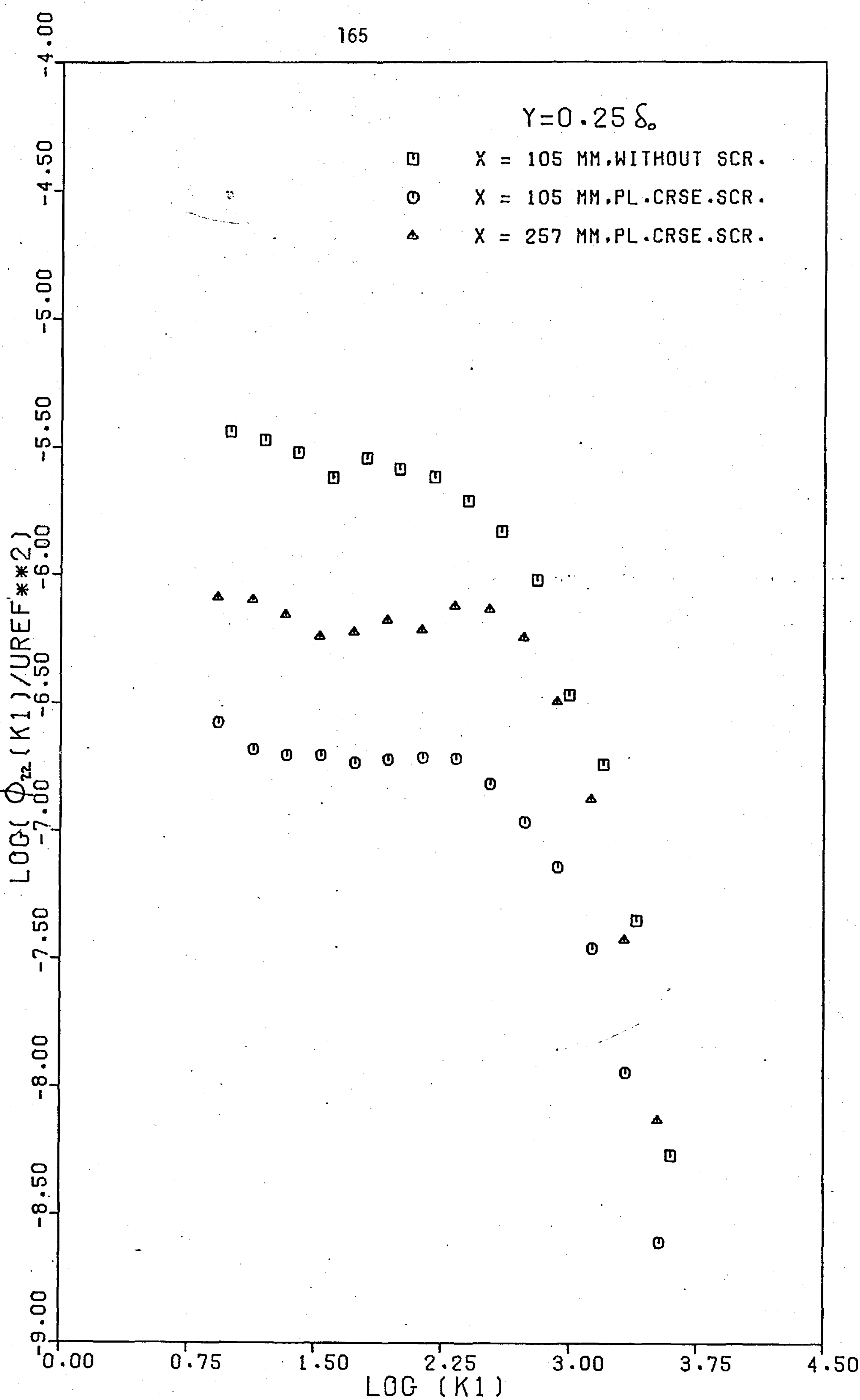

Fig. 3.55 ϕ_{22} spectra at $y = 0.25\ \delta_0$

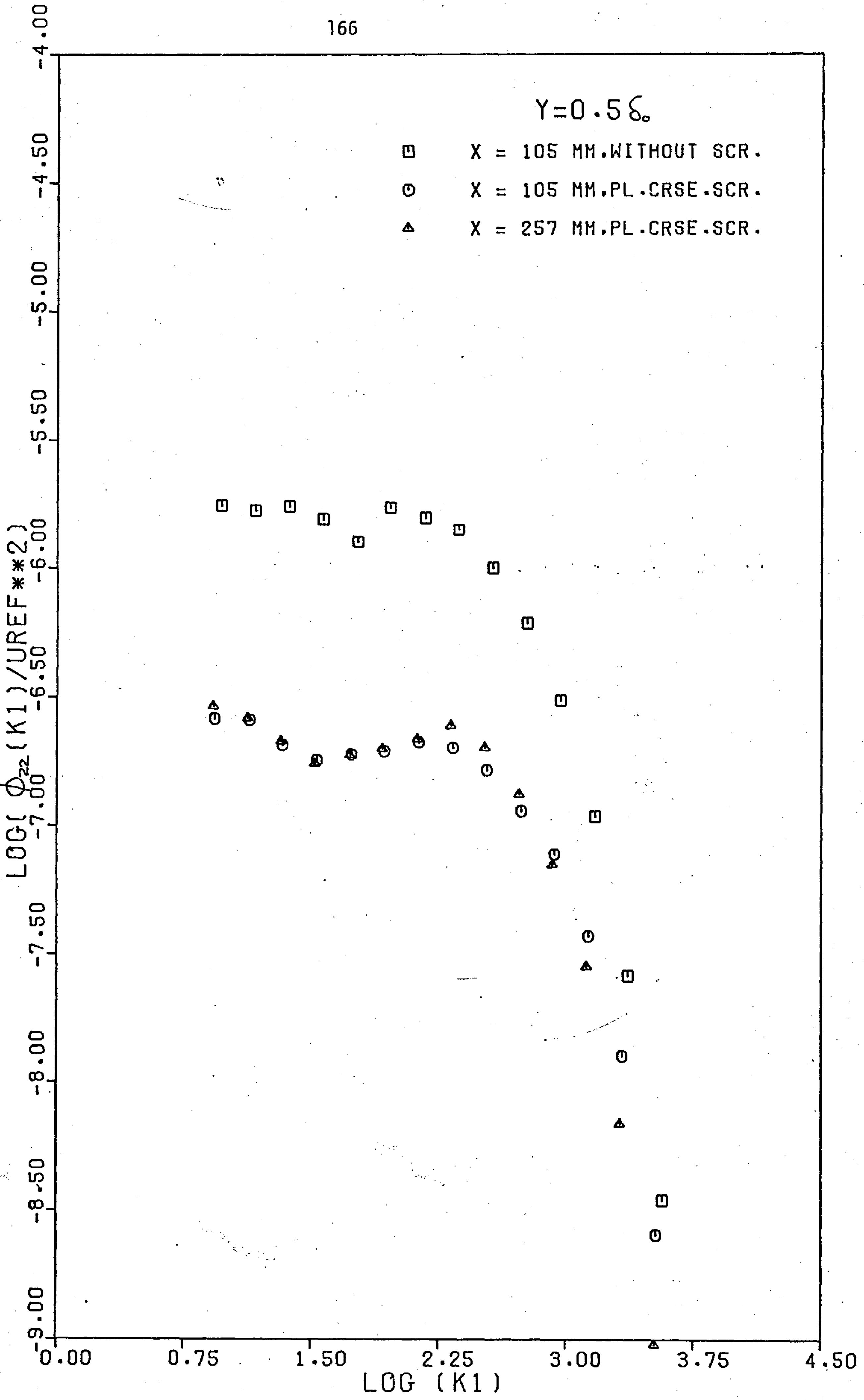

Fig. 3.56 ϕ_{22} spectra at $y = 0.50\ \delta_0$

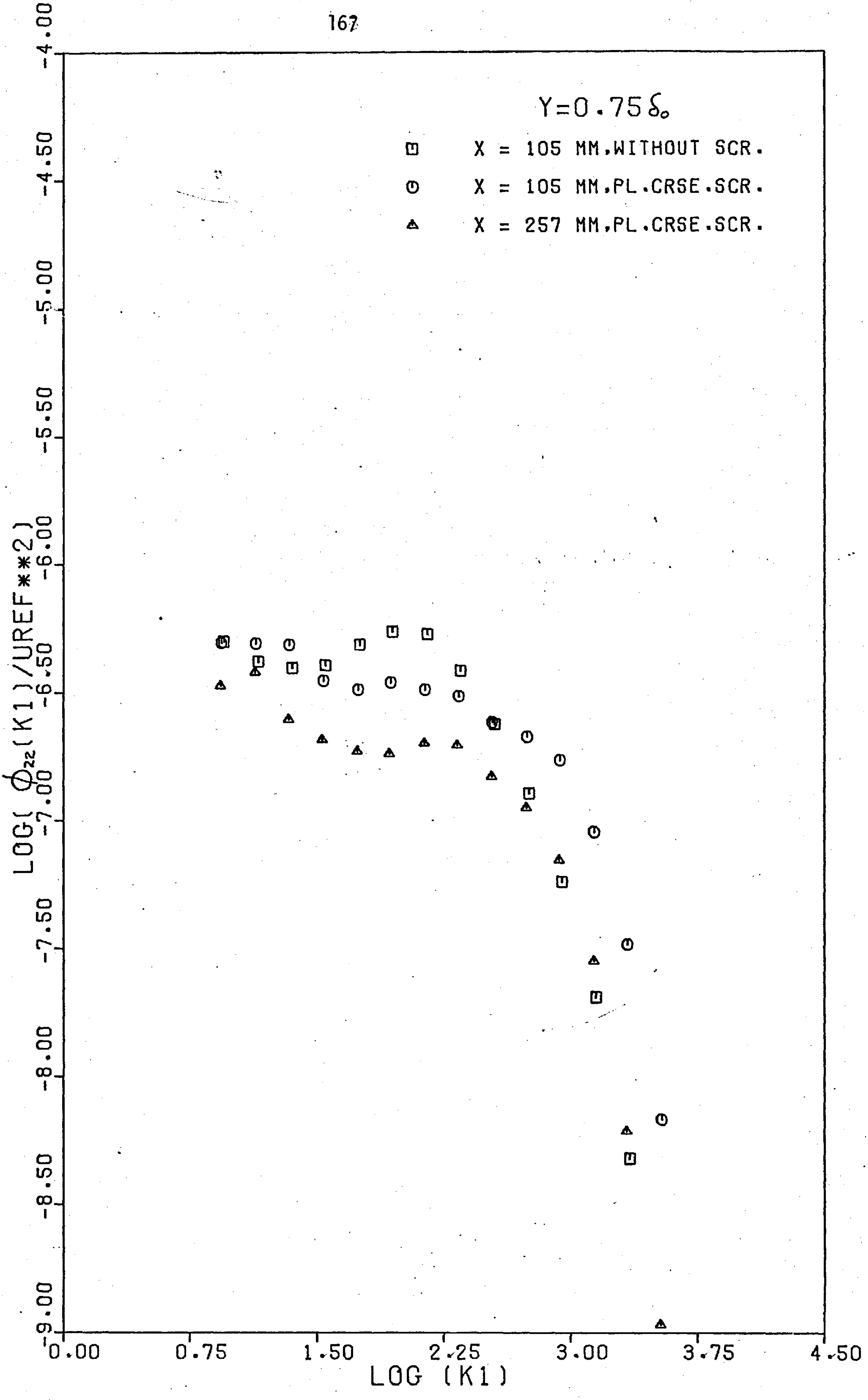

Fig. 3.57 ϕ_{22} spectra at $y = 0.75\ \delta_0$

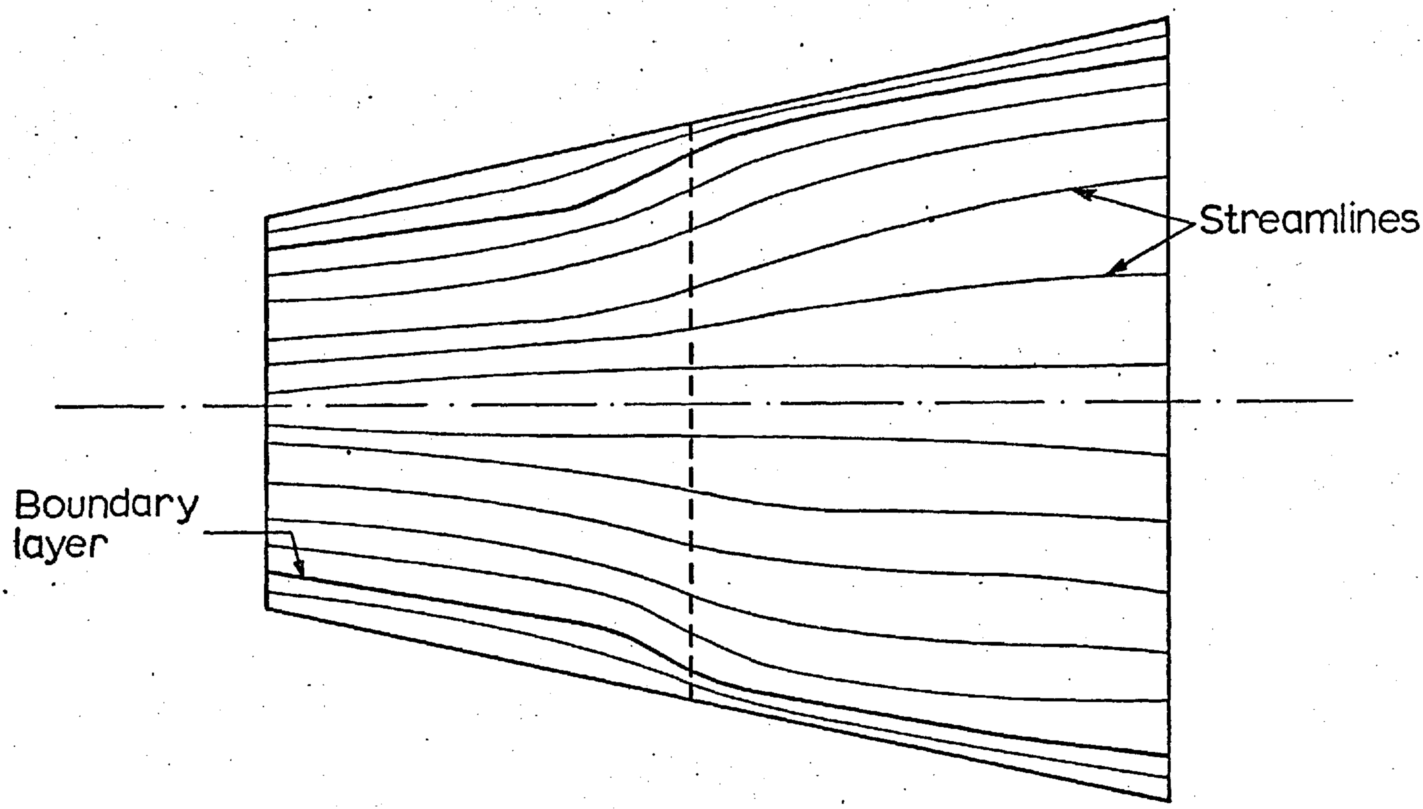

Fig. 3.58 Simplified case of flow through a plane screen in a wide-angle diffuser.

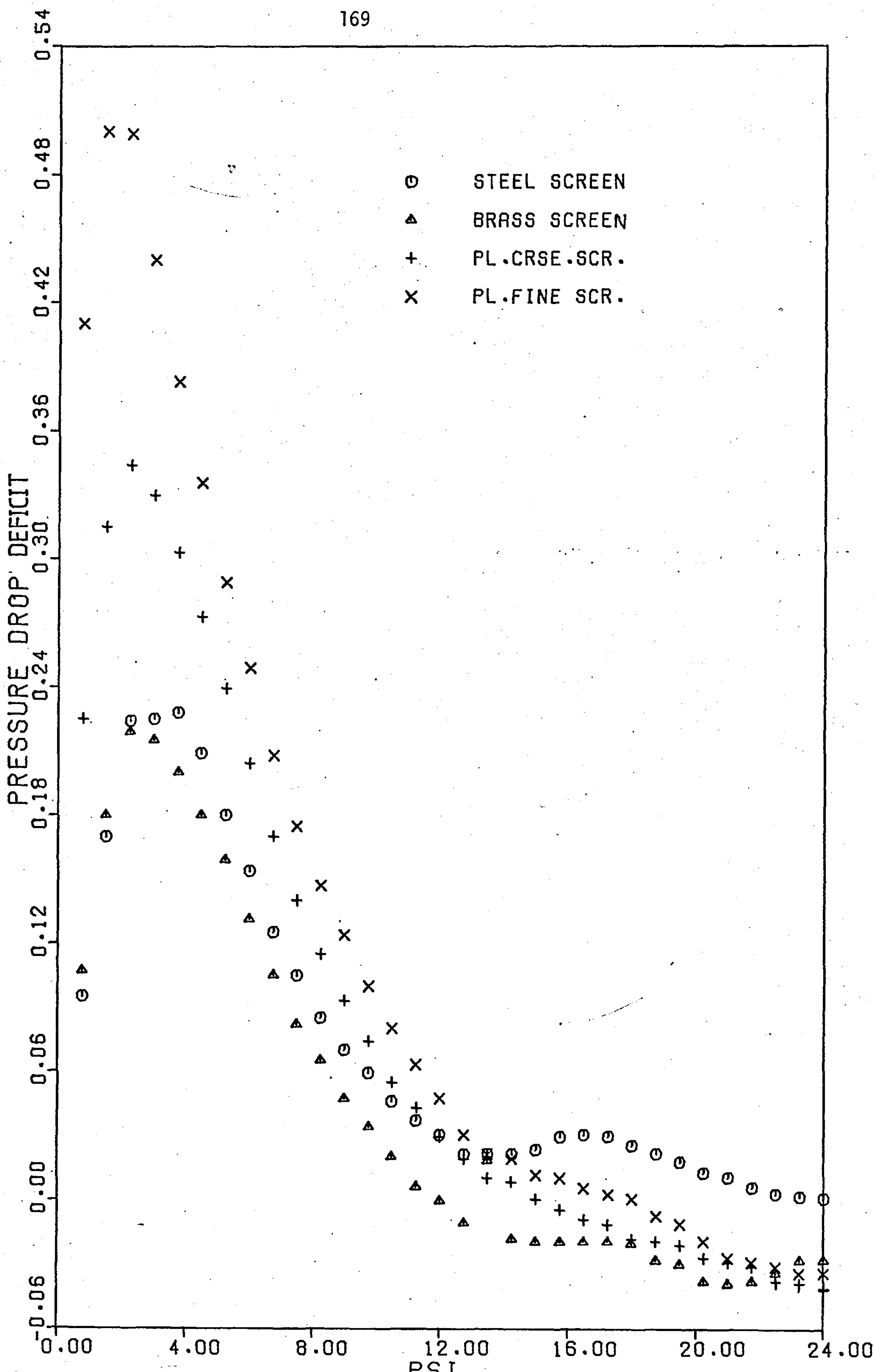

Fig. 3.59 Pressure-loss deficit $\left[\frac{(p_1 - p_2) - \Delta P}{\frac{1}{2}\rho U^2}\right]$ along streamlines.

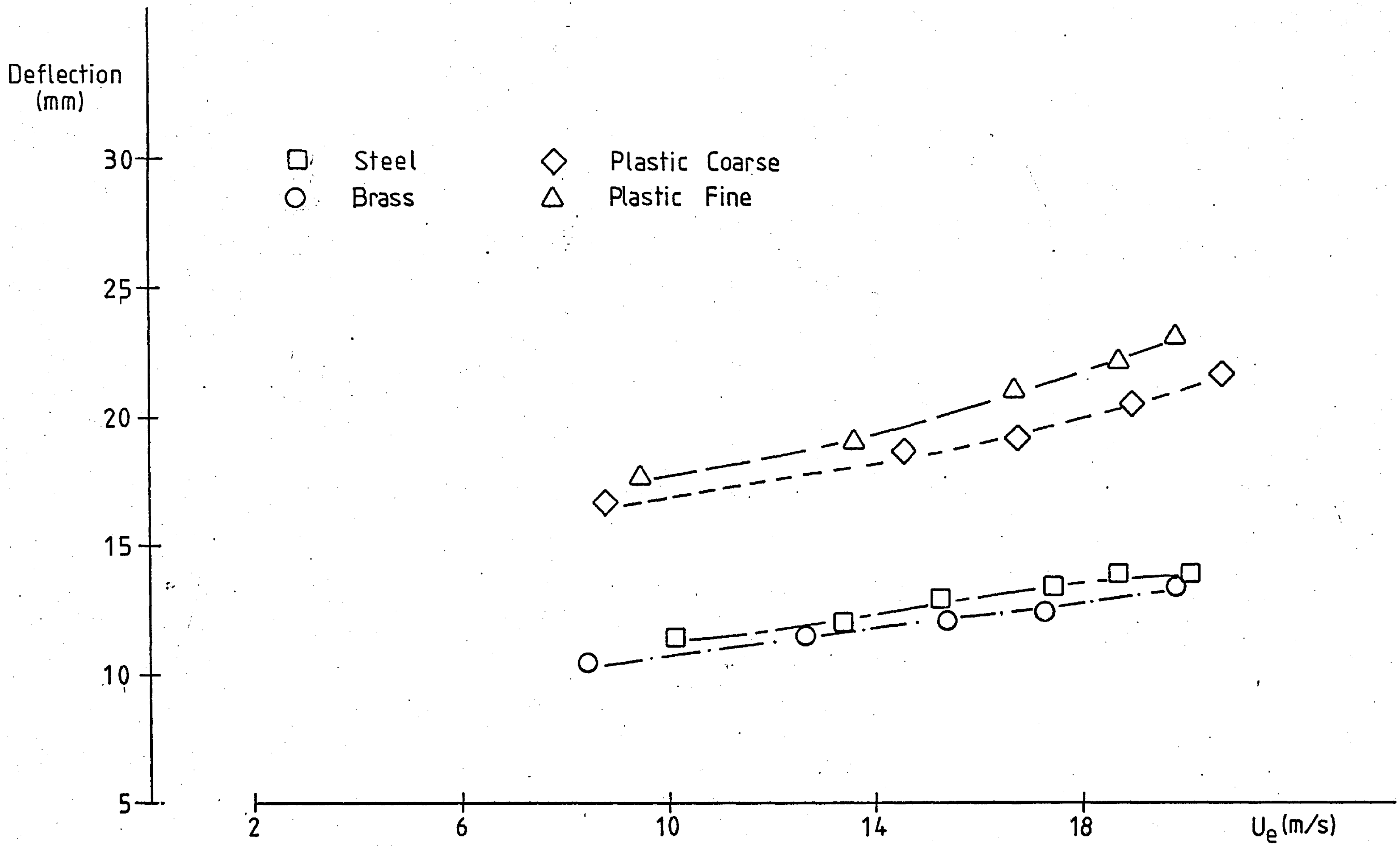

Fig. 3.60 Screen deflections with flow speed.

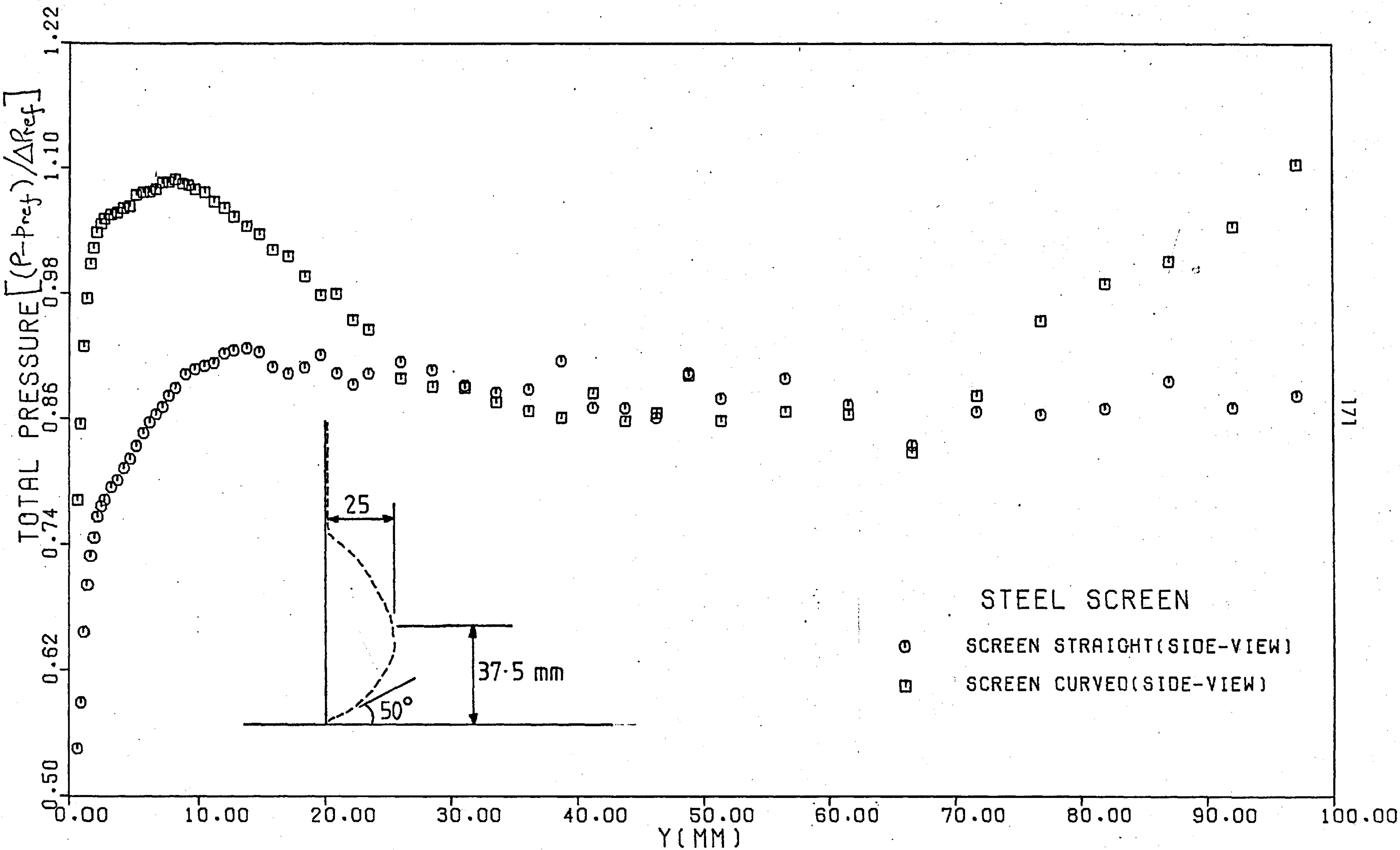

Fig. 3.61 Effect of screen curvature on total pressure profile at x = 50 mm.

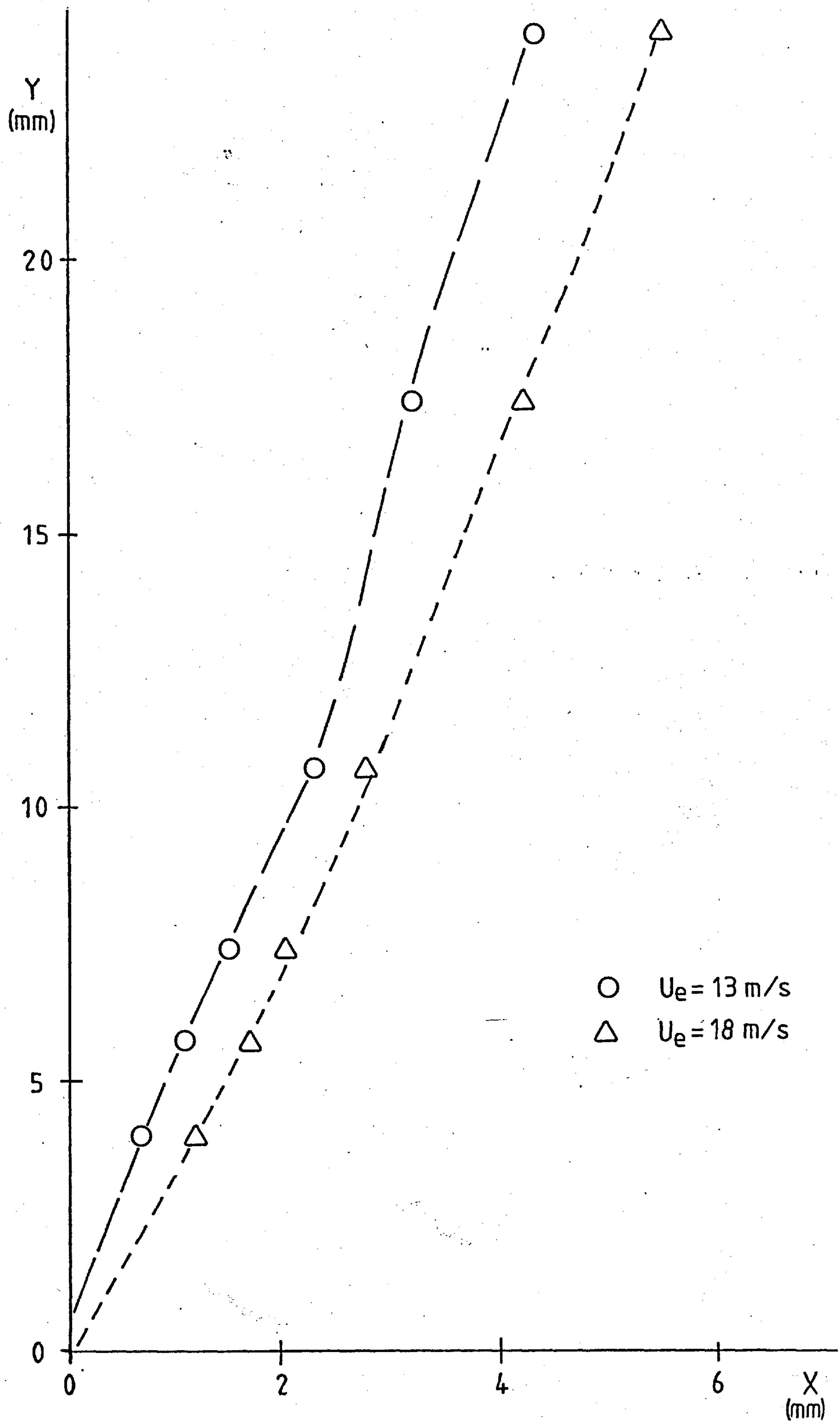

Fig. 3.62 Plastic fine screen shape at two free stream velocities.

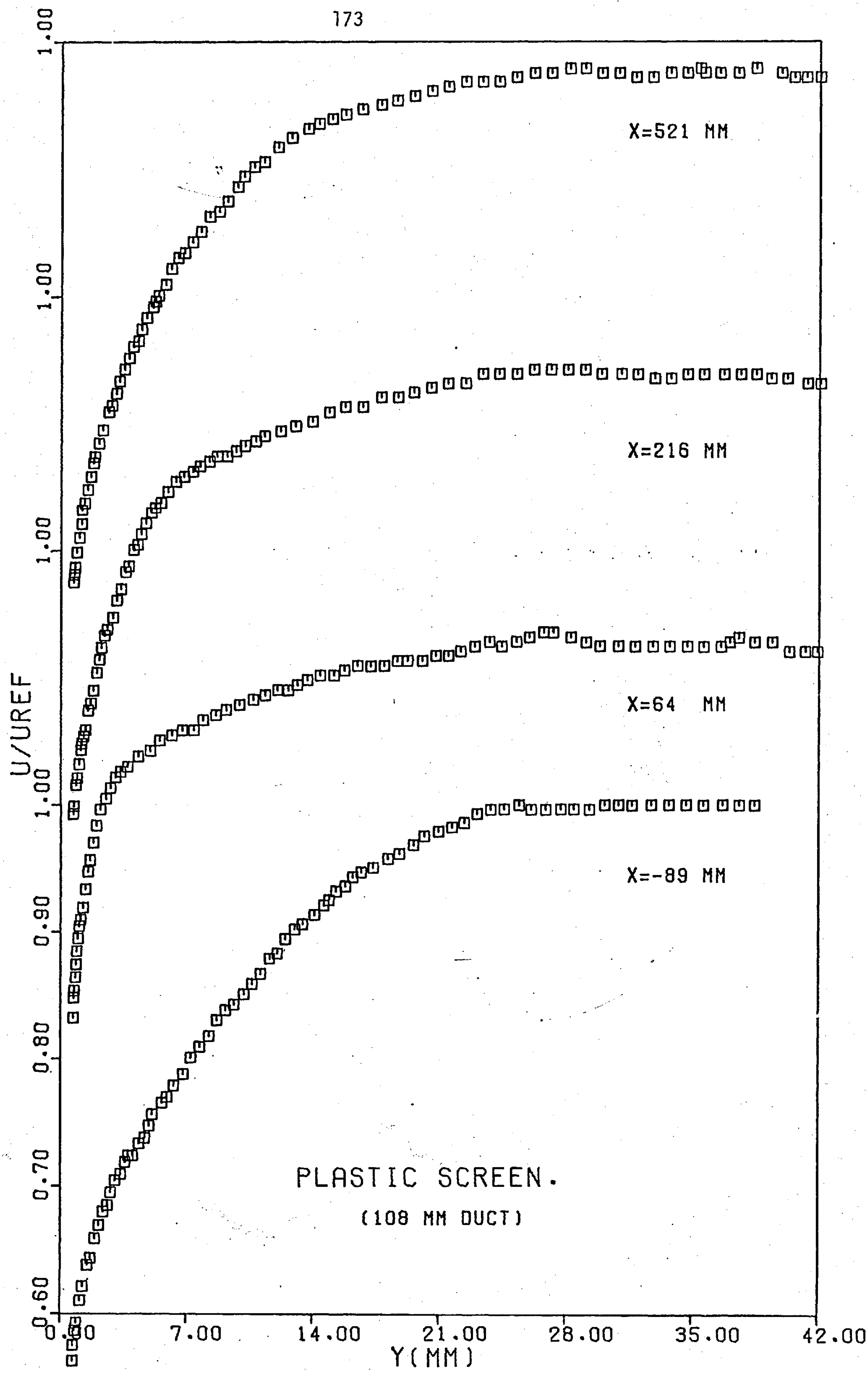

Fig. 3.63a Mean velocity profiles near the plastic screen in the 108 mm duct.

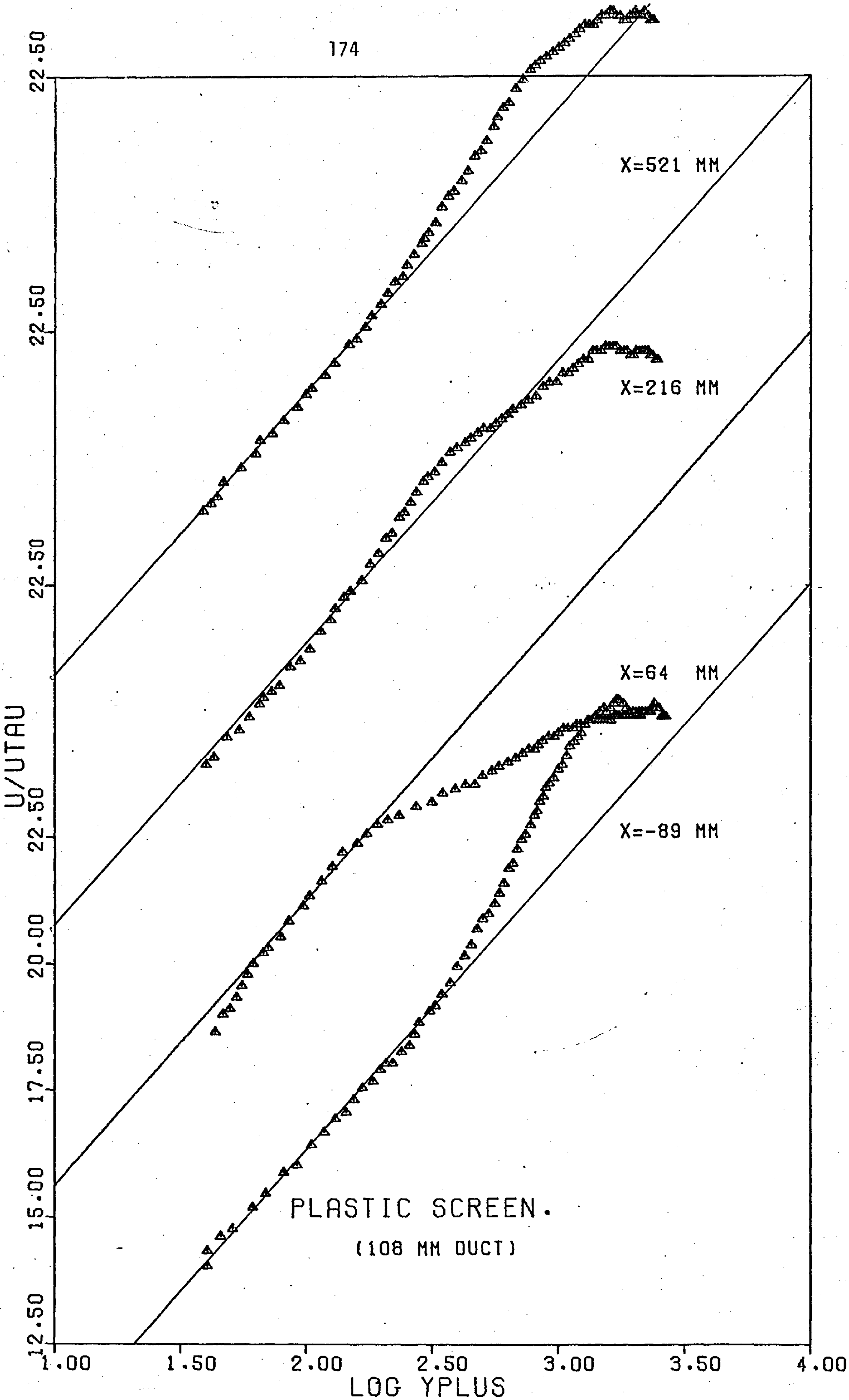

Fig. 3.63b Semi-log. profiles near the plastic screen.

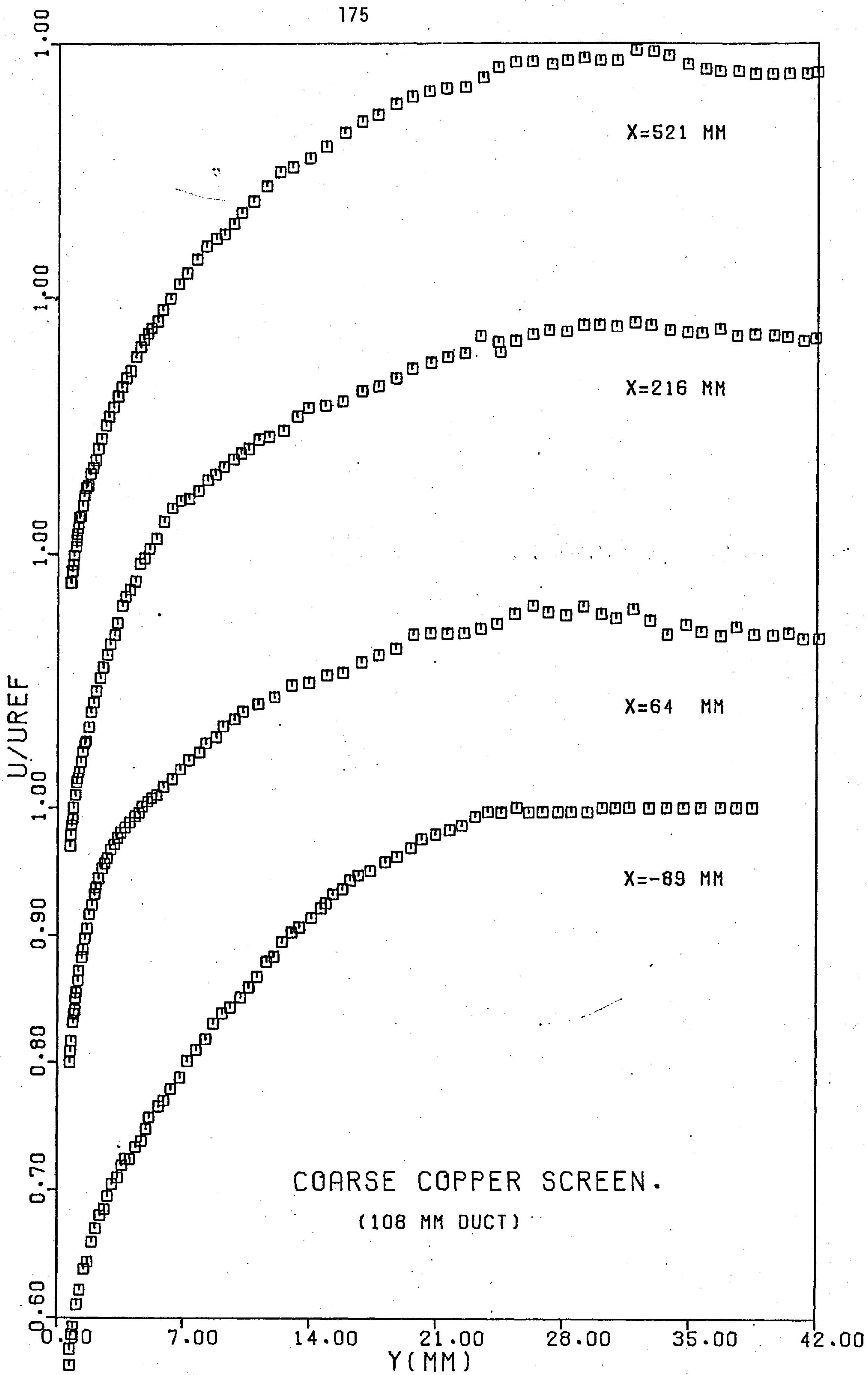

Fig. 3.64a Mean velocity profiles near the coarse copper screen.

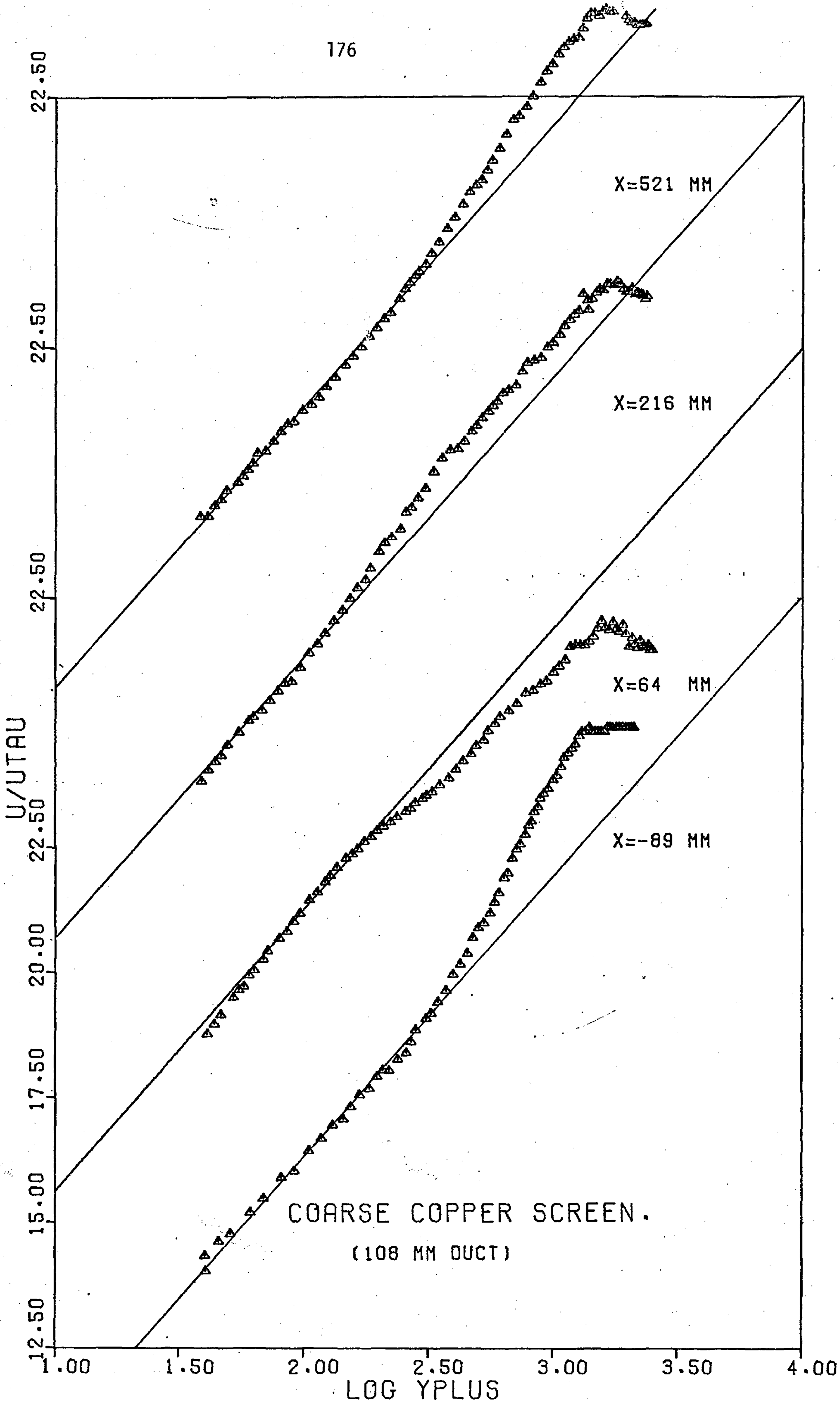

Fig. 3.64b Semi-log. profiles near the coarse copper screen.

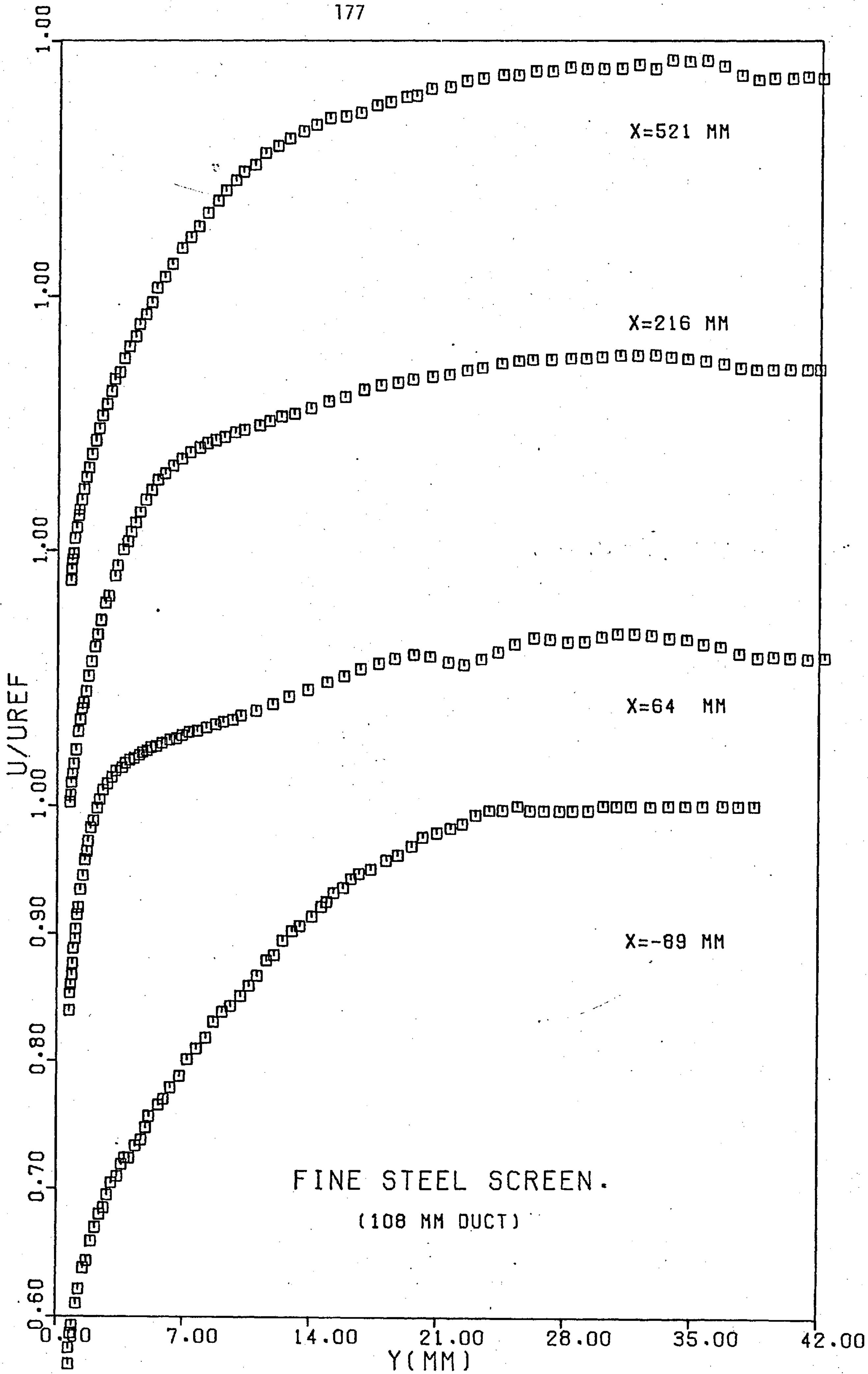

Fig. 3.65a Mean velocity profiles near the fine steel screen.

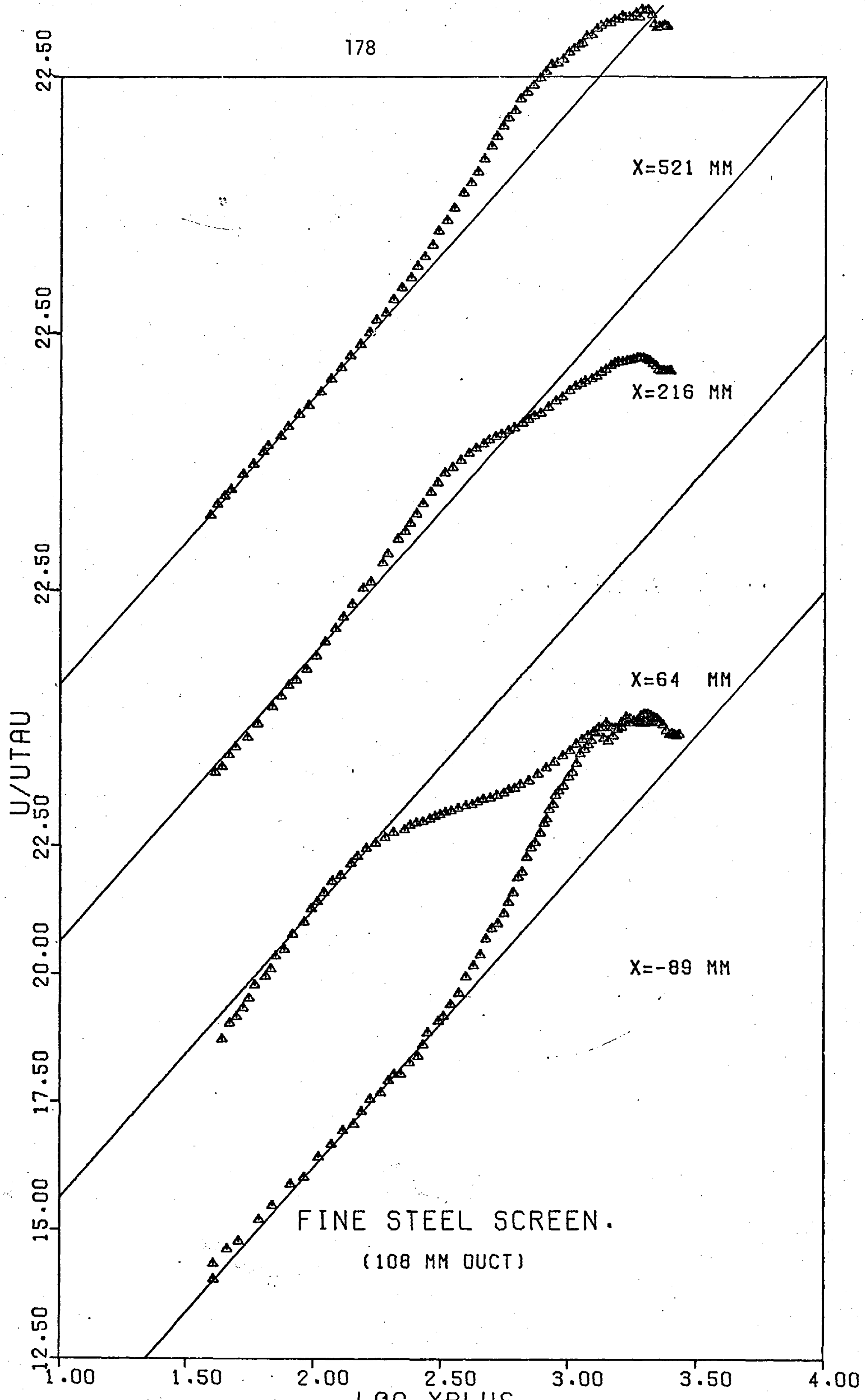

Fig. 3.65b Semi-log. profiles near the fine steel screen.

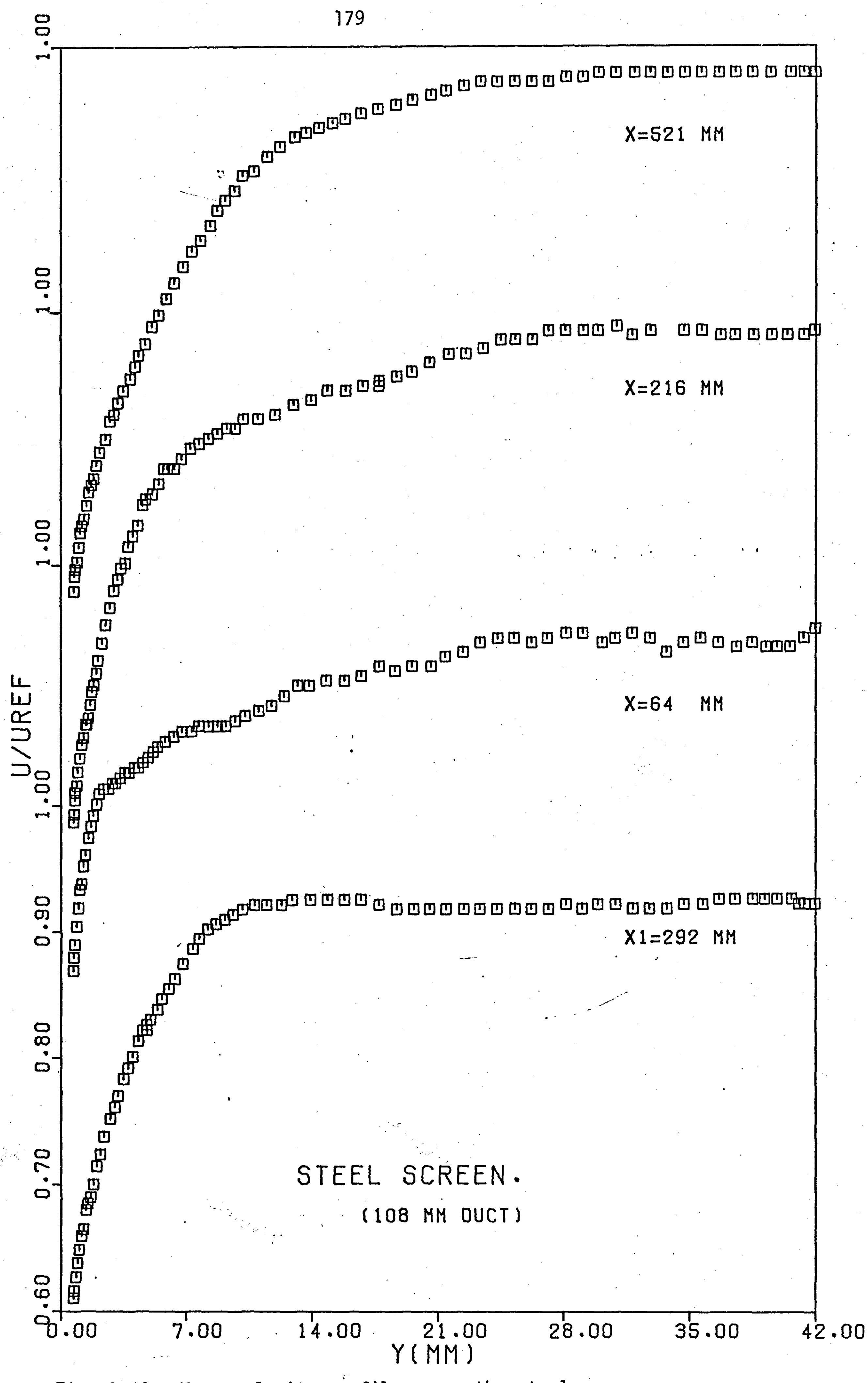

Fig. 3.66a Mean velocity profiles near the steel screen.

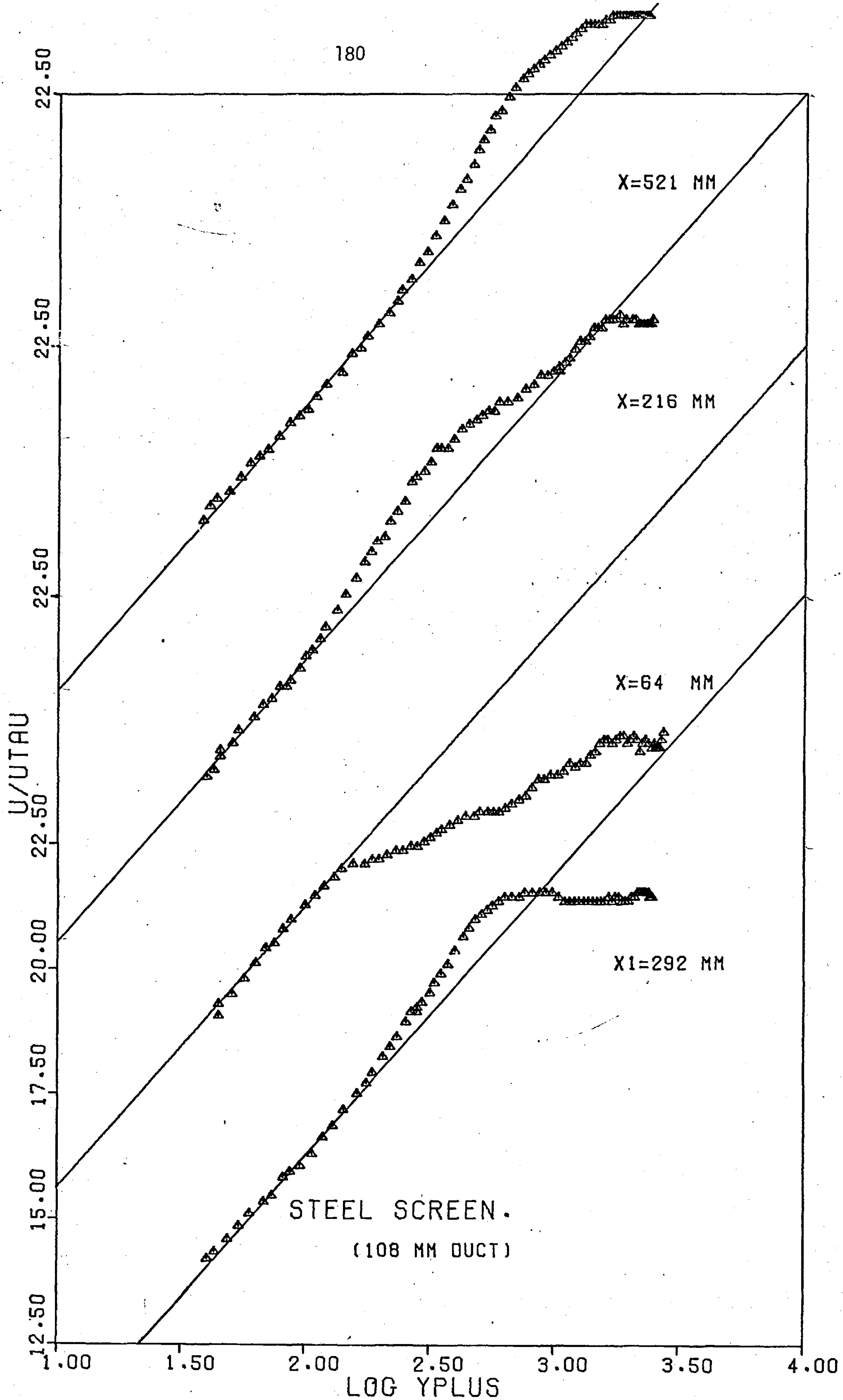

Fig. 3.66b Semi-log. profiles near the steel screen.

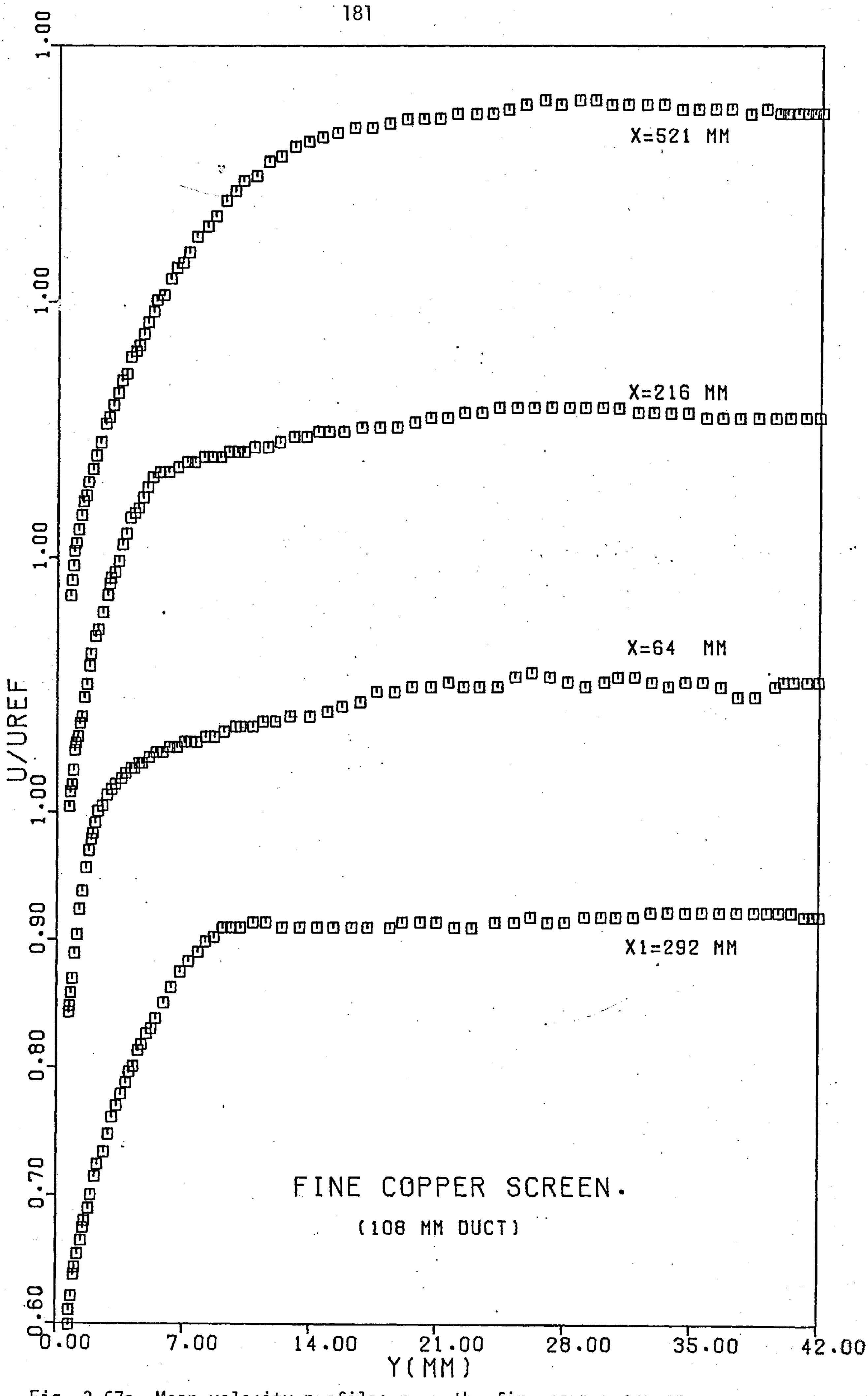

Fig. 3.67a Mean velocity profiles near the fine copper screen.

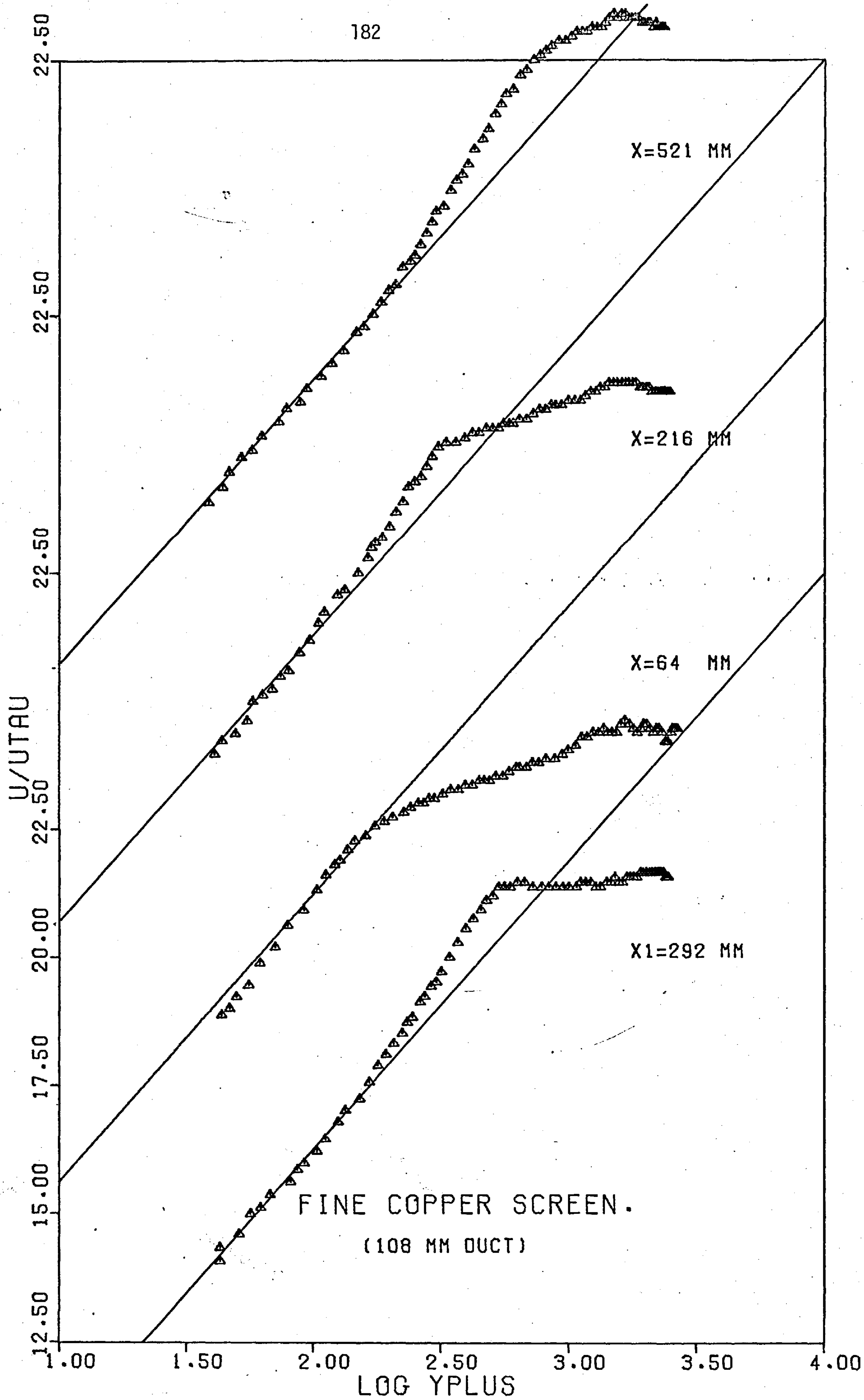

Fig. 3.67b Semi-log. profiles near the fine copper screen.

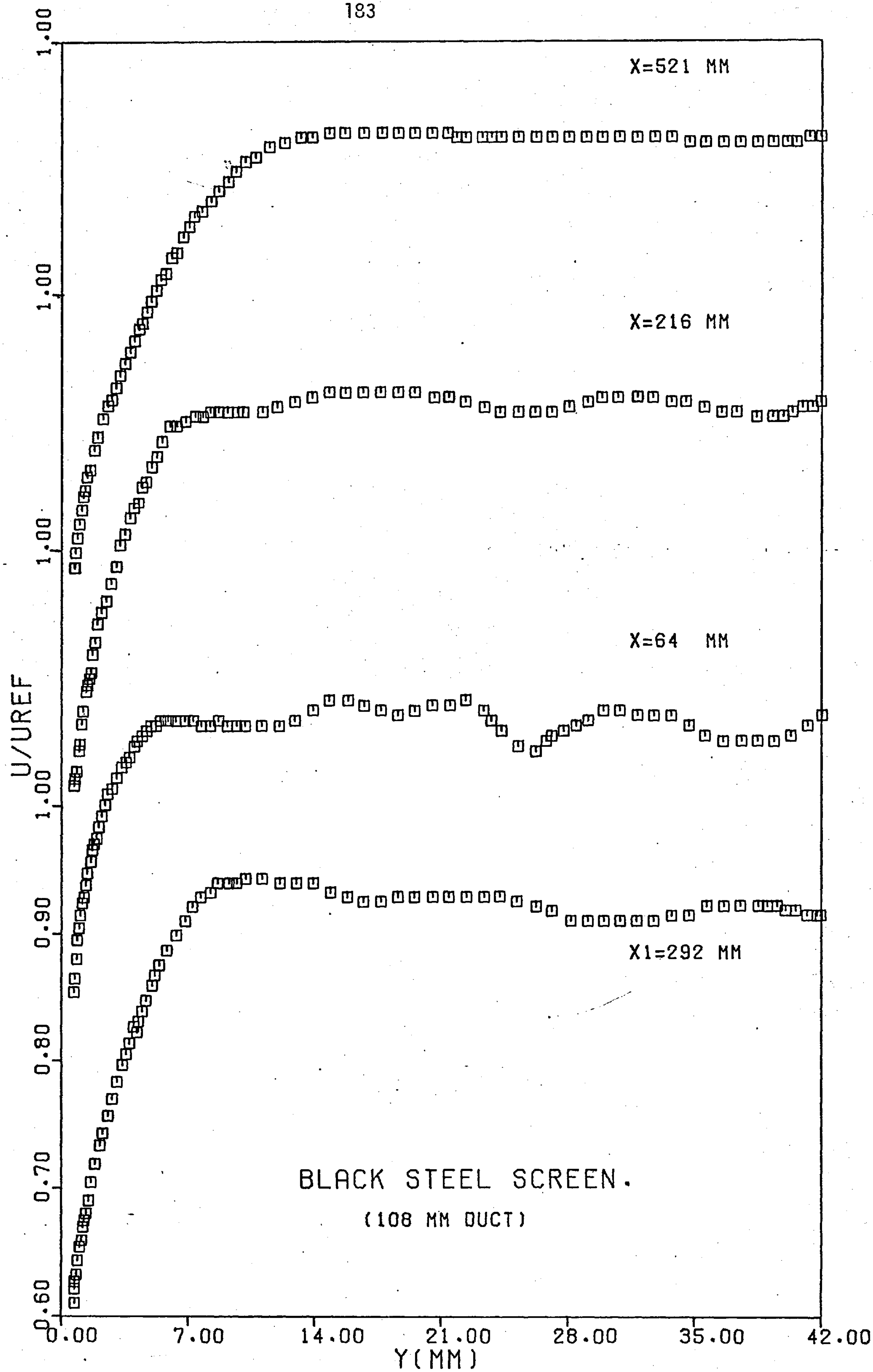

Fig. 3.68a Mean velocity profiles near the black steel screen.

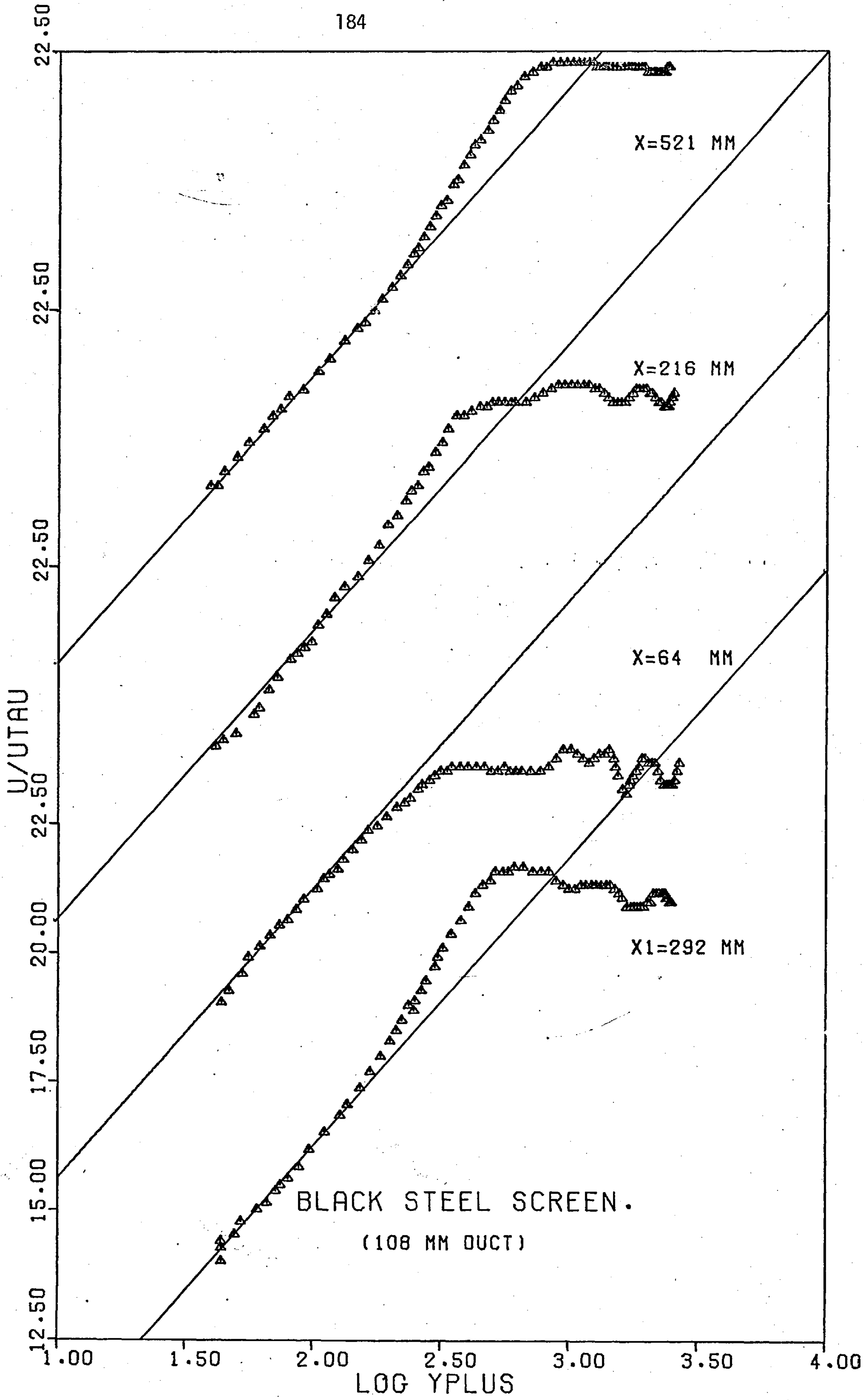

Fig. 3.68b Semi-log. profiles near the black steel screen.

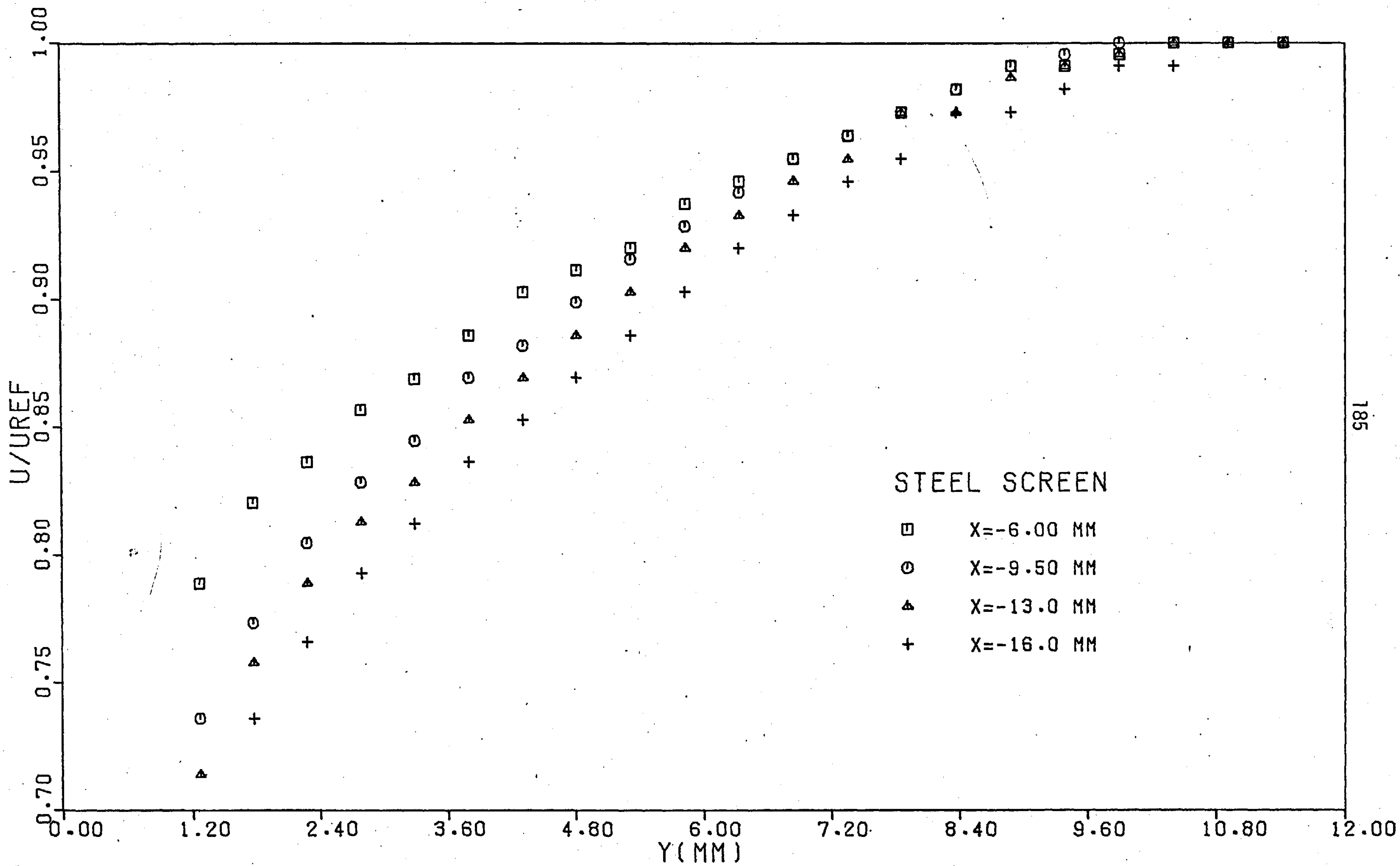

Fig. 3.69 Hot-wire mean velocity profiles upstream of the steel screen.

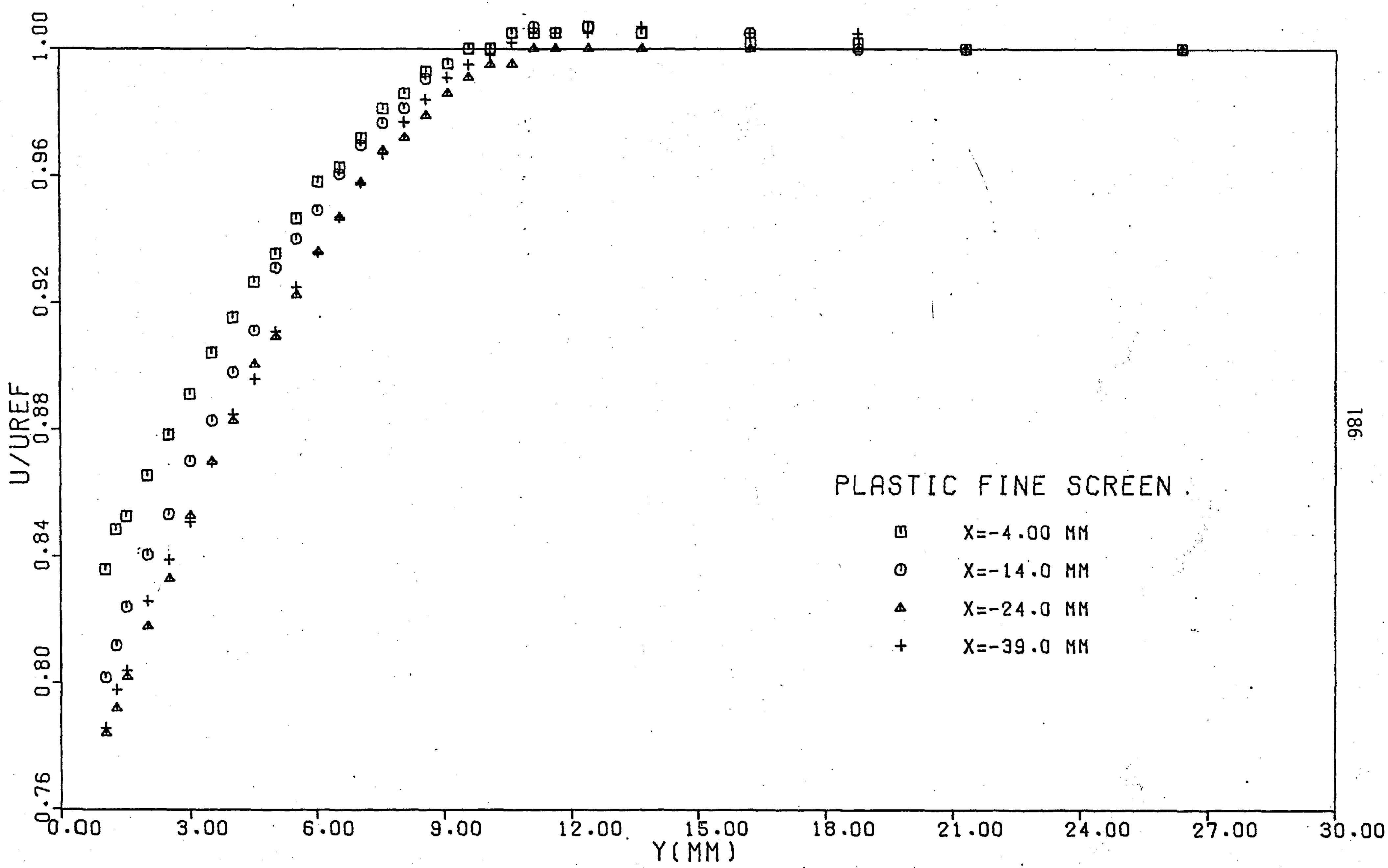

Fig. 3.70 Hot-wire mean velocity profiles upstream of the plastic fine screen.

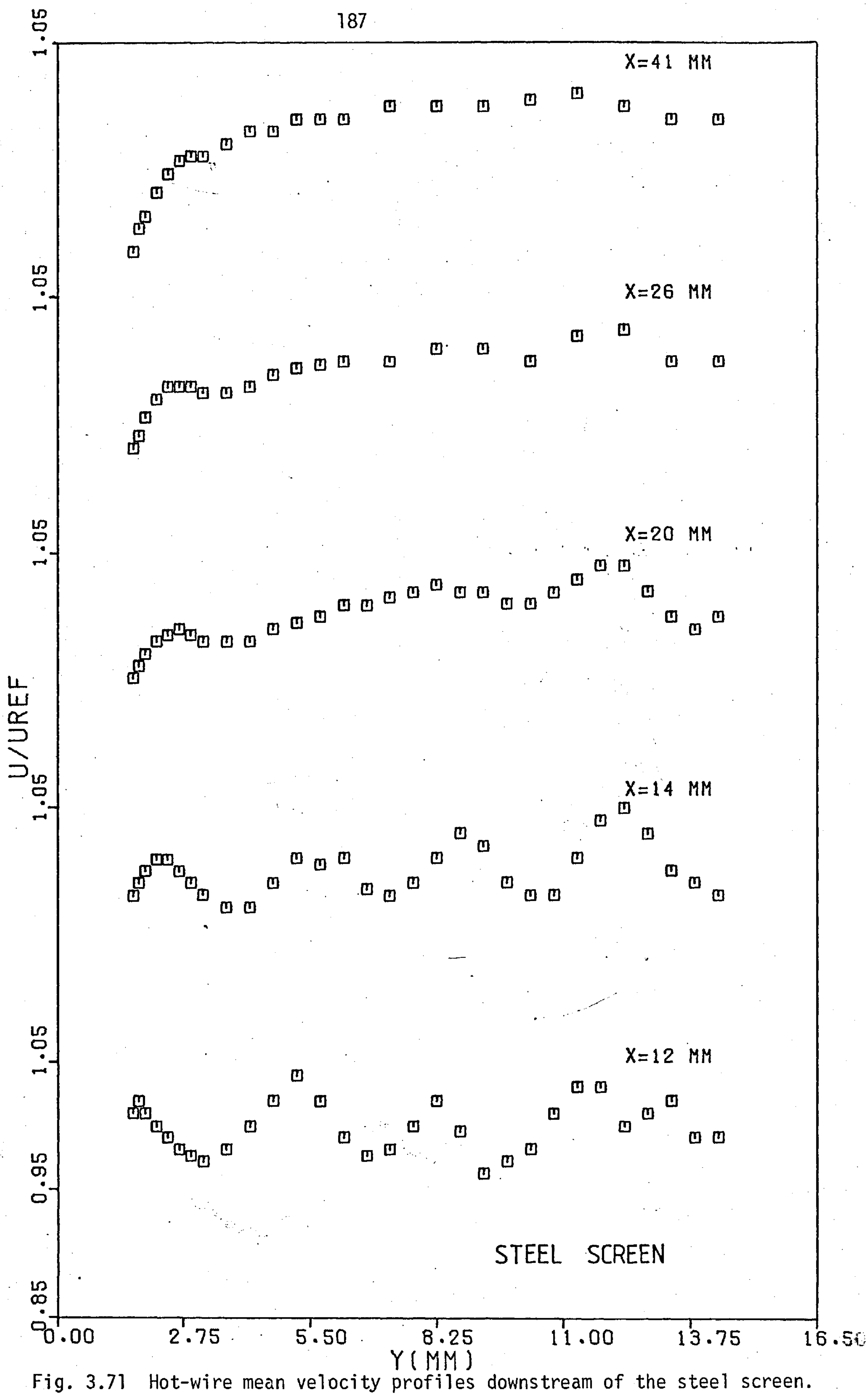

Fig. 3.71 Hot-wire mean velocity profiles downstream of the steel screen.

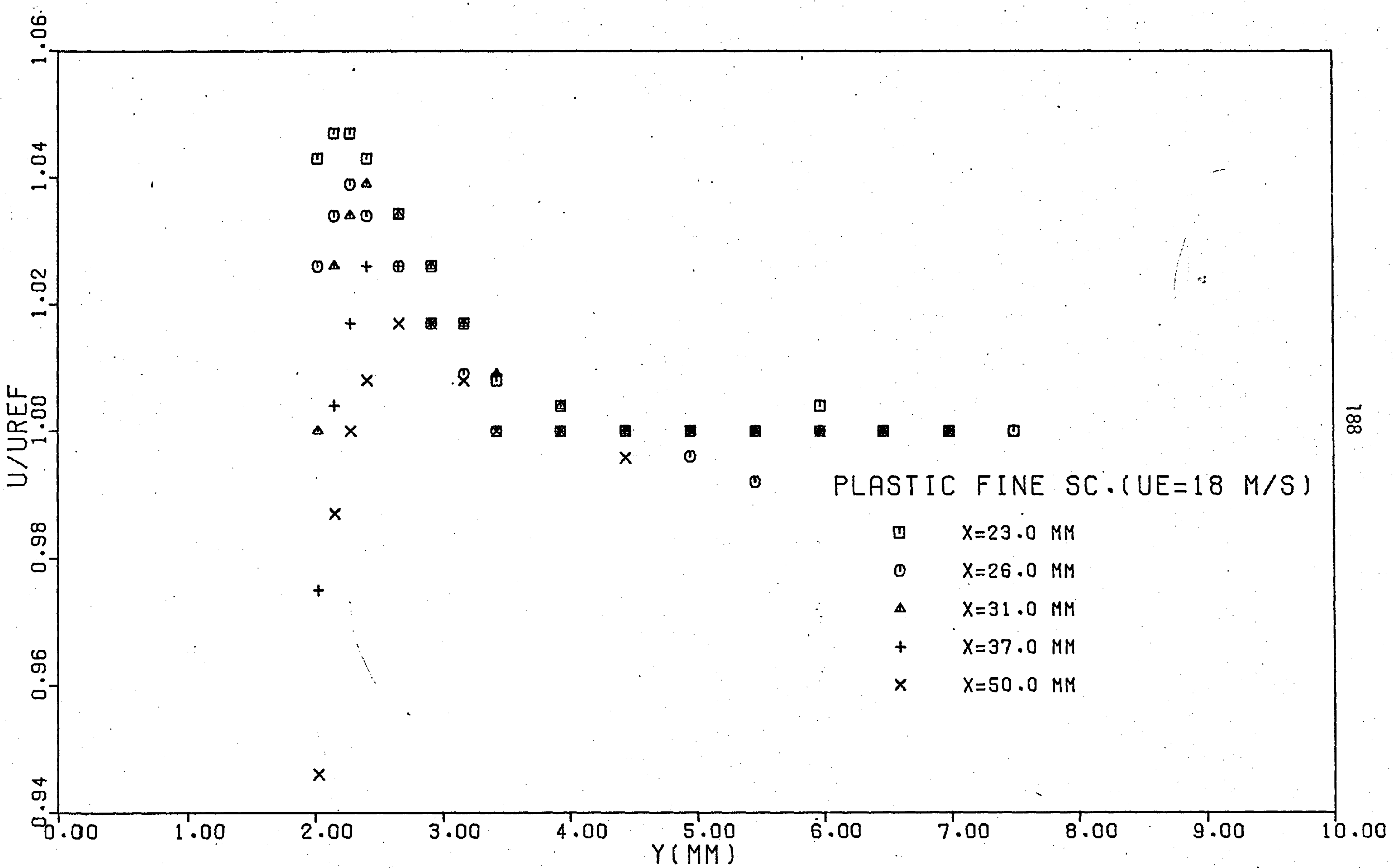

Fig. 3.72 Hot-wire mean velocity profiles downstream of the plastic fine screen (U_e = 18 m/s)

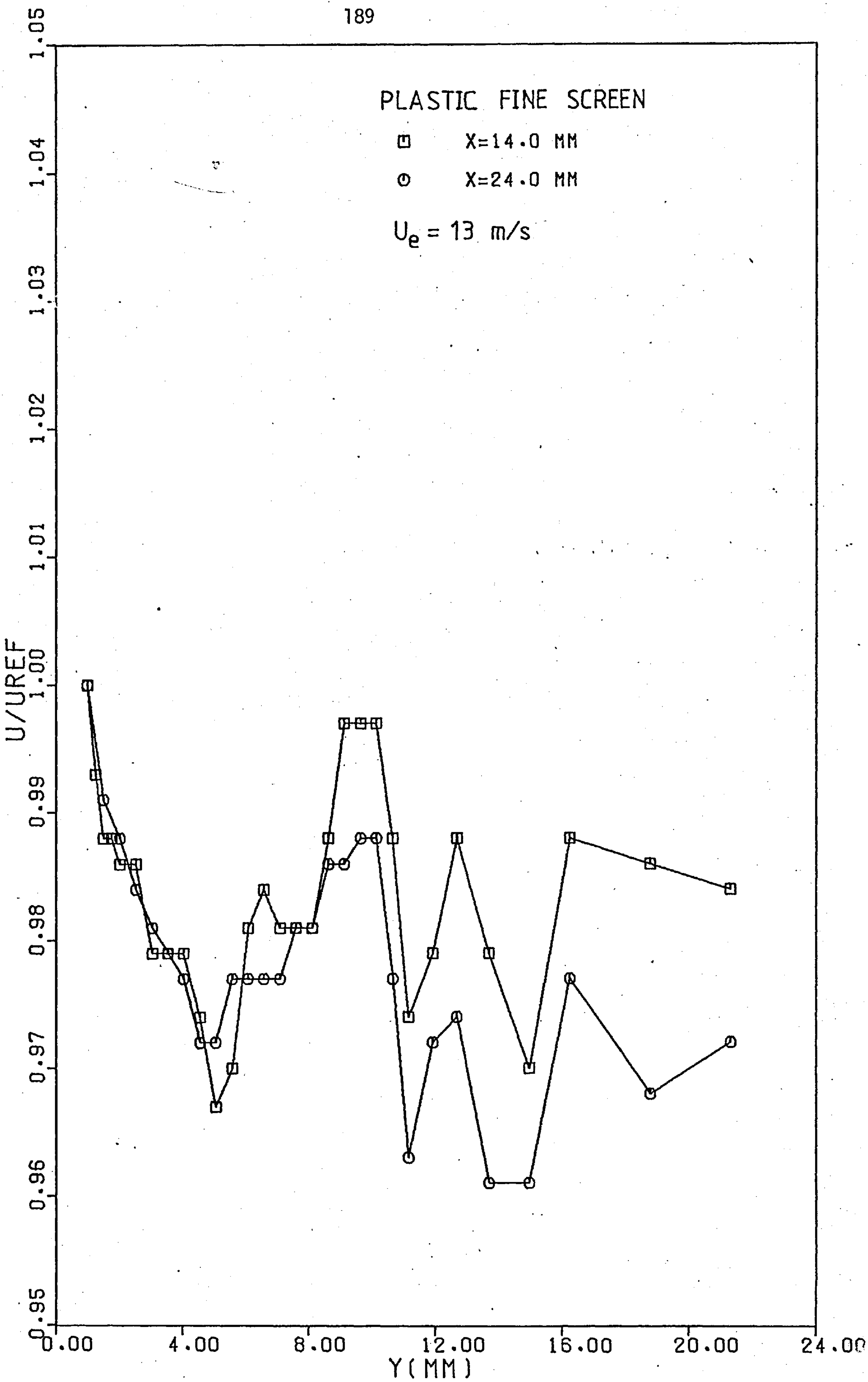

Fig. 3.73 Hot-wire mean velocity profiles downstream of the plastic fine screen (U_e = 13 m/s)

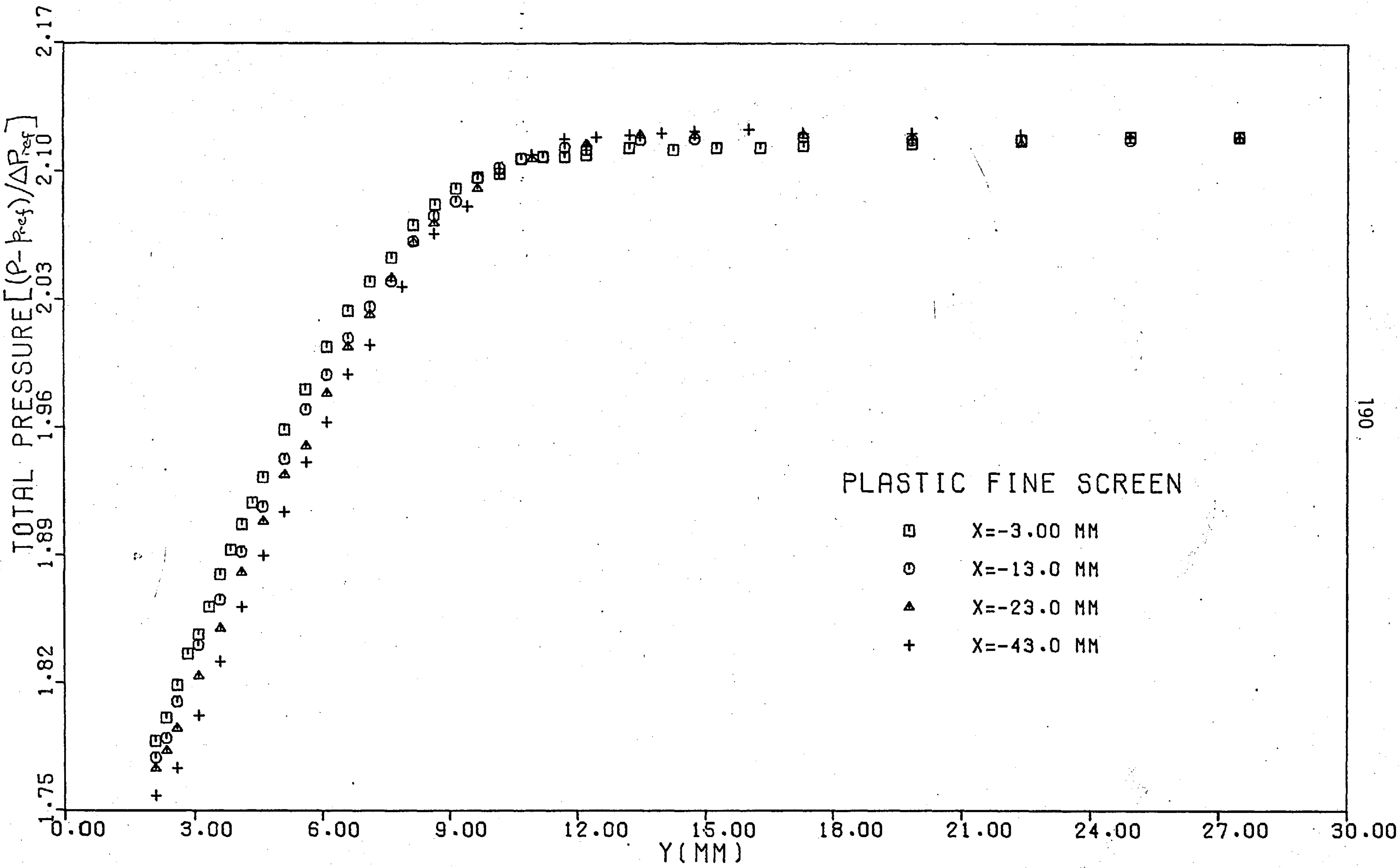

Fig. 3.74 Total pressure profiles upstream of the plastic fine screen.

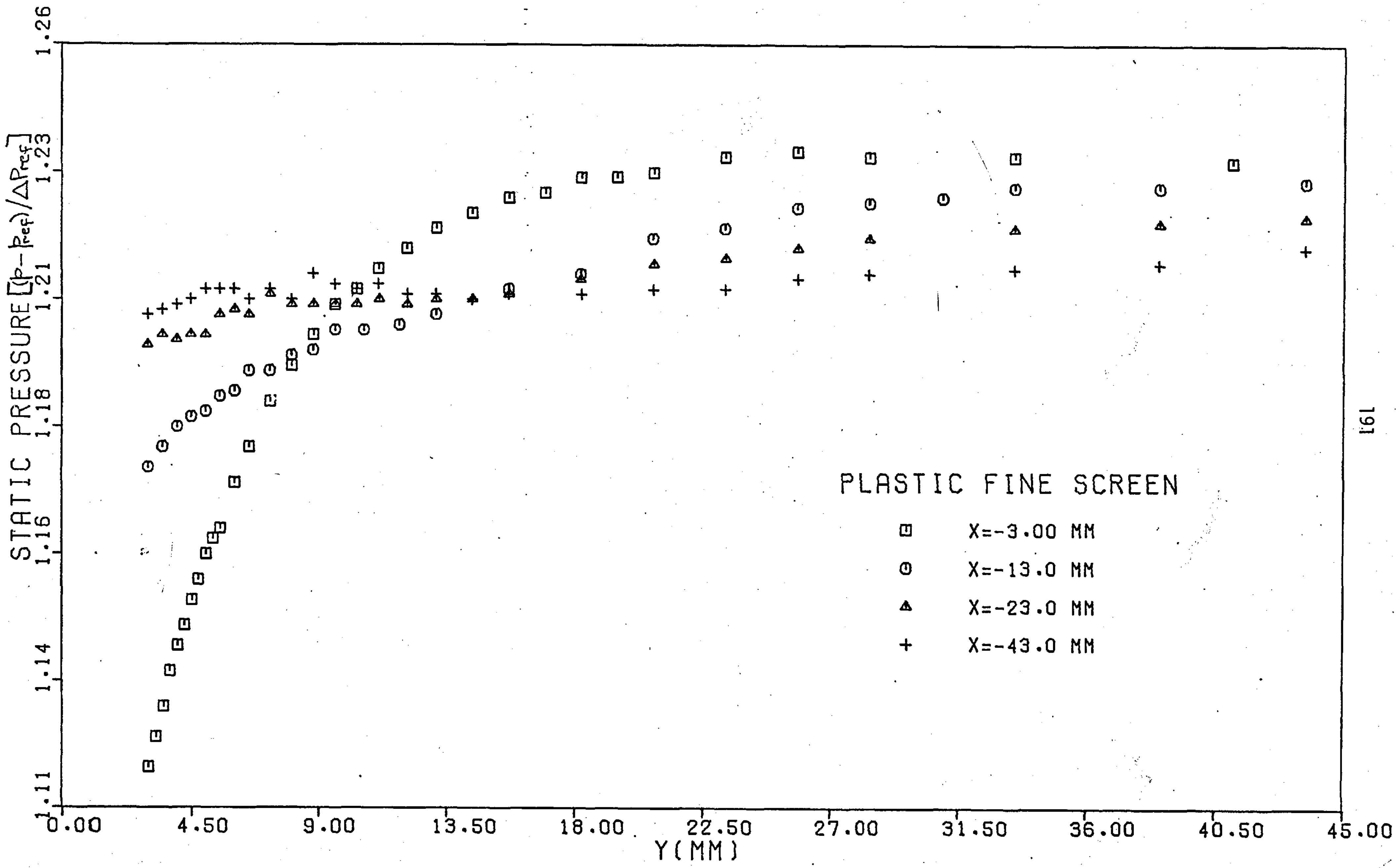

Fig. 3.75 Static pressure profiles upstream of the plastic fine screen.

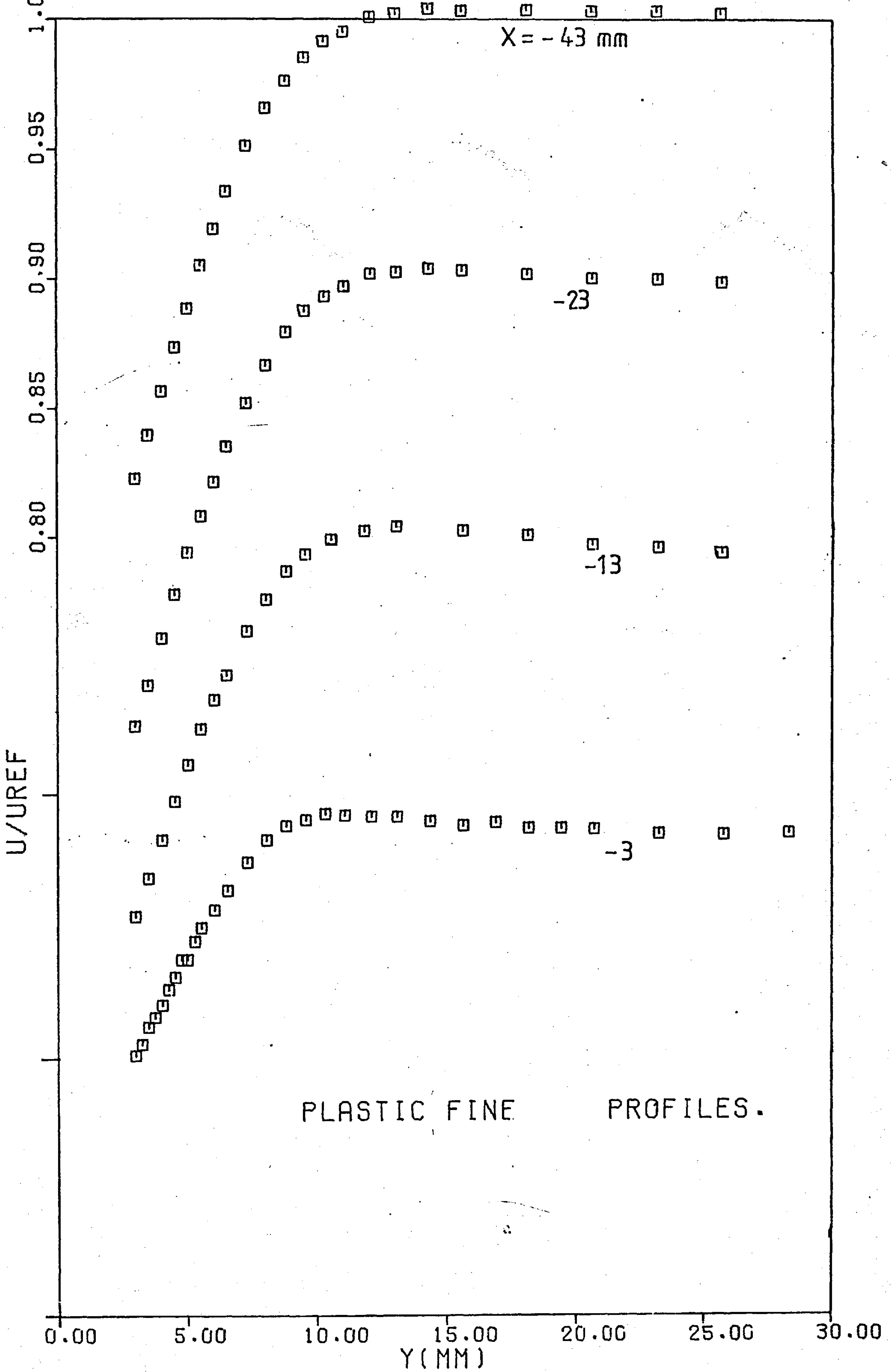

Fig. 3.76 Mean velocity profiles upstream of the plastic fine screen.

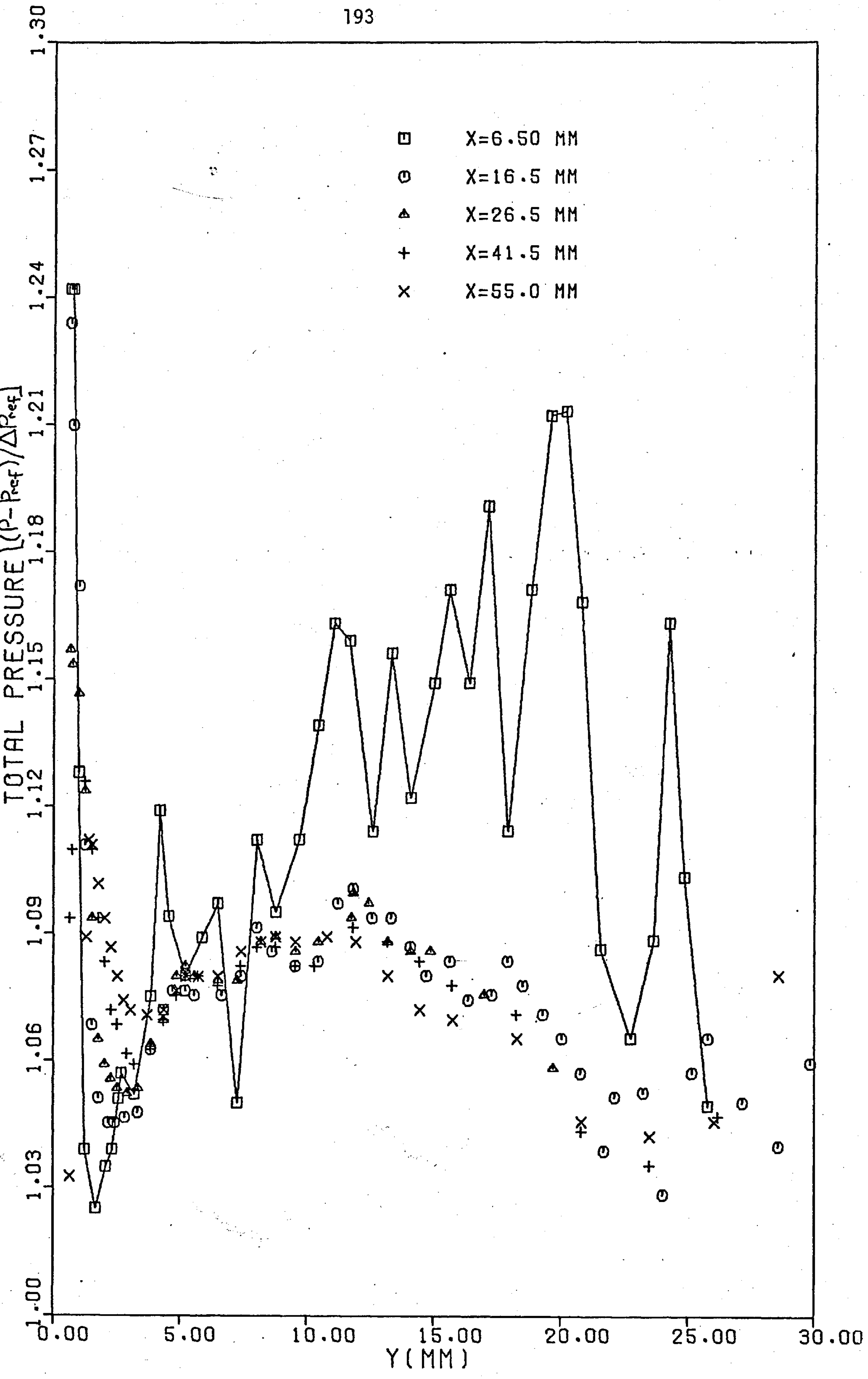

Fig. 3.77 Total pressure profiles downstream of the plastic fine screen.

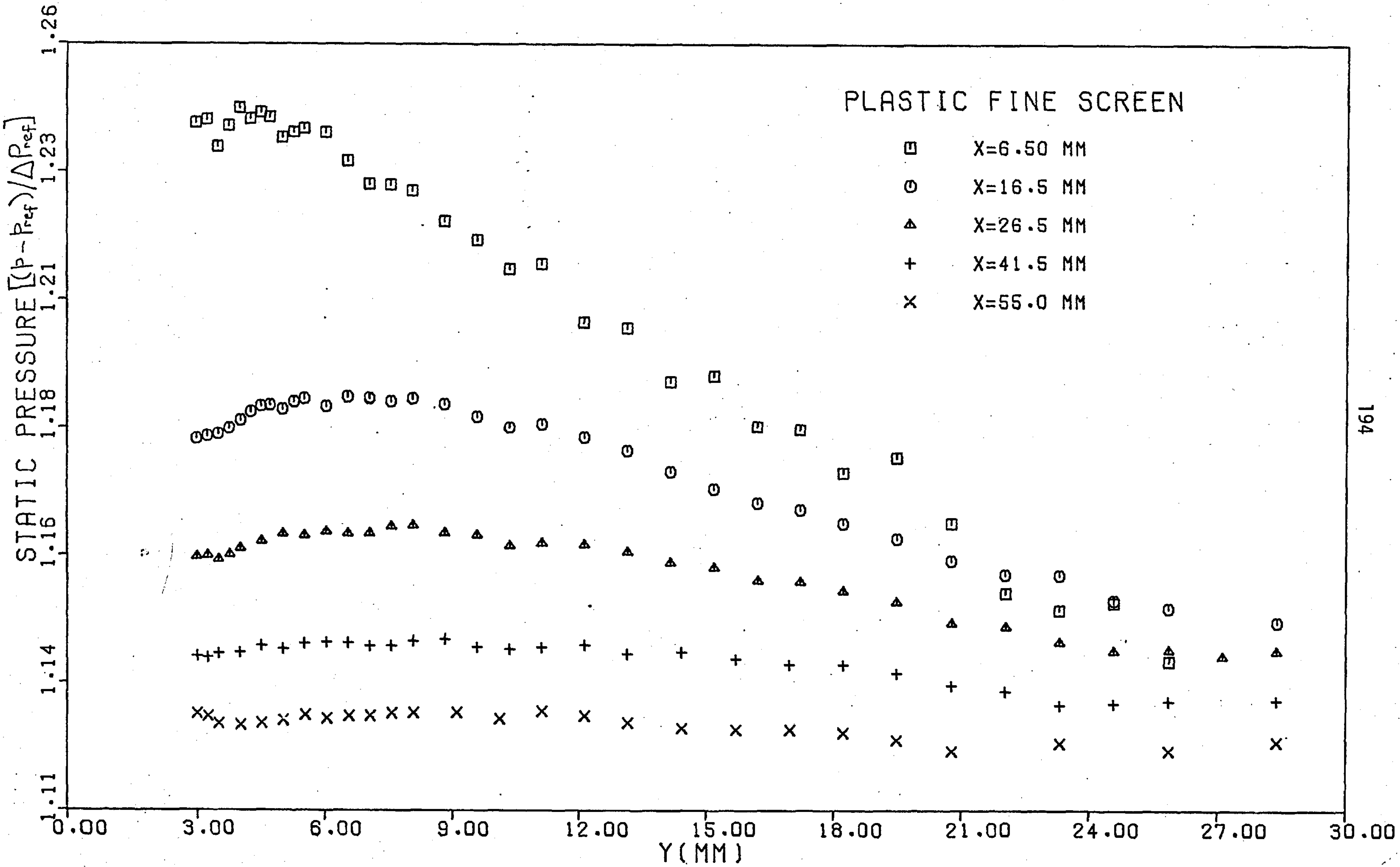

Fig. 3.78 Static pressure profiles downstream of the plastic fine screen.

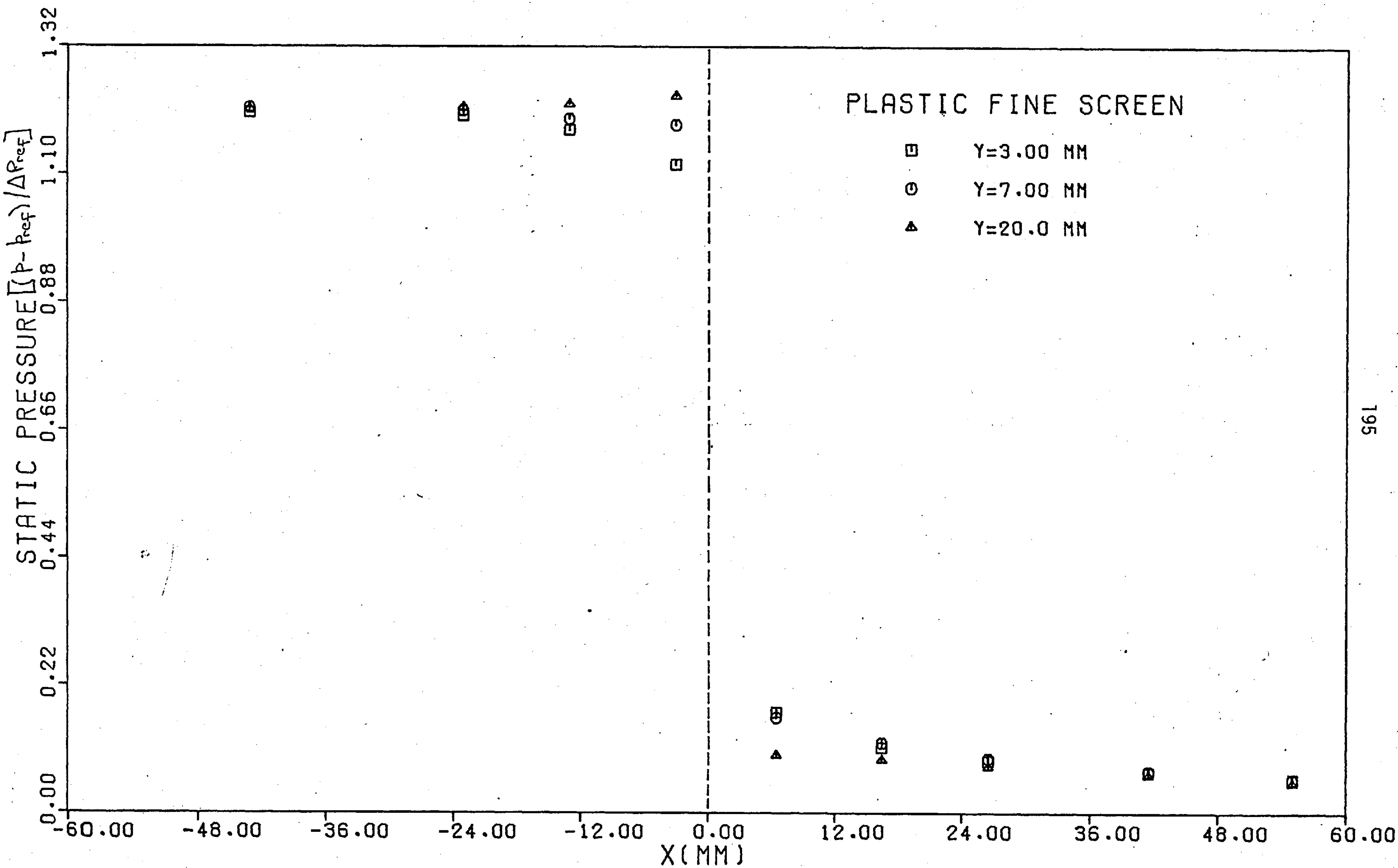

Fig. 3.79 Static pressure distribution near the plastic fine screen.

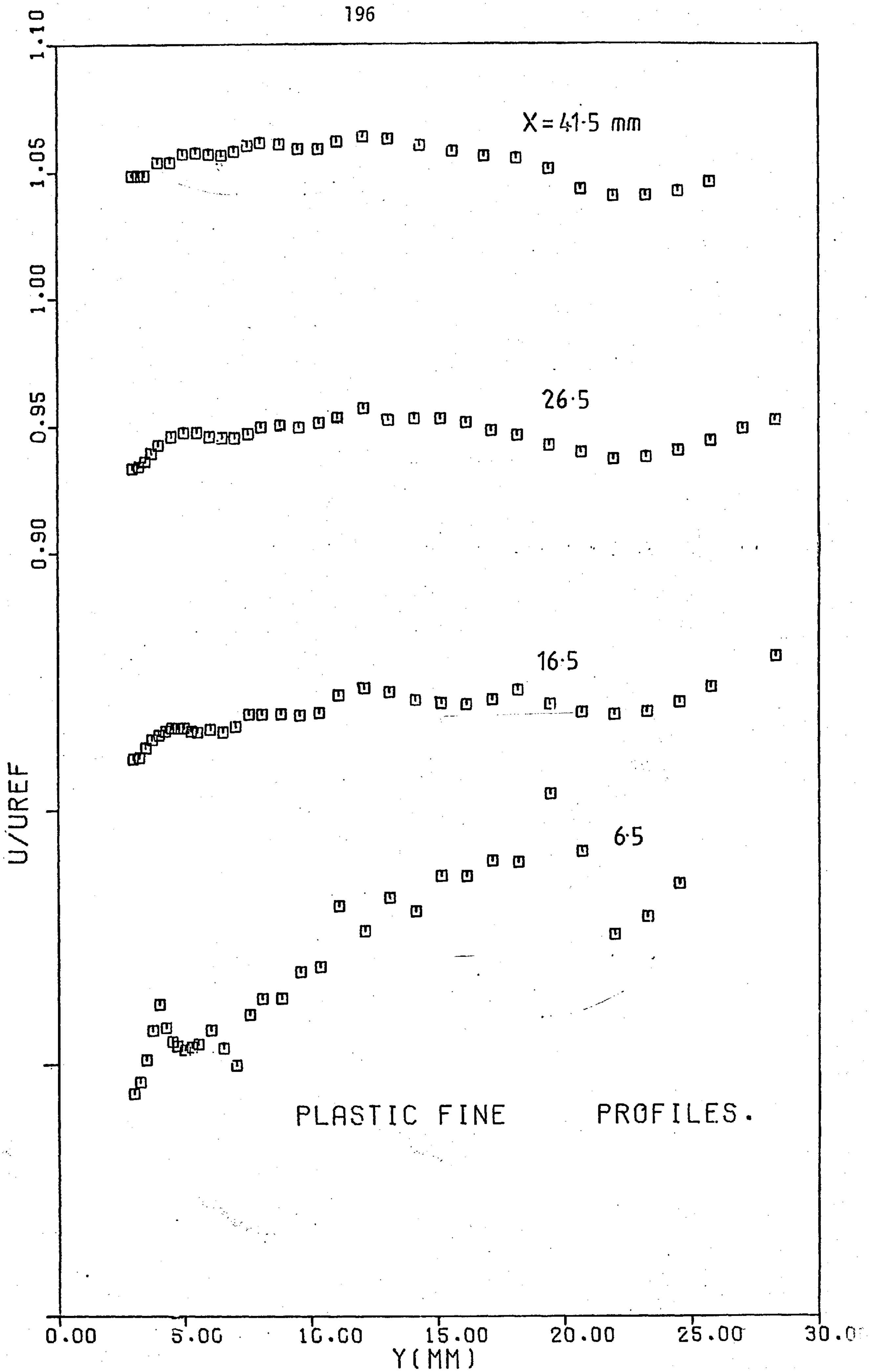

Fig. 3.80 Mean velocity profiles downstream of the plastic fine screen.

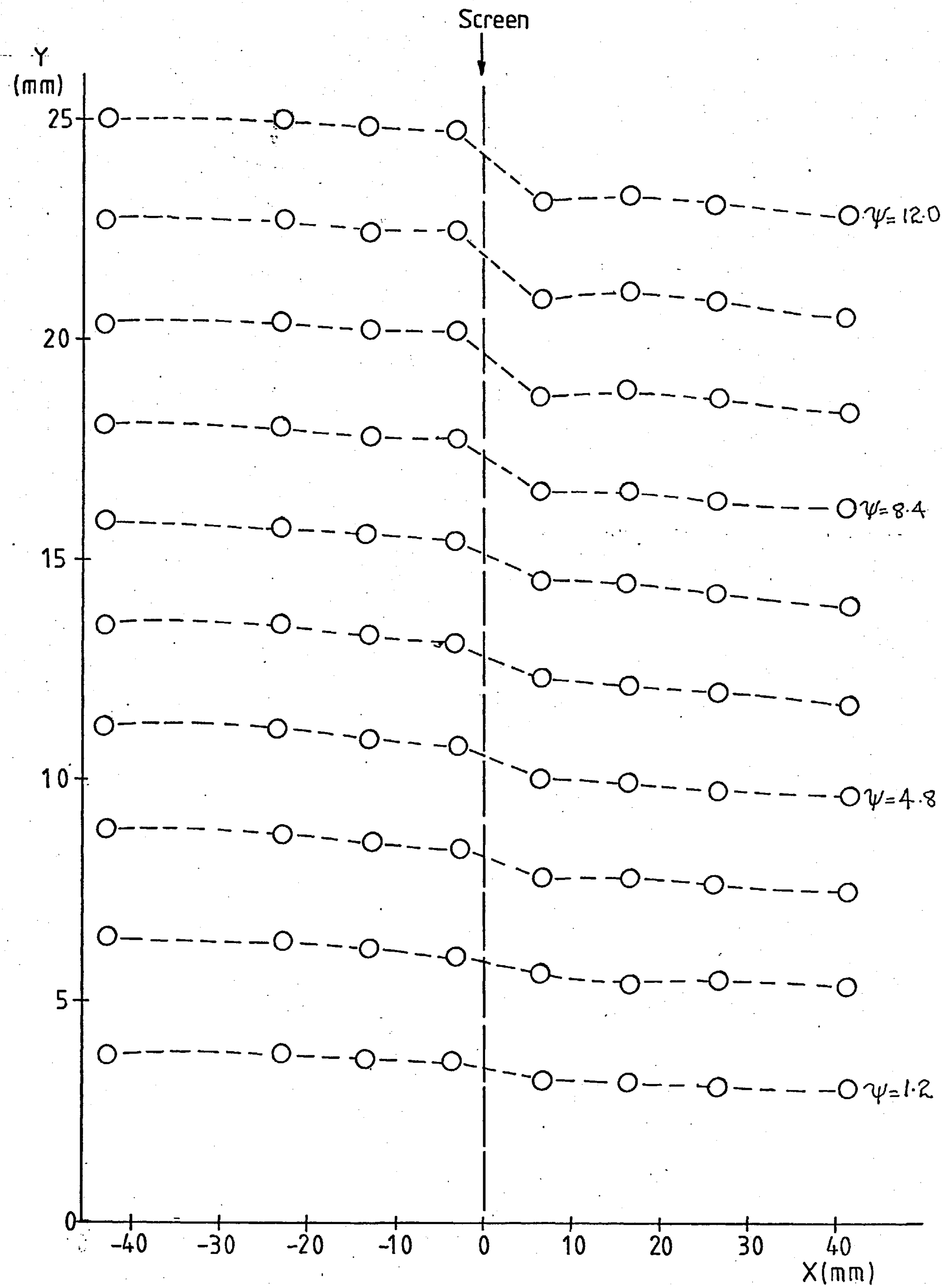

Fig. 3.81 Streamline shapes near plastic fine screen.

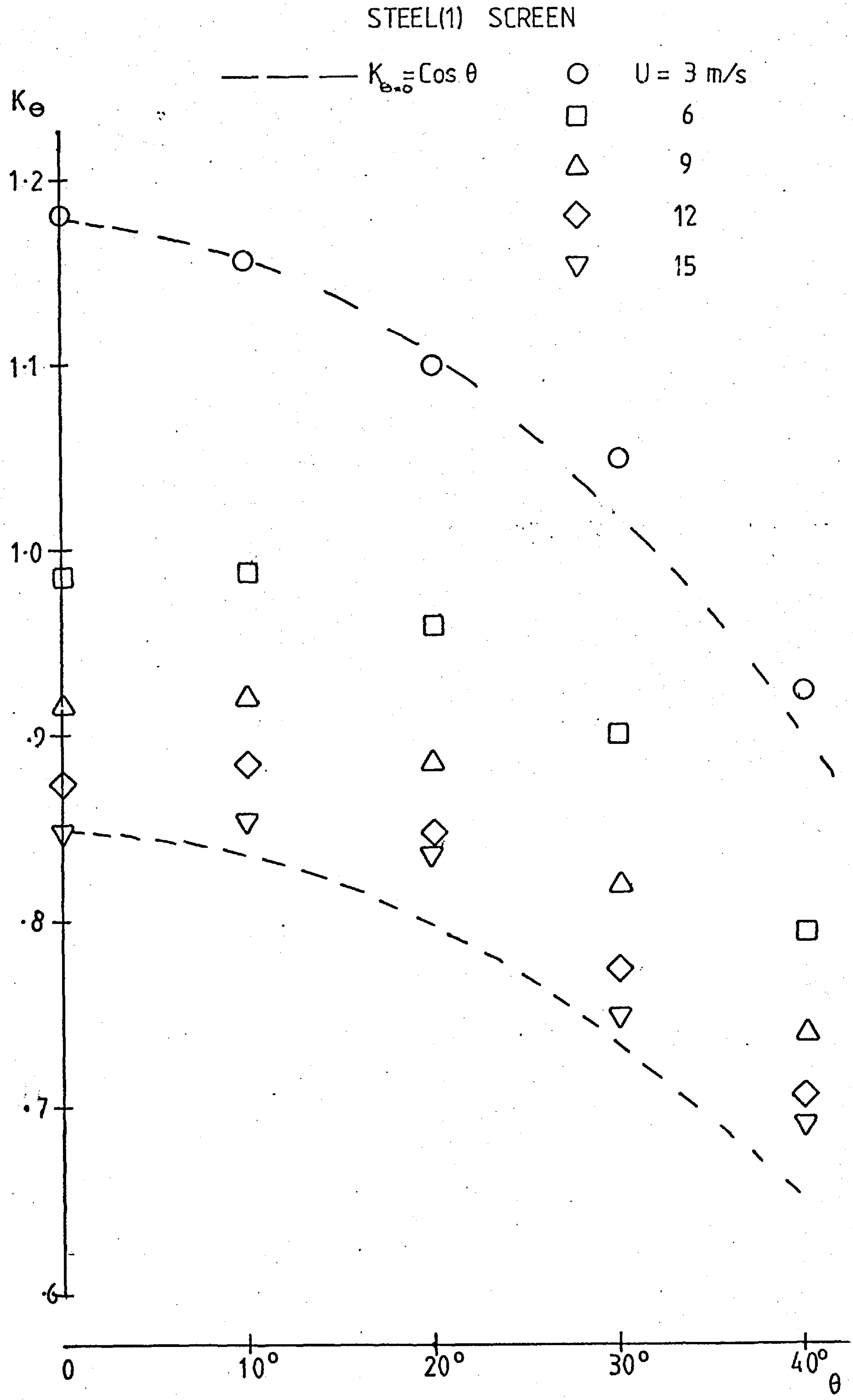

Fig. 3.82 K_θ vs θ for steel (1) screen.

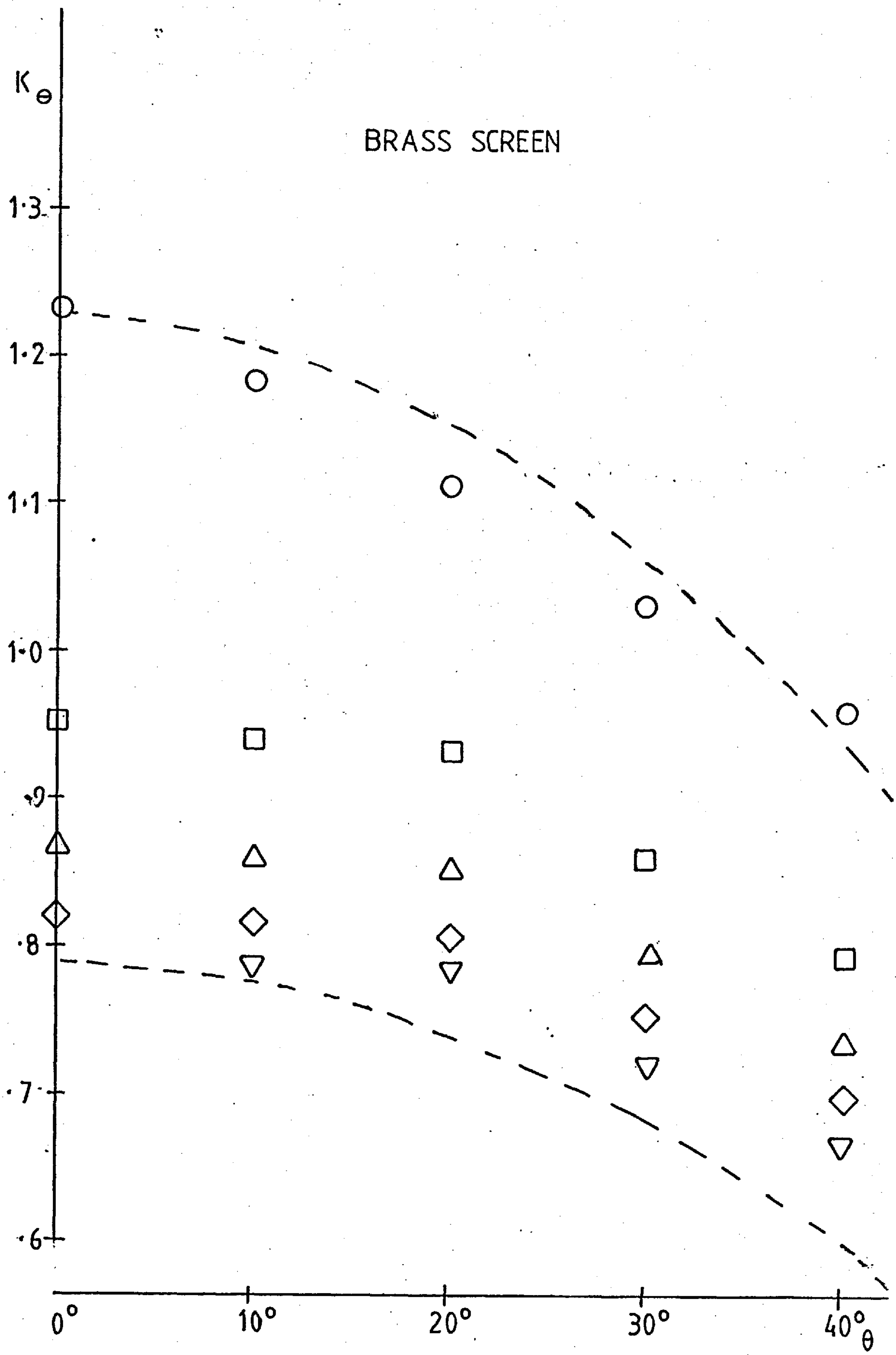

Fig. 3.83 K_θ vs θ for brass screen. (For legend, see Fig. 3.82).

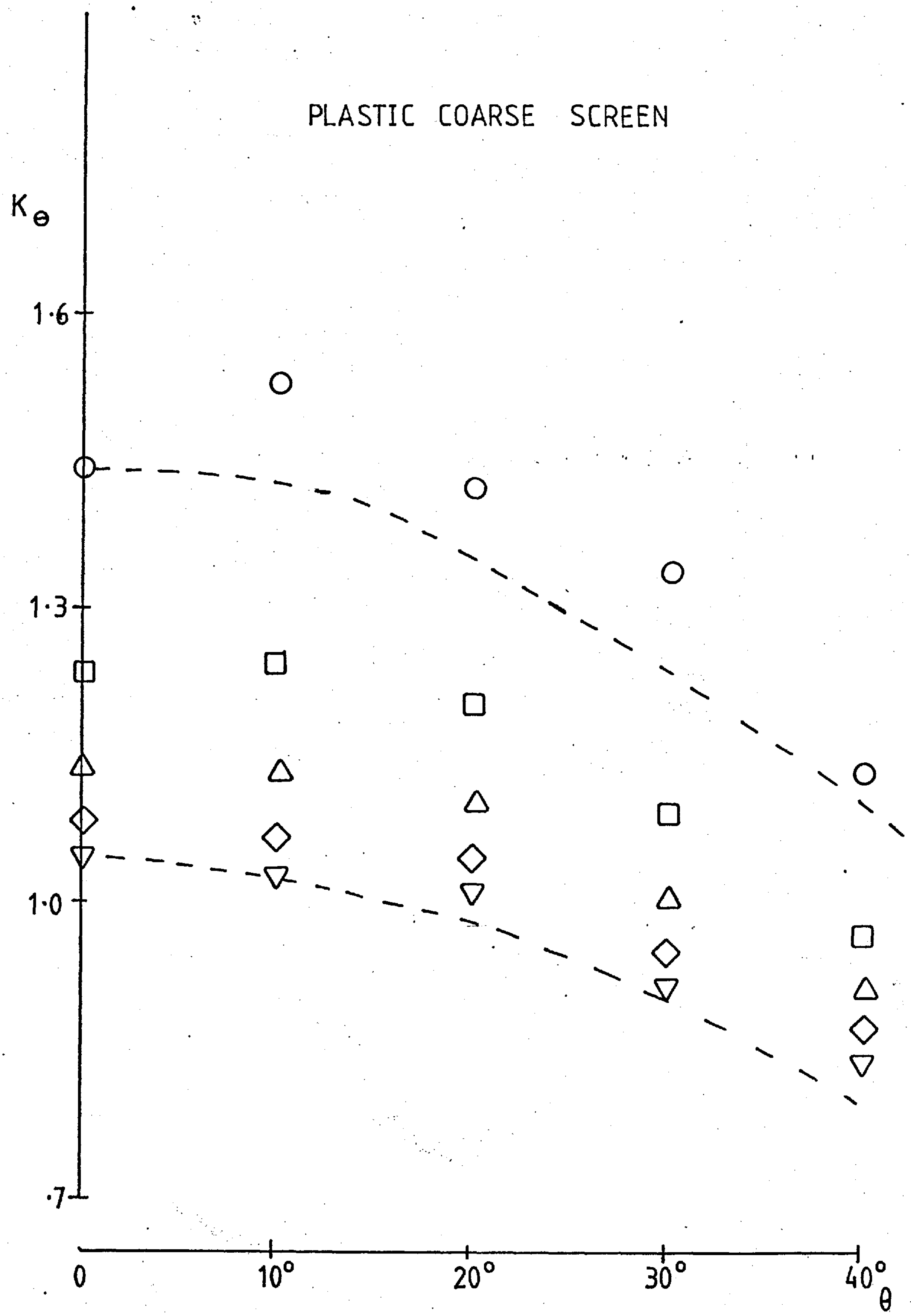

Fig. 3.84 K_θ vs θ for plastic coarse screen. (For legend, see Fig. 3.82).

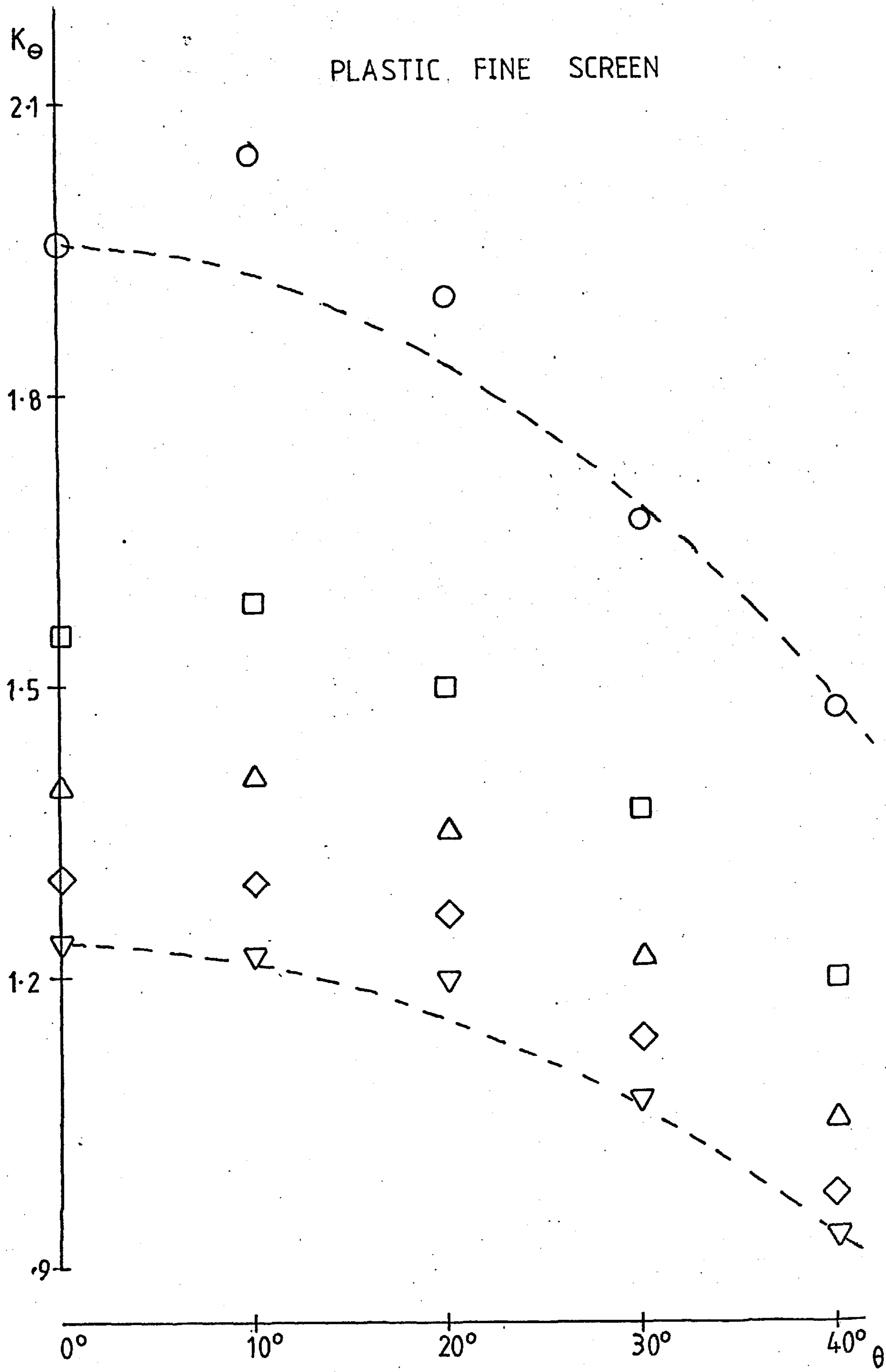

Fig. 3.85 K_θ vs θ for plastic fine screen. (For legend, see Fig. 3.82).

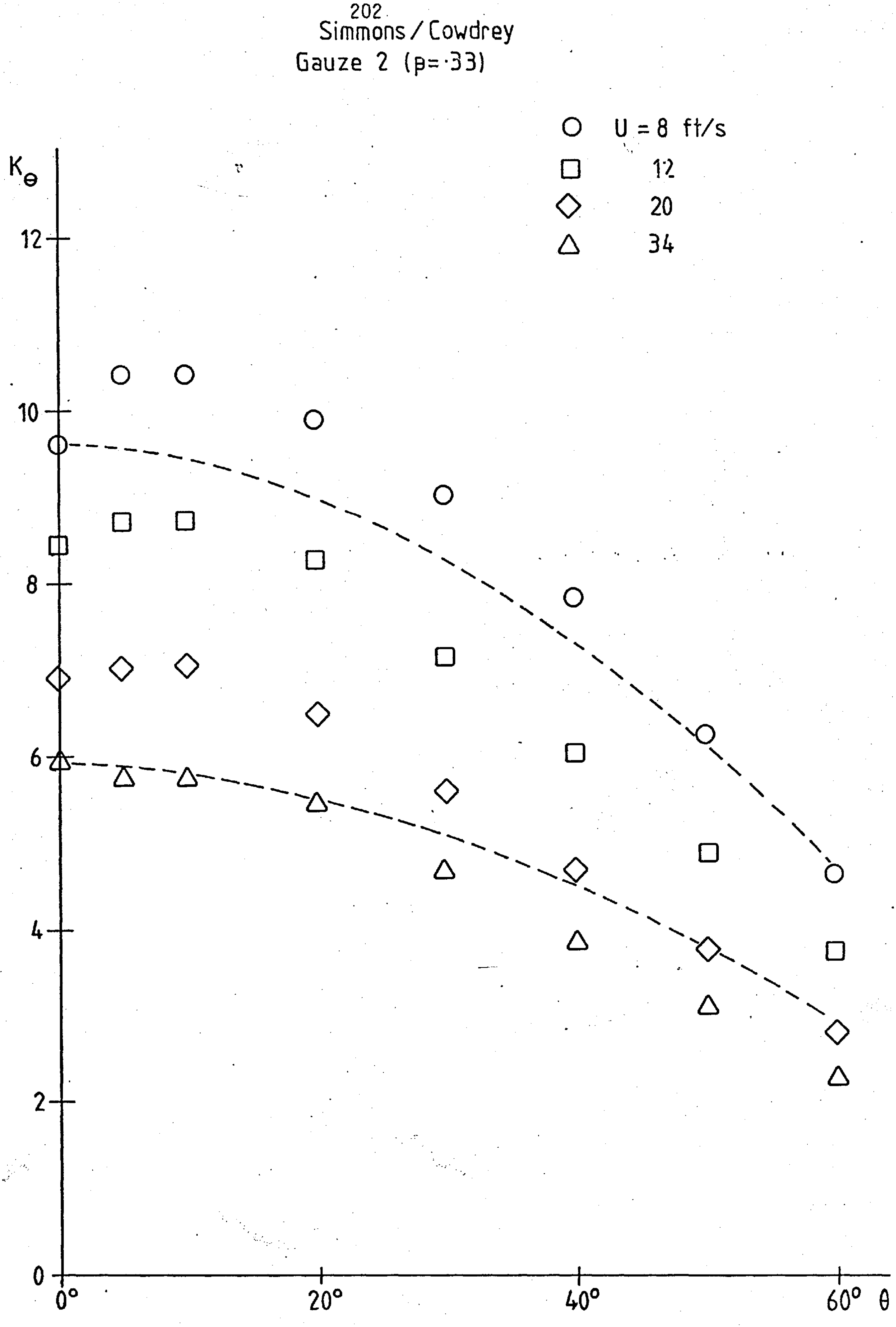

Fig. 3.86 K_θ vs θ for Simmons and Cowdrey's (1945) Gauze 2.

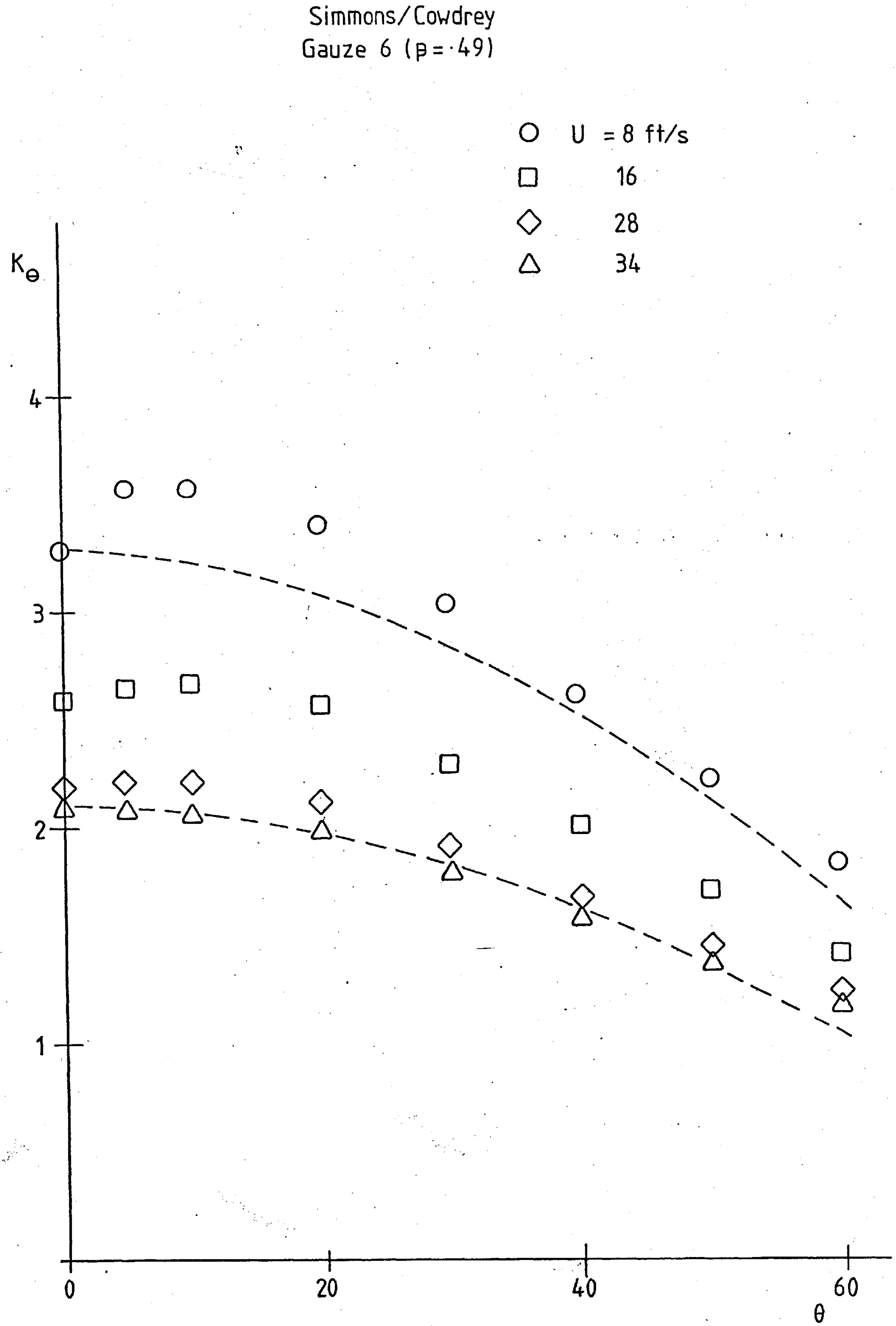

Fig. 3.87 K_θ vs θ for Simmons and Cowdrey's (1945) Gauze 6.

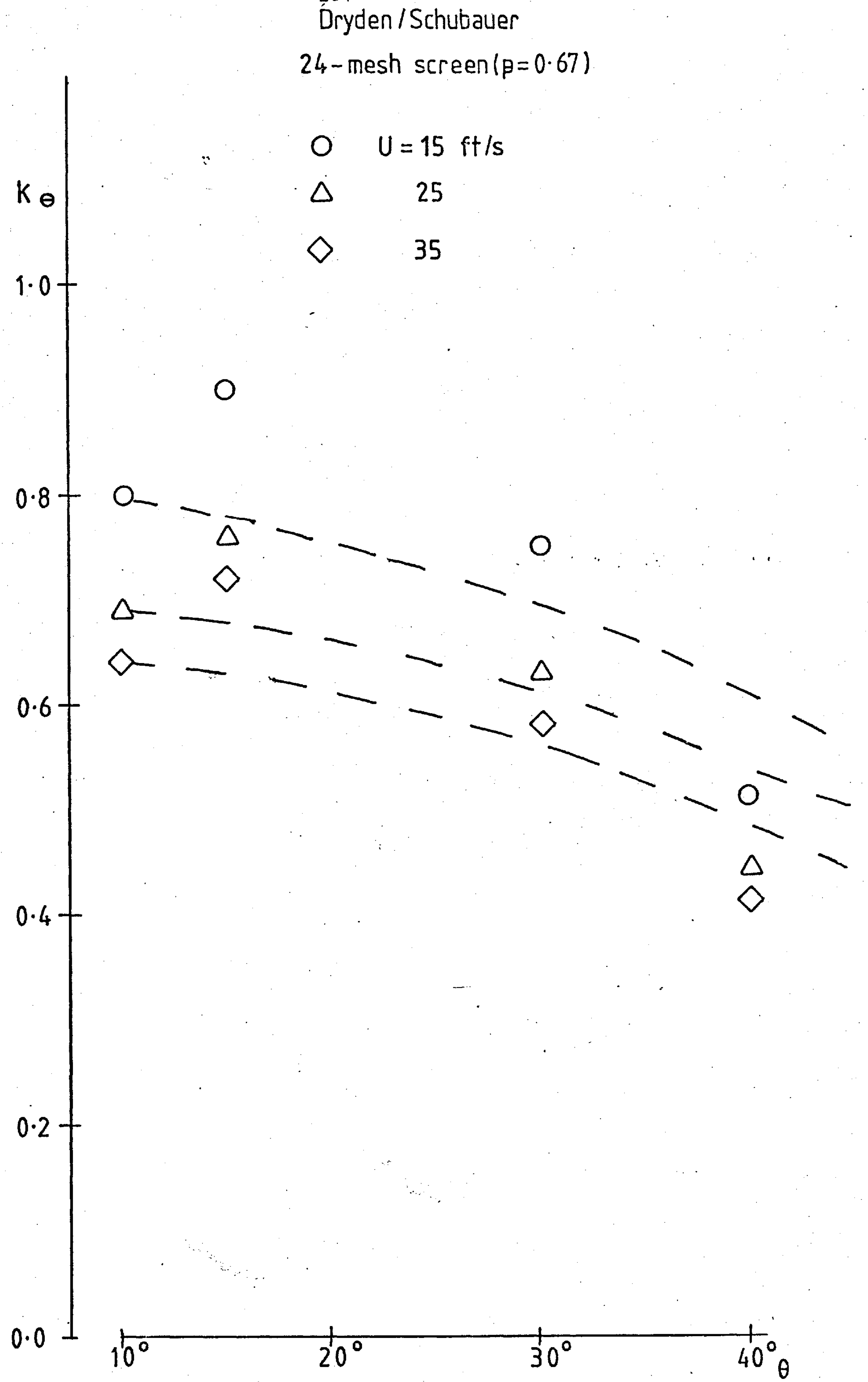

Fig. 3.88 K_θ vs θ for Dryden and Schubauer's (1949) 24-mesh screen.

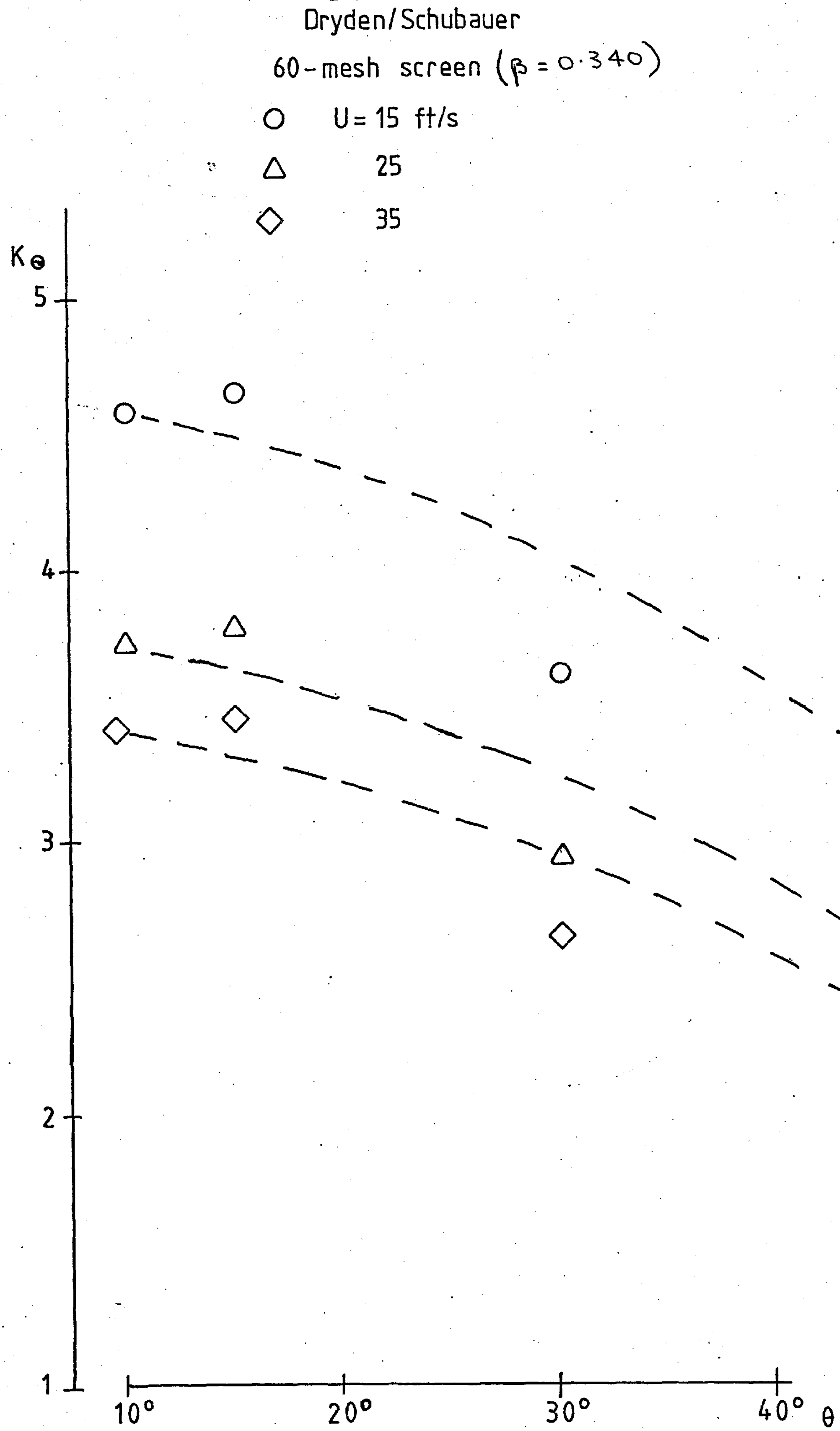

Fig. 3.89 K_θ vs θ for Dryden and Schubauer's (1949) 60-mesh screen.

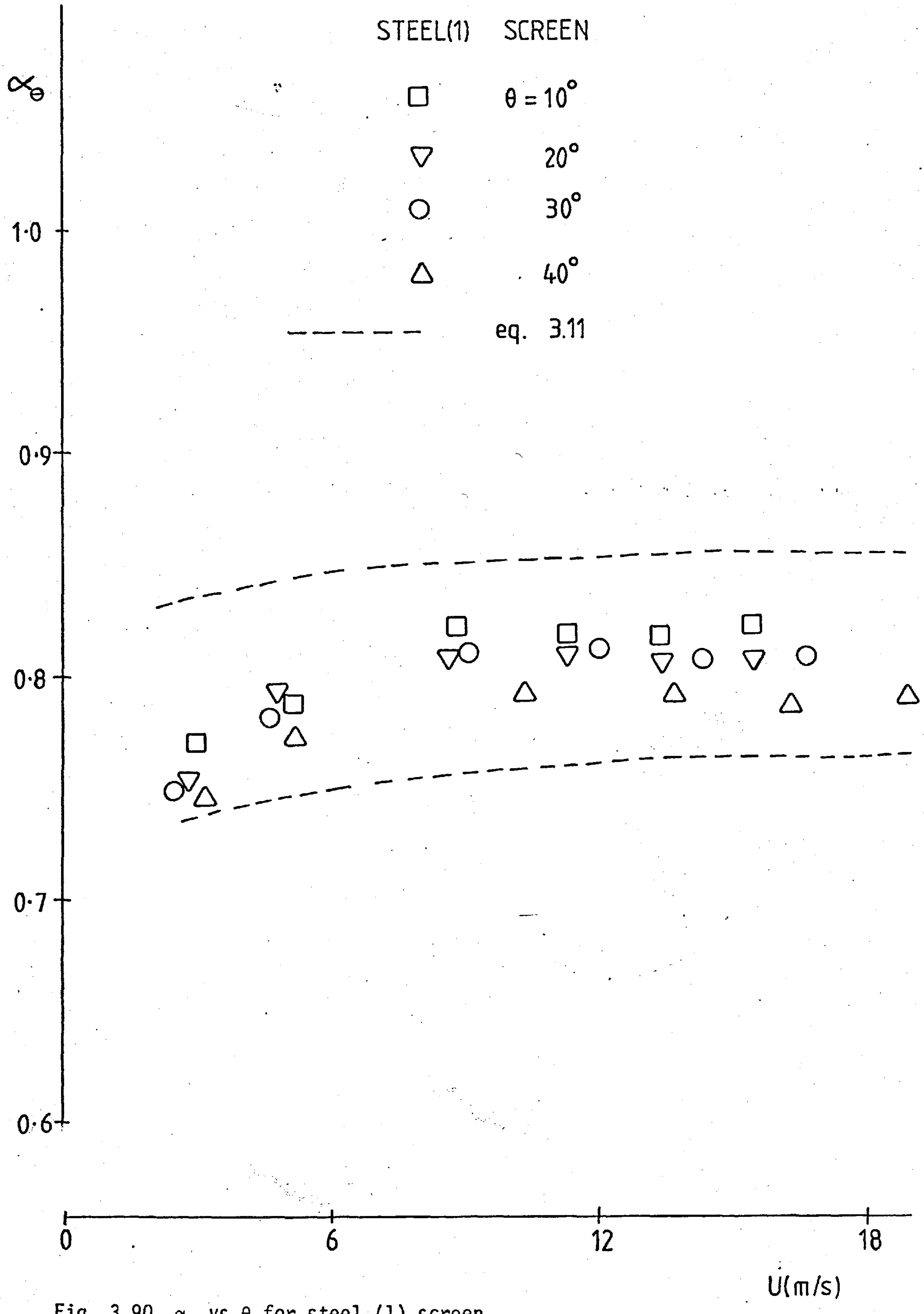

Fig. 3.90 α_θ vs θ for steel (1) screen.

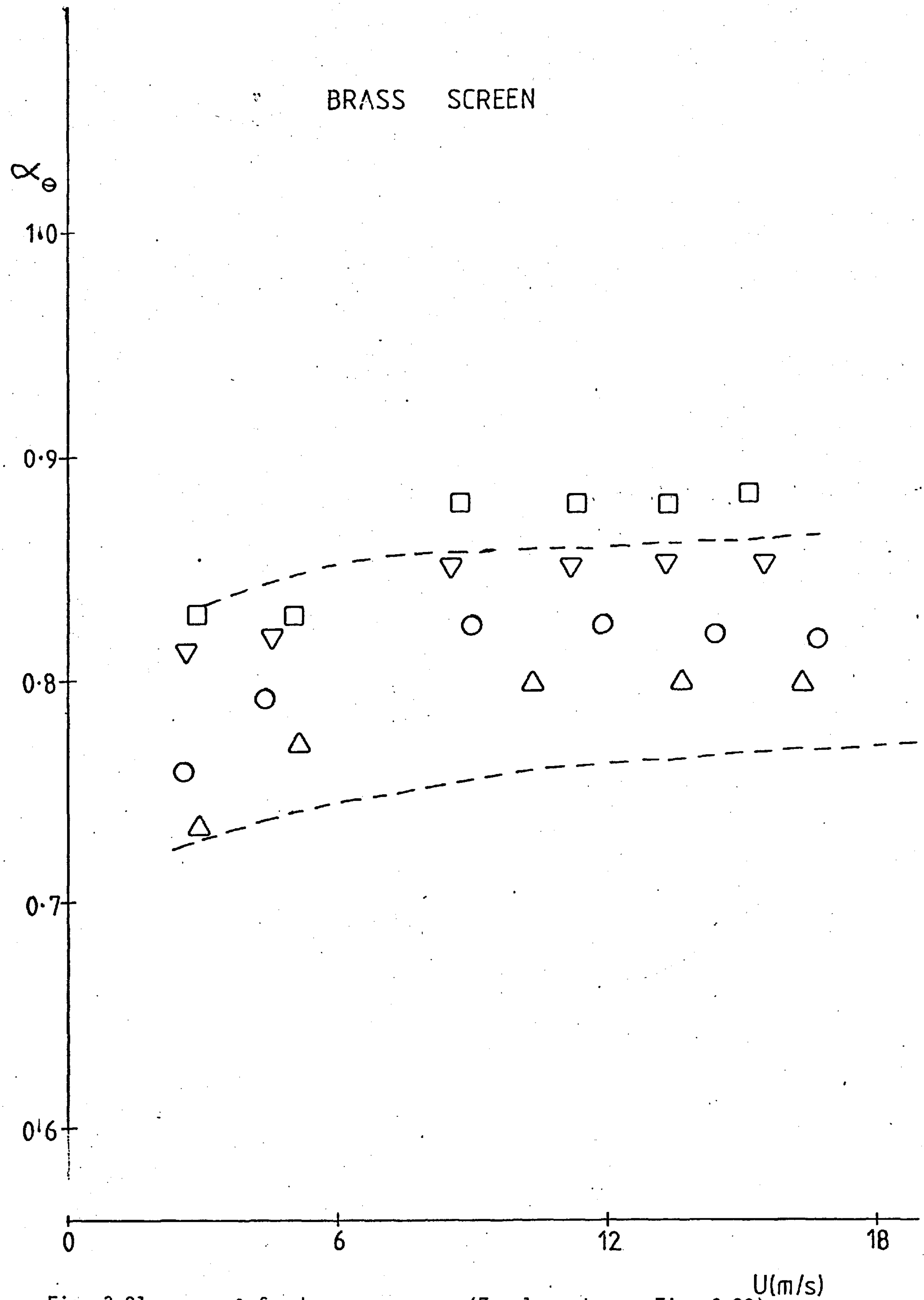

Fig. 3.91 α_θ vs θ for brass screen. (For legend, see Fig. 3.90).

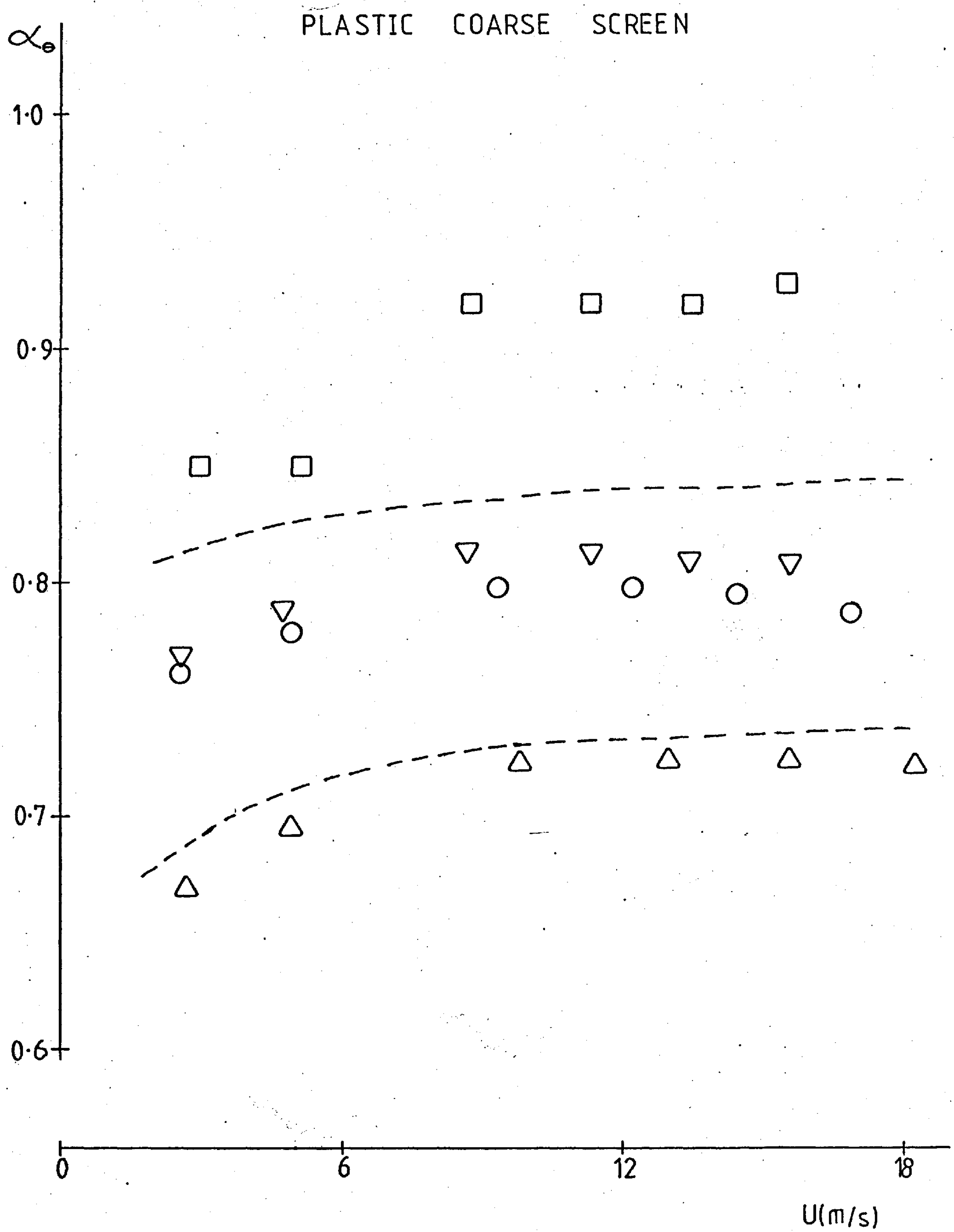

Fig. 3.92 α_θ vs θ for plastic coarse screen. (For legend, see Fig. 3.90).

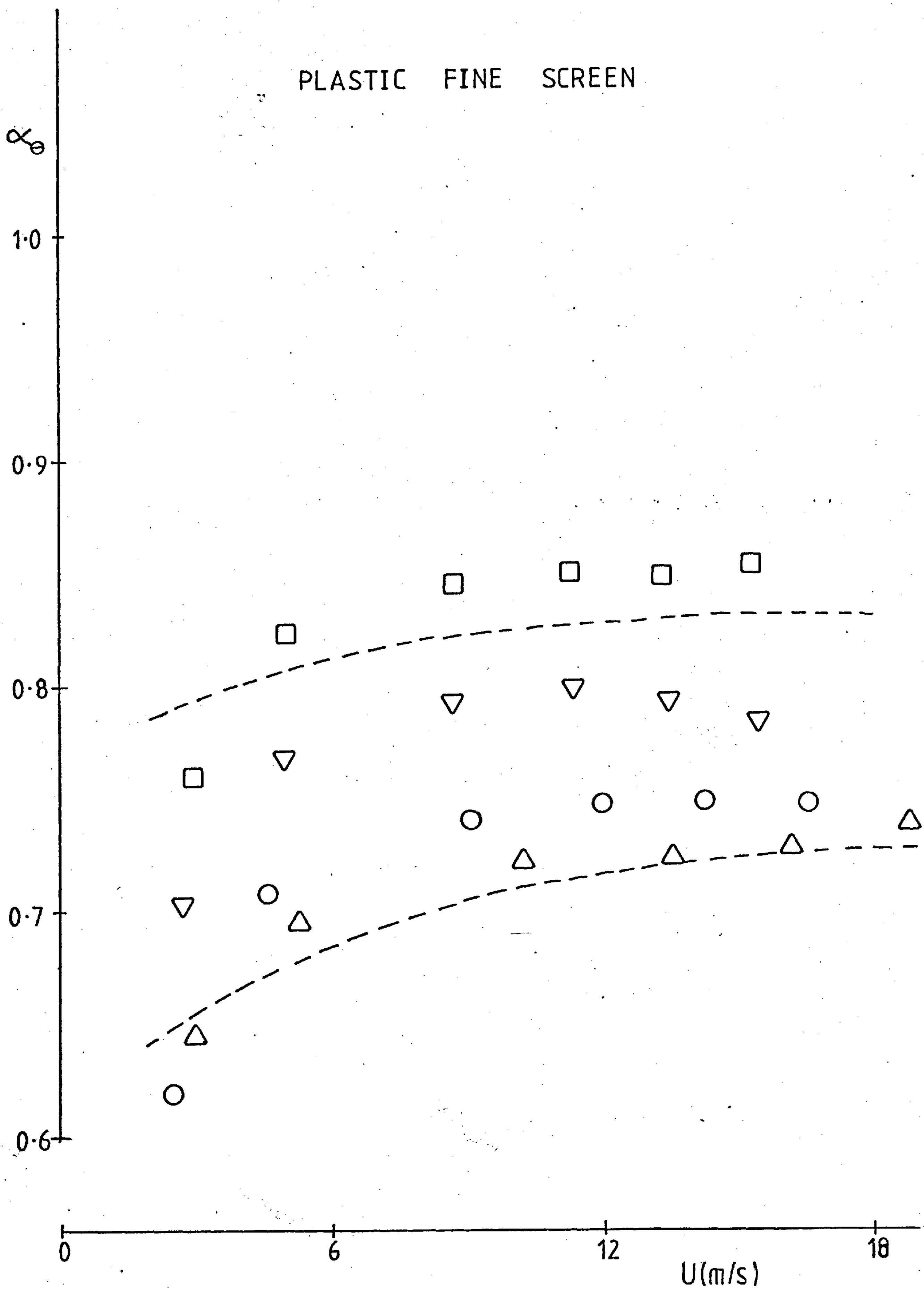

Fig. 3.93 α_θ vs θ for plastic fine screen. (For legend, see Fig. 3.90).

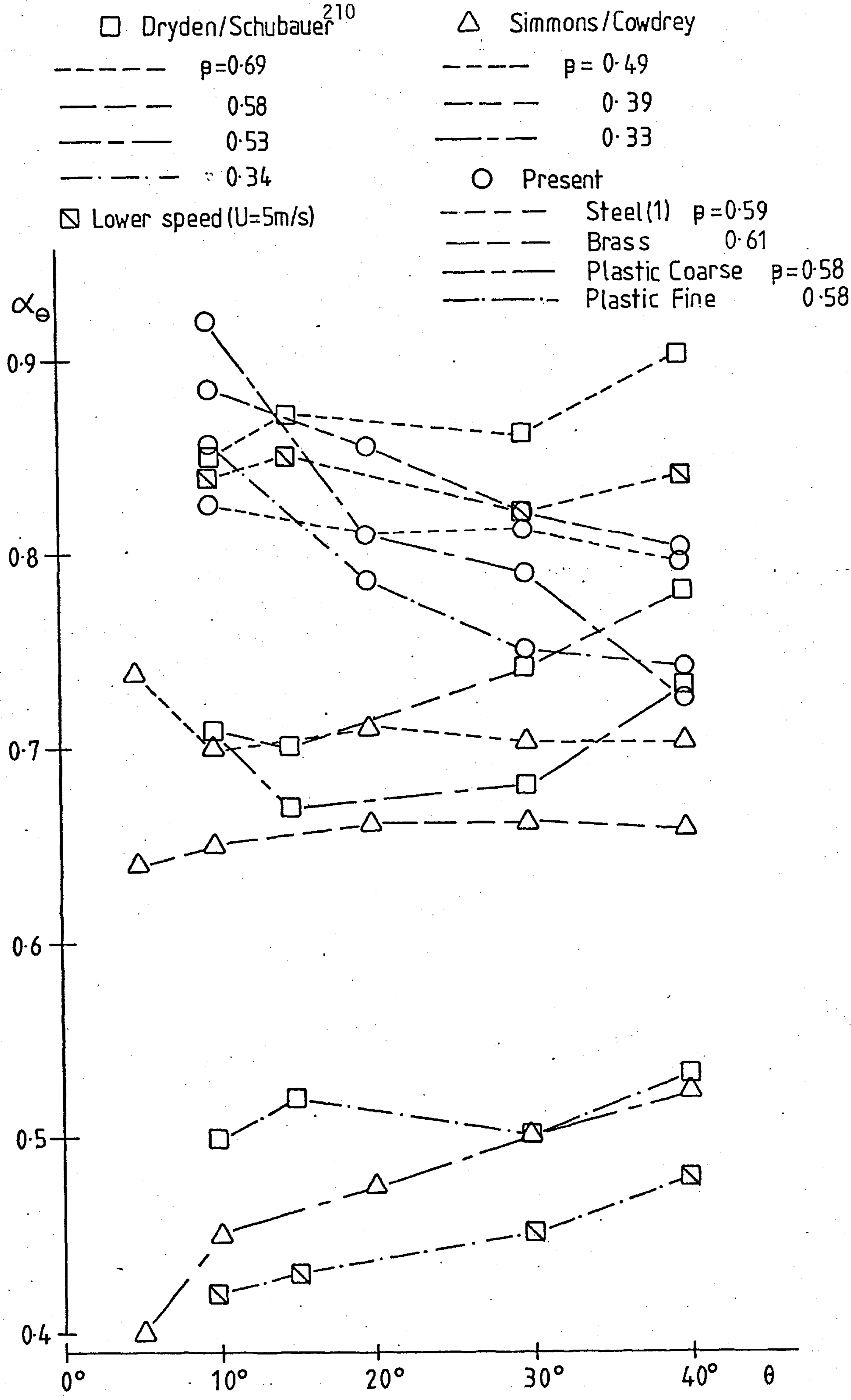

Fig. 3.94 α_θ vs θ for all results (in the high Re limit).

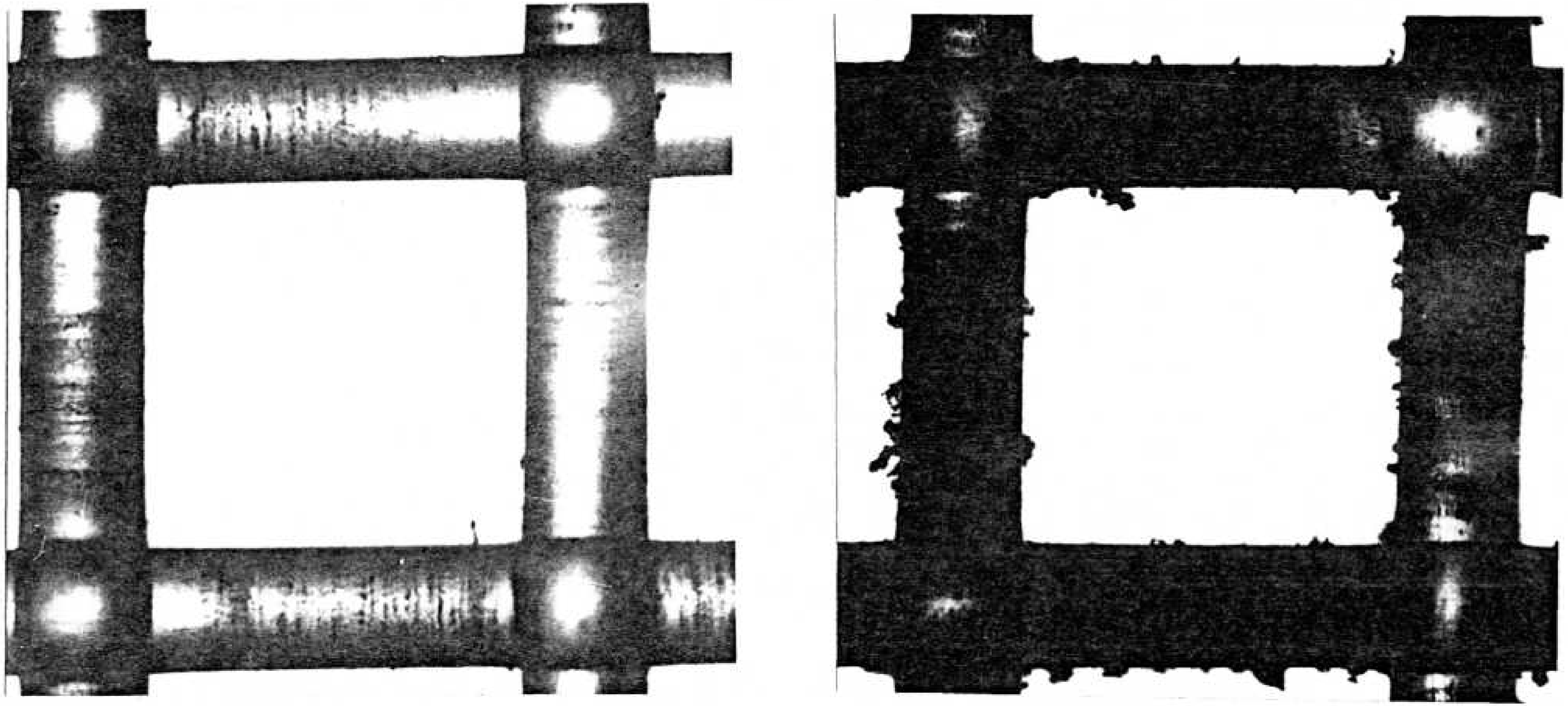

Pre-run Post-run

Fig. 3.95 Screen sample (plastic fine screen) before and after a 4000 Km run. (I am indebted to Mr. P. Inman for supplying this screen sample).

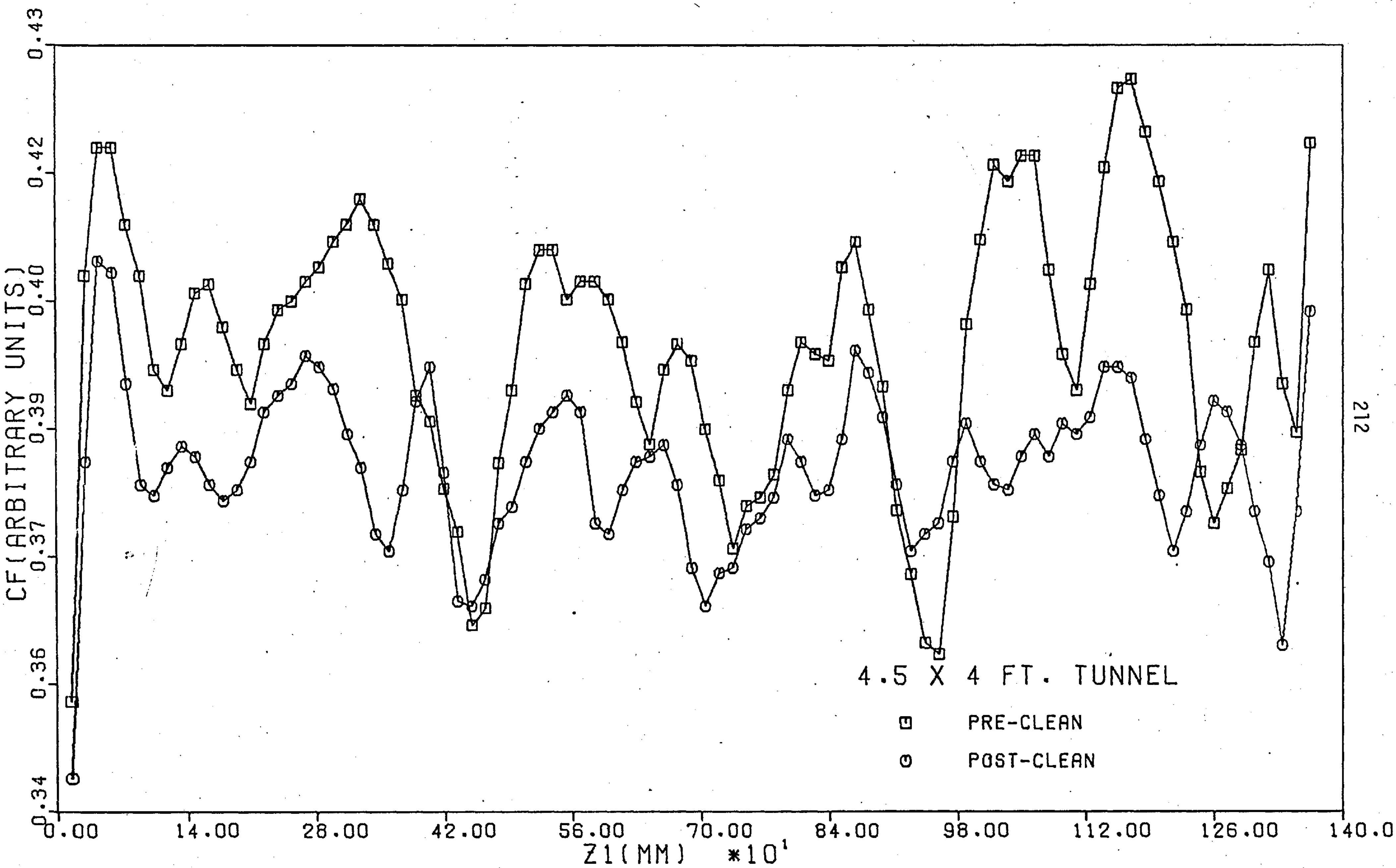

Fig. 3.96 Spanwise skin-friction distribution on the 4.5 x 4 ft. working section floor before and after cleaning the last screen in the settling chamber.

CHAPTER 4

CENTRIFUGAL BLOWERS

4.1 Characteristics of Centrifugal Blowers

Over the past decade, centrifugal fans with "aerofoil-type" impellers have emerged as the optimum choice for driving open-circuit blower tunnels. Centrifugal blowers are suitable for high performance tunnels and test rigs, especially when a large variation in power factor is expected.

The aerofoil-type blades are usually "backward-facing", (Fig. 4.1) - if forward-facing, they are less efficient - and, in blowers with single inlets, the rotor occupies only about half the width of the volute casing (Fig. 4.2). The rotor is asymmetrically positioned so as to accommodate the entry bellmouth within the blower casing, thus reducing the overall width. A bellmouth presents a fairly uniform flow to the blower inlet. The larger blowers tend to have double inlets and the rotor in these is centrally placed, occupying nearly all the width of the casing. For typical blower tunnel speeds and small working section sizes, however, single-inlet blowers are adequate. Besides the rotor, another important component in a centrifugal blower is the splitter plate or "tongue", shown in Fig. 4.1. The main function of the tongue is to split the flow which emerges from the blower from that which rotates with the rotor.

The backward-facing, aerofoil-type impeller arrangement has certain advantages over the radial-vane type, which it effectively replaced. Unlike the older type, the aerofoil type blower does not depend on "centrifugal force" to produce the dynamic pressure rise. It does, however, depend on the increase in blade peripheral velocity from the inlet to the outlet, which explains the rather curious "backward" blade arrangement. Fig. 4.3 shows the velocity triangle for this sort of blade arrangement. The static pressure rise is mainly obtained by expanding the flow through the volute casing. The radial-vane type blower often produced noise and flow pulsations which rendered it unsuitable for high performance tunnels. The aerofoil-type blower on the other hand is much quieter.

The ability of centrifugal blowers to run with reasonable steadiness and efficiency over a wide range of flow conditions can be attributed to the operation of the whole blade span at the same lift coefficient, whereas an axial fan can achieve this only at a single advance ratio $(U/\omega r_2)$ - notation of Fig. 4.1.

Since the whole blade area is at the periphery, the pressure rise obtainable at a given peripheral speed and operating condition is also greater in an aerofoil-type blower than in an axial-flow fan. In fact, it is also greater than that usually obtained from a radial-vane blower, which is always less than $\frac{\rho\,(\omega r_2)^2}{2}$. An axial-flow fan, with a central boss diameter acceptable for wind tunnel use, stalls first at the roots and produces negative thrust first at the tips because the effective blade incidence is greater at the roots. Consequently, the flow uniformity at the outlet of an aerofoil-type blower does not alter as much with advance ratio as does that from an axial-flow fan, although, as will be seen below, the uniformity of flow emerging from the blower may not be desirable. Furthermore, the swirl produced by an aerofoil-type blower with a single inlet, (Fig. 4.4), is roughly independent of the advance ratio because it results from the asymmetry of the rotor position rather than directly from the motion of the blades as in an axial fan.

All these factors help to reduce the noise and pulsations generated by an aerofoil-type blower to a level well below that of an axial-flow fan, particularly at off-design conditions, although an axial-flow fan in a closed-circuit tunnel has a smaller annoyance value because some of the noise is absorbed by the surrounding tunnel walls. Most commercially available blowers are found to have favourable noise characteristics. Bradshaw (1967) used a single inlet centrifugal blower with a backward-facing, aerofoil-type impeller on a 15" x 10" (0.38 m x 0.25 m) blower tunnel. Measurements of the frequency spectrum of surface pressure fluctuations and u-component turbulence in the working section showed no appreciable trace of the blade passage frequency and the tunnel was found to have a very low noise level. However, besides the impeller type, the tongue size and position can also affect the noise characteristics of a blower (see Section 4.3).

The maximum attainable efficiency of an aerofoil-type blower may be as high as 80%, which is competitive with commercial axial-flow fans.

All these favourable characteristics seem to justify the choice of aerofoil-type centrifugal fans for driving blower tunnels, especially since the ability of the blower tunnel to run with the working section exhausting directly to atmosphere means that it can be fitted with a wide range of working sections having a wide range of power-factor contributions, leading to a wide range of blower operating conditions.

Although centrifugal blowers are known to produce a satisfactory flow condition in the working section, very little is known about the flow quality at their outlets because they are primarily designed as suction devices for ventilating systems where the outlet flow is not important. It was felt that this was of major importance in relation to wide-angle diffuser performance and thus an experimental investigation, described in Section 4.2, was conducted. Section 4.3 contains a discussion of these results and some suggestions for the choice or design of the optimum blower for a given tunnel configuration.

4.2 An Experimental Investigation of the Aerodynamic Properties of Centrifugal Blowers

4.2.1 Experimental Details

During this investigation, four centrifugal type blowers were tested. The dimensional details and test conditions for these blowers are given in Fig. 4.2 and Table 7. Although all the blowers had single inlets and backward-facing impellers, the impeller size and shape of each was different. The impeller sizes ranged from 15" (0.4 m) on blower B to 27" (0.7 m) on blower C. Blowers B and C had conventional aerofoil-type blading, which is perhaps the most efficient and thus the most popular type of blading in centrifugal blowers. Blower D had a simplified version of this, consisting of curved metal plates whereas blower A had what appears to be a new concept of S-shaped blades (Fig. 4.1). Two of the blowers (A and D) exhausted vertically upwards and blower D was also connected at the downstream end of an open-circuit tunnel and so the inlet flow may be expected to be non-uniform. The tests comprised flow visualization using wool tufts and smoke, and total pressure scans with varying loading conditions. The smoke was produced by a Taylor generator (Type 3020) by heating high grade kerosene. The total pressures were measured with 2 mm diameter pitot tubes connected to a "Combist" null-reading micromanometer (0.01 mm accuracy). The volume flow rate was monitored by measuring the dynamic

TABLE 7

Details of Centrifugal Blowers Tested

BLOWER TYPE		DIMENSIONS (mm)										TEST CONDITIONS			Blower Exit Direction and Specification of Duct
												Zero Loading		Full Load	
		a	b	c	d	e	f	g	h	i	j	Fan rpm	Volume Flow Rate	Operating Point	
A	Keith Blackman 'TORNADO' 20" Impeller 'S' type metal sheet blades.	311	559	502	400	400	622	51	191	152	51	810	1.89 m^3/sec (4,000 ft^3/min)	60	Vertical Exit 0.8 m Parallel Duct
B	Airscrew Fan Centa/Fugal 15" Heba/B type Aerofoil Blades	203	508	356	305	305	406	25	102	89	114	690	0.87 m^3/sec (1,850 ft^3/min)	10	Horizontal Exit 0.3m Diffuser ($2\theta \approx 19^{o}$)
C	Airscrew-Weyroc 27" Heba/B Type Aerofoil Blades	279	838	660	559	559	724	76	165	140	216	1450	7.08 m^3/sec (15,000 ft^3/min)	6	Horizontal Exit 0.5m Parallel Duct
D	Airscrew-Weyroc 21" curved Metal Sheet Blades (Narrow Width)	373	430	530	375	321	479	51	191	152	51	800	1.51 m^3/sec (3,200 ft^3/min)	-	Vertical Exit 0.4m Parallel Duct

head at the blower inlet using fixed pitot and static tubes connected to a Combist. Depending on convenience, the blower RPM was either measured by a tachometer held against the blower shaft or by shining a stroboscope on the impeller. The photographs in this investigation were taken in the exit plane of the blower, operated at a very low RPM, while all the plotted total pressure measurements were taken in the duct exit plane at a typical operating speed.

4.2.2 Experimental Results

Flow visualization results revealed a vortex-type motion emerging from all the blowers. Fig. 4.4 is a smoke photograph of the vortex emerging from blower B while Fig. 4.5 shows the one emerging from blower A, with the centre quite well-defined in this wool tuft photograph.

The reason for this vortex type flow is the asymmetric positioning of the fan, (Fig. 4.2), causing the flow to deflect into the "empty" regions in the volute. The total pressure distribution at the duct outlet to blower A is shown in Fig. 4.6. The plotted total pressures (C_p) have been non-dimensionalized with respect to P_{at} and the blower inlet dynamic pressure. The flow is seen to emerge from near the sides of the duct, leaving a small region of reversed flow towards the centre of the vortex. In order to assess the flow quality in the absence of a vortex, blower B was partitioned so that the fan was now centrally placed in its half, as in double-entry blowers with full-width rotors. With the vortex almost completely removed, the total pressure distribution was found to be far from uniform (of a parabolic nature). Thus it seems that the vortex might be doing the exit flow uniformity more good than harm. The presence of this vortex might improve the uniformity of the blower exit flow, but what is perhaps more important to establish is the effect of this swirling flow on the wide-angle diffuser performance. In order to determine these effects, a wide-angle diffuser ($A = 2.25$, $2\theta = 15^{0}$) was attached to blower B. This wide-angle diffuser had straight walls and a rectangular cross-section, and expanded in two sections, in one plane at a time. Total pressure scans were taken at the diffuser exit for three different swirl-strength configurations. For the first test, the swirling flow produced by the blower was fed into the diffuser. The swirl strength was then reduced by inserting two screens in the diffuser: a plane screen was installed at the entry to the first section of the diffuser and a curved screen at the entry to the second section. The pressure drop coefficient of the screens was about 1.5 and thus each screen factored the swirl by, at most, about 0.7 (see Section 3.4.3). For the next stage, a paper honeycomb (9.5 mm cell) was installed at the blower outlet and this eliminated almost all signs of the vortex. Figs. 4.7a and 4.7b show the total pressure traverses at the diffuser outlet along the centre-line in each plane. These results are discussed in Section 4.3.

As the loading on blower A was increased by imposing a static pressure drop through screens (comprising of muslin cloth and a slotted plate) at entry, the uniformity of the total pressure distribution was found to improve. Fig. 4.8 shows the total pressure distribution at the duct exit for this blower at "full" load. Compared to the no-load case, (Fig. 4.6), the profile is much more uniform, especially in the central areas. The flow uniformity was found to improve even further when a screen ($K \sim 1.5$) was installed about a third of the way along the duct. On two other blowers tested for loading effects (B and C), the flow uniformity seems to get worse, or at least does not improve noticeably, as the loading is increased (Figs. 4.9a and 4.9b and 4.10a and 4.10b). The answer to the unique behaviour of blower A could lie in the impeller type. While blowers B and C have backward-facing, aerofoil-type impellers, blower A has an S-type backward curved impeller, (Fig. 4.1). A possible explanation is that, when loaded, the S-type blades stall relatively early compared to the aerofoil-type and, through increased mixing, the flow is distributed more evenly at the expense of efficiency, since a higher RPM would be required for a given volume flow rate. Also a higher turbulence level must be expected in the exit flow.

It was noticed during this investigation that although basically the flow emerged from near the blower or duct side walls, it was more prominent along two adjacent sides. In the case of blower D, this prominence switched over to the opposite two sides when the duct was attached, but with blower A, no such switching was observed. Total pressure measurements along two opposite duct walls on blower A, in the streamwise direction, (Fig. 4.11), seem to explain this phenomenon. The pressures are seen to vary in anti-phase thus confirming that the orientation of the exit flow is dependent on the duct length: the flow pattern rotates with the vortex.

These tests show the general and unique aerodynamic properties of centrifugal blowers with single inlets. The desirable properties sought are those suited to a blower used at the upstream end of an open-circuit wind tunnel.

4.3 Discussion of Blower Tests

Two of the four blowers tested (B and C), are normally attached to blower tunnels at the upstream end. These tunnels have fairly uniform flow profiles (0.2% on total pressure) and low turbulence intensity levels (< 0.1%) in the working section. The flow emerging from these blowers with load is, however, far from uniform (Figs. 4.9b and 4.10b). Bradshaw (1967) confirmed that sufficient screening in the wide-angle diffuser and settling chamber eradicated the non-uniformity of the flow emerging from the blower. It must be noted, however, that non-uniform flow from the blower, notably the presence of thick boundary layers, may lead to separation and thence to higher losses and flow unsteadiness in the wide-angle diffuser. These tests thus seem to indicate that departures from a steady and uniform outlet flow are acceptable, although at an expense in tunnel power factor due to the extra smoothing devices needed.

Although the vortex-type flow is characteristic of all the single-inlet centrifugal blowers tested, the strength of swirl generated by each is probably dependent on the ratio of rotor to blower size.

Figs. 4.7a and 4.7b show how this swirling flow, if fed directly into a wide-angle diffuser, ensures an attached flow along the walls but reversed flow in the central regions. With the swirl almost completely eliminated by the honeycomb, the profiles resemble those of a fully developed flow with complete separation on the wall adjacent to the tongue. With the strength of the vortex reduced by the two screens in the wide-angle diffuser, the flow uniformity has somewhat improved and the region of reversed flow in the centre is reduced. This is, in fact, the configuration employed when this blower-diffuser combination is connected to form part of a blower tunnel. It is clear that a swirling component in the flow aids wall flow attachment in the wide-angle diffuser, and by installing screens the uniformity can be improved. It is probably better to have a small region of reversed flow in the centre of the core than one on the walls which can be more susceptible to intermittency and unsteadiness. A swirling component in the blower exit flow may, therefore, be a property to be sought rather than avoided.

A similar vortex-type flow is unlikely to emerge from a double inlet blower, where the rotor is symmetrically placed, though it could produce two small contra-rotating vortices if the ratio of rotor width to casing width is small. Due to the absence of the strong vortex motion, it has been found that the flow is uniformly inclined and takes a relatively longer distance to reattach downstream of the tongue. It may, therefore, be beneficial to have a straight section (with a screen) between the blower exit and the wide-angle diffuser entry. Also, one should be more conservative in designing wide-angle diffusers for double-inlet blowers.

Since blowers of many sizes are commercially available, very few tunnel designers will wish to design their own. For a given blower tunnel, once the maximum required fan-static pressure and volume flow rate have been estimated, the makers' performance charts can be consulted. Optimization between the efficiency, RPM and required power leads to the blower choice. For the benefit of designers who may wish to design or modify blowers for specific purposes, some of the critical components are now discussed.

It is essential to have a tongue that splits the flow efficiently since any malfunction in this respect could seriously affect the uniformity of flow in the vertical plane. It is apparent from the test results that the flow near the wall adjacent to the tongue is better on blower C than on any of the other blowers. One of the reasons for this is that the ratio of tongue height to the casing height is smallest on blower C. A tongue that is too big or badly angled could be improved upon by adding a cusped fairing downstream, as shown dotted in Fig. 4.1. Besides the height and shape of the tongue, the gap between it and the rotor is also critical. In the noise produced by a blower, the blade passing frequency tone and its harmonics are shown (Krishnappa, 1976) to be produced by the interaction of the flow emerging from the impeller and the splitter (tongue). There exists an optimum gap size for which these tones are reduced to a minimum but for aerodynamic reasons, the gap needs to be as small as possible. An optimization process is, therefore, necessary. In axial flow machines, the gaps between blade rows play a similar part in determining noise production and aerodynamic efficiency.

Although blade design may influence the flow uniformity at the blower outlet (as seen in Section 4.2), it is certainly less critical than that of axial-flow fans. If blower efficiency is not too important, these blades could be designed in the same way as corner vanes, by choosing a leading edge angle of 4 - 5 degrees and a zero trailing edge angle. The most common blade shape, as on blowers B and C, is that of a cambered aerofoil, with finite thickness. The above tests seem to indicate that S-shaped blades, although perhaps less efficient, produce exit profiles which are more uniform than those produced by aerofoil-type blades.

The inlet bellmouth can be shaped into a quarter of an ellipse, with its major semi-axis equal to the equivalent inlet diameter and its minor semi-axis equal to three-eighths of the major axis. It is always advisable to attach a filter to the blower inlet so that the screens and honeycomb are protected from foreign particles.

This filter would also help to reduce inlet disturbances. Two or more grades of demembraned polyurethane foam, bonded to a non-rusting internal reinforcement, would make a typical inlet filter. The pressure losses through the filter can be reduced by constructing a "filter box" around the inlet so that the air velocity at the filter panels is lower.

The blower and motor should, if possible, be attached to the same framework. This makes it much easier to manoeuvre the smaller tunnels, often necessary when more than one blower tunnel is housed in the same laboratory. With the larger blowers, it is advisable to bolt the framework to the floor through anti-vibration mountings so as to reduce resonant effects due to vibration. In this respect, it is helpful to couple the blower to the tunnel with a flexible coupling. Besides reducing vibration, this makes it easier to remove components like screens for cleaning.

The results and suggestions presented in this section have been generalized for most single-inlet centrifugal blowers with backward-facing impellers and indicate that, for most purposes, commercially available blowers are adequate.

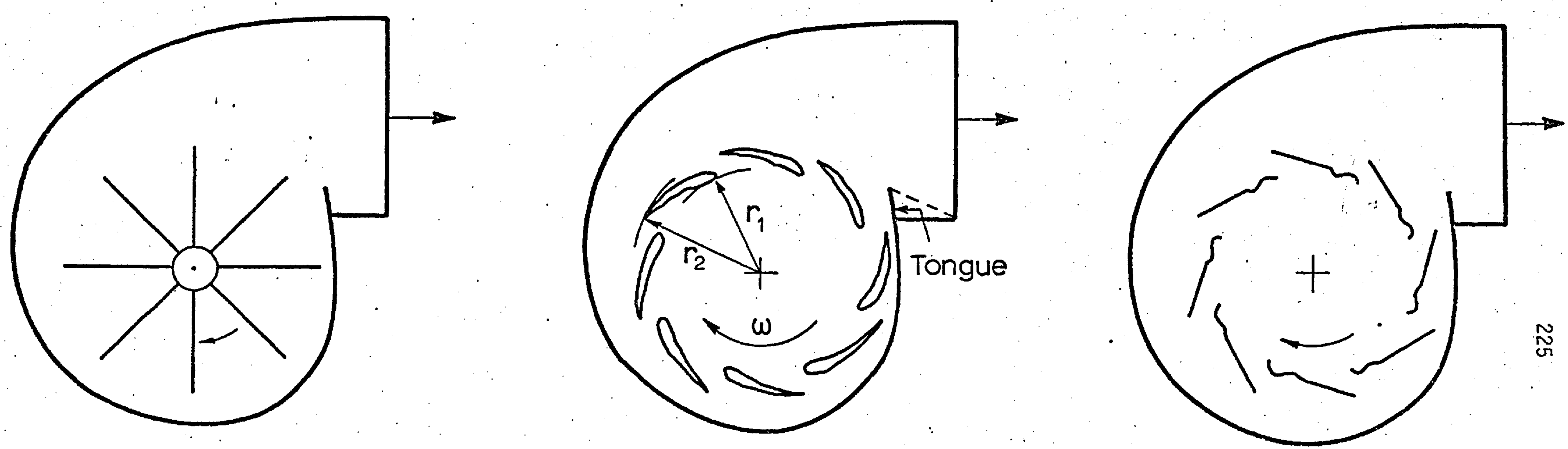

a. Radial-vane blower

b. Backward aerofoil blower

c. Backward S-type blower

Fig. 4.1 Different impeller-types used in centrifugal blowers.

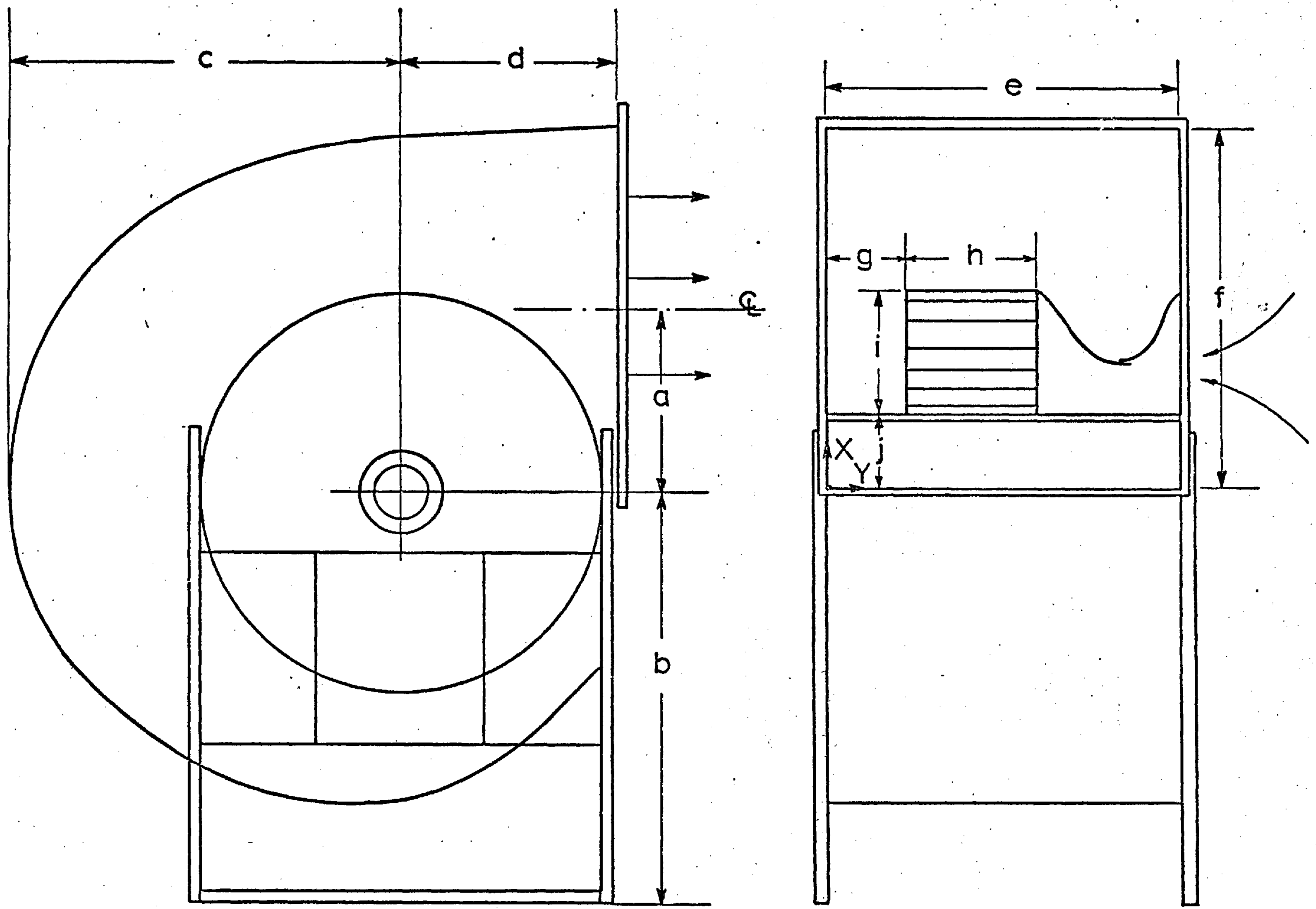

Fig. 4.2 Centrifugal blower dimensions (lettering refers to Table 7).

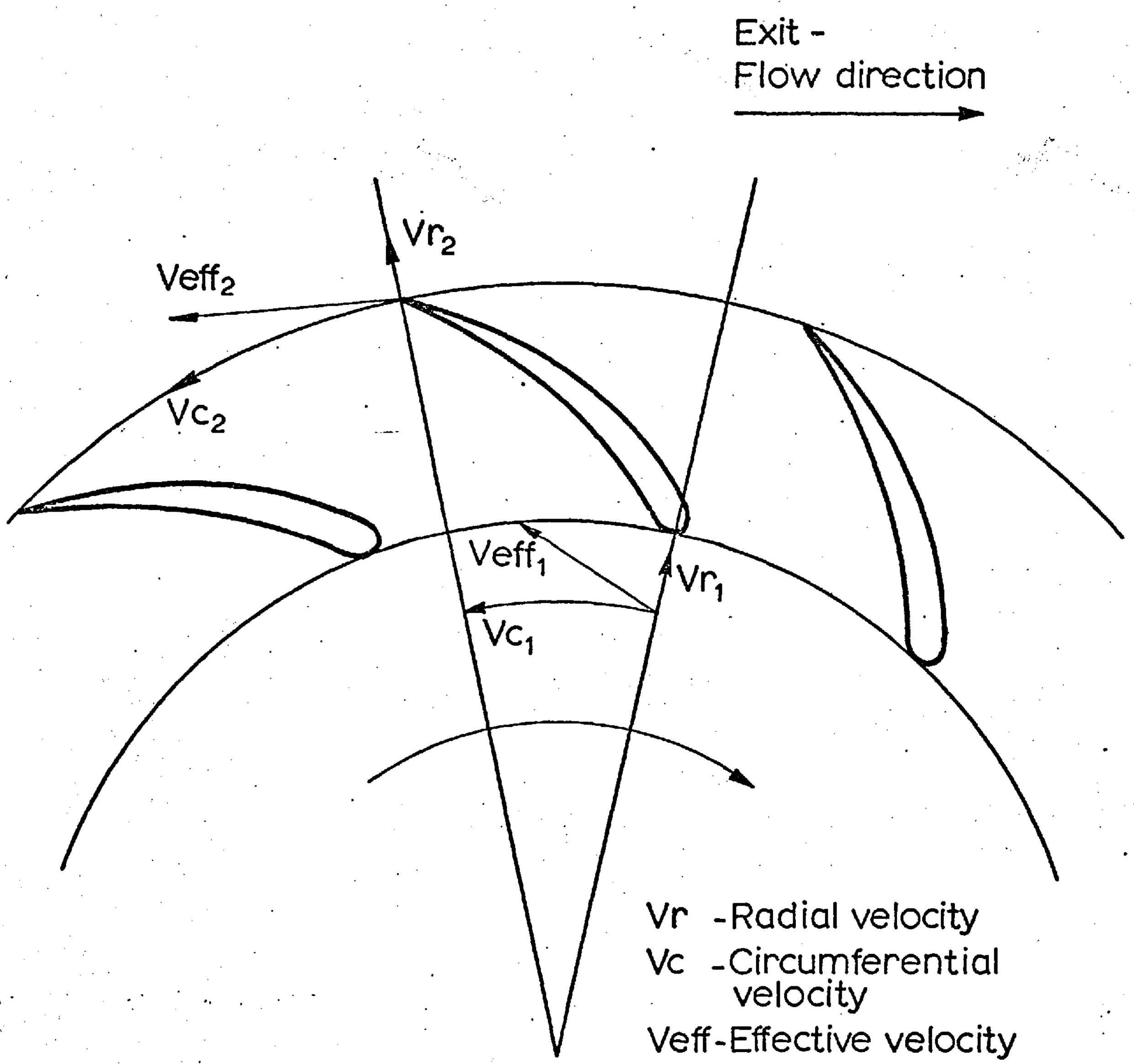

Fig. 4.3 Velocity triangles for an aerofoil-type rotor.

Fig. 4.4 Smoke photograph of the flow emerging from blower B. (The tongue is adjacent to the bottom wall and the rotor is biased towards the right-hand side wall).

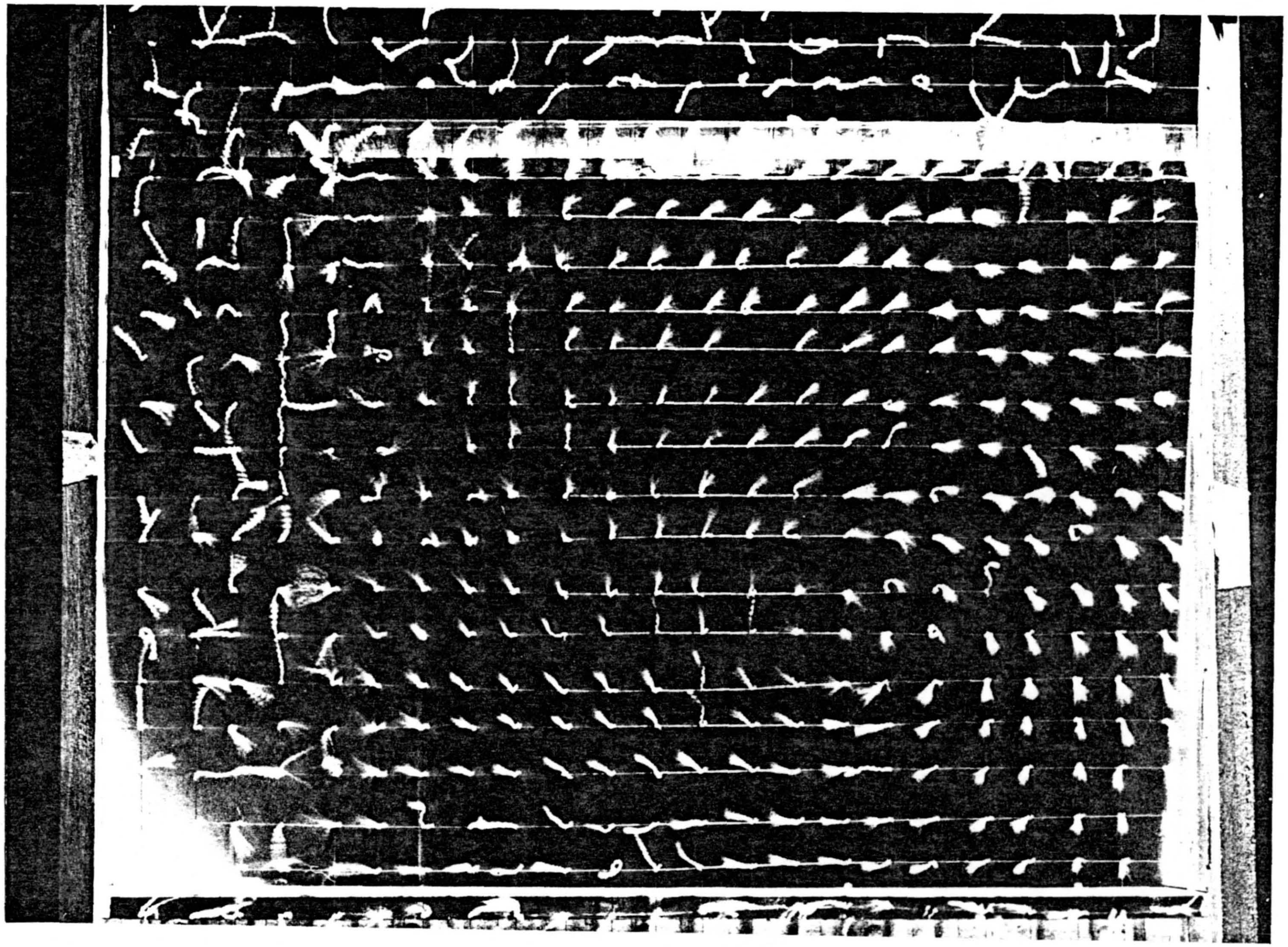

Fig. 4.5 Wool-tuft photograph of the flow emerging from blower A. (The tongue is adjacent to the left-hand side wall and the rotor is biased towards the top wall).

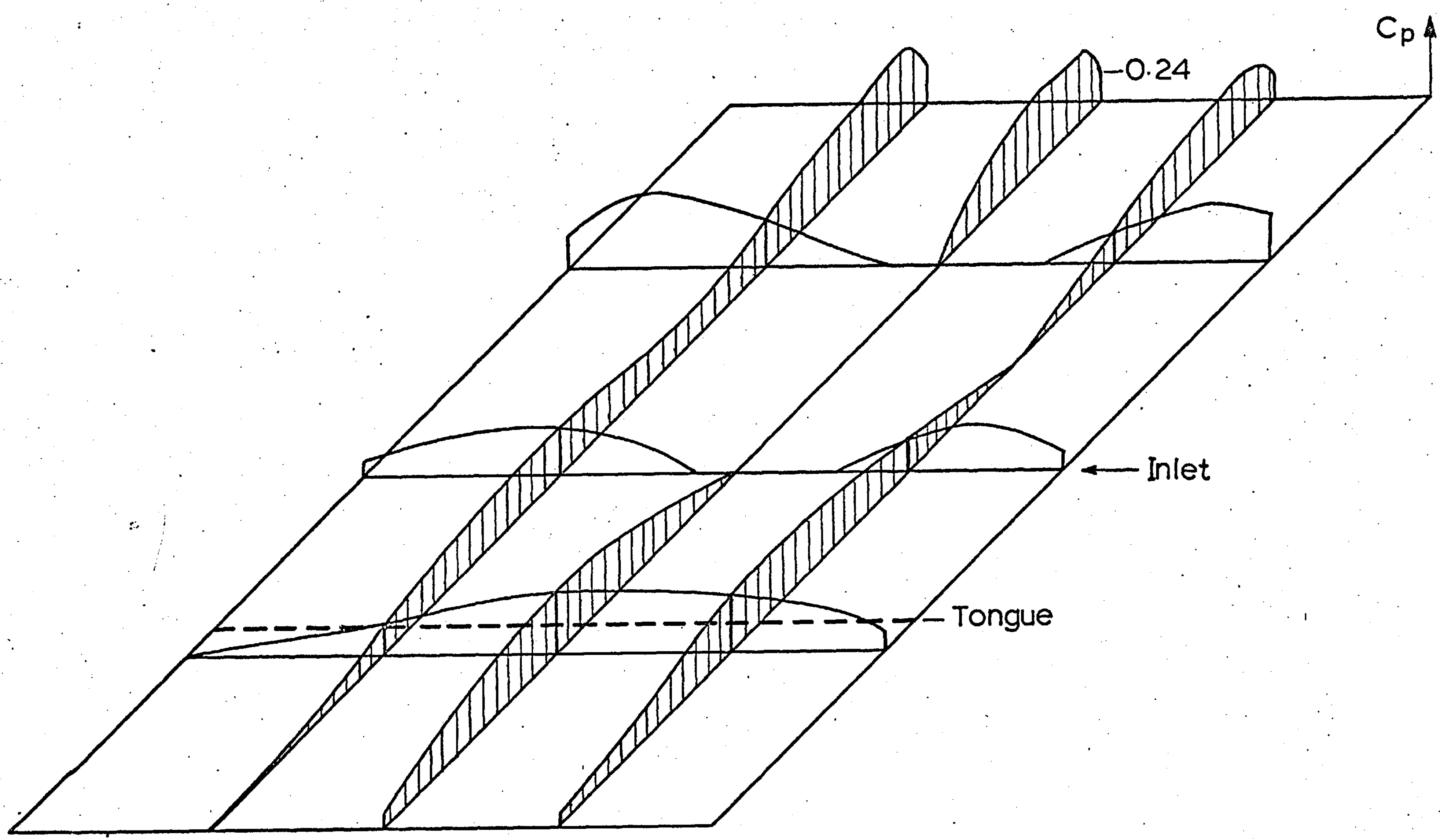

Fig. 4.6 Total pressure distribution at duct exit : blower A with "no-load".

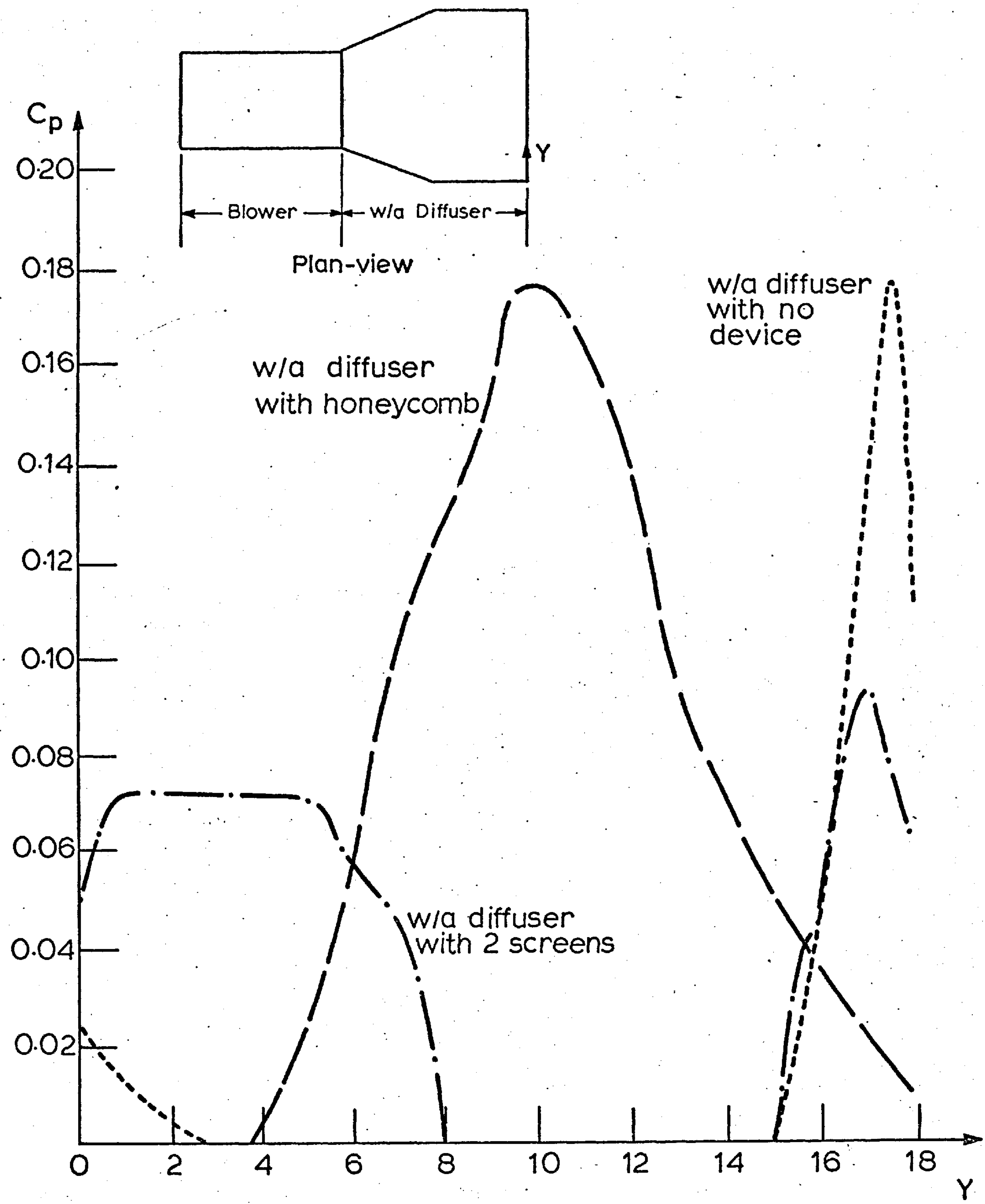

Fig. 4.7a Horizontal total pressure distribution at the wide-angle diffuser exit : blower B with varying degrees of swirl.

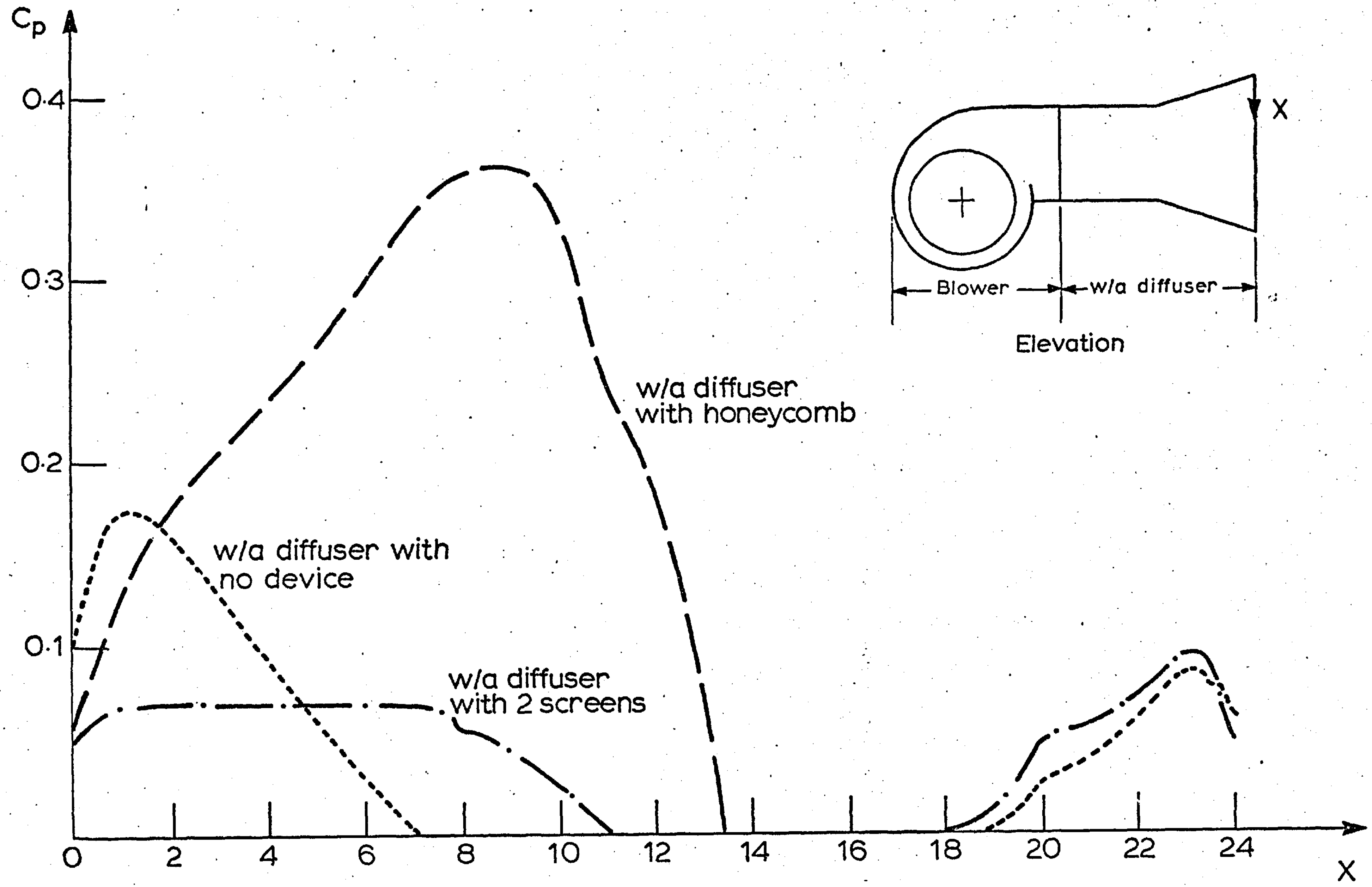

Fig. 4.7b Vertical total pressure distribution at the wide-angle diffuser exit : blower B with varying degrees of swirl.

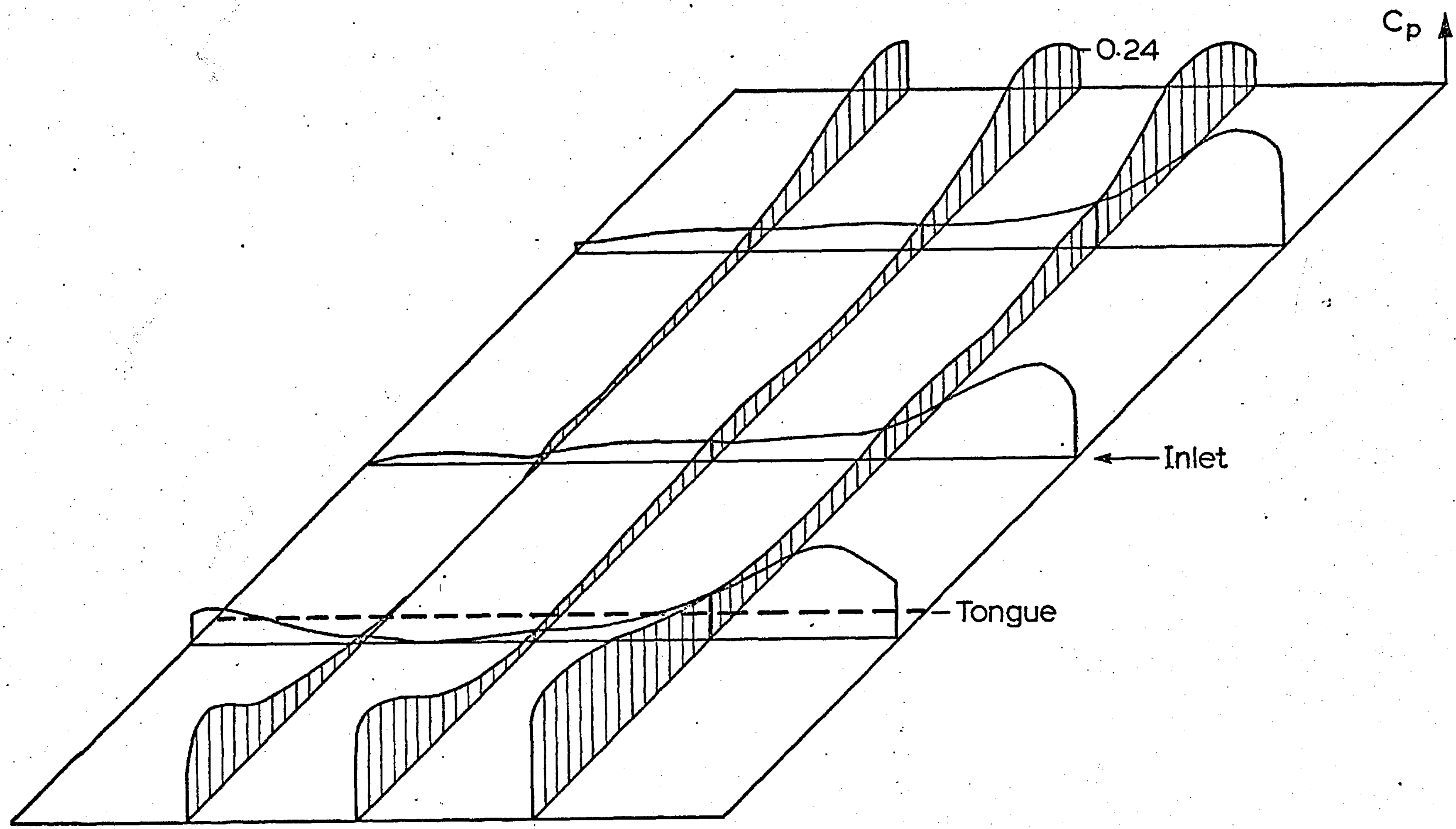

Fig. 4.8 Total pressure distribution at duct exit : blower A with "full load". Operating point ≡ 460.

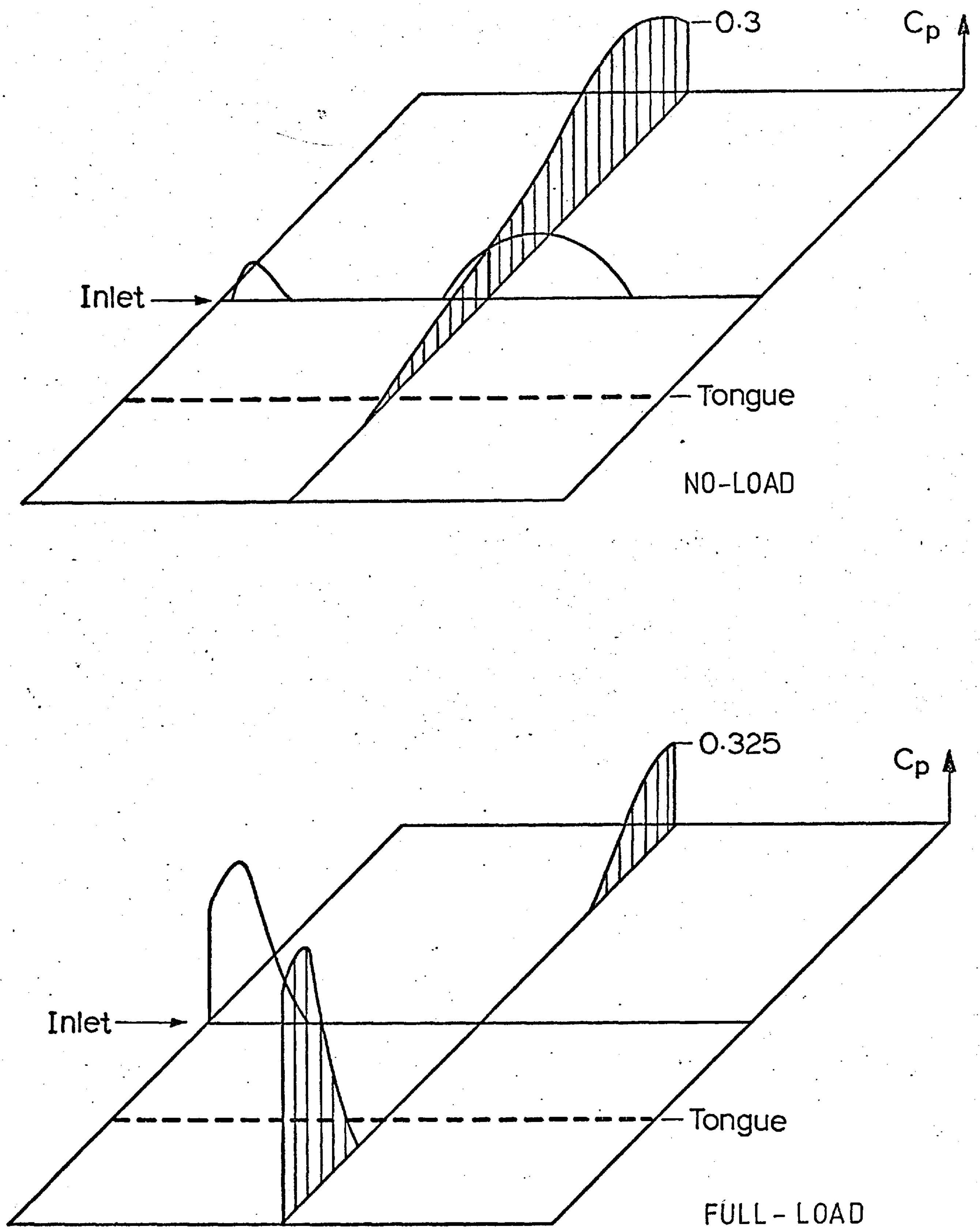

Fig. 4.9 Total pressure distributions at duct exit : blower B showing effect of loading. Operating point ≅ 10.

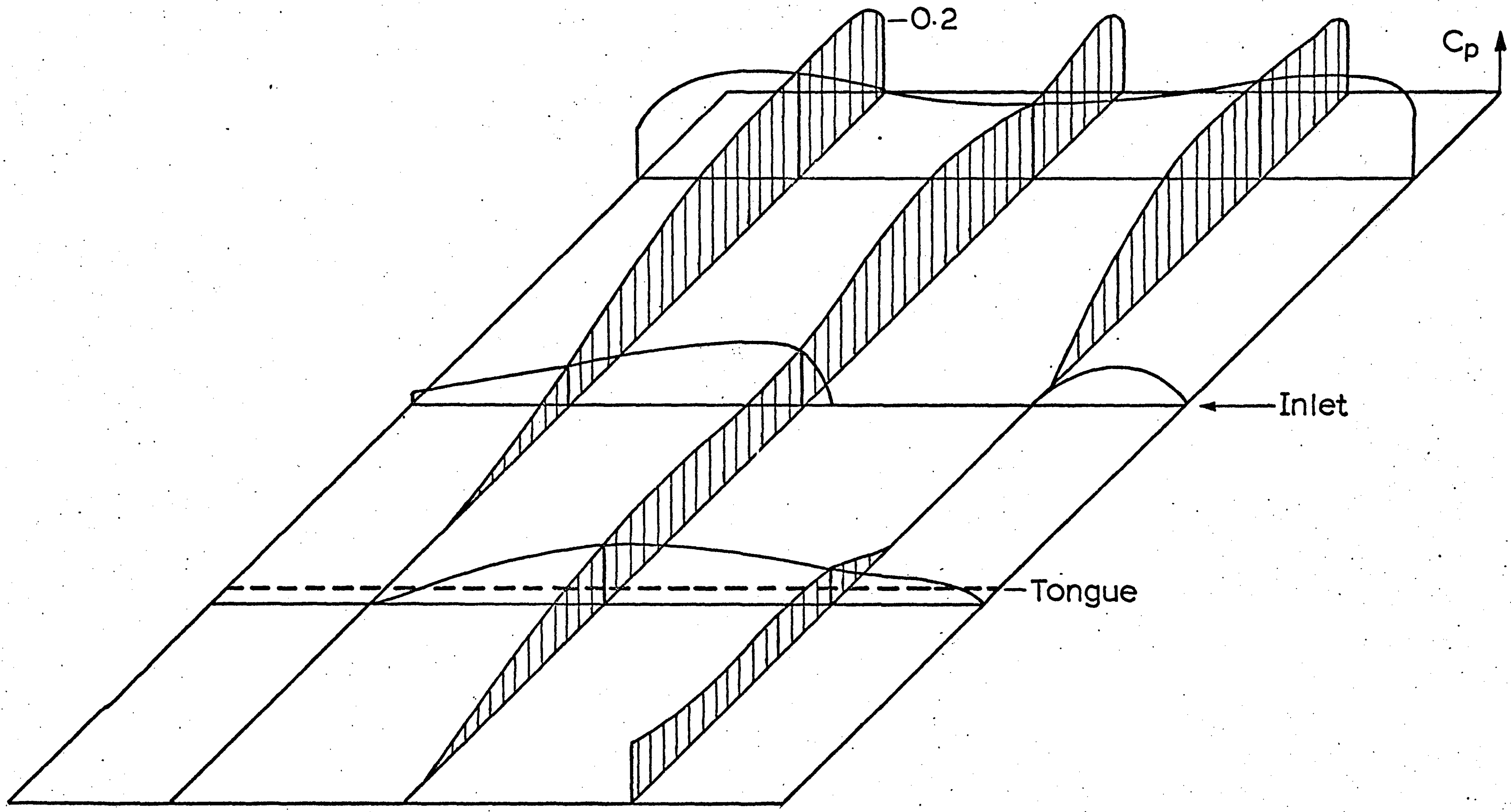

Fig. 4.10a Total pressure distribution at duct exit : blower C with "no-load".

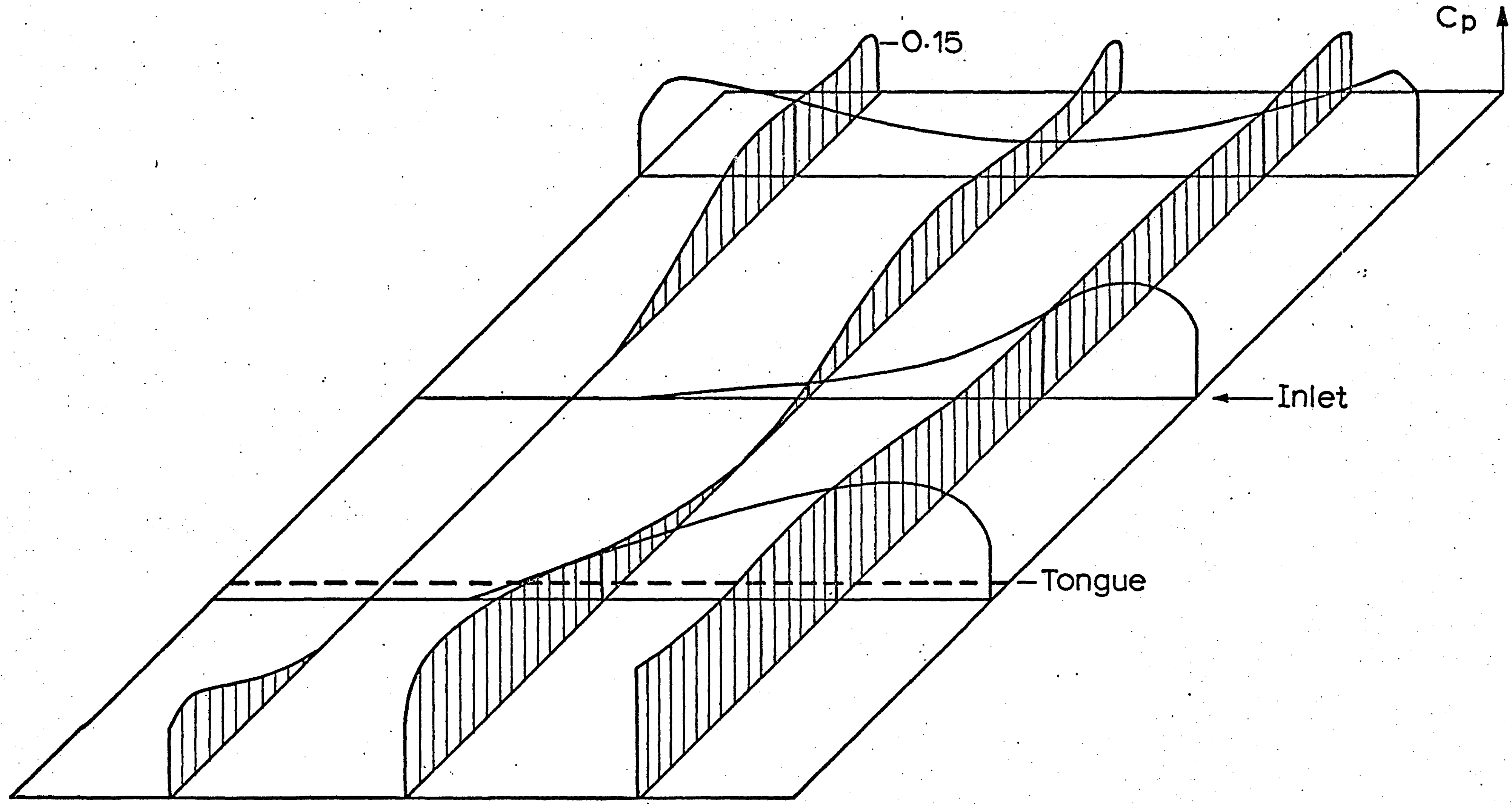

Fig. 4.10b Total pressure distribution at duct exit : blower C with loading. Operating point ≡ 5.5.

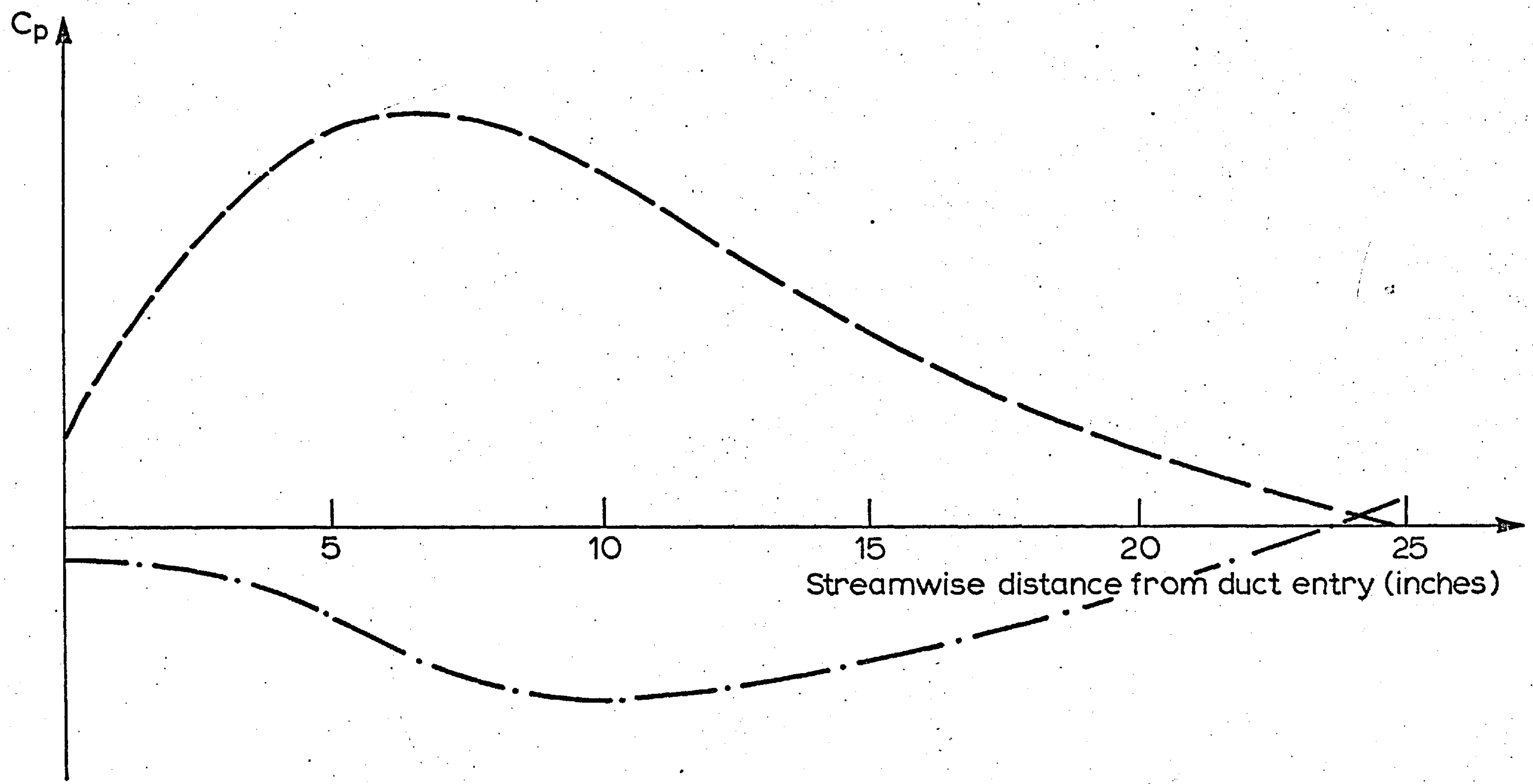

Fig. 4.11 Streamwise total pressure variation on opposite walls of duct on blower A.

CHAPTER 5

DESIGN OF THE OTHER BLOWER TUNNEL COMPONENTS

5.1 Contractions

5.1.1 General Considerations

Practically all wind tunnels have a contracting nozzle fitted upstream of the working section, for two main reasons:-

(i) A contraction increases the flow mean velocity and this allows the honeycomb and screens to be placed in a low speed region, thus reducing the pressure losses and the tunnel power factor.

(ii) Since the total pressure remains constant through the contraction, both mean and fluctuating velocity variations are reduced to a smaller fraction of the average velocity at a given cross section. The most important single parameter in determining these effects is c, the contraction ratio.

The factors of reduction of mean velocity variation and turbulence intensity derived theoretically for axisymmetric contractions, with $c \gg 1$, by Batchelor (1953) are given below:-

(i) U-component mean velocity: $\frac{1}{c}$

(ii) V or W-component mean velocity: $\sqrt{c}$

(iii) u-component r.m.s. intensity: $\frac{1}{2c}\{3(\ln 4c^3 - 1)\}^{\frac{1}{2}}$

(iv) v or w-component r.m.s. intensity: $\frac{(3c)^{\frac{1}{2}}}{2}$

(The factor of reduction of fractional velocity variation is given by dividing the above expressions by c).

It is seen that a contraction is less efficient in suppressing longitudinal turbulence than mean velocity variation. The reduction of mean velocity variation can be easily demonstrated by applying Bernoulli's equation to a non-uniform flow through the contraction (see Bradshaw, 1970, p.58). The transverse fluctuations are enhanced, in absolute level, in a contraction: this effect is best explained qualitatively by considering the motion of the vortex elements which constitute the turbulence field. It is sufficient to treat the vortex filaments aligned with and perpendicular to the streamwise direction. The effect of the contraction is to stretch the filament with its axis in the streamwise direction, thus increasing v and w and compressing the filaments perpendicular to the streamwise direction, so decreasing u. The reduction of fractional variation of the lateral component is much less than that of the longitudinal component, so that it is often the desired reduction in the former which decides the contraction ratio. Typically $\sqrt{\overline{v^2}}$ is two or three times $\sqrt{\overline{u^2}}$ after a large contraction.

The design of a contraction of given area ratio centres on the production of a uniform and steady stream at its outlet and requires the avoidance of flow separation in the contraction. Two of the more desirable criteria are minimum exit boundary layer thickness, and minimum contraction length which also reduces the length and cost of the tunnel. The danger of boundary layer separation results from the presence, in any contraction of finite length, of regions of significant adverse pressure gradient on the walls at each end. Near the wide end the streamlines are necessarily convex outward. By applying an order-of-magnitude argument to the V-component Navier-Stokes equation, we obtain the "centrifugal force" equation (Cebeci and Bradshaw, 1977, p.41):-

$$\frac{\partial p}{\partial y} \approx - \rho U \frac{\partial V}{\partial x} \approx \frac{\rho U^2}{R}$$

where R is the radius of curvature of the surface or strictly the considered streamline.

So the static pressure near the walls is greater than that near the centre-line and, therefore, greater than the average pressure over the cross-section. But the cross-sectional-average pressure at the start of the contraction is closely equal to the pressure far upstream since the cross-sectional area and average velocity are the same. Thus the wall pressure increases from a point far upstream to a point in the wide end, before decreasing as the effect just described is overwhelmed by the effects of decreasing cross-sectional area. The converse applies at the narrow end. However, the boundary layer at the contraction exit is less liable to separate, because of its reduced thickness, unless it has relaminarized in which case care must be taken. A laminar boundary layer, however, is often sought at the contraction exit if the working section floor boundary layer is to be investigated; a trip can then be used to ensure well-documented transition.

It is always possible to avoid separation by increasing the contraction length sufficiently, provided it has a reasonable wall shape. Increasing the length, however, increases boundary layer growth due to skin friction, not to mention the space/cost consideration. On the other hand, a contraction that is too short may suffer from boundary layer separation leading to flow unsteadiness and non-uniformity, besides reducing the effective contraction ratio. It is worth noting that when a contraction is shortened, say by ΔL, the upstream and downstream distances within which local velocity profile distortions are still important on the parallel walls increase, and the effective saving is less than ΔL.

A design satisfying all criteria will be such that separation is just avoided and the exit non-uniformity is equal to the maximum tolerable level for a given application (typically $\pm \frac{1}{2}\%$ velocity variation outside the boundary layers).

5.1.2 Contraction Ratio

There are certain advantages in using large contraction ratios. The power-factor contribution of the screens varies as $\frac{1}{c^2}$ and velocity variations are reduced with increasing c. In particular, the effects of small separations at the wide end may be obliterated in contractions with large c. On the other hand, a contraction with a very large area ratio and a reasonable length would have large wall angles and, consequently, large curvature near the ends, which could result in separation. Also problems due to blower noise could be magnified when large contraction ratios are used because the contraction acts like a horn. Therefore, contraction ratios of between about 6 - 9 are normally used. If c = 6, a screen with a pressure drop coefficient of 1.5 produces a power factor contribution of 0.05, 5 or 10% of the power factor of a typical blower tunnel. The upper limit on c is often fixed by the maximum acceptable length of the contraction or the maximum acceptable distance of the tunnel centre-line from the floor of the room, 1.5 m approximately.

5.1.3 Cross-Sectional Shape

Another important contraction parameter is the cross-sectional shape. In a contraction with an irregular polygonal cross-section, the flow near the walls tends to migrate across the corners between adjacent walls. Even if such crossflows are avoided, as in a "two-dimensional" contraction or one with a symmetrical cross-section, the boundary layers near the corners will be more liable to separate. The optimum cross-section in this respect is, therefore, circular. Small contractions can be moulded from fibre-glass, but this is not convenient for large units, and so to compromise between difficulties of construction and undesirable boundary layer effects in the corners, contraction cross-sections in large tunnels are often octagonal. It is often assumed for design purposes that both the potential flow and the boundary layers behave as in a contraction of circular cross-section.

In order to assess the importance of corner flow separation, an experimental investigation was conducted on some existing contractions in the Aeronautics Department. Spanwise skin friction measurements were made with a 2 mm pitot tube in the working sections of three tunnels (an 18" x 18" blower tunnel, a 3' x 3' return-circuit and a 4½' x 4' return-circuit tunnel). In each case, the boundary layer was tripped at the contraction exit by an 18 SWG wire. The results, presented in Fig. 5.1, show that the skin friction distribution in the 18 in tunnel is highly non-uniform. The longitudinal pressure gradient is small and virtually constant over the cross-section; the changes in skin friction are far too large to ascribe to circumferential changes in Reynolds number based on boundary layer thickness, and it may, therefore, be deduced that secondary flows are responsible. This contraction has fillets in the corners, specifically installed to avoid separation, which taper down to zero in the working section, (see Fig. 3.2). Tapered fillets can act as (rather inefficient) vortex generators, and the skin friction pattern is comparable with the arrangement of vortices sketched in Fig. 5.1.

On the other hand, the distribution in the $4\frac{1}{2}'$ x 4' tunnel, which also has fillets in the contraction corners, shows no signs of any such secondary flows, except very near the corners. The fillets in this tunnel taper down to zero within the contraction and so the boundary layer growth and hence the strength of the vortices must be negligible compared to the previous case. The fillets in this contraction help to form a roughly octagonal cross-section and this, together with the other tunnel legs, form a transition section to the circular cross-section where the axial fan is housed.

The 3' x 3' tunnel contraction has a square cross-section, without fillets, and the skin friction distribution for this tunnel also indicates that no severe secondary flows exist, except very near the corners. The reason for the better distribution in this tunnel, away from the corners, is probably the better quality of the last screen rather than a better contraction design.

So it seems that the corner flow separation in a contraction may not be of primary importance to the quality of the working section flow and that a square (or rectangular) cross-section, without fillets, may be adequate. This is especially advantageous in blower tunnels since all the other components are also almost always square or rectangular.

Two-dimensional contractions are not very common, although they present fewer constructional difficulties. If the inlet boundary layers are thick, the plane walls tend to develop strong secondary flows, in the form of two contra-rotating vortices. This is mainly due to the lateral convergence of the boundary layers (Bansod and Bradshaw, 1972). Also, they require about a 25% longer distance to attain the same wall pressure coefficient and non-uniformity decay rate as an axisymmetric one. Moreover, for a contraction of given area ratio and length, the adverse pressure gradients are greater in a two-dimensional contraction and thus a bigger safety margin is necessary. However, they are sometimes preferred on tunnels used for boundary layer studies, where the working section is wide but shallow.

5.1.4 Wall Shape (Side-View)

The contraction wall shape is another important parameter and several theoretical design methods have been developed.

(i) Potential Flow Calculation Methods

In the absence of separation, the flow in a contraction may be adequately described by the Laplace equation. The solution of this linear equation is relatively easy for simple geometries and many analytical solutions have been derived. The solutions for axisymmetric contractions are based on a series solution of either the Laplace equation for the velocity potential (Thwaites, 1946), or the Stokes-Beltrami equation for the stream function (Cohen and Ritchie, 1962), for a given velocity distribution along the centreline. (Note that the Stokes-Beltrami equation is not quite of the same form as the axisymmetric Laplace equation: see Batchelor (1967), p. 451). The solution produces an infinite set of stream-surfaces at different distances from the axis, and the most distant one with tolerable pressure gradient (leading to the shortest contraction) is chosen as the wall contour.

Two-dimensional cases are usually solved in the hodograph (U, V) plane. In the hodograph technique, one specifies the relation between the wall velocity $\left[(U^2+V^2)^{\frac{1}{2}}\right]$ and the wall angle $\left[\mathrm{Tan}^{-1}\ (U/V)\right]$ as a curve in the hodograph (velocity) plane and then transforms this to the real plane. Jordinson's (1961) hodograph method, for large contraction ratios, deserves special mention because he solves the flow in each end of the contraction separately, assuming that, in the limit of high contraction ratios, the shape of the wide end becomes independent of that of the narrow end (and vice versa) because the flow in between is closely radial without significant longitudinal streamline curvature. This technique has been found to work very well for $c \geq 10$.

Attempts to derive axisymmetric contraction shapes from two-dimensional ones have had limited success. Since most contractions have large contraction ratios, any simple scaling of cross-sectional area can lead to unacceptable wall shapes. An exception is the approximate method of Whitehead et al (1951) for calculating the flow in an axisymmetric contraction, once the flow in the two-dimensional contraction with the same wall shape is known. Although it is assumed that the streamlines are the same in both cases, the velocity along the streamlines in the axisymmetric case is made to satisfy the axisymmetric continuity equation.

With the onset of computers, numerical methods have now taken precedence. Smith and Pierce (1959) gave a numerical method for calculating the two-dimensional or axisymmetric flow within a given boundary using a distribution of sources on the boundary. More recently, Laine and Harjumäki (1975) computed the potential flow in axisymmetric contractions by an accurate method in which the Stokes-Beltrami equation is solved with a finite difference approach. Morel (1975) in his numerical study, starts with a given wall shape (formed of two cubic arcs) and solves for the velocities within it. He also plots design charts in which the parameters are the maximum wall pressure coefficients at the inlet (as an indication of the danger of separation at this end) and at the exit (as an indication of the non-uniformity of exit velocity). For any choices of these two parameters, (optimum values vary with Re), the charts yield the "shape parameter" and the nozzle length, for this particular family of shapes.

There is no wholly satisfactory method of theoretical contraction design. Most of the methods, except perhaps that of Morel (1975), are only mathematical tools to be used for the analysis of the flow and offer little concrete design information. The application of all the methods described above require the establishment of some criteria and then the application of trial-and-error techniques, for which limited guidance is given. Also, the methods necessarily simplify the problem by assuming that the velocity profile at inlet is perfectly uniform, which is unlikely in practice even though non-uniformities bad enough to affect contraction performance are probably unacceptable for other reasons.

(ii) <u>Design by Eye</u>

Because of all the drawbacks mentioned above and because it is often just as easy to choose a boundary shape as it is to choose a suitable criterion, designers have often used the rather unscientific method of design by eye. If this method is employed, it should be noted that the actual form of a contraction contour is not very important except near the inlet and outlet.

Hussain and Ramjee (1976) confirmed this by studying the effects of axisymmetric contraction wall shapes on incompressible turbulent flow. They analysed four different contraction contour shapes and found that variations within the nozzle, but outside the boundary layers, of the mean velocity and the longitudinal and radial components of turbulence intensity were independent of the contour shape, at least as long as separation did not occur. The nozzle with the cubic equation ($R = a_0 + a_1 x + a_2 x^2 + a_3 x^3$), and the smallest inlet curvature, was regarded as the optimum wall shape. This nozzle gave the smallest boundary layer thickness and the lowest boundary layer turbulence intensities in the exit plane.

In general, the wall radii of curvature should be less at the narrow end of the contraction than at the wide end, but large enough to avoid separation. A too-gradual transition to the parallel working section delays the development of a uniform velocity profile and this increases the effective contraction length unnecessarily. Also, the radii of curvature at the wide end should be large enough to avoid separation. Undue thickening or separation of the boundary layers near the contraction entry causes, in addition reduction of the contraction ratio. The flow through the last screen tends to be distorted when the adverse pressure gradient present in the contraction entry extends up to it. This distortion is in the form of a non-uniform pressure drop; the higher-pressure, low velocity regions near the walls undergo a smaller pressure drop than the high speed, low pressure regions. This results in a non-uniform total pressure distribution which will persist indefinitely. The screen, by way of its refractive properties, also transfers some of the adverse pressure gradient upstream, but this is not necessarily detrimental. Also, a screen placed too near the contraction entry may affect the turbulence level in the working section, particularly in small tunnels where the ratio of screen wire diameter to contraction length is greater. However, these undesirable effects can always be avoided by installing the last screen sufficiently upstream of the contraction entry (see Section 5.2.3).

A slowly tapering "infinite-length" contraction can conveniently be terminated at the last screen and the walls made parallel upstream of this, since any extra adverse gradient introduced by the truncation will occur upstream of the screen: again the undesirable effects of placing a screen too near the contraction entry must be considered. Ideally, each end must join the parallel sections so smoothly that at least the first and second derivatives of the contour curve are zero (or very small) at the ends. Thus, design as well as constructional care must be taken if a successful contraction is to be produced.

5.1.5 Optimum Design Procedure

The design methods and analysis described above seem to indicate that a contraction wall shape formed of two smoothly-joined cubic arcs should give acceptable results for normal shapes of cross-section. Theoretical design methods are shown to provide useful guidelines (rather than infallible design techniques) for contraction wall shape design. It seems that in most cases an "eye-design" or a design based on one that is known to be good can serve as well as any other technique, and with less design effort. Both in design and in construction, it must be remembered that smoothness in contour shape is much more important than the exact dimensions. If the contraction to be designed is of large dimensions and if the design is thought to be critical, then it is advisable to test a model first.

If a model contraction is tested, care must be taken in simulating the exact transition behaviour of the full-size version. It is often most convenient to use a "well-behaved" suck-down arrangement (with a honeycomb and screens) for model testing. The model can then be tested with a non-uniform or asymmetric inlet profile, by simply obstructing part of the bellmouth. It is worth ensuring that any small-scale non-uniformities in the full-scale tunnel can be accepted, particularly since the flow out of a centrifugal blower is so non-uniform.

5.2 Settling Chambers

5.2.1 General Arrangement

In open-circuit blower tunnels, settling chambers are created rather than designed since the frames containing the honeycomb and screens, clamped together, usually form the settling chamber. The usual arrangement consists of a honeycomb (with about 25,000 cells) followed by screens, the number and K-value depending on the turbulence level requirements in the working section. However, more than about two or three screens ($K \sim 1.5$) are not normally required in a well-designed blower tunnel with screens in the wide-angle diffuser. The optimum choice for gauze screens has already been discussed in Chapter 3. We now briefly discuss the choice and effects of honeycombs.

5.2.2 Honeycombs

Screens are not very effective for removing swirl and lateral mean velocity variations. It is preferable, for this purpose, to employ honeycombs, as long as the flow yaw angles are not greater than about 10^{o}. Large yaw angles cause the honeycomb cell to "stall" which reduces their effectiveness besides increasing the pressure loss. In order to diminish the transverse and swirl components to an acceptable level, and increase the directive effect of a honeycomb, the cell length must be at least 6 - 8 times its diameter. The cross-sectional shape of honeycomb cells is usually hexagonal, but sometimes square or triangular, the shape being chosen mainly for ease in construction (see below).

An incidental effect of honeycombs in wind tunnels is to reduce the turbulence level in the flow. Essentially, the lateral components of turbulence like those of mean velocity, are inhibited by the honeycomb cells and almost complete annihilation is achieved in a length equivalent to about 5 - 10 cell diameters. Honeycombs themselves shed small scale turbulence, the level of which is found to be higher when the cell flow is laminar than when it is turbulent. This is attributed to a basic instability of the laminar near wakes (Lumley and McMahon, 1967).

Lumley and McMahon calculated performance charts for honeycombs with fully developed cell flow and $Re_d > 2000$ which give the turbulence reduction factors, if the scale and intensity level of the existing turbulence are known. They also took account of the turbulence created by the honeycomb and concluded that a higher net reduction was obtained when the cell flow was turbulent. However, their analysis and tests were originally intended for honeycombs in high-Re water tunnels, where at the relatively high dynamic pressures gauze screens suffer from problems of high loads and "singing" due to vortex shedding from the wires. The minimum Re_θ for the existence of a turbulent boundary layer is 320 according to Preston (1958); this corresponds to an Re_x of about 3×10^5. So in a wind tunnel with a typical settling chamber velocity of 5 m/s, a honeycomb length of at least 0.9 m is required to attain a fully turbulent cell flow. Also, (circular) pipe flow remains laminar, even in the presence of large inlet disturbances, for $Re_d <$ 2000. Thus, at 5 m/s airspeed, turbulence will never occur, however long the honeycomb, if the cell diameter is less than about 6 mm.

Loehrke and Nagib (1976) tested straw honeycombs made of plastic drinking straws at an airflow velocity of 4.8 m/s, giving a Re_d of 1250. For the longest honeycomb ($\ell/d \sim 56$), the Re_x was about 8×10^4 and a fully developed laminar flow was obtained. They found that although the <u>internal</u> reduction of turbulence was a maximum for this honeycomb, the <u>net</u> reduction was greater for the shortest one ($\ell/d \sim 5.6$). It turns out that the shear layer instability in the near wake is sort of proportional to the shear layer thickness and so for the longest honeycomb, the ratio of turbulence generated to that suppressed is greater.

Therefore, in order to obtain the maximum overall benefit from a honeycomb, the optimum cell length to diameter ratio should be about 6 - 8. The cross-sectional size and shape of the honeycomb cells are not critical and are often determined by availability. For the suppression of turbulence, however, it is advisable to use small cell sizes; in any case, the cell size should be smaller than the smallest lateral wavelength of the velocity variation. In most cases very roughly 150 cells per settling chamber diameter (say, a total of 25,000 cells) are adequate.

Impregnated paper honeycombs with cell "diameters" down to about 5 mm are usually adequate when small sizes, less than about 1 m x 1 m, are needed. Any form of deflection or distortion of a honeycomb can change its aerodynamic properties considerably, and thus, for larger sizes, metal honeycombs must be considered. Aluminium honeycombs made for aircraft sandwich construction have more precise dimensions than paper honeycombs and are to be preferred for high performance tunnels. Metal honeycombs can also be made by spot-welding corrugated strips between flat strips, giving a roughly triangular shape.

With any choice of honeycomb, it is important to ensure that the cells are straight and uniform.

5.2.3 Optimum Layout of Components

As mentioned above, a flow with large yaw angles often causes the honeycomb cells to stall thus reducing the effectiveness and increasing the pressure loss. Therefore, if severe yaw or swirling flow is expected from the wide-angle diffuser, it is advisable to install one screen upstream of the honeycomb, so that the swirl angles are reduced. A screen with $K = 1.5$ reduces yaw or swirl angles by a factor of about 0.7, for swirl angles of about 40° (see Section 3.4.3).

The honeycomb should be installed some way downstream of the diffuser exit anyway so that the flow static pressure and angles have had a chance to become more uniform.

As mentioned in Section 3.1.2, screens with small open-area ratios (less than about 0.57) tend to produce strong longitudinal vortices formed by coalescing jets which persist through the length of the contraction, possibly amalgamating with the Taylor-Görtler vortices produced in the longitudinal concave curvature. These persisting vortices cause a spanwise variation in the working section skin friction and hence in the boundary layer thickness as well. So if a purely two-dimensional boundary layer is required in the working section, a screen with a large open-area ratio ($\beta > 0.57$) should be placed in the most downstream position. Another alternative is to place the honeycomb (with the larger β) downstream of the screens. Bradshaw (1972) did this successfully and found that the corresponding rise in turbulence level was quite acceptable (less than 0.1% final level).

In a multiple screen combination, an important parameter is the spacing between successive screens. There are two important properties to consider; the pressure drop and the turbulence reduction. For the pressure drops through the screens to be completely independent, the spacing should be such that the static pressure has fully recovered from the perturbation (i.e. $\frac{dp}{dy} = 0$). For full benefits from the turbulence reduction point of view, the minimum spacing should be of the order of the large energy containing eddies. It has been found that a screen combination with a spacing equivalent to about 0.2 settling chamber diameters performs successfully. The effectiveness of a honeycomb, as far as the reduction of turbulence is concerned, can be improved upon by installing the next screen fairly close to it (Loerkhe and Nagib, 1976). The optimum spacing is probably a function of the uniformity of the mean flow and the scale and isotropy of the oncoming turbulence.

The optimum distance between the last screen and the contraction entry has been found (Morel, 1975; Laine and Harjumäki, 1975) to be about 0.2 cross-section diameters. If the distance is much shorter, significant distortion of the flow through the last screen may be expected, as discussed in Section 5.1.4. On the other hand, if this distance, or for that matter the overall length of the settling chamber, is too long, then unnecessary boundary layer growth occurs.

In small tunnels, screens are normally tacked onto wooden frames so that when clamped tightly together, the high spots of the woven-wire screen sink into the frames, giving a firmer hold. More care must be taken when tacking-on plastic screens since these, being more flexible than the metal ones, tend to wrinkle along the lines of tension. The honeycomb is usually just push-fitted into a screen frame. A useful arrangement, for the smaller tunnels, is to rest the wide-angle diffuser, screen frames and contraction on a table and clamp them by drawbolts, so that frames can be withdrawn easily (e.g. for cleaning and replacing screens). On larger tunnels, it is advisable to equip the settling chamber (and wide-angle diffuser) components with castors for ease of removal.

5.3 Working Sections

Working section design is totally dependent on the requirements of each individual experiment. Many blowers have detachable working sections without exit diffusers, a very flexible arrangement. An exit diffuser, the design of which was briefly discussed in Section 2.1, must be fitted if the tunnel power factor is critical. The wide variety of blower tunnel working sections range from quasi-two-dimensional ones (for boundary layer studies or smoke tests) to ones with special features such as slotted walls and flexible roofs. In Fig. 1.3, some of the many different working section configurations used on the small blower tunnels at Imperial College are shown.

For tunnels which are used for testing models mounted in the working section, the working section size and shape are usually dictated by the need to minimize tunnel interference for a predetermined model size. The most popular cross-sectional shape for these working sections is a rectangle of about $\sqrt{2}$ to 1 ratio, with corner fillets. If models like those of aircraft are to be tested, then it is usual for the large (spanwise) dimension to be horizontal, for convenience in measuring forces.

The flow out of a contraction often takes a distance equivalent to about 0.5 diameters before the non-uniformities are reduced below an acceptable level. Also, if a turbulence grid is installed, it may take up to 10 - 15 mesh lengths before a homogeneous flow is obtained. These requirements often fix the minimum length of the working section. On the other hand, a very long working section (more than about 3 equivalent diameters) results in excessive boundary layer growth which could lead to separation in an exit diffuser.

The inevitable boundary layer growth in the working section results in a static pressure drop in the axial direction. Any increase in cross-sectional area to compensate for this growth is usually accomplished by tapering the fillets or sometimes by tapering the walls themselves, although the latter makes the mounting of vertical traverse gears and balances more difficult. It is sometimes convenient to obstruct the outlet of the tunnel with a screen to produce an over-pressure in the working section, so that boundary layer control by suction, if necessary, is achieved by merely opening holes.

Most blower tunnel working sections are made of plywood in timber frames. Drumming of panels leads not only to structural fatigue, but also to unsteadiness in the working section, and this must, therefore, be kept to a minimum, preferably by keeping the panel resonant frequencies above the rotor blade frequency at maximum speed. It is the deflection and vibrational properties and not the ultimate strength which decide the material size. Almost all working sections have removable side panels and it is suggested here that these be mounted on pinned hinges. This makes "single-handed" removal of these panels much easier, besides rendering them less susceptible to damage.

A blower tunnel working section without an exit diffuser gives almost as easy access to the model as does the open-jet arrangement sometimes used on return-circuit wind tunnels.

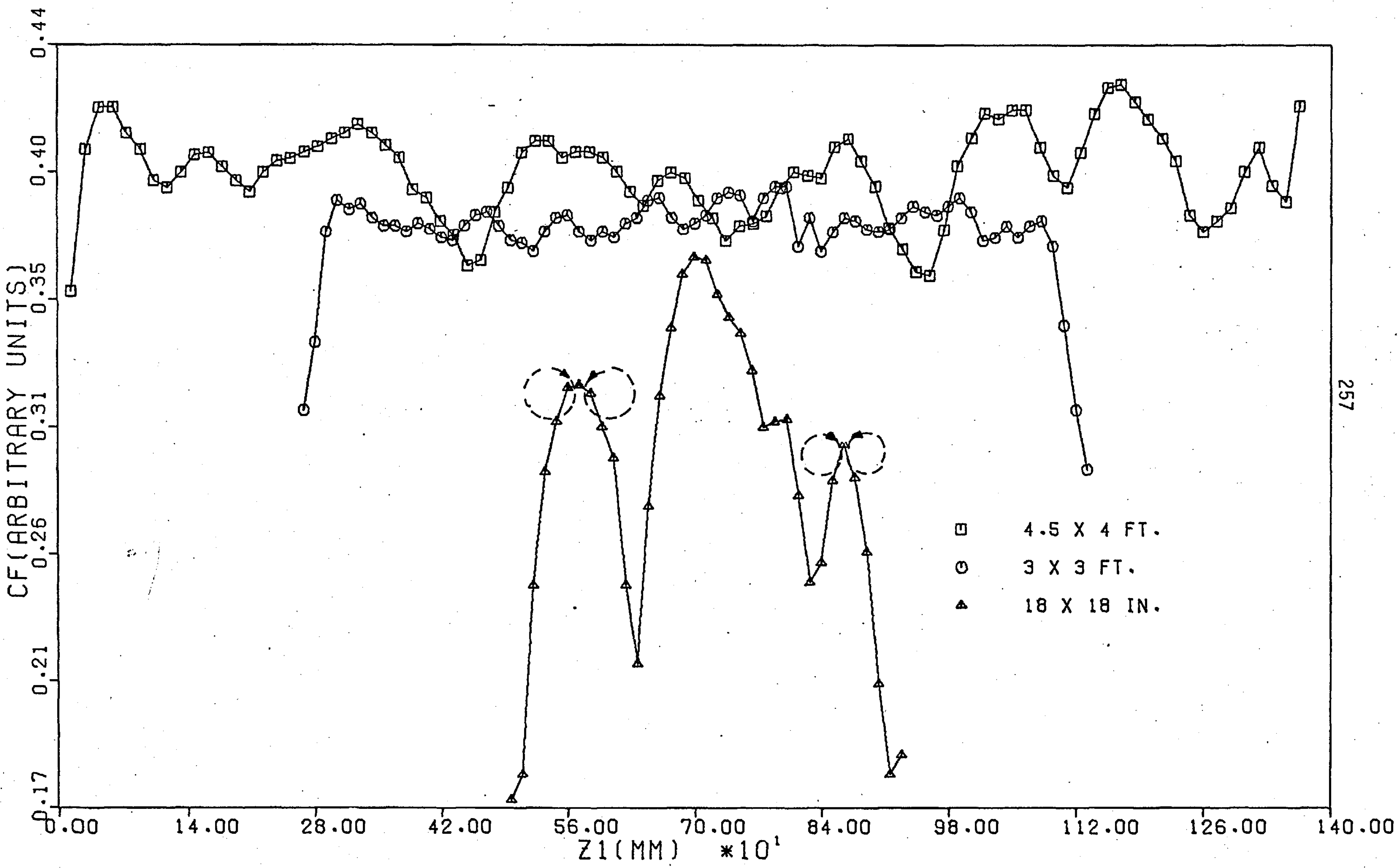

Fig. 5.1 Spanwise skin friction distributions on the working section floors of three tunnels.

CHAPTER 6

CONCLUSIONS

Since each chapter is nearly self-contained, detailed conclusions are not repeated here.

However, since the whole object of this work was to improve the design procedure for blower tunnels, the overall conclusions are presented below in the form of design rules and suggestions derived from or inferred by all the analyses described in the preceding chapters.

6.1 Wide-Angle Diffusers

6.1.1 Design Rules

(i) Keep to the left of the relevant curve and the separation limit line (dotted), in Fig. 2.2.

(ii) Area ratio must be less than ($1.14\ K_{sum} + 1$), where K_{sum} is the sum of the pressure-drop coefficients of all screens.

6.1.2 Further Suggestions

(i) Use screens for boundary layer control if area ratio is less than about 5 and diffuser angle less than about 50^{o}.

(ii) It is safe to use a rectangular cross-section (with corners filleted) unless pressure recovery is important: if so, use circular cross-section.

(iii) Use curved walls if $2\theta > 10\ (A - 1)$ degrees.

(iv) Use curved screens to prevent separation.

(v) Avoid sharp corners at inlet and outlet - use fairings.

(vi) For screen location set: $M_1 \simeq 0.5$

$M_2 \simeq 0.17$ (Sharp Inlet)

$\simeq 0.04$ (Radiused Inlet)

(M_1 and M_2 are defined in eqs. 2.3 and 2.4 respectively).

6.2 Screens

(i) For a given pressure drop, it is better to use multiple screens with relatively low K:-

(a) Less than about 1.5 ($\beta > 0.57$) to minimize screen produced non-uniformities.

(b) About 2.4 for maximum reduction of existing longitudinal mean velocity variation. An optimum value is $K \simeq 2.0$.

(ii) Use plastic screens for uniform flow beyond the boundary layers.

(iii) Use metal screens for acceptable uniformity throughout the flowfield - provided the screens are uniformly woven and free of wrinkles.

(iv) For estimation of K, we can use Wieghardt's formula for metal screens BUT accuracy probably suffers with increasing β.

It is NOT entirely safe to use any of the existing formulae for plastic screens because of the possible dependence on parameters other than β and Re.

(v) For estimation of K_θ, a Cos θ relation (eq. 3.7) works well for screens normally used in wind tunnels ($\beta \sim 0.6$).

(vi) For screens with $\beta \sim 0.6$, α should be estimated using eq. 3.9 (rather than eq. 3.1) and α_θ (for large θ) can be estimated satisfactorily using eq. 3.11.

(vii) It is essential to clean wind tunnel screens regularly. Dirt accumulated on the last screen in the settling chamber can result in large variations in the spanwise c_f distribution in the working section (see Fig. 3.96).

6.3 Honeycombs

(i) For most purposes, impregnated paper honeycombs are adequate.

(ii) For high performance tunnels, or if high loads are expected, use aluminium honeycombs.

(iii) Optimum length-to-diameter ratio of cells is about 6 - 8.

(iv) For suppressing turbulence, use small cell "diameters".

(v) Make sure cells are straight and uniform.

6.4 Blowers

(i) Commercially available, single-inlet centrifugal blowers are preferable for most blower tunnels.

(ii) The level of non-uniformity in the outlet flow of a typical blower with a backward-facing, aerofoil-type impeller is acceptable for most purposes.

(iii) Uniformity of the outlet flow is better with an S-type backward-facing impeller - but with a lower efficiency, which probably implies higher outlet turbulence.

(iv) Vortex type flow is characteristic of all single-inlet blowers - and, if reduced using screens, can be used to advantage in the wide-angle diffuser because total pressure is higher near the walls.

(v) It is advisable to connect blower to tunnel with a flexible coupling.

6.5 Contractions

(i) Use contraction ratios between about 6 - 9.

(ii) Square or rectangular cross-sectional shapes (without fillets) are adequate for most purposes - but for small contractions, it is advisable to use axisymmetric shapes.

(iii) For wall shape, "eye-design" or an imitation of a successful design is adequate for most purposes. A wall shape contour with a cubic equation also seems to work well.

6.6 Settling Chambers

(i) Install the honeycomb ahead of the screens unless swirl angles greater than about 10^{0} - if so, install one screen upstream of the honeycomb.

(ii) Optimum spacing between successive screens is about 0.2 settling chamber "diameters".

(iii) Optimum distance between the last screen and contraction entry is also about 0.2 duct diameters.

6.7 Working Sections

(i) Use rectangular cross-section of about $\sqrt{2}$ to 1 ratio, unless for special purposes.

(ii) Control the streamwise pressure gradient by tapering fillets or walls.

(iii) Use an exit diffuser if tunnel power factor is more important than flexibility of working section arrangement.

REFERENCES

ADKINS, R. C. (1975)
A short diffuser with low pressure loss. ASME J. Fluids Engng., 97I, 297.

ALI, M. S. (1968)
Experimental investigation of flow through a wide-angle diffuser. Imperial College, Department of Aeronautics, M.Sc. Thesis.

ANNAND, W. J. D. (1953)
The resistance to airflow of wire gauzes. J. Roy. Aero. Soc., 57, 141.

AZZOUZ, D. and PRATT, N. H. (1968)
Supersonic turbulent mixing, II: Design and construction of Mach 3 blowdown wind tunnel and its instrumentation. University of Southampton, Department of Aeronautics and Astronautics, A.A.S.U. Report 282.

BACHMEIER, A. J. (1968)
VTOL Propulsion tunnel. Quarterly Bulletin of the D.M.E. and the N.A.E. Report No. DME/NAE 1968 (1), NRC, Canada.

BAINES, W. D. and PETERSON, E. G. (1951)
An investigation of flow through screens. Trans. ASME, 73, 467.

BANSOD, P. and BRADSHAW, P. (1972)
The flow in S-shaped ducts. Aeronaut. Q., 23, 131.

BATCHELOR, G. K. (1967)
Introduction to Fluid Dynamics, Cambridge University Press.

BATCHELOR, G. K. (1970)
The Theory of Homogeneous Turbulence, pp. 55 - 75, Cambridge University Press.

BEARMAN, P. W. (1971)
Correction for the effect of ambient temperature drift on hot-wire measurements in incompressible flows. DISA Information, No. 11.

BOLDMAN, D. R. and NEUMANN, H. L. (1973)
Experimental and analytical study of a conically diffused flow with a nearly separated boundary layer. NASA TN D-7486.

BRADSHAW, P. (1965)
The effect of wind tunnel screens on nominally two-dimensional boundary layers. J. Fluid Mech., 22, 679.

BRADSHAW, P. (1967)
A low turbulence wind tunnel driven by an aerofoil-type centrifugal blower. J. Roy. Aero. Soc., 71, 132.

BRADSHAW, P. (1968)
Simple wind tunnel design. NPL Aero. Report 1258.

BRADSHAW, P. (1970)
Experimental Fluid Mechanics, Pergamon Press, Oxford.

BRADSHAW, P. (1972)
Two more wind tunnels driven by aerofoil-type centrifugal blowers. Imperial College Aero. Report 72 - 10.

BRADSHAW, P. and HELLENS, G. E. (1964)
The NPL 59 in x 9 in boundary layer tunnel. ARC R & M 3437.

BRADSHAW, P. and PANKHURST, R. C. (1964)
The design of low-speed wind tunnels. Prog. Aerospace Sci., 5, 1.

BREDERODE, V. de (1973)
VELPROF - a boundary layer data analysis program. Imperial College Aero. Tech. Note 73 - 107.

BRYER, D. W. and PANKHURST, R. C. (1971)
Pressure-probe methods for determining wind speed and flow direction. Her Majesty's Stationery Office, London.

CAMPBELL, A. J. (1957)
Investigation of a wide-angle diffuser with air augmentation for use as a jet muffler. Institute of Aerophysics, University of Toronto, UTIA T-N 15.

CARLSON, J. J., JOHNSTON, J. P. and SAGI, C. J. (1967)
Effects of wall shape on flow regimes and performance in straight, two-dimensional diffusers. ASME J. Basic Engng., 89D, 151.

CARROTHERS, P. J. G. and BAINES, W. D. (1965)
Forces on screens inclined to a fluid flow. ASME J. Fluids Engng., 97I, 116.

CEBECI, T. and BRADSHAW, P. (1977)
Momentum Transfer in Boundary Layers, McGraw-Hill.

CHANDRSUDA, C. (1975)
A reattaching turbulent shear layer in incompressible flow. Ph.D. Thesis, Imperial College, University of London.

CLAUSER, F. H. (1954)
Turbulent boundary layers in adverse pressure gradients. J. Aero. Sci., 21, 91.

COCKRELL, D. J. and MARKLAND, E. (1974)
Diffuser behaviour - a review of past experimental work - relevant to-day. Aircr. Engng., 46, 16 (reprint of Vol. 35, p. 286).

COHEN, M. J. and RITCHIE, N. J. B. (1962)
Low-speed three-dimensional contraction design. J. Roy. Aero. Soc., 66, 231.

COLES, D. E. (1962)
The turbulent boundary layer in a compressible fluid. RAND Corp., Rep. R-403-PR.

COLLAR, A. R. (1939)
The effect of a gauze on the velocity distribution in a uniform duct. ARC R & M 1867.

CORNER, J. C. (1971)
The effect of a gauze on a turbulent boundary layer. M.Sc. Thesis, Imperial College, University of London.

DOMHOLDT, L. C. and MOSZYNSKI, J. R. (1964)
A low turbulence water tunnel-design and performance. ASME Paper 64-FE-21.

DRYDEN, H. L. and ABBOTT, I. H. (1949)
The design of low-turbulence wind tunnels. NACA Report No. 940.

DRYDEN, H. L. and SCHUBAUER, G. B. (1947)
Use of damping screens for reduction of wind tunnel turbulence. J. Aero. Sci., 14, 221.

FEIL, O. C. (1964)
Vane systems for very-wide-angle subsonic diffusers. ASME J. Basic Engng., 86D, 759.

FIELDER, R. A. and GESSNER, F. B. (1972)
Influence of tangential fluid injection on the performance of two-dimensional diffusers. ASME J. Basic Engng., 94D, 666.

GIBBINGS, J. C. (1973)
The pyramid gauze diffuser. Ing.-Arch., 42, 225.

GIBSON, A. H. (1910)
On the flow of water through pipes and passages having converging or diverging boundaries. Proc. Roy. Soc. London, 83A, 366.

GIBSON, M. (1959)
Design and performance of a streamline diffuser with a rapid expansion. ARC 21, 126.

GREEN, D. J. and LILLEY, G. M. (1955)
Preliminary report on the use of the wide-angle diffuser in ground mufflers of type used for silencing jet aircraft. College of Aeronautics, Cranfield, Note 27.

GRIFFITH, A. A. and MEREDITH, F. W. (1936)
The possible improvement on aircraft performance due to the use of boundary layer suction. ARC Report 2315.

HAIGHT, C. H. and O'DONNELL, R. M. (1974)
Experimental mating of trapped vortex diffusers with large area ratio thrust augmentors. Aerospace Research Labs., Wright-Patterson Air Force Base, Ohio, ARL TR 74-0115.

HUSSAIN, A. K. M. F. and RAMJEE, V. (1976)
Effects of the axisymmetric contraction shape on incompressible turbulent flow. ASME J. Fluids. Engng., 98I, 58.

JOHNSTON, J. P. and POWARS, C. A. (1969)
Some effects of inlet blockage and aspect ratio on diffuser performance. ASME J. Basic Engng., 91D, 551.

JORDINSON, R. (1961)
Design of wind tunnel contractions. Aircr. Engng., 33, 294.

JUHASZ, A. J. (1974)
Performance of an asymmetric short annular diffuser with a non-diverging inner wall using suction. NASA TN D-7575.

JUHASZ, A. J. (1975)
Effect of wall suction on performance of a short annular diffuser at inlet Mach Numbers up to 0.5. NASA TM-X-3302.

KACHHARA, N. L. (1973) Wide-angle axisymmetric diffusers employing a specified steep pressure rise on the boundary walls. University of Salford, Internal Report FM/14/73. (See also KACHHARA, N. L., LIVESEY, J. L. and WILCOX, P. L. (1977). An initial approach to the design of very wide-angle axisymmetric diffusers with gauzes to achieve uniform outlet velocity profiles. ASME J. Fluids Engng., 99I, 357).

KLINE, S. J., MOORE, C. A. and COCHRAN, D. L. (1957)
Wide-angle diffusers of high performance and diffuser flow mechanisms. J. Aero. Sci., 24, 469.

KRISHNAPPA, G. (1976)
Centrifugal blower noise studies - literature survey and noise measurements. N.R.C. Canada, Report ME-244.

KÜCHEMANN, D. and WEBER, J. (1953)
Aerodynamics of Propulsion, pp. 274 - 279, McGraw Hill, London.

LACHMANN, G. V., Ed. (1961)
Boundary Layer and Flow Control, Vol. 2, Pergamon Press, Oxford.

LAINE, S. and HARJUMÄKI, J. (1975)
A theoretical study of axisymmetric contractions for low-speed wind tunnels, Helsinki University of Technology, Laboratory of Aerodynamics, Report No. 75-A2.

LAU, Y. L. and BAINES, W. D. (1968)
Flow of stratified fluid through curved screens. J. Fluid Mech., 33, 721.

LAWS, E. M. and LIVESEY, J. L. (1978)
Flow through screens. Ann. Rev. Fluid Mech., 10, 247.

LAWSON, T. V. (1971)
Rapid diffuser based on the egg-box principle. Proceedings, Symposium on Internal Flows, University of Salford, 20 - 22 April, (J. L. Livesey, Ed.), pp. A42 - A46.

LIVESEY, J. L. (1956)
The behaviour of transverse cylindrical and forward-facing total pressure probes in transverse total pressure gradients. J. Aero. Sci., 23, 949.

LOEHRKE, R. I. and NAGIB, H. M. (1976)
Control of free-stream turbulence by means of honeycombs: A balance between suppression and generation. ASME J. Fluids Engng., 98I, 342.

LUMLEY, J. L. and McMAHON, J. F. (1967)
Reducing water tunnel turbulence by means of a honeycomb. ASME J. Basic Engng., 89D, 764.

MABEY, D. G. and SAWYER, W. G. (1974)
Reduction of flow unsteadiness in the 3 ft x 4 ft supersonic tunnel. RAE TR 73194.

MacMILLAN, F. A. (1954)
Viscous effects on pitot tubes at low speeds. J. Roy. Aero. Soc., 58, 570.

McLELLAN, C. H. and NICHOLS, M. R. (1942)
An investigation of diffuser resistance combinations in duct systems. Aeronautical Research Committee Report No. AE 1990.

MEHTA, R. D. (1976)
The design of wide-angle diffusers. Imperial College Aero. Report 76-03.

MEHTA, R. D. (1977)
The aerodynamic design of blower tunnels with wide-angle diffusers. Prog. Aerospace Sci., 18, 59.

MOORE, C. A. and KLINE, S. J. (1958)
Some effects of vanes and of turbulence in two-dimensional wide-angle subsonic diffusers. NACA-TN-4080.

MOREL, T. (1975)
Comprehensive design of axisymmetric wind tunnel contractions. ASME J. Fluids. Engng., 2I, 225.

MORGAN, P. G. (1960)
The stability of flow through porous screens. J. Roy. Aero. Soc., 64, 359.

NEVE, R. S. and WIRANSINGHE, N. E. A. (1978)
Changes in conical diffuser performance by swirl addition. Aeronaut. Q., 29, 131.

OWEN, P. R. and ZIENKIEWICZ, H. K. (1957)
The production of uniform shear flow in a wind tunnel. J. Fluid Mech., 2, 521.

PANKHURST, R. C. and HOLDER, D. W. (1952)
Wind Tunnel Technique, Pitman, London.

PATEL, V. C. (1965)
Calibration of the Preston tube and limitations on its use in pressure gradients. J. Fluid Mech., 23, 185.

PATTERSON, G. N. (1938)
Modern diffuser design. Aircr. Engng., 10, 267.

PINKER, R. A. and HERBERT, M. V. (1967)
Pressure loss associated with compressible flow through square-mesh wire gauzes. J. Mech. Eng. Sci., 9, 11.

PIRRELLO, C. J., HARDIN, R. D., HECKART, M. V. and BROWN, K. R. (1971)
An inventory of aeronautical ground research facilities I, Wind Tunnels. NASA-CR-1874.

POPE, A. and GOIN, K. L. (1965)
High Speed Wind Tunnel Testing, pp. 97 - 99, John Wiley, New York.

PRANDTL, L. (1933)
The attainment of a steady air stream in wind tunnels. NACA-TM-726.

PRESTON, J. H. (1958)
The minimum Reynolds number for a turbulent boundary layer and the selection of a transition device. J. Fluid Mech., 3, 373.

RAJU, K. N. and RAO, D. M. (1964)
Experiments on the use of screens and splitters in a wide-angle conical diffuser. National Aeronautical Laboratory, Bangalore, TN-AE-24-64.

RAO, D. M. (1967)
Flow stabilization in a large area ratio wide-angle diffuser. Paper presented at CAARC, Specialist meeting on Boundary Layers, Bangalore, 11 - 13th December.

REID, E. G. (1953)
Performance characteristics of plane wall two-dimensional diffusers. NACA-TN 2888.

REYNOLDS, A. J. (1969)
Flow deflection by gauze screens. J. Mech. Engng. Sci., 11, 290.

RHODEN, H. G. (1951)
Development of a wind tunnel. Engineering, 171, 677.

RINGLEB, F. O. (1961)
Separation control by trapped vortices. In Boundary Layer and Flow Control, pp. 265 - 294, (G. V. Lachmann, Ed.), Pergamon Press, Oxford.

ROBERTSON, J. M. and FRASER, H. R. (1960)
Separation prediction for conical diffusers. ASME J. Basic Engng., 82D, 201.

RUNSTADLER, P. W. and DOLAN, F. X. (1973)
Further data on the pressure recovery performance of straight-channel, plane-divergence diffusers at high subsonic Mach numbers. ASME J. Fluids Engng., 95I, 373.

SAVAGE, S. B. (1960)
A short low-speed wind tunnel with wide-angle diffuser. McGill University, Montreal, Mech. Eng. Research Labs. (Aerodynamics Section), Report No. Ae 2.

SCHLICHTING, H. (1968)
Boundary Layer Theory, McGraw-Hill.

SCHUBAUER, G. B. and SPANGENBERG, W. G. (1948)
Effect of screens in wide-angle diffusers. NACA-TN-1610.

SCHUBAUER, G. B., SPANGENBERG, W. G. and KLEBANOFF, P. S. (1950)
Aerodynamic characteristics of damping screens. NACA-TN-2001.

SENOO, Y. and NISHI, M. (1977)
Prediction of flow separation in a diffuser by a boundary layer calculation. ASME J. Fluids Engng., 99I, 390.

SIMMONS, L. F. G. and COWDREY, C. F. (1945)
Measurements of the aerodynamic forces acting on porous screens. ARC R & M 2276.

SMITH, C. R. (1975)
A note on diffuser generated flow unsteadiness. ASME J. Fluids Engng., 97I, 377.

SMITH, A. M. O. and PIERCE, J. (1959)
Exact solution of the Neumann problem. Calculation of non-circulatory plane and axially symmetric flows about or within arbitrary boundaries. Douglas Aircraft Inc. Report ES 26988. Also, ARC 20, 660. (See also HESS, J. L. and SMITH, A. M. O. Prog. Aerospace Sci., 8, 1).

SMYTH, E. (1950)
Factors determining the choice of wire-mesh screens in wind tunnels. Vickers Ltd. W.T. Tech. Note No. 1869, ARC 13055.

SQUIRE, H. B. (1953)
Experiments on conical diffusers. ARC R & M 2751.

SQUIRE, H. B. and HOGG, H. (1944)
Diffuser-resistance combinations in relation to wind tunnel design. RAE Report No. Aero 1933.

SQUIRE, H. B. and HUGHES, N. J. F. (1944)
Addendum to Report No. Aero. 1933, "Diffuser-resistance combinations in relation to wind tunnels design". RAE Report No. 1933a.

SQUIRE, H. B. and WINTER, K. G. (1953)
The R.A.E. 4 ft x 3 ft experimental low turbulence wind tunnel. ARC R & M 2690.

TAYLOR, G. I. and BATCHELOR, G. K. (1949)
The effect of a wire gauze on a small disturbance in a uniform stream. Q. J. Mech. Appl. Math., 2, 1. (With appendix by DRYDEN, H. L. and SCHUBAUER, G. B.)

TAYLOR, H. D. (1950)
United Aircraft Research Department summary report on vortex generators. Report R-05280-9.

TENNANT, J. S. (1973)
A subsonic diffuser with moving walls for boundary layer control. AIAA J., 11, 240.

THWAITES, B. (1946)
On the design of contractions for wind tunnels. ARC R & M 2278.

TOWNSEND, A. A. (1951)
The passage of turbulence through wire gauzes. Q. J. Mech. Appl. Math., 4, 308.

TOWNSEND, A. A. (1976)
The Structure of Turbulent Shear Flow, p. 176, Cambridge University Press.

VOGEL, W. M. (1968)
General description and calibration of the McGill 30-inch diameter blower cascade wind tunnel. McGill University, Montreal. TN 68-I.

WATTS, K. C., BRUNDRETT, E., NICOLL, W. B. and STRONG, A. B. (1974)
Design and construction of a wind tunnel for mass transfer studies in incompressible boundary layers. ASME J. Fluids Engng., 96I, 311.

WELSH, M. C. (1976)
Flow control in wide-angled conical diffusers. ASME J. Fluids Engng., 98I, 728 - 735.

WHITEHEAD, L. G., WU, L. Y. and WATERS, M. H. L. (1951)
Contracting ducts of finite length. Aeronaut. Q., 2, 254.

WIEGHARDT, K. E. G. (1953)
On the resistance of screens. Aeronaut. Q., 4, 186.

YANG, T., HUDSON, W. G. and NELSON, C. D. (1973)
Design and experimental performance of short curved wall diffusers with axial symmetry utilizing slot suction. NASA-CR-2209.

APPENDIX A

LARGE STRUCTURE IN TURBULENT MIXING LAYERS

This appendix contains details of work on the effects of free-stream turbulence on large structures in turbulent mixing layers. A copy of the paper published under joint authorship in the Journal of Fluid Mechanics, Volume 85, p. 693 (1978) is included here. The present author's main contribution was in conducting the two-stream mixing layer experiments. A brief discussion of the work together with additional details of the experimental set-up and some unpublished results are presented below.

The whole controversy about large structures in mixing layers was re-ignited when Brown and Roshko (1974) published shadowgraphs of their two-stream mixing layer which showed highly two-dimensional vortex rollups persisting through the length of their rig. Because of similarities in the spreading rate and self-preservation of the mean flow with previous data on mixing layers, they suggested that this was a unique form of a fully turbulent mixing layer. The presence and importance of large structures in turbulent shear flows were generally accepted already - indeed even in 1956, Townsend* used the large eddies as the basis of a general hypothesis about turbulence structure.

The question here is very basic, yet very important and concerns the persistence of the two-dimensionality of the large structures. In the classical view of turbulence, it is mainly in the large eddies that turbulent energy production $\left(-\overline{u_i u_j}\,\frac{\partial U_i}{\partial x_j}\right)$ takes place

---

* Townsend, A. A. (1956). The Structure of Turbulent Shear Flow, Cambridge University Press.

since with their larger length scale, they are affected more by the mean shear. This energy is then passed up the wave number spectrum by a three-dimensional vortex stretching process to the smallest eddies where it is dissipated into heat. So in a fully turbulent mixing layer, three-dimensionality is a pre-requisite to the process of producing and transfering the energy necessary to "drive" the turbulence. Some earlier work on a single stream mixing layer in this Department (Chandrsuda and Bradshaw, 1975) showed that the two-dimensional vortex roll-up broke down into conventional turbulence through a process of helical pairing, evidently because of the relatively high turbulence level in the laboratory "still air" (Figs. 1, 2 and 3). Some correlation measurements made in the same rig by Mr. D. H. Wood confirmed these observations (Fig. 4).

In order to test this hypothesis further, the present author converted an existing 1.2 x 0.6 m suck-down smoke tunnel into a two-stream mixing layer rig, (Fig. A1). The splitter plates were made of 3 mm thick plywood and the strips between the screens were glued together, through the screens, with "Araldite" to minimize leaks. A square sectioned smoke injector (50 x 50 mm) was attached to the underside of the entry splitter which spanned from the honeycomb to the nearby wall (1040 mm). Kerosene-droplet smoke was supplied to the injector by a Taylor generator (Type 3020). Although the injected smoke sheet spanned the whole width of the mixing layer, only a thin slice of the flow was illuminated for photographic purposes - about 30 mm wide on the tunnel centre-line. The velocity ratio of the mixing layer was altered by changing the thickness of a porous baffle placed over one half of the entry honeycomb. So the turbulence level and velocity ratio of the mixing layer were varied at the same time. The typical velocity of the high-speed flow was about 1 m/s which gave an Re_θ of about 50.

We were able to produce the "Brown and Roshko structure" when the low-speed stream velocity was only a few per cent of the mainstream flow but eventual breakdown of the two-dimensional vortex roll-up into large-scale eddies, containing small-scale (three-dimensional) turbulence, was very evident, (Fig. 5). In this case, the free-stream turbulence level in both streams was low (about 0.2%) since the air was delivered through the honeycomb and four screens ($K \sim 2$, for each screen). Attempts to check the effect of artificially increasing the turbulence level in the faster stream were not very successful. A turbulence grid (37 mm mesh) made from 25 mm strips of 3 mm thick plywood was attached to the last screen. However, the smoke tended to diffuse into the low pressure, recirculating regions behind the bars, thus producing a rather unclear picture, although the breakdown of the orderliness in the mixing layer was evident (Fig. A2).

A significant change occurred when the secondary stream was shut-off completely, producing effectively flow over a backward-facing step. The transitional oscillations became three-dimensional almost immediately and although large structures were observed, they were fully three-dimensional (Fig. 6). In this case, the entrainment flow was supplied from the highly turbulent recirculating region. A strong, long-lived vortex could still be produced by artificially exciting the mixing layer. Fig. A3 shows a strong structure breaking off from the main mixing layer when the rig was thumped and Fig. A4 shows a very well-defined (two-dimensional) vortex formed by closing the inlet baffle suddenly. The first effect is easily produced in practice on an aircraft engine where this kind of vortex induction, in the form of a vortex ring, can affect its noise characteristics.

Our results thus indicate that the Brown and Roshko structure will only appear if the free-stream turbulence in both streams is low and is hence rare in practice. If it does appear, then it must eventually breakdown into conventional three-dimensional turbulence. Further discussion, to which the present author has contributed, is given in the main paper.

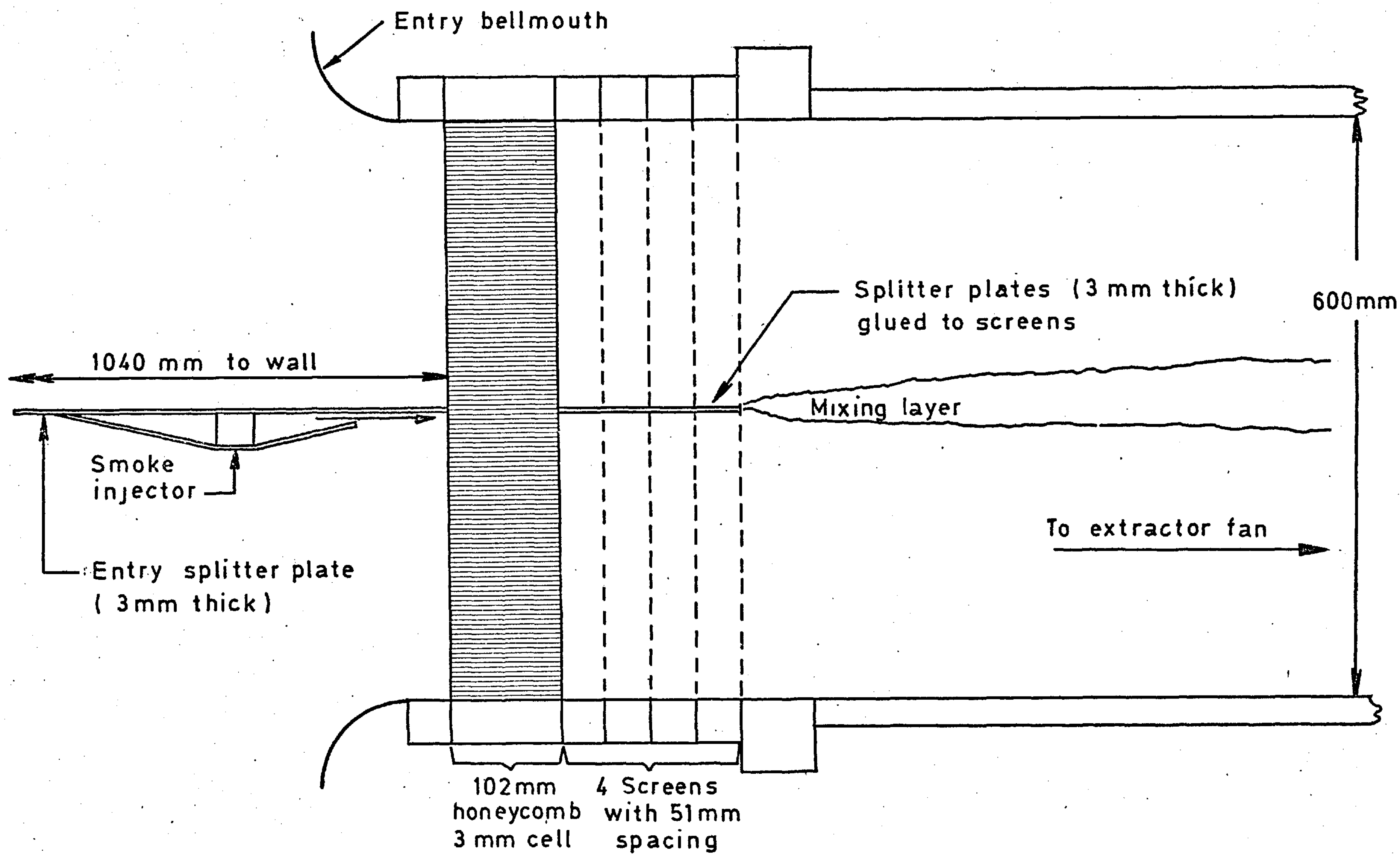

Fig. A1 The two-stream mixing layer rig.

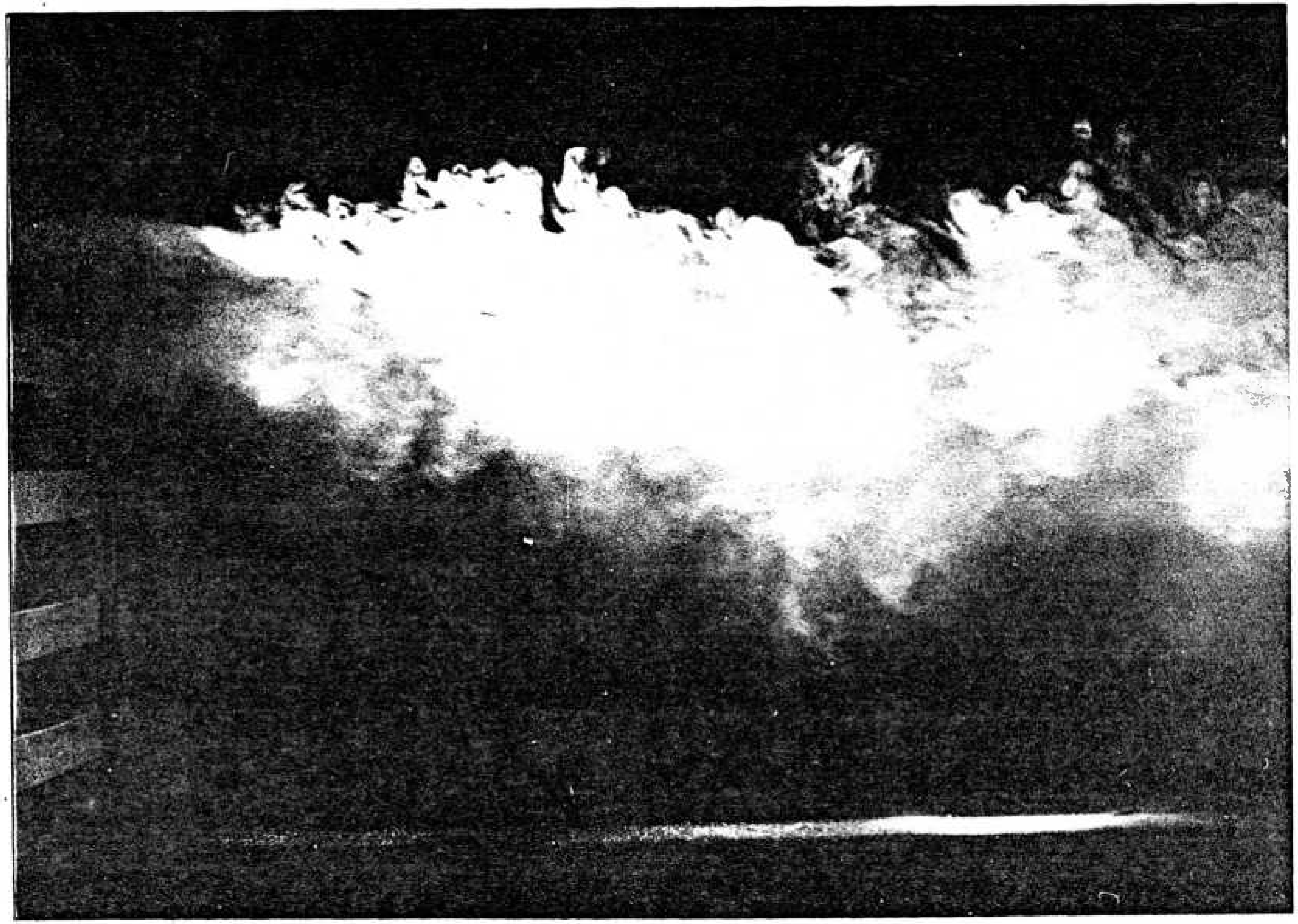

Fig. A2 Breakdown of the orderliness in the mixing layer by installing a turbulence grid in the faster stream. (Note this photograph is inverted and so the faster stream is on the lower side).

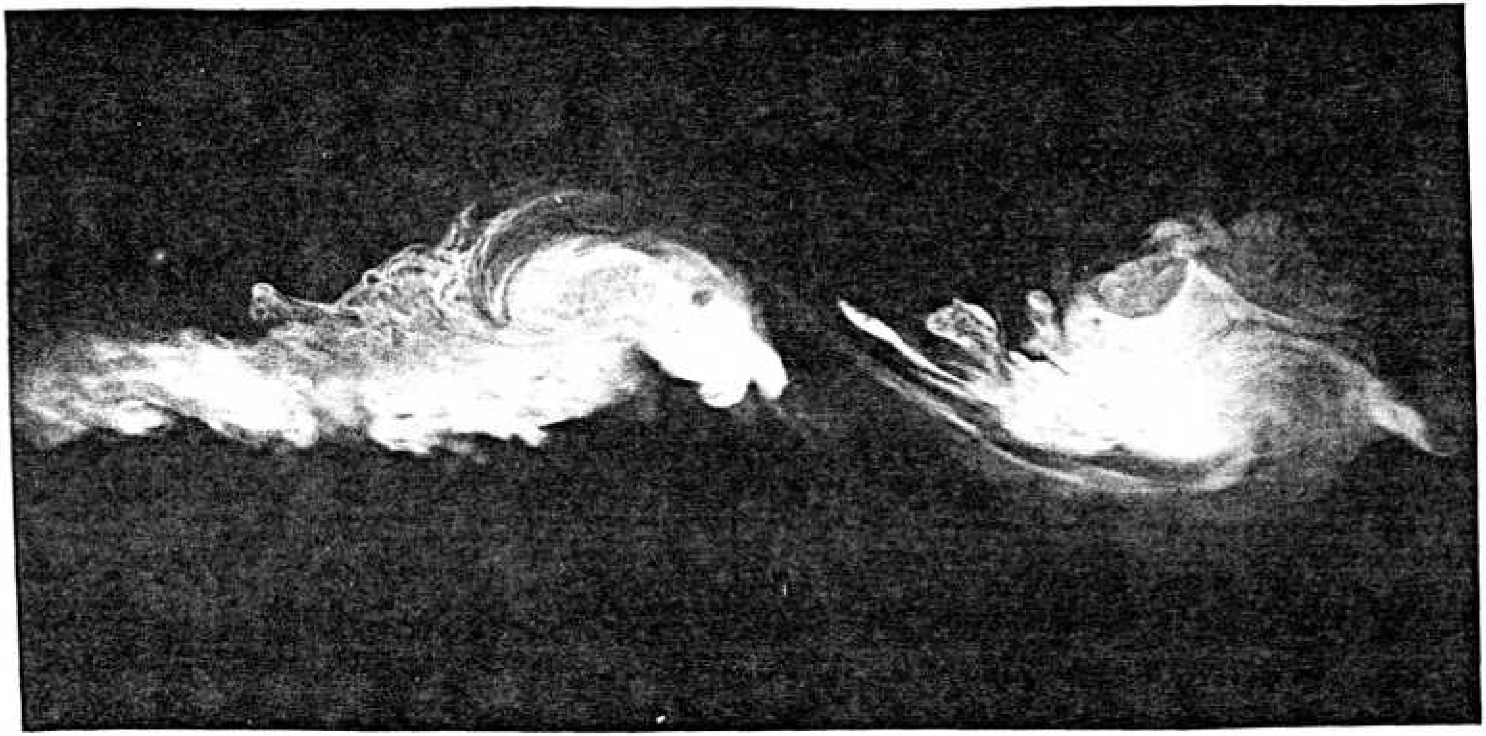

Fig. A3 Strong long-lived structure produced by artificial excitation - rig thumped.

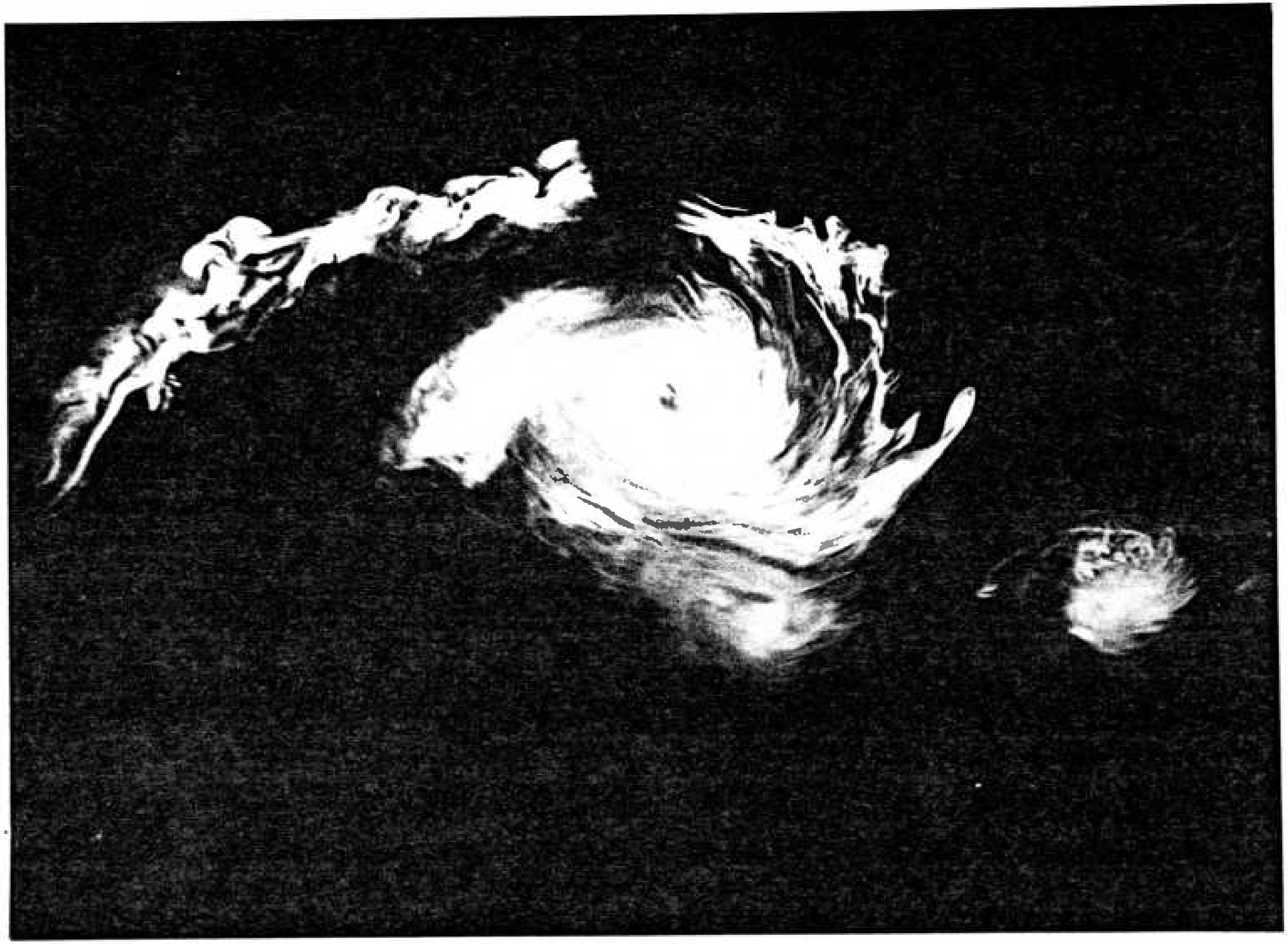

Fig. A4 A well-defined (two-dimensional) vortex formed by artificial excitation - inlet baffle closed suddenly.

J. Fluid Mech. (1978), *vol.* 85, *part* 4, *pp.* 693–704 693
Printed in Great Britain

Effect of free-stream turbulence on large structure in turbulent mixing layers

By C. CHANDRSUDA,† R. D. MEHTA,
A. D. WEIR‡ AND P. BRADSHAW
Department of Aeronautics, Imperial College, London

(Received 1 May 1976 and in revised form 7 November 1977)

Flow-visualization investigations and correlation measurements show that the essentially two-dimensional structures which dominated the turbulent mixing layer of Brown & Roshko (1974) are formed only if the free-stream turbulence is low. If free-stream disturbances are significant, as is likely in most practical cases, including a mixing layer entraining 'still air' from the surroundings, three-dimensionality develops at an early stage in transition. Other recent experiments strongly suggest that the Brown–Roshko structure will not form if the initial mixing layer is turbulent or subject to instability modes other than spanwise vortices. Therefore the Brown–Roshko structure will be rare in practice. The alternative large structure in a mixing layer, found by several workers, is intense, but fully three-dimensional and thus less orderly than the Brown–Roshko structure.

The balance of evidence suggests that if the Brown–Roshko structure does appear it will eventually relax into the alternative fully three-dimensional form: the Kármán vortex street behind a bluff body provides a precedent for slow development of three-dimensionality. However the Brown–Roshko structure, if formed, may well relax so slowly as to be identifiable for the full length of a practical flow.

1. Introduction

The flow visualizations of a two-stream mixing layer produced by Brown & Roshko in 1971 (see Brown & Roshko 1974) showed that the two-dimensional 'vortex roll' disturbances which are the eigenmodes of instability of a laminar mixing layer persisted down the length of the test rig. Pairing of vortex rolls occurred at intervals, so that the wavelength was on the average proportional to the shear-layer thickness. Some smaller-scale three-dimensional fluctuations were evident, but most of the fluctuation energy appeared to reside in the two-dimensional structures. Since mean velocity profiles were closely self-preserving and the spreading rate was normal, Brown & Roshko suggested that this was the unique fully developed form of a turbulent mixing layer. Below, we refer to this form as the Brown–Roshko structure. Winant & Browand (1974), again using a two-stream mixing layer, showed that approximate self-preservation could persist through many stages of vortex pairing at low Reynolds numbers, without complete breakdown to the fully three-dimensional flow which is characteristic of turbulence in other types of shear layer. Dimotakis & Brown (1976)

† Present address: Royal Thai Air Force Academy, Bangkok, Thailand.
‡ Present address: University of the South Pacific, Suva, Fiji.

found some evidence for the Brown–Roshko type of structure in another two-stream mixing layer at high Reynolds number. Oster, Wygnanski & Fiedler (1977) measured velocity correlations with spanwise separation in a two-stream mixing layer, and found very large integral scales compatible with the presence of two-dimensional disturbances, albeit only in the irrotational region outside the shear layer.

Previously, Crow & Champagne (1971) had demonstrated the variety and long streamwise persistence of vortex-ring disturbances in circular jets. Here, fairly rapid changes with Reynolds number were observed and the disturbance wavelength was strongly influenced by the jet diameter, so that the vortex-ring structure was evidently a mixture of columnar oscillations and shear-layer transition modes rather than a self-preserving mode like Brown & Roshko's. Since jet columns are known to be subject to various forms of instability, Crow & Champagne's work was not universally accepted as evidence for anomalous behaviour of the turbulence itself.

The received view of mixing-layer transition and turbulence previous to the above-mentioned work was that the mixing layer became unstable, at a very low value of the Reynolds number based on local thickness, to two-dimensional (or axisymmetric) disturbances; that these disturbances then grew, and paired once or more before appreciable three-dimensionality appeared (Wille 1963); that, perhaps after a considerable time (Bradshaw 1966), the flow reached a self-preserving, fully turbulent state independent of the Reynolds number based on local thickness; and that the large eddies in the fully turbulent mixing layer, although very strong compared with those in a boundary layer, were fully three-dimensional, with correlation integral scales of the same order of magnitude in all three directions. Bradshaw, Ferriss & Johnson (1964), whose correlation measurements were confirmed by Weber (1974), described these large eddies as 'mixing jets' in the sense used by Grant (1958). The question of three-dimensionality is highly important, because three-dimensionality is a prerequisite for the development of a vortex-stretching energy 'cascade', and distinguishes turbulence from various quasi-two-dimensional random flows such as large-scale motion in the atmosphere.

In the present paper we seek to reconcile this received view of classical, fully three-dimensional turbulence with the more recent observations, and to show that the two-dimensional Brown–Roshko structure is rare. Our results show that the vortex-pairing process is sensitive to small three-dimensional disturbances, such as free-stream turbulence, in the early stages when the vortex-roll amplitude is itself small. In Brown & Roshko's experiments, but few others, these disturbances were so small that the laminar instability modes remained two-dimensional and grew to a very large intensity. However, the sensitivity to three-dimensional disturbances is unlikely to disappear completely, and it seems probable that the associated small-scale turbulence will eventually cause the two-dimensional Brown–Roshko structure to break up. If this is so, there is only one truly self-preserving state,† which is fully three-dimensional in accord with the classical view of turbulence. If not, there are *two* self-preserving

† The ratio of the velocity of the low-speed stream, U_2, to that of the high-speed stream, U_1, will affect the asymptotic turbulence structure quantitatively but not qualitatively. Even the quantitative effect is likely to be small if the velocity difference $U_1 - U_2$ is used as a normalizing scale; in particular, $U_2 = 0$ (the mixing layer in still air) is not a singular case, because the most relevant parameter is the ratio of $U_1 - U_2$ to the average velocity $\frac{1}{2}(U_1 + U_2)$, rather than U_2/U_1 itself.

states, of which the three-dimensional one is probably much the more common in engineering practice. Other recent investigations have revealed cases in which the Brown–Roshko structure does not develop. Pui & Gartshore (1977), in measurements in a mixing layer between two streams of nearly equal velocities, find that, if transition first occurs within the wake of the splitter plate rather than in a fully formed mixing layer, the Brown–Roshko structure does not appear and the spanwise coherence lengths (integral scales) are small. Yule (1977) finds that in a circular jet in still air the 'vortex-ring' instability patterns develop circumferential periodicity and break down quite suddenly into fully three-dimensional turbulence. Finally, the balance of evidence discussed below suggests that the Brown–Roshko structure does not form at all if the nozzle-exit boundary layer is fully turbulent.

2. Measurements in a single-stream mixing layer

Figure 1 (plate 1) shows the side view, and figure 2 (plate 1) the plan view on a reduced scale, of a mixing layer formed on the 75 cm side of a 75×12 cm air stream emerging into 'still air' in a room about $10 \times 7 \times 5$ m, free of draughts from other sources. The rig was a blower wind tunnel, without a diffuser or a working-section roof, so that the floor and walls of the working section minimized bodily oscillations (and three-dimensionality) of the mixing layer formed in the plane normally occupied by the roof. The walls extended well above the roof position and thus acted as end plates. The Reynolds number of the exit boundary layer, based on momentum thickness, was about 50, well below the Blasius instability value of about 200. The turbulence level of the tunnel stream was less than 0·1 % at 20 m s^{-1}, and while the level may have been somewhat higher at the speed of about 0·5 m s^{-1} used in the present tests it was certainly within the range typical of good laboratory test rigs. Kerosene-droplet 'smoke' was injected into the entrainment flow at the contraction exit. The streaks in figure 2 were caused by spacers in the injector slot, and their persistence shows that the smoke introduced no significant turbulence. However the second of the spanwise vortex cores in figure 2 shows spanwise non-uniformity on a larger scale than the local shear-layer thickness; this is also the explanation of the multiple streaks seen in the side view (figure 1), the whole spanwise extent of the smoke being illuminated. The third and fourth vortex cores in figure 2 are in the process of pairing, in a three-dimensional (helical) fashion. The last core, evidently the remains of a pair, is virtually turbulent in the conventional sense, with a fully three-dimensional small-scale structure.

Further visual observations showed that vortex pairing in the presence of naturally occurring three-dimensional disturbances led to a double-helix pattern like that seen in figure 3 (plate 2), and conventional turbulence soon ensued. Occasionally two-dimensionality would persist through two or three stages of pairing but helical pairing and breakdown always occurred eventually. These observations do not contradict the linear theory of Jiminez (1975) that adjacent co-rotating vortices of small amplitude are stable: transitional disturbances in a mixing layer can attain large amplitudes, the maximum Reynolds shear stress attained being as much as 1·5 times that in the fully turbulent flow (Bradshaw 1966). An incipient double-helix pattern can be seen in figure 2 of Rockwell (1977), which shows a low-Reynolds-number mixing layer of finite span in a simulated fluidic device. A very clear sequence of movie frames by

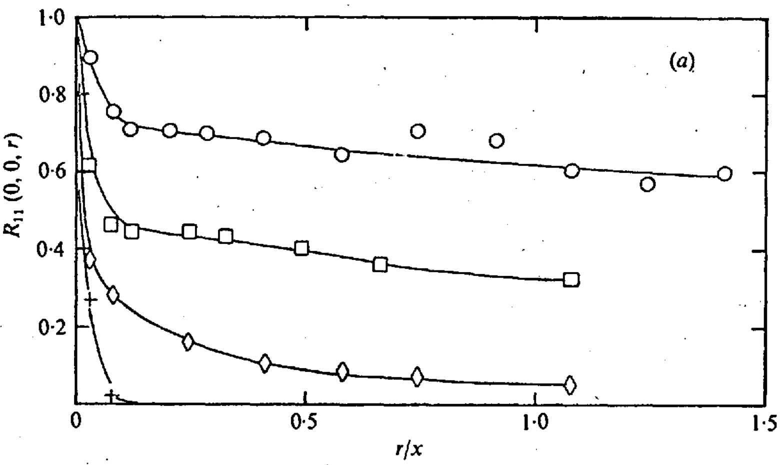

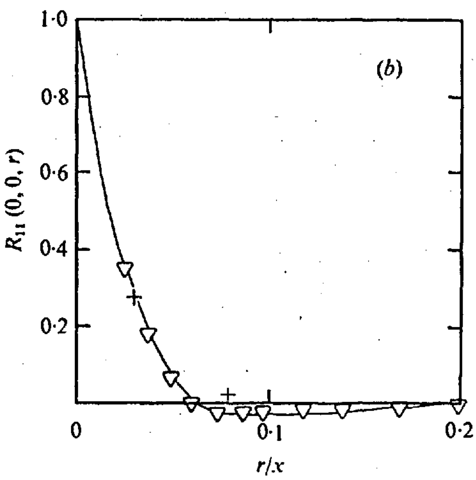

FIGURE 4. Spanwise correlations of longitudinal-component velocity fluctuations in mixing layer in 'still air', $\eta = -0{\cdot}056$. (*a*) $x = 12{\cdot}2$ cm. Jet speed U_1(m s^{-1}) and Reynolds number $U_1 x/\nu$: ○, 3·1, $2{\cdot}6 \times 10^4$; □, 5·5, $4{\cdot}6 \times 10^4$; ◇, 8·8, $7{\cdot}7 \times 10^4$; +, 15·3, $1{\cdot}3 \times 10^5$. (*b*) Fully turbulent region. +, $x = 12{\cdot}2$ cm, $U_1 = 15{\cdot}3$ ms^{-1}, $U_1 x/\nu = 1{\cdot}3 \times 10^5$; ▽, Bradshaw *et al.* (circular jet, circumferential traverse at $\eta = -0{\cdot}05$, $U_1 x/\nu = 7 \times 10^5$).

Lam Kit (1977) shows strongly three-dimensional pairing in a confined two-dimensional jet, effectively a mixing layer over a backward-facing step. Helical pairing of steady co-rotating trailing vortices from a wing with flaps is often observed (e.g. Bilanin *et al.* 1976). The rapid onset of three-dimensionality in our experiments was in marked contrast to the persistence of two-dimensionality in Brown & Roshko's work. This phase of our work was reported briefly by Bradshaw (1975): a more detailed description of work on the 75×12 cm rig, and of previous work on mixing-layer transition, is given by Chandrsuda & Bradshaw (1975), but their discussion is superseded by the present one.

To check the flow-visualization result that two-dimensionality rapidly disappeared, measurements of $R_{11}(0, 0, r)$, the correlation of the longitudinal components of velocity fluctuations with separation in the spanwise direction, were made over a range of speeds in the same mixing layer. The results are shown in figure 4 (*a*). At small values of $U_1 x/\nu$, i.e. in the transition region, large value of R_{11} are found at large r, indicating a strong tendency to two-dimensionality. At higher $U_1 x/\nu$ the spanwise scale decreases, which is consistent with the conventional development of three-dimensionality in the later stages of transition as shown in figure 3. At the highest speed, where transition is complete at the traverse position, the lateral integral scale is very roughly $0{\cdot}03x$, or $0{\cdot}15\delta_\omega$, where δ_ω is the 'inflexion thickness' or 'vorticity thickness' $\Delta U/(\partial U/\partial y)_{\max}$, introduced by Bradshaw *et al.* (1964). The values of $R_{11}(0,0,r)$ measured by the latter authors at $\eta = 0{\cdot}05$, $x/d = 2$ in a circular jet with $U_1 x/\nu = 7 \times 10^5$ are in agreement with the present measurements at the highest speed (figure 4*b*): figure 1 (*c*) of Bradshaw *et al.* shows that their flow was undoubtedly turbulent at this x/d. Jones, Planchon & Hammersley (1973) and Wygnanski (private communication) find lateral integral scales of order $0{\cdot}03x$ within two-stream mixing layers, but $0{\cdot}2$–$0{\cdot}3x$ in the irrotational flow on either side (see also Oster *et al.*). The reason is not clear, but the strong two-dimensional structure seen in Brown & Roshko's photographs would surely have produced large scales *within* the shear as well.

An incidental finding of our correlation measurements was that the long tail in $R_{11}(0,0,r)$ at $\eta \simeq -0{\cdot}05$ reappeared at large downstream distances, R_{11} asymptoting to as much as $0{\cdot}2$. This was found to be due to the proximity of the mixing layer to the floor of the test rig, the spanwise influence presumably being propagated via the irrotational fluctuations. When the working-section height was reduced, the long tail reappeared at a value of x giving nearly the same ratio of shear-layer thickness to working-section height. The correlation curves for $r/x < 0{\cdot}05$ agreed quite closely with the data of figure 4 (*b*). The large effect of a nearby solid surface on a mixing layer was pointed out by Castro & Bradshaw (1976); the present measurements were made during a study of this effect by Mr D. H. Wood, which will be reported separately by him. Clearly, the proximity of a solid surface can lead to unsound conclusions about two-dimensionality of large structure, and may have been *partly* responsible for the long tail in the above-mentioned correlations in the irrational flow.

The correlation measurements were not sensitive to the height of the tunnel side walls nor to the insertion of a vertical plate above the exit so that the jet emerged from a 'semi-infinite' wall. This suggests that the present single-stream mixing layer is a representative one and not subject, for instance, to unusually large external disturbances. Rodi (1975) cites the data for a plane mixing layer of Castro & Bradshaw (1976), obtained in the same rig at a speed of about 30 m s^{-1}, as among the most reliable: their spreading rate agrees closely with the measurements of Liepmann & Laufer (1947).

3. Measurements in a two-stream mixing layer

It seemed likely that the transitional disturbances in the two-stream mixing layers of Brown & Roshko and other workers kept their two-dimensionality, while ours did not, because the turbulence in each stream of the two-stream test rigs was much lower than that of the 'still air' in our single-stream rig (the latter turbulence level being no higher than in other typical single-stream rigs and at least one order of magnitude less than that of the mixing layer). This hypothesis was tested in another rig. A $1{\cdot}2 \times 0{\cdot}6$ m suck-down smoke tunnel, which had no contraction but whose intake was fitted with a honeycomb and four screens giving a turbulence level of about $0{\cdot}2\%$, was converted into a two-stream mixing-layer rig. The streams were separated by a $1{\cdot}2$ m wide partition extending all the way from the room wall, which was perpendicular to the tunnel axis, to the last screen. The velocity ratio was altered by fitting layers of cloth, or a solid baffle, over one half of the honeycomb, at which station a sheet of smoke was injected tangential to the partition and parallel to the flow. The faster stream velocity was typically $1\ \mathrm{m\,s^{-1}}$, so that the Reynolds number was of the same order as in our blower-tunnel tests.

Various combinations of velocity ratio and free-stream turbulence showed that the strength and persistence of the two-dimensional pattern increased as the velocity ratio departed from unity and decreased as the turbulence intensity in the low-velocity stream increased. The most spectacular change (figures 5 and 6, plate 3) occurred when the velocity of the low-speed stream was reduced from a few per cent of the mainstream velocity – just sufficient to supply the entrainment required by a mixing layer in still air – to zero. When the entrained air was delivered via the screens and honeycomb the turbulence level was low, and the two-dimensional structure in the shear layer was at least as strong as in Brown & Roshko's pictures. When the secondary stream was shut off, the flow became that over a backward-facing step, the entrained air was deflected upstream from the reattachment line and was thus highly turbulent, and the transitional oscillations became strongly three-dimensional almost as soon as they appeared. Similar results were obtained with a turbulence grid in the secondary stream, but the photographs are not so clear because smoke diffused into the reversed flow behind the grid bars and filled most of the high-speed stream. Even with the secondary stream shut off, the turbulence level in the entrained air is very much less than in the mixing layer itself: the mechanism is the distortion of weak oscillations in the transition region, not the disruption of fully developed turbulence structure by free-stream turbulence of the same order.

Figures 5 and 6 are photographs of thin illuminated longitudinal sections of a smoke-filled flow: this gives less clear results than the shadowgraph technique, which yields a spanwise average and therefore accentuates tendencies to two-dimensionality. It should be emphasized that even in the conditions of figure 6 the large-eddy structure is still very strong, so that in longitudinal sections we observe a fairly regular large-scale structure, having a spatial distribution which is not radically different from the later stages of the Brown–Roshko flow. The difference in the smaller-scale structure is easily seen in the figures, however, and of course results from the three-dimensionality of the larger eddies, as evidenced by the correlation measurements in the single-stream rig.

Even when two-dimensionality was normally absent, one strong and long-lived travelling vortex roll could be induced by thumping the test rig or suddenly altering the setting of the inlet baffle. Evidently the well-known sensitivity of free-shear-layer transition to mechanical or acoustic excitation implies a corresponding sensitivity of the Brown–Roshko structure. This could provide an explanation of many forms of resonance in jets.

4. Discussion

The above results show that, in the presence of free-stream turbulence of an intensity typical of many test rigs or engineering situations, the spanwise-vortex mode of mixing-layer instability can break down, via helical pairing, into fully three-dimensional turbulence with a spanwise integral scale of a fraction of the shear-layer thickness. The contrast between our flow-visualization results and those of Brown & Roshko and the contrast between our correlation measurements and those of Oster *et al.* leave little doubt that the Brown–Roshko structure did not persist in our experiments except for the case of the two-stream mixing layer with low turbulence in each stream. The large eddies that appear in our mixing layers are clearly of the conventional three-dimensional 'mixing jet' type, found in annular mixing layers by Bradshaw *et al.* (1964) and also found in other common types of shear layer. Equally clearly, Brown & Roshko's results indicate a quasi-two-dimensional pattern persisting for the full length of their test rig, and the free-stream turbulence level in their rig was undoubtedly lower than in the 'still air' surrounding our single-stream mixing layer. Before discussing the persistence of the Brown & Roshko pattern once it has formed, we review recent experiments which reveal more mechanisms for suppressing the Brown–Roshko pattern. We also attempt to distinguish the question of Brown–Roshko structure from questions about the effect of transition trips on the spreading rate.

Brown & Roshko stated that placing wire transition trips just upstream of the trailing edge of the splitter plate did not disrupt the large structure. However Hill, Jenkins & Gilbert (1976) present schlieren flow-visualization photographs of a plane jet, at rather low Reynolds number, which show a transitional/Brown–Roshko structure when the exit boundary layer is laminar and small-scale (presumably three-dimensional) structure when the exit boundary layer is turbulent. Both Bradshaw (1966) and Yule (1977) show that the turbulence intensity on, say, the line $\eta = 0$ in a circular jet rises monotonically with x to its self-preserving value if the exit boundary layer is turbulent but has a pronounced peak when the exit boundary layer is laminar, which suggests that the structure in the initial region is markedly different in the two cases. The trip used by Champagne, Pao & Wygnanski (1976) did not produce a fully turbulent boundary layer at the nozzle exit. The function of a trip wire is to cause separation, and thus produce an inflexionally unstable *mixing-layer* velocity profile; unless the shear layer reattaches some distance upstream of the exit, the transition process will be typical of a mixing layer rather than a boundary layer, i.e. it will be qualitatively the same as if the trip wire were not there. Batt (1975) and Oster *et al.* (1976) found that the spreading rate of a plane mixing layer could be increased by putting a trip wire near the nozzle exit. The trip wire of Oster *et al.* was 1·6 mm in diameter and only 10 mm (six diameters) upstream of the exit, and the shear layer can barely have reattached at all. Indeed the most plausible explanation for the increased spreading rate is intermittent reattachment leading to flapping of the mixing layer, perhaps involving a feedback mechanism. In this case the spreading rate would eventually return to normal. Birch (1977*a*, *b*) presents data for a mixing layer whose initial boundary layer was undoubtedly fully turbulent and, in agreement with Bradshaw (1966), finds closely the same asymptotic spreading rate as when the exit boundary layer is laminar although large differences occur in the initial region.

The spreading rate measured by Brown & Roshko (without a trip wire) agreed well with previous measurements at similar values of U_2/U_1 and, when extrapolated to $U_2/U_1 = 0$, agreed equally well with the consensus value of Liepmann & Laufer (1947), Birch and others, $d\delta_\omega/dx \simeq 0{\cdot}16$ in Brown & Roshko's notation. The most likely conclusions are

(i) that the Brown–Roshko structure does not appear when the initial boundary layer is fully turbulent (Hill *et al.*);

(ii) that the asymptotic spreading rate is independent of the state of the initial boundary layer (Birch) at least in the case $U_2/U_1 = 0$;

(iii) that the spreading rate found in the presence of Brown–Roshko structure is consistent with that mentioned in (ii); and, consequently,

(iv) that the questions of an anomalous spreading rate and of the existence of Brown–Roshko structure are not directly related.

Pui & Gartshore, in measurements in a two-stream mixing layer with

$$0{\cdot}65 < U_2/U_1 < 0{\cdot}83,$$

find that if the splitter-plate wake is strong enough for transition to occur via a vortex street (with contra-rotating vortices) the Brown–Roshko structure of co-rotating vortices does not appear. The flow-visualization results of Sabin (1963, figure 16) seem to show the same effect. Pui & Gartshore also show that free-stream turbulence increases the growth rate, but this is qualitatively expected and does not necessarily provide evidence about the Brown–Roshko structure. Pui & Gartshore's results suggest, again, that the Brown–Roshko structure will not appear if forestalled by transition.

Yule has recently studied the transition process in a circular jet (annular mixing layer) in 'still air'. As in the present experiment, the laminar flow instability pattern (in this case annular vortices rather than two-dimensional ones) breaks down rapidly into conventional turbulence: ring vortices are not observable in this turbulent region, no harmonics or subharmonics are seen in the frequency spectra, and although large eddies can be identified by flow visualization of the turbulent region they are not circumferentially coherent and their movements are more disorganized than those of the traditional vortex rings. However, three-dimensionality seems to appear in a different way from that found in our plane mixing layer: Yule's flow-visualization pictures, at Reynolds numbers based on jet diameter of order 10^4, show that a regular spanwise (i.e. circumferential) periodicity appears at an early stage, and after it has grown sufficiently a final pairing or entanglement of distorted vortices results in turbulent flow. The circumferential periodicity in the transition region was observed by Bradshaw *et al.* (1964; see the left-hand sides of figures 1*b*, *c*), who attributed it to the Lin–Benney mechanism (Benney 1961). As pointed out by Yule, the vortex-ring instability theory of Widnall & Sullivan (1973) is more relevant. The numerical results of Widnall & Sullivan show that the number of circumferential wavelengths is about 1·5 times the ratio of ring radius to vortex-core radius (i.e. wavelength $\sim 4\times$ core radius). In figure 1 (*b*) of Bradshaw *et al.* (1964), with a flow speed of $12\,\mathrm{m\,s^{-1}}$, there are about 18 wavelengths around the circumference while in figure 1 (*c*), at $85\,\mathrm{m\,s^{-1}}$, there are about 50. This agrees quite well with the expectation that the thickness of the laminar shear layer (which forms the core) will vary as $Re^{-\frac{1}{2}}$: $(\frac{85}{12})^{\frac{1}{2}} = 2{\cdot}66$; $\frac{50}{18} = 2{\cdot}78$. The observed radius of the rolled-up vortex sheet (the equivalent core) at the onset of

Authors	Situation	Breakdown mechanism
Bradshaw (1966) Hill *et al.* (1976) Yule (1977)	Circular jet, turbulent boundary layer	Existing turbulence
Bradshaw *et al* (1964) Yule (1977)	Circular jet, laminar boundary layer	Circumferential periodicity (Widnall–Sullivan)
Sabin (1963)	Two-stream mixing layer	Wake (vortex street) instability
Pui & Gartshore (1977)	Two-stream mixing layer, strong splitter-plate wake	Wake (vortex street) instability
Present	One-stream and two-stream mixing layer, high 'free-stream' turbulence	Helical pairing
Brown & Roshko (1974) Winant & Browand (1974) Oster *et al.* (1976)	Two-stream mixing layer, low free-stream turbulence	

TABLE 1

circumferential periodicity at $12\,\mathrm{m\,s^{-1}}$ does seem to be roughly one-twelfth of the jet radius as required for the 18-wavelength mode, but as the 'core' size grows rapidly the quantitative application of Widnall & Sullivan's mechanism to the annular mixing layer is not straightforward. The application to a *plane* mixing layer is also dubious: nominally the wavelength tends to a constant multiple of the core radius as the vortex-ring radius tends to infinity, but the higher modes of instability are very selective and it appears that the likelihood of excitation decreases as the mode number increases. Brown & Roshko's plan-view shadowgraph (their figure 8*b*) shows longitudinal streaks which are probably due to the Lin–Benney mechanism of longitudinal-vorticity generation: the relation of the latter to the Widnall–Sullivan mechanism is obscure because Widnall & Sullivan do not consider the details of the viscous region at all, but both mechanisms are aspects of self-induced distortion of vortex lines. In Brown & Roshko's figure 8 (*b*) the breakdown of two-dimensionality is – at most – very slow and not rapid as in Yule's experiments, so strong effects of spanwise periodicity are apparently confined to the circular jet. At least in the experiments of Bradshaw *et al.* and of Yule, 'free-stream' turbulence has no significant effect. Probably it would act in the same way as in a plane mixing layer if not forestalled by Widnall–Sullivan instability, but it is possible that vortex rings are more resistant to distortion than straight vortex lines.

The experiments discussed above and summarized in table 1 strongly suggest that the Brown–Roshko structure appears only when not forestalled by three-dimensionality in the transition region or by pre-existing turbulence. It remains to discuss the circumstances in which the Brown–Roshko structure will appear, and to speculate on its persistence.

It seems that the main case in which Brown–Roshko structure (nearly two-dimensional, nearly self-preserving spanwise vortices in the presence of small-scale three-dimensional turbulence) can appear and persist is the plane mixing layer with a low turbulence level in the fluid on either side. Unless special precautions are taken this implies a two-stream mixing layer fed from a high-quality contraction. This is a rather rare type of flow, and seems not to have been the subject of detailed turbulence measurements and flow visualization prior to Brown & Roshko's work. Another group of possible cases are flows with a feedback mechanism or artificial excitation, such as a bluff-body vortex street or the Crow–Champagne oscillations in a circular jet: however this kind of orderly structure is likely to vary too much from case to case to be usefully compared with Brown & Roshko's mixing layer.

At present it is not certain whether or not the Brown–Roshko structure will persist indefinitely, once formed. The instability mechanism in a laminar mixing layer is effectively inviscid at practical Reynolds numbers, the critical Reynolds number based on shear-layer thickness being much less than 100. Therefore if no secondary instabilities occur, the primary instability mode can continue to increase in amplitude in the presence of small-scale turbulence (very crudely speaking, it will grow if the Reynolds number based on the eddy viscosity ν_T is higher than the critical Reynolds number mentioned above, which is the case even in a fully turbulent mixing layer where $\Delta U\delta_\omega/\nu_T \equiv \rho\Delta U^2/\tau_{\max} \simeq 100$).

The amplitude will presumably self-limit at some fraction of ΔU, the energy input going into an increase in spatial scale (shear-layer growth). Thus energy considerations alone reveal no reason why the Brown–Roshko pattern should not continue indefinitely, and it cannot be dismissed as a laminar-flow instability mode which automatically decays in turbulent flow. Conversely, the lack of influence of viscosity on the original instability implies that the presence of the Brown–Roshko structure at high Reynolds numbers does not *prove* that it is real turbulence rather than a relic of transition. Taylor–Görtler (longitudinal) vortices in a curved or rotating flow provide a precedent for an instability pattern common to laminar and turbulent flow. However the instantaneous vortex pattern in curved or rotating turbulent flows is usually quite unsteady, with random spanwise migration (Johnston, Halleen & Lezius 1972), and a given streamwise vortex cannot be reliably identified for a long axial (streamwise) distance. If the spanwise vortices of the Brown–Roshko pattern start to lose axial (spanwise) coherence it seems inevitable that the pairing process will enhance the three-dimensionality, causing eventual breakdown to fully three-dimensional turbulence. The vortex street behind a two-dimensional bluff body is an example of a structure that can maintain two-dimensionality for a long distance downstream but eventually subsides into conventional turbulence. Our view of Brown & Roshko's shadowgraph pictures is that they do show increasing disorganization and three-dimensionality as the downstream distance increases, to a greater extent than can be explained by the presence of small-scale three-dimensional turbulence cascaded from an essentially two-dimensional large structure. However, the question of indefinite persistence is almost an academic one because, as has been well pointed out by Dimotakis & Brown (1976), the total length of a typical flow is only a few large-eddy life 'times': thus the Brown–Roshko structure, if formed, may very well persist to the end of the flow. The present experiments were not, of course, designed to achieve an asymptotic state.

The above discussion does not constitute a denial of the importance of large eddies (or 'large structure') in turbulent flow. Indeed it is because of their importance that we must be as clear as possible about the degree of orderliness of the large eddies, in particular their spanwise extent (ratio of spanwise integral scale to shear-layer width) and streamwise periodicity (sharpness of peak in longitudinal wavenumber spectrum). The results of the present paper imply that inferences, drawn by other authors from Brown & Roshko's results, about the orderliness (and therefore the tractability) of turbulence may be much too optimistic.

5. Conclusion

The present experiments in plane mixing layers, and the foregoing review of other recent work, suggest that the two-dimensional vortex-roll disturbances found by Brown & Roshko (1974) arise in the transition region, and will appear only in plane mixing layers with laminar boundary layers at the nozzle exit and low turbulence in the external flow. It appears that the turbulence level in the 'still air' on one side of a plane single-stream mixing layer (which is in fact fluid recirculated from the mixing layer itself) is high enough to induce three-dimensionality at an early stage in transition, followed by helical vortex pairing. In a circular jet three-dimensionality appears via a vortex-ring instability (Yule 1977). The Brown–Roshko structure also fails to appear if transition occurs in the wake of the splitter plate of a two-stream mixing layer rather than in the mixing layer itself (Pui & Gartshore 1977); this and other evidence suggests that the Brown–Roshko structure will not appear if the exit boundary layer is turbulent.

We conclude that the Brown–Roshko structure is rare in practice, the normal form of large structure in a mixing layer being fully three-dimensional. When the Brown–Roshko structure does appear it may still be identifiable at the downstream end of a typical flow, simply because most flow-rig lengths are not many times a large-eddy life 'time' (Dimotakis & Brown 1976). However the sensitivity of the transitional instability mode to three-dimensionality suggests that the Brown–Roshko structure will slowly succumb to three-dimensionality generated by its associated small-scale turbulence: if this is so, which we are strongly inclined to believe, there is only one asymptotic state of a plane mixing layer and its large structure, though strong and undoubtedly of great importance in determining flow development, is fully three-dimensional and less orderly than the Brown–Roshko structure.

We are grateful to Professor I. S. Gartshore, Professor A. Roshko and Dr A. J. Yule for helpful correspondence, to Mr D. H. Wood for obtaining the results shown in figure 4, and to Mr Wood and a referee for comments on the manuscript. C. C. wishes to acknowledge the support of the Royal Thai Air Force. The work was partly supported by the Science Research Council under Grant B/SR/8978.

REFERENCES

Batt, R. G. 1975 *A.I.A.A. J.* **13**, 245.

Benney, D. 1961 *J. Fluid Mech.* **10**, 209.

Bilanin, A. J., Teske, M. E., Donaldson, C. DuP. & Snedeker, R. S. 1976 *N.A.S.A. Symp. Wake Vortex Minimization, Wash.*, p. 55.

Birch, S. F. 1977*a* In *Turbulence in Internal Flows* (ed. S. N. B. Murthy), p. 89. Hemisphere.

Birch, S. F. 1977*b* Paper presented at *Penn. State Univ. Symp. Turbulent Shear Flow.*

Bradshaw, P. 1966 *J. Fluid Mech.* **26**, 225.

BRADSHAW, P. 1975 In *Turbulent Mixing in Nonreactive and Reactive Flows* (ed. S. N. B. Murthy), p. 243. Plenum.
BRADSHAW, P., FERRISS, D. H. & JOHNSON, R. F. 1964 *J. Fluid Mech.* **19**, 591.
BROWN, G. L. & ROSHKO, A. 1974 *J. Fluid Mech.* **64**, 775.
CASTRO, I. P. & BRADSHAW, P. 1975 *J. Fluid Mech.* **73**, 265.
CHAMPAGNE, F. H., PAO, Y. H. & WYGNANSKI, I. J. 1976 *J. Fluid Mech.* **74**, 209.
CHANDRSUDA, C. & BRADSHAW, P. 1975 *Imp. Coll. Aero. Rep.* no. 75-03.
CROW, S. C. & CHAMPAGNE, F. H. 1971 *J. Fluid Mech.* **48**, 547.
DIMOTAKIS, P. E. & BROWN, G. L. 1976 *J. Fluid Mech.* **78**, 535.
GRANT, H. L. 1958 *J. Fluid Mech.* **4**, 149.
HILL, W. G., JENKINS, R. C. & GILBERT, B. L. 1976 *A.I.A.A. J.* **14**, 1513.
JIMINEZ, J. 1975 *Phys. Fluids* **18**, 1580.
JOHNSTON, J. P., HALLEEN, R. M. & LEZIUS, D. K. 1972 *J. Fluid Mech.* **56**, 533.
JONES, B. J., PLANCHON, H. P. & HAMMERSLEY, R. J. 1973 *A.I.A.A. J.* **11**, 1146.
LAM KIT 1977 M.Phil. thesis, Mech. Engng Dept., University of Hong Kong.
LIEPMANN, H. W. & LAUFER, J. 1947 *N.A.C.A. Tech. Note* no. 1257.
OSTER, D., WYGNANSKI, I. & FIEDLER, H. 1977 In *Turbulence in the Internal Flows* (ed. S. N. B. Murthy), p. 67. Hemisphere.
PUI, N. K. & GARTSHORE, I. S. 1977 Paper presented at *6th Can. Cong. Appl. Mech.*
ROCKWELL, D. O. 1977 *J. Fluid Engng* **99**, 240.
RODI, W. 1975 In *Studies in Convection* (ed. B. E. Launder), vol. 1, p. 79. Academic Press.
SABIN, C. M. 1963 *Thermosci. Div., Stanford Univ. Rep.* MD-9.
WEBER, D. P. 1974 Ph.D. thesis, University of Illinois at Urbana Champaign.
WIDNALL, S. & SULLIVAN, J. P. 1973 *Proc. Roy. Soc.* A **332**, 335.
WILLE, R. 1963 *Z. Flugwiss.* **11**, 222.
WINANT, C. D. & BROWAND, F. K. 1974 *J. Fluid Mech.* **63**, 2.
YULE, A. 1977 Submitted to *J. Fluid Mech.*

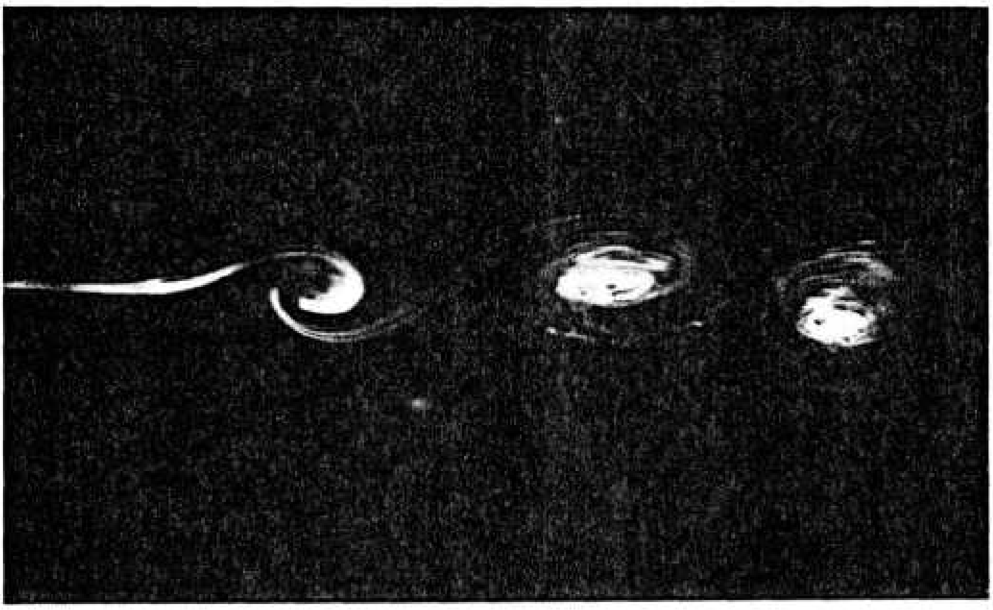

FIGURE 1. Side view of vortex-roll growth and breakdown in mixing layer in 'still air'. High-velocity stream is on upper side. Reynolds number based on length of photograph approximately 10 000.

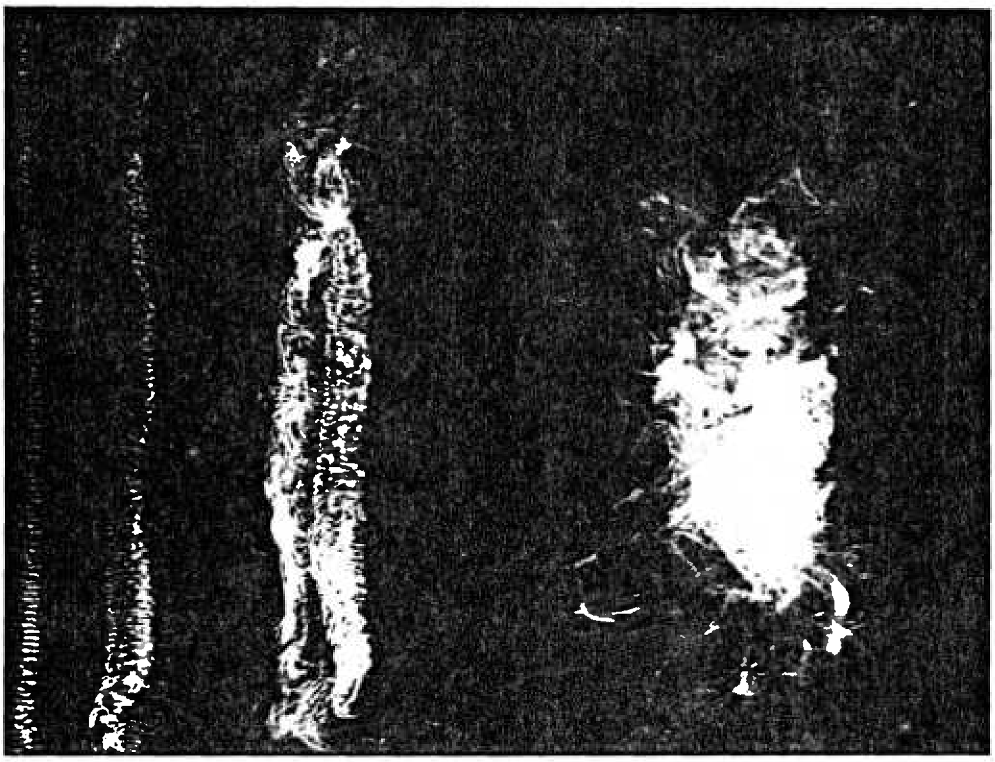

FIGURE 2. Plan view of vortex-roll growth and breakdown in mixing layer in 'still air', viewed from still-air side. Reynolds number based on length of photograph approximately 40 000.

Journal of Fluid Mechanics, Vol. 85, part 4 *Plate 2*

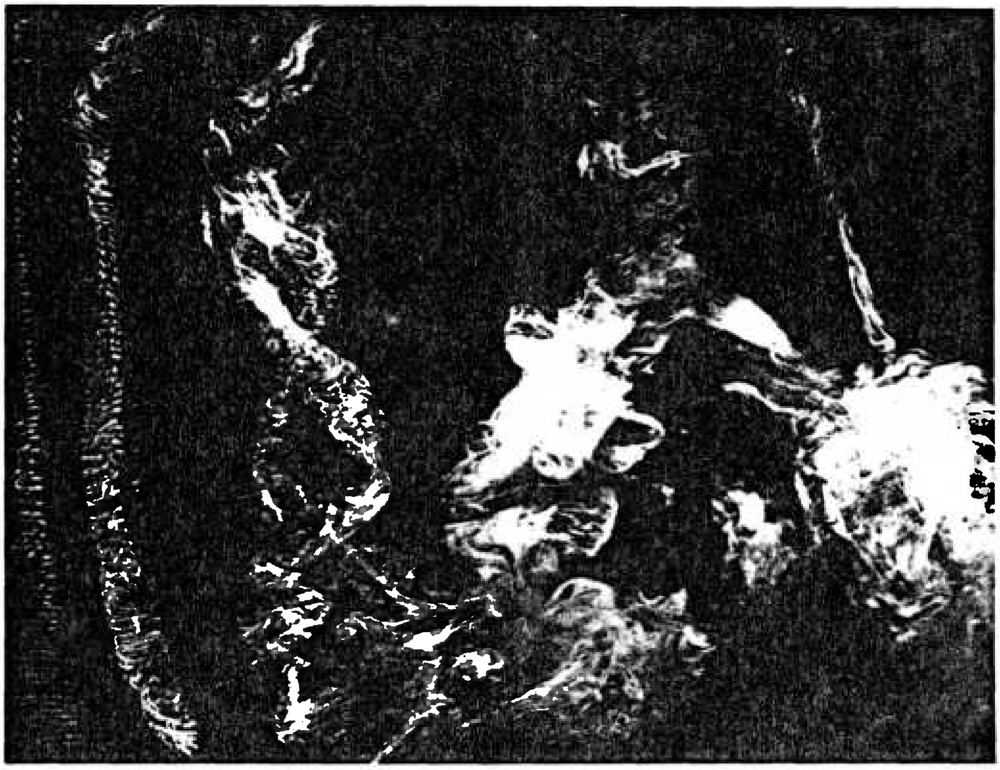

FIGURE 3. Plan view of double-helix vortex pairing. Conditions as in figure 2.

Journal of Fluid Mechanics, Vol. 85, part 4 *Plate 3*

FIGURE 5. Side view of persistent two-dimensional structure in two-stream mixing layer. Stream speed ratio about 30 : 1. Reynolds number based on length of photograph approximately 60000. Illuminated longitudinal section of smoke-filled flow.

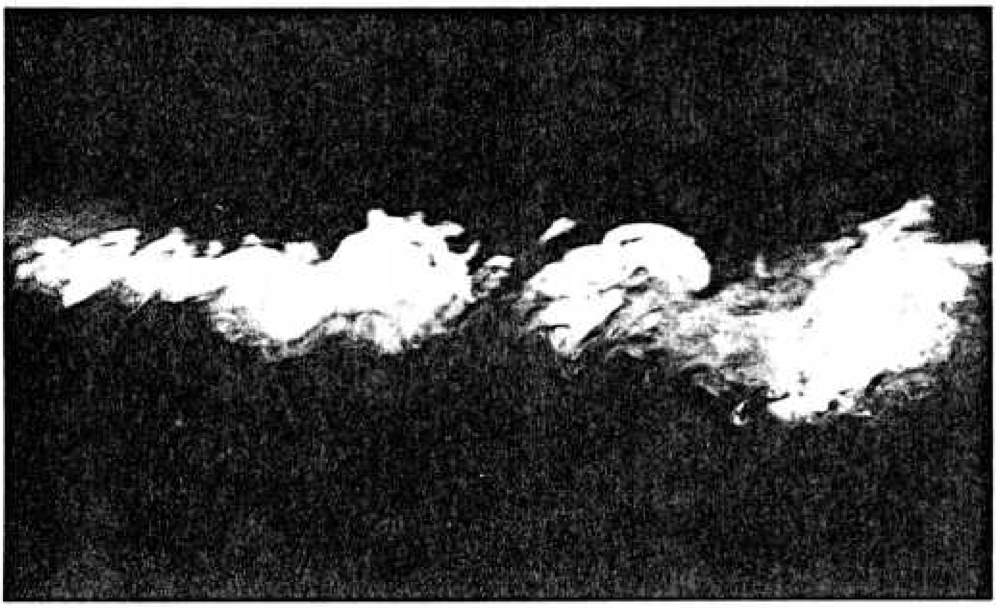

FIGURE 6. Conventional turbulence in two-stream mixing layer. Conditions as in figure 5 except that low-speed stream has been stopped completely and entrainment flow is provided by highly turbulent recirculating air. Again only a longitudinal section is illuminated.

APPENDIX B

VELPROF PROGRAM

The VELPROF program is a boundary layer data analysis program. It accepts total (and if necessary, static) pressure readings on paper tape and external data such as fluid properties, apparatus calibration curves, station parameters, etc., and outputs velocity, static pressure and log. profiles, integral parameters and other information.

For the present analysis, the paper tape input consisted of the probe position, dynamic pressure, tunnel reference pressure and a discrete voltage used to distinguish points in the boundary layer from those in the free-stream. The dynamic pressure readings were factored by the change in tunnel reference pressure so that the evaluated profile was that at a constant tunnel dynamic head. The program applied MacMillan's (1956) shear correction to the profile.

The routines to work out the integral parameters in the program were defeated by the abnormalities in the measured boundary layer profiles and were thus ignored.

The LOGLAW option in the program works out the best semi-logarithmic fit to the experimental points in the log. law range, calculates the skin friction coefficient from the Clauser chart and computes the Pearson's correlation coefficient as a statistical measure of the accuracy of the fitting.

A best fit line is worked out in the Clauser chart co-ordinates $\ln(U_e y/\nu)$, U/U_e for a specified pair of points $\left(\frac{u_\tau y}{\nu} = 50 \text{ and } y = 0.2\delta\right)$. For this analysis, the pair of points were supplied externally, from preliminary plots.

Now writing the log. law as:-

$$\frac{U}{u_\tau} = \frac{1}{K}\left(\ln \frac{u_\tau y}{\nu} + A\right)$$

where K (the Karman constant) = 0.41, A = 2.05 (Coles' values). Substituting $u_\tau = U_e \sqrt{c_f/2}$, we get:-

$$\frac{U}{U_e} = \frac{1}{K}\sqrt{\frac{c_f}{2}}\left(\ln \frac{U_e y}{\nu}\sqrt{\frac{c_f}{2}} + A\right)$$

or:-

$$Y = A' + B'X$$

where $Y = \frac{U}{U_e}$, $A' = B'\left(\ln \sqrt{\frac{c_f}{2}} + A\right)$, $B' = \frac{1}{K}\sqrt{\frac{c_f}{2}}$, $X = \ln \frac{U_e y}{\nu}$

The parameters A′ and B′ are worked out by the least squares method. The value of c_f yielding the best fit to Coles' law is then computed by an iterative process.

APPENDIX C

HOT WIRE CALIBRATIONS AND CORRECTIONS

1. CALIBRATIONS

(a) Velocity Calibration

The important relation required when operating a hot wire at constant temperature is that of the Nusselt number with Reynolds number. A universally accepted relation is that due to King:-

$$Nu = A + BRe^n$$

where:-

$$Nu = \frac{\dot{H}_f/\ell}{\pi k_f(T_w - T_f)} \quad \text{and } Re = \frac{Ud_w}{\nu}$$

Although King gave a value of 0.5 for the semi-empirical index, n, recent work has shown that a value of 0.45 gives a better correlation for flow speeds of less than 50 m/s; consequently, n = 0.45 was used throughout the present analysis.

Since the heat transfer rate from the wire is proportional to the power input, the above relation can be reduced to one which is more directly usable:-

$$E^2 = A + BU^n$$

Fig. C1 shows a typical velocity calibration.

(b) Yaw Calibration

For a wire inclined to the mean flow at an angle ψ, to a first approximation the heat transfer from the wire is independent of the axial component of velocity. This approximation is known as the "cosine law" and gives for the effective cooling velocity for calibration in the free-stream (V = 0):-

$$U_{eff} = U \cos \psi$$

Other expressions have been proposed for the cooling velocity, with empirical constants which depend on the length to diameter ratio of the wire, but for "infinitely long" wires and for $0 < \psi < 60^{\circ}$, the cosine law is adequate. Also, it is quite difficult to measure the geometric wire angles accurately, a necessity for the other correlations.

The best solution, as described by Bradshaw (1971), is to assume the cosine law and work out an "effective angle" of the wire which is the ratio of the v-component sensitivity to the u-component sensitivity.

Considering just one wire, when the probe is yawed through an angle δ, we obtain:-

$$E_i^2 = A_1 + B_1 \left[U \cos (\psi_1 + \delta) \right]^n$$

Assuming δ is independent of the small changes in wire calibration that may occur during the yaw calibration, we obtain for $\delta = 0$:-

$$E^2_{1_{\delta=0}} = A_1 + B_1 \left[U \cos \psi_1 \right]^n$$

and hence:-

$$\frac{\text{Cos }(\psi_1 + \delta)}{\text{Cos }\psi_1} = \left[\frac{E_1^2 - A_1}{E^2_{1\,\delta=0} - A_1}\right]^{\frac{1}{n}}$$

and rearranging this:-

$$\text{Cos }\delta - \left[\frac{E_1^2 - A}{E^2_{1\,\delta=0} - A}\right]^{\frac{1}{n}} = \text{Tan }\psi_1 \text{ Sin }\delta$$

So having obtained A from the velocity calibration, the left-hand side of the above equation is plotted against Sin δ, for various δ, and the slope of the resulting straight curve gives Tan ψ_1. The same procedure is followed for the second wire. A typical yaw calibration is shown in Fig. C2. All the linear fits were calculated by the least squares method.

2. CALIBRATION DRIFT CORRECTIONS

(a) Temperature Corrections

Changes in fluid temperature affect both mean and fluctuating data. The mean calibration data was corrected using Bearman's (1971) correction:-

$$\frac{\Delta E}{E} = - \frac{\alpha}{2(R - 1)} \Delta\theta$$

where R is the overheat ratio, α is the temperature resistivity of the wire, $\Delta\theta$ is the temperature change in the fluid and ΔE is the "error" voltage.

Various expressions exist for temperature corrections to fluctuating quantities in terms of changes in the velocity calibration constants. The procedure followed here, for the profiles, was to recalculate the velocity calibration constants for each profile point temperature, using the above correction. By doing this both mean and fluctuating quantities are corrected for changes in fluid temperature.

(b) <u>Spurious Drift Corrections</u>

Apart from fluid temperature, hot wire calibrations are also affected by physical changes in the wire itself. This could be in the form of dirt accumulating on the wire and is important particularly during long runs, as in this case. Although changes in the calibration constants due to this were small, (Fig. C1), account for it was made by assuming a linear variation of the calibration constants through the profile. A typical change in calibration constant due to this, per profile point, was less than 1%.

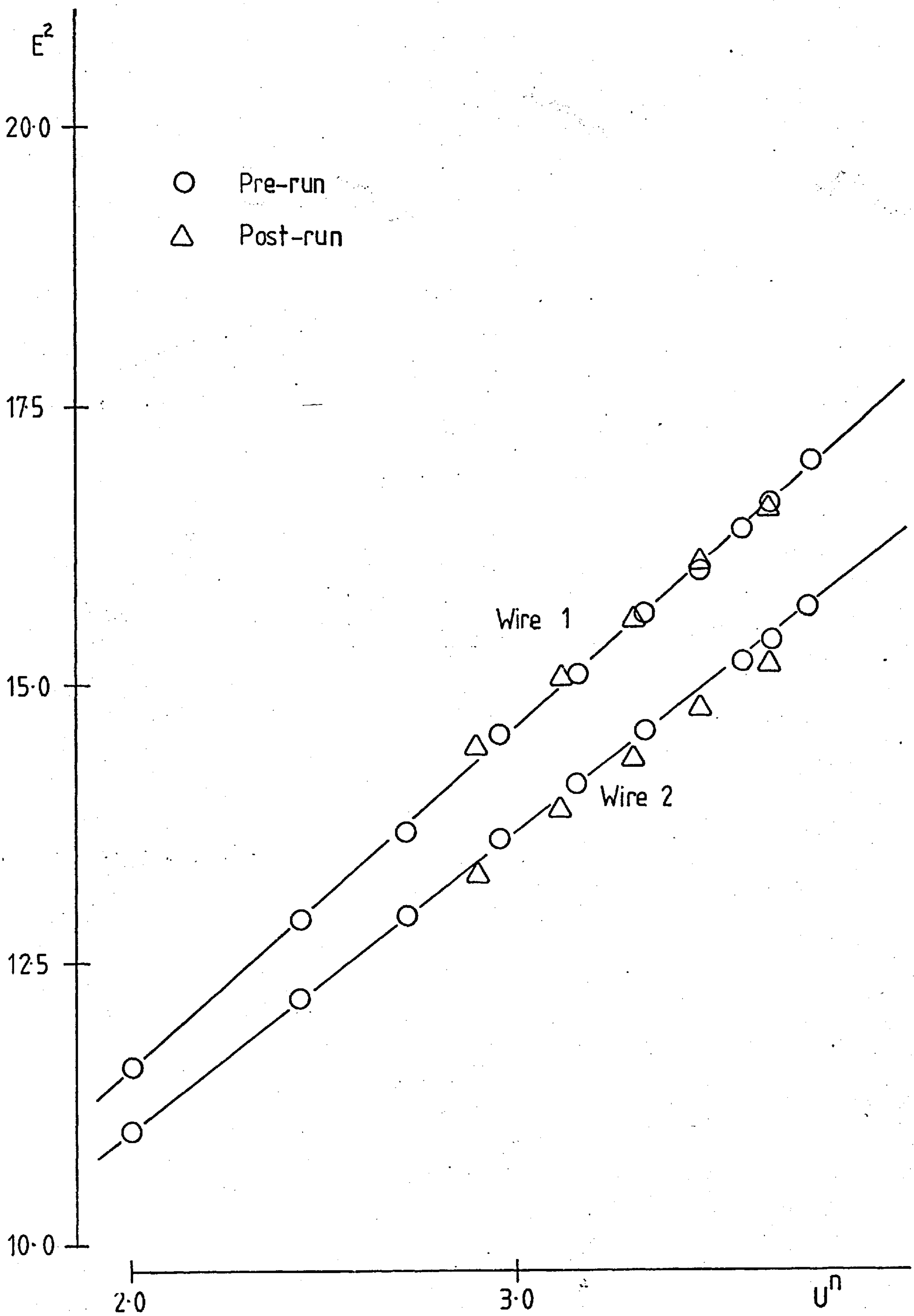

Fig. C1 A typical X-wire velocity calibration.

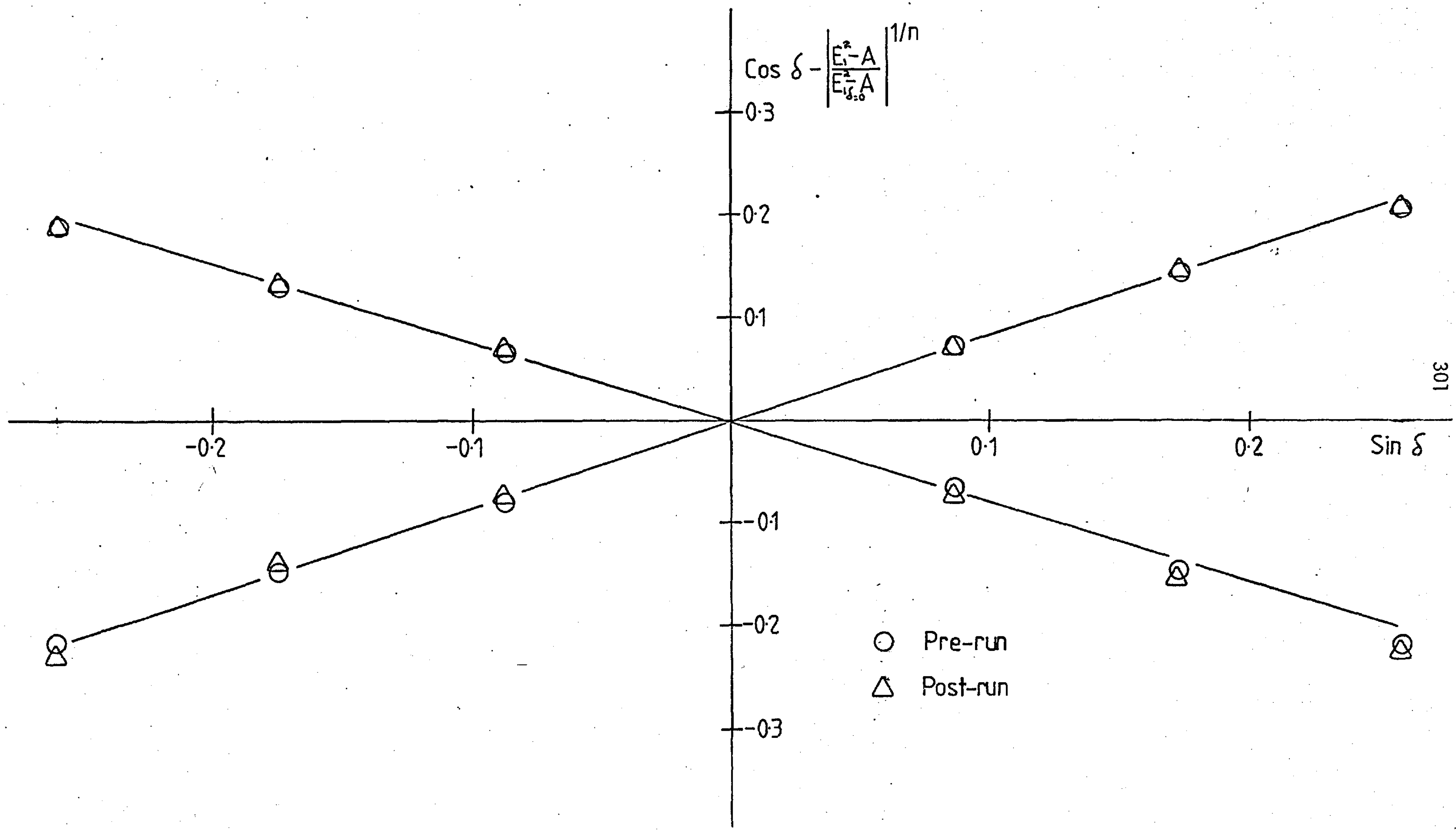

Fig. C2 A typical X-wire yaw calibration

APPENDIX D

TURBULENCE DATA ANALYSIS

(a) Mean Quantities

A X-wire with effective wire angles ψ_1 and ψ_2 has the response:-

$$E_1^2 = A_1 + B_1(U \cos\psi_1 + V \sin\psi_1)^n \tag{D1}$$

$$E_2^2 = A_2 + B_2(U \cos\psi_2 - V \sin\psi_2)^n \tag{D2}$$

Rearranging these:-

$$U \cos\psi_1 + V \sin\psi_1 = \left[(E_1^2 - A_1)/B_1\right]^{\frac{1}{n}} = C1, \text{ say} \tag{D3}$$

$$U \cos\psi_2 - V \sin\psi_2 = \left[(E_2^2 - A_2)/B_2\right]^{\frac{1}{n}} = C2, \text{ say} \tag{D4}$$

In matrix form:-

$$\begin{bmatrix} \cos\psi_1 & \sin\psi_1 \\ \cos\psi_2 & -\sin\psi_2 \end{bmatrix} \begin{bmatrix} U \\ V \end{bmatrix} = \begin{bmatrix} C1 \\ C2 \end{bmatrix} \tag{D5}$$

Therefore:-

$$U = \begin{vmatrix} C1 & \sin\psi_1 \\ C2 & -\sin\psi_2 \end{vmatrix} \Bigg/ \begin{vmatrix} \cos\psi_1 & \sin\psi_1 \\ \cos\psi_2 & -\sin\psi_2 \end{vmatrix} \tag{D6}$$

$$V = \begin{vmatrix} \text{Cos } \psi_1 & C1 \\ \text{Cos } \psi_2 & C2 \end{vmatrix} \Bigg/ \begin{vmatrix} \text{Cos } \psi_1 & \text{Sin } \psi_1 \\ \text{Cos } \psi_2 & -\text{ Sin } \psi_2 \end{vmatrix} \tag{D7}$$

(b) <u>Fluctuating Quantities</u>

Now, since $E_1 = f(U, V)$, on differentiating:-

$$dE_1 = \frac{\partial E_1}{\partial U} dU + \frac{\partial E_1}{\partial V} dV \tag{D8}$$

or:-

$$e_1 = \frac{\partial E_1}{\partial U} (u + v \text{ Tan } \psi_1) \tag{D9}$$

for small fluctuations and assuming the Cosine law.

Differentiating eq. (D1) with respect to U gives:-

$$2E_1 \frac{\partial E_1}{\partial U} = n \; B_1 \; U^{n-1} \; \text{Cos}^n \; \psi_1 \tag{D10}$$

Therefore:-

$$\frac{\partial E_1}{\partial U} = \frac{n}{2E_1 U} \; (E_1^2 - A_1) \tag{D11}$$

Substituting for $\frac{\partial E_1}{\partial U}$ in eq. (D9):-

$$e_1 = \frac{n(E_1^2 - A_1)}{2E_1 U} (u + v \text{ Tan } \psi_1) \tag{D12}$$

or:-

$$e_1 = k_1(u + \alpha_1 v) \tag{D13}$$

where:-

$$k_1 = \frac{n(E_1^2 - A_1)}{2E_1 U} \quad \text{and } \alpha_1 = \text{Tan } \psi_1$$

Similarly:-

$$e_2 = k_2(u - \alpha_2 v) \tag{D14}$$

Taking the mean squares of eqs. (D13) and (D14):-

$$\overline{e_1^2} = k_1^2 \; \overline{u^2} + (k_1\alpha_1)^2 \; \overline{v^2} + 2k_1^2\alpha_1 \; \overline{uv}$$

$$\overline{e_2^2} = k_2^2 \; \overline{u^2} + (k_2\alpha_2)^2 \; \overline{v^2} - 2k_2^2\alpha_2 \; \overline{uv}$$

$$\overline{(e_1 - e_2)^2} = (k_1 - k_2)^2 \; \overline{u^2} + (k_1\alpha_1 + k_2\alpha_2)^2 \; \overline{v^2} +$$

$$+ 2(k_1 - k_2)\;(k_1\alpha_1 + k_2\alpha_2)\; \overline{uv}$$

Expressing the coefficients of the RHS as elements in a matrix A and those of the LHS as matrix B:-

$$\begin{bmatrix} A11 & A12 & A13 \\ A21 & A22 & A23 \\ A31 & A32 & A33 \end{bmatrix} \begin{bmatrix} \overline{u^2} \\ \overline{v^2} \\ \overline{uv} \end{bmatrix} = \begin{bmatrix} B1 \\ B2 \\ B3 \end{bmatrix}$$

Therefore:-

$$\overline{u^2} = \begin{vmatrix} B1 & A12 & A13 \\ B2 & A22 & A23 \\ B3 & A32 & A33 \end{vmatrix} \Bigg/ |A|$$

$$\overline{v^2} = \begin{vmatrix} A11 & B1 & A13 \\ A21 & B2 & A23 \\ A31 & B3 & A33 \end{vmatrix} \Bigg/ |A|$$

and:-

$$\overline{uv} = \begin{vmatrix} A11 & A12 & B1 \\ A21 & A22 & B2 \\ A31 & A32 & B3 \end{vmatrix} \Bigg/ |A|$$

All the calibration constants together with the mean and fluctuating voltages and the profile and calibration temperatures were fed into a computer program which reduced and plotted the results.

APPENDIX E

TRANSPORT EQUATIONS

The exact transport equation for any turbulent stress in tensor notation is:-

$$\frac{D}{Dt}(\overline{u_i u_k}) = -\left[\overline{u_i u_j}\frac{\partial U_k}{\partial x_j} + \overline{u_j u_k}\frac{\partial U_i}{\partial x_j}\right] \quad \text{Production Term}$$

$$-\frac{\partial}{\partial x_j}(\overline{u_i u_j u_k}) - \frac{1}{\rho}\left[\frac{\overline{\partial p' u_i}}{\partial x_k} + \frac{\overline{\partial p' u_k}}{\partial x_i}\right] \quad \text{Turbulent Diffusion Term}$$

$$+\overline{p'\left[\frac{\partial u_i}{\partial x_k} + \frac{\partial u_k}{\partial x_i}\right]} \quad \text{Pressure-Rate of Strain Term}$$

$$+\nu\overline{\left[u_i\frac{\partial^2 u_k}{\partial x^2_j} + u_j\frac{\partial^2 u_i}{\partial x^2_j}\right]} \quad \text{Viscous Term}$$

By putting k = i, we obtain the turbulent kinetic energy transport equation:-

$$\frac{D\frac{1}{2}\overline{u_i^2}}{Dt} = -\overline{u_i u_j}\frac{\partial U_i}{\partial x_j} - \frac{\partial}{\partial x_j}(\overline{p' u_j} + \frac{1}{2}\overline{u_i^2 u_k}) + \nu\overline{u_i\frac{\partial u_i}{\partial x_j^2}}$$

Advection Production Diffusion Dissipation

APPENDIX F

EVALUATION OF THE PRESSURE DROP ALONG A STREAMLINE

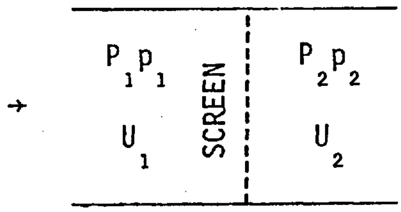

Along a streamline:-

$P_1 = P_2 + \Delta P$, where ΔP is the total pressure drop across the screen (F1)

Therefore:-

$$p_1 + \frac{1}{2}\rho U_1^2 = p_2 + \frac{1}{2}\rho U_2^2 + \Delta P \qquad \text{(F2)}$$

therefore:-

$$\frac{\Delta P}{\frac{1}{2}\rho U_e^2} = \frac{p_1 - p_2}{\frac{1}{2}\rho U_e^2} - \left(\frac{U_2^2 - U_1^2}{U_e^2}\right) \qquad \text{(F3)}$$

Now in the free stream, by definition:-

$$\Delta P = \frac{1}{2}\rho U_e^2 K \neq p_1 - p_2 \text{ in a finite tunnel} \qquad \text{(F4)}$$

However, once the static pressure has equalized, downstream of the screen, p_2 is constant across the boundary layer and the first term on the right-hand side of eq. (F3) is a constant for a given screen.

From the measured velocity profiles at x = 140 mm, $\psi(=\int U dy)$ was calculated using Simpson's rule and plotted against $(U/U_e)^2$. Values of $(U_2/U_e)^2$ and $(U_1/U_e)^2$ were then determined graphically for given values of ψ. Fig. 3.59 shows $\frac{U_2^2 - U_1^2}{U_e^2}$ (pressure loss deficit) plotted against ψ.